

Bibliothèque nationale du Canada

Canadian Theses Service

Service des thèses canadiennes

Ottawa, Canada K1A 0N4

NOTICE

The quality of this microform is heavily dependent upon the quality of the original thesis submitted for microfilming. Every effort has been made to ensure the highest quality of reproduction possible.

If pages are missing, contact the university which granted the degree.

Some pages may have indistinct print especially if the original pages were typed with a poor typewriter ribbon or if the university sent us an inferior photocopy.

Reproduction in full or in part of this microform is governed by the Canadian Copyright Act, R.S.C. 1970, c. C-30, and subsequent amendments.

AVIS

La qualité de cette microforme dépend grandement de la qualité de la thèse soumise au microfilmage. Nous avons tout fait pour assurer une qualité supérieure de reproduction.

S'il manque des pages, veuillez communiquer avec l'université qui a conféré le grade.

La qualité d'impression de certaines pages peut aisser à désirer, surtout si les pages originales ont été dactylographiées à l'aide d'un ruban usé ou si l'université nous a fait parvenir une photocopie de qualité inférieure.

La reproduction, même partielle, de cette microforme est soumise à la Loi canadienne sur le droit d'auteur, SRC 1970, c. C-30, et ses amendements subséquents.



INVESTIGATION OF VAPOR EXPLOSIONS WITH SINGLE MOLTEN METAL DROPS IN WATER USING FLASH X-RAY

Thesis by

Gaby Ciccarelli

Department of Mechanical Engineering

McGill University

Montreal, Quebec, Canada

Submitted September 30, 1991

A Thesis Submitted to the Faculty of Graduate Studies and Research in Partial Fulfillment of the Requirements for the Degree of Doctor of Philosophy



Bibliothèque nationale du Canada

Canadian Theses Service

Service des thèses canadiennes

Ottawa, Canada K1A 0N4

> The author has granted an irrevocable nonexclusive licence allowing the National Library of Canada to reproduce, loan, distribute or sell copies of his/her thesis by any means and in any form or format, making this thesis available to interested persons.

> The author retains ownership of the copyright in his/her thesis. Neither the thesis nor substantial extracts from it may be printed or otherwise reproduced without his/her permission.

L'auteur a accordé une licence irrévocable et non exclusive permettant à la Bibliothèque nationale du Canada de reproduire, prêter, distribuer ou vendre des copies de sa thèse de quelque manière et sous quelque forme que ce soit pour mettre des exemplaires de cette thèse à la disposition des personnes intéressées.

L'auteur conserve la propriété du droit d'auteur qui protège sa thèse. Ni la thèse ni des extraits substantiels de celle-ci ne doivent être imprimés ou autrement reproduits sans son autorisation.

ISBN 0-315-74626-2



ABSTRACT

In the present study, flash x-ray photography as well as high speed regular photography was used to investigate the fragmentation process during the vapor explosion of single drops of molten metal in water. For drops heated to 700°C, a vapor bubble is formed around the drop after a short induction time of about 80 µs which grows to a maximum diameter and then collapses. X-ray radiographs, which can "see through" the vapor bubble, show that filaments of metal protruding from the drop surface are produced during the bubble growth. At the time of the bubble collapse, the drop surface is highly convoluted and a second interaction is initiated producing an even larger second bubble in the case of tin drops. A mechanism based on nonuniform superheating and evaporation of the water upon unstable film collapse is proposed to describe the origin of the melt filaments. For liquid drops under isothermal conditions with the water, fragmentation occurs as mass is stripped off the surface due to relative motion of the water. For hot drops at higher flow velocities (i.e., > 45 m/s) initially a vapor bubble forms but it is quickly displaced downstream. It is proposed that evaporation at the upstream surface of the bubble generates a vapor flow around the drop surface which strips the drop surface. The vapor flow carries the fragments into the bubble region behind the drop. The vapor later condenses leaving a cloud of fragments which are subsequently dispersed by the water. The dynamics of the vapor bubble produced by the explosion of a hot drop under low flow conditions is modeled using a parametric model incorporating the Rayleigh equation for bubble dynamics and an energy equation for the vapor to account for added heat transfer from the distorting drop surface. Estimates of the total heat transferred from the drop show that only 3% of the initial drop thermal energy is converted into work done by the vapor bubble.

RESUME

Au cours de cette étude, des techniques radiographiques à rayons X ainsi que des caméras ultra rapides ont été utilisées afin d'examiner le processus de fragmentation d'une gouttelette de métal en fusion, plongée dans de l'eau, au cours d'une explosion de vapeur. Dans le cas de gouttelettes chauffées à 700°C, une bulle de vapeur se forme autour de celleci après un délai d'induction de l'ordre de 80 µs, augmente jusqu'à atteindre une taille critique, puis se rétracte. Les radiographies à rayons X, qui permettent d'observer à travers la bulle de vapeur, montrent que la formation de protubérances filamentaires s'effectue durant la croissance de la bulle. Lors de l'effondrement de cette dernière, la surface de la goutte présente des circonvolutions importantes, tandis qu'une deuxième interaction s'initie entraînant, de nouveau, la formation d'une plus grosse bulle, dans le cas de gouttelettes d'étain. Un mécanisme, basé sur une surchauffe et une évaporation non uniforme de l'eau au cours de l'effondrement du film instable, est proposé afin d'expliquer l'origine de ces filaments de métal fondu. Pour des gouttes de liquide en équilibre thermique avec l'eau, la fragmentation s'effectue lorsque la masse est arrachée de la surface du fait du mouvement relatif de l'eau. Pour des vitesses d'écoulement plus élevées (c.à.d. > 45 m/s), la bulle de vapeur se forme, mais est rapidement entraînée en aval. Le schéma proposé suppose que l'évaporation en amont de la surface de la bulle génére un écoulement de vapeur autour de la surface de la gouttelette qui arrache la surface de cette dernière. L'écoulement de vapeur entraîne les fragments dans la région de la buile, derrière la goutte. La vapeur se condense, par la suite, laissant un nuage de fragments, qui est alors dispersé par l'eau. La dynamique d'une bulle de vapeur, produite lors de l'explosion d'une goutte chauffée dans un écoulement basse vitesse, a été modelée en utilisant une formulation paramétrique incorporant l'équation de Rayleigh pour la dynamique de la bulle et une équation d'énergie pour la vapeur, afin de tenir compte du transfert de chaleur à la surface perturbée de la goutte. L'estimation de la quantité totale de chaleur, transférée depuis la goutte, montre que seulement 3% de l'énergie thermique initiale de la gouttelette est converti en travail effectué par la bulle de vapeur.

ACKNOWLEDGEMENTS

I would like to thank my advisor Professor David Frost for his invaluable guidance, patience and freedom to pursue new and sometimes unorthodox ideas. I am also very grateful to my co-advisor Professor Rom Knystautas for his continuous support throughout the years. A special thanks goes to Professor John Lee for the many discussions and sometimes heated arguments concerning the subject matter of the present work. I have gained much from his unique approach to research, education and general philosophy of life. The fresh ideas and interpretations of experimental results provided by Professor Joseph Shepherd is appreciated. Furthermore, I would like to acknowledge Phil Watts for the work he did on the experimental apparatus and especially on the calibration of the x-ray system and Julian Lee for his valuable help on the electronics. I am also grateful to Olivier Peraldi for his translation of the abstract and to all the members, past and present, of the Shock Wave Physics Group (I will abstain from listing their names at the risk of leaving some out) at McGill for their support and friendship. A special thanks goes to Aris Makris for his unique personality which made it easier to cope with the everyday life in the SWPG group. This research was sponsored by the Natural Sciences and Engineering Research Council and Les Fonds pour la Formation de Chercheurs et l'aide a la Recherche. The patience and understanding from my family, especially my wife, in the last months of the thesis preparation are deeply appreciated.

TABLE OF CONTENTS

AB	STRACT	i
RE	SUME	ü
AC	KNOWLEDGEMENTS	iii
LIS	ST OF FIGURES	vii
NC	MENCLATURE	xiv
1	INTRODUCTION	
	1.1 Previous Experimental Work	
	1.2 Fragmentation Models	
	1.2.1 Thermal fragmentation effects	
	1.2.2 Hydrodynamic fragmentation effects	
	1.2.3 Experimental drop fragmentation data	
	1.3 Vapor Explosion Modelling	
	1.3.1 Parametric Models	
	1.3.2 Thermal Detonation Model	
	1.3.3 Steady-state models	
	1.3.4 Transient models	
	1.4 Objectives and Outline of the Present Work	
	1.4.1 Objectives of the present investigation	23
	1.4.2 Outline of the thesis	
2	EXPERIMENTAL DETAILS	25
	2.1 Experimental Facility	25
	2.2 Photography	26
	2.3 Shock pressure recording	27
	2.4 Event Timing and Recording	28
	2.5 Description of drop and coolant materials	28
3	EXPERIMENTAL RESULTS	30
	3.1 Explosion of a Single Hot Drop Under Low Flow Conditions (Thermal	
	Fragmentation)	30
	3.1.1 Introduction	30
	3.1.2 Fragmentation of a Cold Alloy Drop	31
	3.1.3 Hot Drop Experiments	32
	3.1.3.1 Vapor Bubble Dynamics	33

3.1.3.2 Fragmentation of a Molten Tin Drop	36
3.1.4 Fragmentation of a Molten Cerrolow Alloy Drop	37
3.2 Effect of Flow Velocity on the Fragmentation of a Single Hot and Cold	
Drop	38
3.2.1 Introduction	38
3.2.2 Flow velocity measurement	39
3.2.3 Effect of shock overpressure on maximum bubble size	40
3.2.4 Effect of flow velocity on the fragmentation of cold alloy	
drops	42
3.2.5 Correlation of Cold Drop Data	43
3.2.6 Effect of flow velocity on the interaction of a hot drop	46
3.2.7 X-ray Visualization of Fragmentation Process	47
4 DISCUSSION	49
4.1 Phenomenological Model for Thermal Fragmentation	49
4.1.1 Formation of Melt Jets	51
4.1.2 Influence of External Flow on the Thermal Fragmentation	
Process	52
4.2 Model for Bubble Dynamics	53
4.2.1 Formulation of model	54
4.2.2 Estimation of Vapor Bubble Initial Conditions	57
4.2.3 Estimation of γ for Ideal Gas Assumption	59
4.2.4 Numerical Results for First Bubble cycle	60
4.2.5 Estimation of the Interaction Efficiency	62
4.3 The Use of Hugoniot Analysis for Predicting the Existence of a Thermal	
Detonation	65
4.3.1 Results for Tin/Water/Steam Mixtures	65
4.3.2 Effect of Mixture Properties on the Detonation State	
4.3.3 Estimation of Reaction Zone Length Based on Experimental	
Drop Breakup Data	67
4.4 Comments on the Initiation of a Thermal Detonation	
4.5 Comments on the Experimental Techniques used to Determine Drop	
Breakup Times	70
5 CONCLUSIONS.	
CONTRIBUTIONS TO ORIGINAL KNOWLEDGE	
REFERENCES	76

•

APPENDIX A	Derivation for the trajectory of a solid sphere in a stream of fluid	83
APPENDIX B	Derivation of Rayleigh's equation for bubble dynamics	84
APPENDIX C	Governing relations for Hugoniot analysis	86

LIST OF FIGURES

- Fig. 1 Schematic showing formation of coarse-mixture and stratified geometry as initial conditions for a large-scale vapor explosion.
- Fig. 2 Illustration of Kim's (1985) coolant entrapment thermal fragmentation model.
- Fig. 3 Schematic of Buchanan's (1973) vortex mixing thermal fragmentation model.
- Fig. 4 Schematic showing hydrodynamic fragmentation models; boundary layer stripping, wave crest stripping, and catastrophic breakup.
- Fig. 5 Illustration showing the structure of the thermal detonation wave proposed by Board et al. (1975).
- Fig. 6 P-V diagram showing the CJ detonation downstream state at the tangency point between the Hugoniot curve and the Rayleigh line.
- Fig. 7 Schematic of experimental facility.
- Fig. 8 Schematic of furnace used to heat up and release drop and subsurface dropping mechanism for cold drop experiments.
- Fig. 9 Schematic of high voltage circuit used for triggering system.
- Fig. 10 Flow chart indicating the different delays used in taking simultaneous x-ray and regular high speed photography.
- Fig. 11 X-ray photographs of the hydrodynamic fragmentation of 0.5 g drops of cerrolow alloy in thermal equilibrium with surrounding water (at 65°C). Each photograph corresponds to a different drop. Times shown denote the time after the triggering shock wave arrives at the drop location. Flow of water from the expansion of the steam bubble from exploding wire trigger at bottom of tank is from bottom to top.

Fig. 12 Position and velocity of vapor bubble generated by trigger system.

1

- Fig. 13 High-speed photographs of the fragmentation of a 0.5 g drop of tin (at 700°C). Dark rectangle at top of each frame is a funnel immersed within the water to guide the drop. Bubble that comes into view at bottom is generated by exploding wire trigger.
- Fig. 14 Double exposures of explosion of 0.5 g tin drops at 700°C. Initial drop shape illuminated by exploding wire. Enlargement of drop in center shows surface ripples on initial vapor film.
- Fig. 15 High-speed photographs of the explosion of a 0.5 g drop of tin at 700°C immersed in water at 65°C.
- Fig. 16 Radial bubble growth time history for drop shown in Fig. 15. Diameter normalized with effective diameter of drop. Solid circles indicate frames shown in Fig. 15.
- Fig. 17 Bubble growth curves for 7 different trials with 0.5 g tin drops at 700°C.
- Fig. 18 High-speed photographs of a the interaction of solid steel sphere at 750°C with a shock.
- Fig. 19 Simultaneous x-ray radiographs (on the right) and regular photographs (on the left) of the vapor explosion of 0.5 g tin drops initially at 700°C. Each set of photographs corresponds to a different experiment. The times given are normalized with $t_{\rm C}$, the time required for the collapse of the first bubble.
- Fig. 20 Radial bubble growth time history for tin drops shown in Fig. 19. Solid circles indicate photographs shown in Fig. 19.
- Fig. 21 Bubble growth curves for 5 different trials with 0.5 g cerrolow alloy drops at 700°C.
- Fig. 22 Simultaneous x-ray radiographs (on the right) and regular photographs (on the left) of the vapor explosion of 0.5 g alloy drops initially at 700°C. The times

- given are normalized with $t_{\rm C}$, the time required for the collapse of the first bubble.
- Fig. 23 Radial bubble growth time history for alloy drops shown in Fig. 22. Solid circles indicate photographs shown in Fig. 22.
- Fig. 24 Trigger bubble surface position time history for different trigger strengths
- Fig. 25 Plot of experimentally measured solid sphere displacement (normalized with the sphere diameter) versus normalized time and calculated sphere trajectory for a drag coefficient of 0.35 shown as a solid line.
- Fig. 26: Pressure traces obtained at drop location for (a) exploding wire discharge, 8 μf capacitor charged to 15 kV (b) blasting cap.
- Fig. 27: Schematic showing experimental set up for experiments looking at the effect of shock overpressure.
- Fig. 28: Pressure trace (the trace is shown twice with two different time scales) recorded at the drop location for a 12 kV charge of an 8 µf capacitor charge
- Fig. 29: Variation in the first (scaled by the initial drop diameter) estimated from high speed film records for tin drops and a solid sphere as a function of the shock overpressure
- Fig. 30a: Photographic sequence showing the hydrodynamic fragmentation of a cold alloy drop at 60°C in a 0.5 m/s (We = 14.5) flow.
- Fig. 30b: Photographic sequence showing the hydrodynamic fragmentation of a cold alloy drop at 60°C in a 3.8 m/s (We = 94) flow.
- Fig. 30c: Photographic sequence showing the hydrodynamic fragmentation of a cold alloy drop at 60°C in a 18.4 m/s (We = 2,440) flow.
- Fig. 30d: Photographic sequence showing the hydrodynamic fragmentation of a cold alloy drop at 60°C in a 53.9 m/s (We = 13,442) flow.

- Fig. 31: Dimensionless drop displacement versus nondimensional time for cold gallium drop experiments and calculated trajectory for a drag coefficient of 4, shown as a solid line
- Fig. 32: Nondimensional time for the quadrupling of the fragmentation cloud projected area from the photographic results of the cold drop gallium experiments
- Fig. 33a: Photographic sequence showing the interaction of an alloy droplet at 700°C in water at 60°C. Water flow velocity is 0.5 m/s (We = 14.5).
- Fig. 33b: Photographic sequence showing the interaction of an alloy droplet at 700°C in water at 60°C. Water flow velocity is 4.8 m/s (We = 186).
- Fig. 33c: Photographic sequence showing the interaction of an alloy droplet at 700°C in water at 60°C. Water flow velocity is 17 m/s (We = 2,654).
- Fig. 33d: Photographic sequence showing the interaction of an alloy droplet at 700°C in water at 60°C. Water flow velocity is 56.7 m/s (We = 14,760).
- Fig. 34a: Photographic sequence showing the interaction of a tin droplet at 700°C in water at 60°C. Water flow velocity is 0.5 m/s (We = 14.5).
- Fig. 34b: Photographic sequence showing the interaction of a tin droplet at 700°C in water at 60°C. Water flow velocity is 51.4 m/s (We = 18,500).
- Fig. 35: Sequence of radiographs showing the interaction of a cold alloy drop at 60°C in 40 m/s (We = 8,500) flow.
- Fig. 36: Sequence of radiographs showing the interaction of a tin droplet at 700°C in water at 60°C. Water flow velocity is 40 m/s (We = 8,500).
- Fig. 37: Schematic of scenario for fragmentation of melt drop following film collapse.
- Fig. 38: Schematic of apparatus used in stratified layer experiments with local pressurization.

- Fig. 39: X-ray radiographs of the growth of disturbances at a liquid metal/water interface subject to rapid bubble growth at the interface at two locations. Two exploding wires, located 2.5 cm apart, are visible just above the surface of the metal in the first radiograph.
- Fig. 40: Physical picture showing the hot drop fragmentation process in the presence of a strong external flow.
- Fig. 41: Control volume used in closed system analysis.
- Fig. 42: Numerically predicted bubble diameter growth curves with ideal gas assumption (for $\gamma = 1.09, 1.25$ and 1.4) and real gas equation of state.
- Fig. 43: Bubble pressure time history for ideal gas (γ = 1.09) and real gas.
- Fig. 44: Steam bubble expansion and compression process predicted using real gas equation of state on P-v plane.
- Fig.45: Numerically predicted bubble diameter growth curves for adiabatic and nonadiabatic cases using ideal gas assumption, superimposed on experimental data from Fig. 17.
- Fig. 46: Graph showing the total heat added to and lost from the bubble as a function of time.
- Fig. 47: Bubble pressure and internal energy as a function of time for nonadiabatic case.
- Fig. 48: Numerically predicted bubble diameter growth curves for three initial drop surface-water contact times (i.e., t=10,40 and $80 \mu s$).
- Fig. 49: Numerically predicted bubble diameter growth curves for three different drop surface area growth factors (i.e., $K(R) = 0.10.100 (R/R_m)$).
- Fig. 50: Experimental bubble diameter time history superimposed on two predicted curves for adiabatic and nonadiabatic cases.

- Fig. 51: Numerically prediction of the first bubble cycle and the expansion phase of the second bubble superimposed on the experimental data from Fig. 17.
- Fig. 52: Total amount of energy transferred from the drop to the bubble starting at the time of film collapse.
- Fig. 53: Ratio of the work done by the vapor bubble and the initial available thermal energy of the drop, and the work done by constant volume mixing of the tin and water until thermal equilibrium followed by isentropic expansion of the mixture.
- Fig. 54: Work done by constant volume mixing of the tin and water until thermal equilibrium followed by isentropic expansion of the mixture and the ratio of this work and the initial available thermal energy of the drop as a function of the water-drop volume ratio.
- Fig. 55: Hugoniot curves for a mixture containing equal initial volumes of tin, water and steam. Tin temperature is 1000°C.
- Fig. 56: Hugoniot curve for tin at 1000°C (equal initial volumes of tin, water and steam).

 Points denoted O, CV, CP, and CJ refer to initial conditions, constant volume process, constant pressure process and Chapman-Jouguet deflagration, respectively.
- Fig. 57: Hugoniot curve for tin at 1250°C (equal initial volumes of tin, water and steam).
- Fig. 58: Variation of entropy change across reaction zone along the Hugoniot curve shown in Fig. 6.
- Fig. 59: Hugoniot curve for tin at 1500°C (equal initial volumes of tin, water and steam).
- Fig. 60: Variation of CJ detonation pressure and velocity as a function of void fraction for a mixture with equal volumes of tin (at 1000°C) and water.

- Fig. 61: Variation of CJ detonation pressure and velocity as a function of tin/water volume ratio for a mixture containing tin at 1000°C. In each case the void fraction is 33.3%.
- Fig. B-1: Schematic showing parameters and nomenclature
- Fig. C-1: Schematic of a steadily propagating energy release zone in a moving reference frame.
- Fig. C-2: P-V diagram showing the CJ detonation downstream state at the tangency point between the Hugoniot curve and the Rayleigh line.

NOMENCLATURE

Symbol	Description	Symbol	Description
		(subscript	s)
d	diameter	b	breakup
g	acceleration due to gravity	В	bubble
h	e nthalpy	BS	bubble surface
j	mass flux	C	coolant
k	thermal conductivity	d	drop
m	mass	DS	drop surface
P	pressure	f	fluid
Q	heat transfer rate	fr	fragmentation
qo	average heat transfer rate	I	interface
R	radius	m	melt
S	entropy	0	initial
t	dimensional time	T	terminal
T	temperature	V	vapor
u	velocity	W	water .
V	specific volume	∞	infinity
α	thermal diffusivity		
γ	ratio of specific heats		
σ	surface tension		
ρ	density		

Nondimensional parameters

Во	Bond number
CD	drag coefficient
F	constant used in breakup correlation
Re	Reynolds number
T	dimensionless time
We	Weber number

Chapter 1

INTRODUCTION

The direct contact of a cold volatile liquid (i.e., water) with a hot liquid (i.e., molten metal) whose temperature is significantly above the boiling temperature of the colder liquid can result in a vapor explosion. A vapor explosion involves the "explosive" production of vapor as a result of rapid heat transfer from the hot to the cold liquid and subsequent phase transition of the superheated volatile colder liquid. In an energetic vapor explosion heat transfer and phase transition occur on a time scale shorter than the time for pressure relief, resulting in a buildup of pressure. The expansion of the high pressure vapor produces strong compression waves and accelerates the coolant ahead placing any surrounding structures under hydrodynamic loading. The rapid heat transfer required for a vapor explosion, which is orders of magnitude higher than that for regular boiling, can only be achieved through the fragmentation of the hot liquid and hence an enhancement of the available surface area for heat transfer. This fact is substantiated by the fine melt debris which is recovered following both small and large-scale vapor explosions involving molten metals and water. Other terms used in the literature which reflect the non-chemical nature of such an explosion are "thermal explosions" and "physical explosions". In the nuclear industry vapor explosions are often referred to as "fuel-coolant interactions". In general the cold volatile liquid participating in a vapor explosion is referred to as the "coolant" and in the nuclear and metal industries the hot liquid is referred to as "fuel" and "melt", respectively.

Vapor explosions occur in many industries where both hot and cold liquids can come into contact. The industry most affected by vapor explosions is the metal industry (e.g. aluminum and steel) where the accidental mixing of molten metal and cooling water is common. There is also the potential for an energetic vapor explosion resulting from the spilling of cryogens, such as liquid natural gas, from transport ocean tankers into the sea. In this particular case the sea water acts as the hot liquid since the boiling point of cryogens is below the freezing temperature of sea water. The nuclear industry has also studied the

possibility of a strong vapor explosion causing failure of the reactor containment in the unlikely event of a core meltdown resulting from the loss of coolant to the reactor core. In this accident scenario a vapor explosion could occur from the mixing of the melted reactor core contents (i.e., uranium dioxide fuel, zircaloy cladding, and stainless steel) and any remaining cooling water in the reactor vessel. An extensive summary of the occurrence of vapor explosions in different industries can be found in Reid (1983).

1.1 Previous Experimental Work

In the past the main industrial concern was to determine what fraction of the initial melt thermal energy could be converted into mechanical work, which ultimately causes structural damage, in a vapor explosion. Theoretical thermodynamic predictions by Hicks and Menzies (1965) set a maximum conversion ratio of about 30% for the mixing of equal volumes of melt and coolant. These calculations are based on the constant volume heating of the coolant and isentropic expansion of the high pressure vapor generated. This prediction is considered very conservative since it neglects the energy required for the physical mechanism of area enhancement via melt fragmentation by which this large energy conversion could be accomplished. As an alternative, large-scale simulation experiments were carried out to get a more realistic measurement of the explosion efficiency or yield (Buxton and Benedick, 1979; Mitchell and Corradini, 1981). The experimentally measured explosion efficiencies vary depending on several experimental parameters but in general they are about an order of magnitude below the theoretical thermodynamic maximum. Energy conversion ratio data is considered valuable, for example, to the nuclear industry where the results can be used in the design or upgrade of reactor containment vessels. Unfortunately, these large-scale experiments give no new insight into the fundamental processes of melt fragmentation and explosion propagation.

In a typical industrial accident scenario a large mass of melt, of the order of several kilograms, is accidently released into a pool of water as shown in Fig. 1. As the melt falls through the coolant it breaks up into large drops of the order of centimeters in size creating a "coarse-mixture" of melt and coolant. This mixing of the melt drops and coolant are possible because a vapor film forms around the drops isolating them both thermally and physically from the coolant. This is one possible geometry where a vapor explosion can occur if a suitable trigger is available (this includes self-triggering). If the explosion is not triggered the melt will descend to the base of the tank and accumulate forming a "stratified

mixture" geometry which can also support a vapor explosion (Ciccarelli and Frost, 1989). In the present study we are only considering vapor explosions in coarse-mixtures which tend to be more energetic. Large-scale experiments have shown that a vapor explosion involves the propagation of an explosion front through the coarse-mixture (Buxton and Benedick, 1979; Mitchell and Corradini, 1981). Therefore, the overall explosion is the result of the propagation of small-scale interactions involving individual components of the coarse-mixture. This phenomenon can clearly be seen in the propagation of a vapor explosion through a linear array of melt drops (Frost and Ciccarelli, 1988a), where the interaction proceeds sequentially from drop to drop from one end of the array to the other. In light of the propagation phenomenon, the study of small-scale vapor explosions involving a single component of the coarse-mixture (i.e., a single drop) is essential to the understanding of the global propagation phenomenon in a vapor explosion.

A large number of single drop experiments have been performed in the past in order to study the effect of certain parameters such as melt and coolant temperature and material, on the vapor explosion phenomenon. A small-scale experiment involves the releasing of a molten metal drop, typically less than 10 g, into a tank of water. If the temperature of the drop/coolant interface is above the Leidenfrost temperature of the water a vapor film immediately forms surrounding the drop as it enters the water. The interface temperature is estimated to be the value which would result if two semi-infinite slabs at different temperatures with constant thermal properties were suddenly brought together. The interface temperature T_I can be estimated from

$$T_I = \frac{T_m \ \beta_m + T_w \ \beta_w}{\beta_m + \beta_w} \tag{1.1}$$

where $\beta = k/\sqrt{\alpha}$, k is the thermal conductivity and α is the thermal diffusivity and the subscripts m and w refer to the melt and water, respectively. For melt and water temperatures of 600°C and 65°C (typical experimental conditions), the interface temperature is estimated from equation (1.1) to be 524°C. Since this temperature is above the superheat limit temperature of the coolant a vapor film forms around the drop. Heat transfer from the drop to the coolant is through conduction across the vapor film and radiation from the drop surface to the vapor/coolant interface (this mode of boiling is referred to as film boiling and is characterized by low heat transfer rates). Film boiling is considered hydrodynamically "quiet" since there is little convective heat transfer. Therefore, the vapor film isolates the drop both physically and thermally from the surrounding coolant and can be considered an

explosion inhibitor. In order for an interaction to occur this insulating vapor film must be locally or completely removed (or collapsed) in order to allow liquid/liquid contact between the molten drop and the coolant which leads to much higher heat transfer rates. If the situation arises where the vapor film is only marginally stable, (i.e., lower initial interface temperature upon film collapse) it is possible that spontaneous fluctuations of the vapor film thickness are sufficient to trigger a local collapse. This phenomena is referred to as a "spontaneous" or "self-triggered" explosion. There exists a range of both melt and coolant temperatures within which a self-triggered explosion can occur. The notion of a self-triggered fragmentation zone was identified by Dullforce et al. (1976) (who used the term "thermal interaction" zone) from experiments with a tin/water system.

If the vapor film is stable an interaction can still be "triggered" by external means, such as a pressure pulse generated in the water. The use of an external disturbance for triggering a vapor explosion in circumstances that would otherwise involve stable film boiling has been investigated by a number of researchers. Board et al. (1974) dropped a few grams of tin into a crucible submerged in subcooled water. Then by applying a 0.1 MPa step pressure pulse an interaction was initiated. They also triggered explosions by placing a rod into the water and striking it with a hammer. They reported that the shock wave generated by the vibration of the rod in the water served to collapse the vapor film leading to the initiation of the explosion.

Fröhlich and Anderle (1980) used an exploding wire to produce a shock wave for initiating interactions between tin drops and water. The maximum overpressures used to trigger the drops were between 2.0 and 6.0 MPa. They used high speed spark shadow photography to investigate the role of the shock wave in the initiation of a vapor explosion. It was determined that there was no direct fragmentation of the drop when the shock wave passed the drop in film boiling. As a result, they concluded that the role of the shock wave was not to cause the direct breakup of the drop but to initiate instability in the otherwise stable film layer.

Nelson and Duda (1982) also used exploding wires to initiate explosions in iron-oxide drops in water. By varying the distance between the drop and the exploding wire, thereby effectively varying the peak overpressure felt by the drop, they found that a threshold pressure existed under which no explosive interactions could be initiated. This minimum overpressure was found to be 0.4 MPa, which is substantially lower than overpressures used by Fröhlich and Anderle (1980) to trigger interactions.

1.2 Fragmentation Models

1

In order to get an explosive interaction it is not sufficient to simply achieve drop/coolant contact, otherwise the state of the drop (e.g. solid or liquid) at the time of contact would be unimportant. The increased heat transfer due to the absence of the vapor film alone cannot account for the large heat transfer rates required for the explosive vapor production observed. The large heat transfer rates can only be obtained by the enhancement of surface area associated with the fine fragmentation of the drop itself. Since a vapor bubble forms engulfing the drop following film collapse it is impossible to observe the fragmentation process directly using regular photography. However, from the debris collected after the interaction, it is evident that the drop fragments into very fine particles of the order of 100 µm in size. It is generally acknowledged that the process of fine fragmentation is the most important process in a vapor explosion and thus warrants the most attention.

If we consider a hot drop in a flow of colder liquid (i.e., resulting from the passage of a shock wave) energy required for drop fragmentation can come from either the thermal energy of the drop or the kinetic energy of the flow. In the past there have been many fragmentation models proposed to describe the fine fragmentation of melt drops under very low or high flow conditions (see the recent comprehensive review by Corradini, Kim and Oh, 1988). In general the existing fragmentation mechanisms can be classified as thermally or purely hydrodynamically driven. The following is a brief review of some of the fragmentation mechanisms which have been proposed for triggered single drop interactions and some experimental results.

1.2.1 Thermal fragmentation effects

The following mechanisms can be grouped under this classification because they all involve heat transfer effects such as coolant evaporation and melt freezing which leads to drop fragmentation and where external flow plays no role.

Coolant entrapment model

One way to cause the drop to fragment is to have the drop explode from within much like the popping of a corn kernel due to superheating of entrapped water. There have been several models based on the entrapment and rapid evaporation of coolant within the melt drop including the models of Kim (1985) and Buchanan (1973). In Kim's entrapment model, shown in Fig. 2, it is assumed that the high pressure associated with a triggering shock wave causes the vapor film to collapse. As the vapor/coolant interface approaches the drop surface, the vapor pressure in the film increases causing the vapor/coolant interface to decelerate. The deceleration of the interface causes it to become unstable due to Rayleigh-Taylor instability. The instability causes waves on the interface to grow forming spikes of coolant which eventually contact and penetrate the drop surface. It is assumed that the penetrating coolant spikes (or jets) breakup, forming a coolant droplet which travels deep into the drop at each impact location. These droplets accumulate creating a subsurface mixture layer of coolant droplets and vapor. The expansion of the vapor generated through the evaporation of the encapsulated droplets causes the melt surface layer of the drop, through which the coolant has penetrated, to expand radially outwards. Subsequently, the expanding melt shell breaks up due to Rayleigh-Taylor instability. Enhanced heat transfer due to the mixing of the fragmented fuel shell and the coolant leads to the production of a vapor bubble which expands outward surrounding the remaining core of the drop which remains molten and intact. The vapor bubble reaches a maximum and collapses starting a new cycle whereby a second layer of the drop is fragmented. This fragmentation by layers continues until all the drop is fragmented or the remainder of the drop freezes.

In Buchanan's model it is assumed that an initial vapor bubble exists on the drop surface. The asymmetric collapse of the bubble causes a jet of coolant to form impacting the drop surface. Jet formation due to asymmetric bubble collapse near a solid surface has been studied extensively both experimentally (Vogel, Lauterborn and Timm, 1989) and theoretically (Plesset and Chapman, 1971). If the impact of the coolant jet is sufficiently strong it penetrates the drop surface and, unlike in Kim's model, it is assumed that the coolant jet mixes with the melt. The mixing involves the formation of a vortex ring which entrains melt, as shown in Fig. 3. In the model it is assumed that the contact surface area between the coolant and the melt increases exponentially. During jet penetration the coolant is continuously heated up to its saturation temperature when evaporation starts, provided nucleation sites are available (heterogeneous nucleation). If nucleation sites are not available the jet is heated to the homogeneous nucleation temperature at the limit of superheat where molecular fluctuations within the liquid become large enough to form a vapor nucleus. In either case, a vapor bubble forms within the drop which expands causing fragmentation of the section of the drop where the jet penetrated. The vapor bubble grows to a maximum and then collapses restarting the process. In this way the drop fragments due to the cyclical local bubble growth and collapse.

The key to both of the above mentioned models is the penetration of the hot drop surface by a coolant jet where the kinetic energy of the jet is much larger than the surface tension energy of the drop. Jet penetration is modeled as an adiabatic process, i.e., heat transfer from the drop surface to the coolant jet is neglected. As stated by Kim (1985), there is very little literature concerning the transient process of jet penetration of one liquid into another. In fact, there is even less data on the penetration of a cold liquid jet into a hot liquid where heat transfer effects can play a dominant role. In most vapor explosion situations the interface temperature between the hot and cold liquids is above the superheat limit of the cold liquid and thus evaporation will occur. Kim (1985) postulated that local pressurization due to thermal expansion of the superheated water could suppress boiling so that penetration could occur unobstructed. However, the duration of this pressure is of the order of 100's of nanoseconds (Cooper and Blewett, 1978) which is much shorter than the time for penetration. It is not clear why explosive evaporation would be suppressed during jet penetration. In Kim's model it is assumed that the expansion of the vapor produced by the injected coolant causes the fragmentation of the drop surface layer while maintaining the core of the drop intact and preserving a smooth surface. This requires perfect radial symmetry in the expansion of the subsurface vapor which in reality is not plausible.

In Buchanan's model it is assumed that an initial vapor bubble exists on the drop surface to start the bubble growth and collapse cycle. It is not clearly stated how this initial state is generated. It is possible that random liquid/liquid contacts which are characteristic of self triggered explosions could lead to the formation of such local surface vapor bubbles. However, it is difficult to envision the generation of this initial vapor bubble for moderately strong pressure wave triggering since the entire film is collapsed. Evidence for the applicability of this model to self triggered vapor explosions can be found in Frost and Ciccarelli (1988b).

Splash theory model

į

Ochiai and Bankoff (1976) proposed a self-mixing theory which is often referred to as the "splash" model. This model was applied to self triggered interactions where random local contacts were assumed to occur due to capillary instability of the vapor film. These contacts generate local high pressure regions due to rapid local superheating and rapid phase transition of the coolant. This local high pressure region acting on the drop surface causes an annular jet of melt to form directed towards the vapor/coolant interface.

Subsequent contact of the n...t annular jet with the coolant promotes further liquid/liquid contact leading to an escalation in the fragmentation.

Annular jets described in this model can be observed when a raindrop falls into a pond. In this case, the local high pressure is produced by the impact of the drop with the water surface. In the case of a jet of coolant impacting a hot drop surface the overpressure generated is due to the subsequent rapid evaporation. However, if an annular jet were to form in this case, the radial expansion of the high pressure vapor formed would likely cause the disintegration of the jet structure. The model does bring out two very important points, (i) that coolant penetration due to film collapse may be inhibited due to superheating and evaporation at the drop surface and (ii) that fragmentation of the melt does not require coolant penetration into the drop.

Shrinking shell model

The fragmentation mechanisms discussed so far have required that the drop remain molten during the breakup. However, it has been proposed that solidification of the drop surface following film collapse could lead to drop fragmentation. Zyszkowski (1976) proposed that thermal stresses arising from the solidification process could be greater than the yield stress of the drop. As a result, the internal pressure induced by the shrinking of the shell ejects some of the molten mass from the core in the form of small jets through fissures which occur on the solidified surface. These small jets act as heat transfer fins and fast cooling of the core proceeds. If the amount of heat transferred is large enough, a vapor explosion can result. Zyszkowski (1976) employed this mechanism to interpret the experimentally observed vapor explosions in a copper-water system.

In most cases, vapor explosions are initiated at temperatures where the interface temperature following liquid/liquid contact is above the freezing point of the fuel. Therefore, this hypothesis can be ruled out as a possible fragmentation mechanism. It does not appear possible that surface freezing and internal pressurization can occur on a sufficiently short time scale to account for observed fragmentation times in triggered interactions. The cracking of the frozen crust is possible for brittle materials but is unlikely for most drop materials which undergo plastic deformation.

Symmetric film collapse model

Drumheller (1979) presented a fragmentation model based on the symmetric collapse of the vapor film. The symmetric vapor film collapse is caused by the passage of a square pressure pulse across a spherical drop undergoing film boiling. It is assumed that the transit time for the shock to pass the drop is short relative to the film collapse time, so that a symmetric pressure is exerted on the vapor/liquid interface. This compresses the vapor and causes it to condense at the interface. This condensation wave moves inward and reaches the drop surface when all of the vapor has been condensed. The collapsing cold liquid which accompanies this condensation wave then impacts the drop. The impact from the cold fluid generates an imploding shock wave inside the drop. When the shock wave converges at the center of the drop a reflected shock wave is generated which propagates radially outward. This motion drives the material from the center of the drop. Eventually the pressure in the core of the drop falls to zero and the drop appears to explode from within.

There are several assumptions in this model which cannot be met in reality. The model is based on the symmetric collapse of the vapor film on the drop surface. In reality the shock wave does not have a square pressure profile, the initial drop surface and especially the vapor/coolant interface is highly asymmetric and corrugated, and the bubble collapse is very unstable as suggested in Kim's model (1985). All these factors make it highly doubtful that a uniform impact of the coolant on the drop surface can occur which is the basis of this model. The experiments of Fröhlich and Anderle (1980) using shadowgraph photography to track the shock wave also showed that the shock wave did not directly cause the breakup of the drop.

1.2.2 Hydrodynamic fragmentation effects

In hydrodynamic fragmentation models it is the relative motion between the drop and the coolant which drives the fragmentation of the drop. Therefore, the energy used in fragmenting the drop comes from the kinetic energy of the coclant flow and not the thermal energy of the drop, as is the case in thermal fragmentation mechanisms.

In order to break up a drop the drop surface must be disrupted. There are three fundamental mechanisms by which the drop surface can be distorted leading to drop

fragmentation: boundary layer stripping, Rayleigh-Taylor and Kelvin-Helmholtz instabilities. All hydrodynamic fragmentation models incorporate one or a combination of these mechanisms. First a brief description of three of the most widely accepted models will be presented followed by a review of some of the experimental data which support these models. Shown in Fig. 4 is a schematic showing the essential features of the three models.

Boundary layer stripping

A boundary layer stripping model was first proposed by Taylor (1965). In this model the coolant flow around the drop exerts a shear force on the upwind surface of the drop which sets the surface layer of the drop into motion. When the melt mass in the drop boundary layer is convected to the equator of the drop it breaks away from the surface as the inertia of the layer overcomes surface tension forces. Through this mechanism there is a continuous stripping of mass from the drop surface.

Wave crest stripping

Enhanced mass stripping is obtained when finite perturbations or waves are present on the upwind drop surface due to interface instability. Since the upstream surface of the drop, which is a density interface, is being accelerated due to drag on the drop, it is susceptible to Rayleigh-Taylor instability. Since the acceleration is in the direction from the lighter liquid (coolant) to the heavier liquid (melt) the interface is unstable and perturbations will tend to grow. The drop surface at the stagnation point is most susceptible to this type of instability as compared to that at the drop equator because this portion of the surface is normal to the direction of acceleration. Also, since there is a relative tangential flow between the drop and the coolant the upstream surface of the drop is also exposed to Kelvin-Helmholtz instability. Kelvin-Helmholtz instability is more prominent at the equator where the relative velocity is at a maximum. As the instability waves grow in amplitude they are convected to the drop equator due to the shear force exerted by the coolant flow around the drop. The coolant flow over the drop surface erodes the wave crests generating a mist of fine droplets which are convected downstream with the coolant flow. It is assumed that the wave crests break off when the wave amplitude reaches some fraction of the perturbation wavelength. In this way mass can be stripped before it reaches the drop equator which is the case in the boundary layer stripping model. This type of model is referred to as "wave crest stripping".

Catastrophic breakup

Instead of the continuous stripping of the drop surface the drop breakup can be more abrupt. This type of fragmentation is referred to as "catastrophic breakup" and is caused by the piercing of the drop by large wavelength Rayleigh-Taylor instability waves. As the coolant flows over the drop, a pressure difference is set up at the drop surface where the pressure at the stagnation point is higher than at the drop equator. This pressure difference causes the drop to flatten perpendicular to the flow. A combination of this drop flattening and the growth of Rayleigh-Taylor instability waves on the upstream surface causes the drop to break up. When the wave amplitude grows to the size of the flattened drop thickness, the drop is pierced and breaks up into smaller drops the size of the perturbation wavelength. Harper, Grube and Chang (1972) first showed theoretically that the acceleration imparted to the drop would cause the windward surface of the drop to become unstable due to Rayleigh-Taylor instability. The smaller drops produced by catastrophic breakup can then continue to be eroded through wavecrest stripping.

Both wavecrest stripping and catastrophic breakup can occur in the same drop at different times during the fragmentation process. Initially the smaller wavelength waves grow faster (linear regime) and therefore wave crest stripping dominates but at later times when the instability enters the nonlinear regime, the larger wavelength waves grow faster resulting in catastrophic breakup of the drop (Pilch et al., 1987).

1.2.3 Experimental drop fragmentation data

There is no direct experimental evidence to support any of the thermal fragmentation models described earlier. This is because during an interaction there is a vapor bubble which is generated which envelopes the fragmenting drop. Due to light refraction at the bubble surface it is impossible to see the fragmentation process inside the bubble by regular back or front lighting photography.

For hydrodynamic driven drop fragmentation the elevated temperature of the melt drop, relative to the coolant, plays no role in the breakup process. Therefore, experiments looking at purely hydrodynamic drop fragmentation are conducted under conditions where the drop and the coolant are at the same temperature during the entire fragmentation process. These types of experiments are referred to as "isothermal" or "cold" drop fragmentation experiments. Experimentally, the difficulty in observing the fragmentation

process which exists in hot drop experiments, due to the vapor bubble formation, is not present. However, there are other difficulties which come into effect which will be discussed later. There is a wealth of experimental data in the literature on relative velocity driven fragmentation of liquid drops in both gas and liquid mediums. A good review of the experimental data and proposed models can be found in Pilch and Erdman (1987).

A nondimensional number which is often used in the study of hydrodynamic fragmentation is the Weber number. The Weber number gives the ratio of destabilizing inertia force to the stabilizing surface tension force, and is defined as

$$We = \frac{\rho_C u^2 R}{\sigma} \tag{1.2}$$

where ρ_c is the density of the continuous medium (i.e., coolant in the case of a coarse mixture), u is the relative velocity between the drop and continuous medium, R is drop radius and σ is the interfacial surface tension. In the literature the Weber number is also often defined in terms of the diameter as the characteristic length. The Bond number is also frequently used and is related to the Weber number by the following expression for the case of constant acceleration due to drag force,

$$Bo = \frac{\rho g d^2}{\sigma} = \frac{3}{8} C_D We$$
 (1.3)

where g is the drop acceleration, C_D is the drag coefficient and d is the drop diameter. In equation (1.3) the Weber number is defined in terms of the drop radius. Note, since the drag coefficient is typically about 2.5, the Bond and Weber numbers are almost identical.

Most fragmentation data is correlated using the following dimensionless time

$$T = \frac{\int u \, dt}{d} \sqrt{\frac{\rho_c}{\rho_d}} \tag{1.4}$$

where t is dimensional time and the subscripts d and c refer to drop and coolant quantities.

There exists a large body of experimental data on the fragmentation of liquid drops in air flows due to early interest in supersonic rain erosion in the field of aerodynamics and liquid spray detonations in the field of combustion. Vapor explosion investigators first turned to

this data for insight since there was no data on the fragmentation of liquid drops in a liquid medium. It was not clear if the dimensionless breakup time data could be extrapolated to different fluid pairs. Ranger and Nicholls (1969) performed experiments investigating at the breakup of water drops in a standard air shock tube. The relative flow is produced by the differential acceleration of the water drop and the surrounding air following the passage of the shock wave. Shadowgraph photography was used to record the drop fragmentation. They characterized the fragmentation process as stripping of the drop surface generating a micromist which collects in the drop wake. Fragmentation was considered complete when only a mist remained. They found that total drop breakup occurred at a dimensionless time of about 5, where the relative velocity used in the definition of the dimensionless time was taken to be the particle velocity behind the shock. They found this breakup time to be independent of the Weber number. There data agreed well with data earlier obtained by Engel (1958). Ranger and Nicholls refined Taylor's original boundary layer stripping analysis to compare with their experimental data. The model predictions showed fairly good agreement with their experimental data.

Later Reinecke and Waldman (1970) performed similar experiments with lead doped water drops in an air shock tube for Weber numbers above 10,000. The novelty in these experiments was that flash x-ray was used in order to differentiate between the parent drop and the micromist produced by surface stripping which was observed in previous experiments. The x-ray penetrated the fine particles making up the micromist but were absorbed by the parent drop. Using microdensitometry traces of the x-ray photographs, they obtained the actual drop mass time history. Their results showed that at late times the drops underwent catastrophic breakup. The dimensionless time for catastrophic breakup was correlated with $T_b = 45We^{-1/4}$ (or approximately $T_b = 3.5$). They also showed by analysis that the times for complete drop breakup obtained using Ranger and Nicholls' (1969) boundary layer stripping model underestimated their experimentally observed breakup time.

Simpkins and Bales (1972) also studied shock-induced fragmentation of water drops in air for Weber numbers higher than 1000. Using shadowgraph photography they found that there was no evidence of instability growth on the windward surface of the drop for Weber numbers below 10,000. The dimensionless time for the onset of what they referred to as Rayleigh-Taylor instability waves was found to be approximated by $T^* = 22Bo^{-1/4}$. This, in effect represents a lower limit for the drop breakup time and is consistent with the observations of Reinecke and Waldman (1970).

It was not until the late 1970's that investigators looking into vapor explosions undertook the task of performing hydrodynamic fragmentation experiments using liquid drops in a liquid medium. Patel and Theofanous (1981) performed experiments in a hydrodynamic shock tube where the fragmentation of mercury, gallium and tetrabromide drops was studied for Weber numbers up to 5000. In these experiments front lit regular photography was used. In their experiments they observed a symmetrical blowup of the drops without any boundary layer stripping. They proposed that the drops underwent catastrophic breakup and suggested that the dimensionless time for total breakup obtained through their experiments could be fitted by $T_b = 1.66Bo^{-1/4}$ (or approximately $T_b = 0.4$). The criterion used for breakup was the doubling of the apparent drop diameter perpendicular to the flow. This breakup time is considerably shorter than that observed for water drops in air $(3 < T_b)$ < 5) and is also shorter than the time determined by Simpkin and Bales (1972) corresponding to the onset of instability waves. Theofanous et al. (1979) carried out further experiments using flash x-ray with an initially stationary drop which they claimed minimizes any initial surface perturbations which may exist in a free falling drop. The new breakup time data were correlated with $T_b = 7.7 Bo^{-1/4}$ (or about $T_b = 2$) which is slower than first reported using free falling drops but still shorter than typical times for a gas/liquid system. The x-ray photographs showed that the symmetric blowup observed using regular photography consisted of a superposition of drop flattening and wave crest stripping which produced an optically opaque wake.

Experiments in a liquid/liquid system were also carried out by Baines and Buttery (1979) where mercury drops were placed on the bottom of a tank and the tank was impulsively accelerated by the impact of a projectile fired from a gas gun. Experiments were carried out for Weber numbers ranging from 100 to 2000. Fragmentation was recorded using shadowgraph photography. Their results yielded a nondimensional breakup time in the range of 3 to 5 which is in agreement with gas-liquid data and in conflict with the data of Patel and Theofanous (1981). The criterion used to obtain these times corresponded to the time when the drop was observed to be completely fragmented and the fragments had been dispersed. Baines and Buttery's data suggest that the mode of breakup is through boundary layer stripping which is consistent with that observed in gas-liquid systems at this Weber number range.

Experiments on fragmentation of gallium drops in water were performed by Kim et al. (1983) for a Weber number range of 30-3600. The water flow was produced by a piston

which was driven by an expanding vapor bubble generated from an exploding wire explosion. The fragmentation process was observed using front lit regular photography. For Weber numbers below 300 a coherent skin was observed to be drawn off the drop surface with subsequent breakup downstream. For Weber numbers above 1300 direct stripping of fragments from the drop surface was observed. A transitional regime occurred for intermediate Weber numbers where the length of the coherent skin drawn off decreased with increasing Weber number. Two approximate fragmentation times were given, $T_b = 2$ and $T_b = 4$, where the first corresponds to the doubling of the projected area and the second corresponds to complete fragmentation identified with the smallness of visible unfragmented parts which were observed by the reflection of light.

In vapor explosion research one is most interested in obtaining the increase in melt surface area with time as a result of fragmentation because this is what characterizes the heat transfer rate to the coolant. For simplicity, if it is assumed that all the stripped particles are of a single size and shape (i.e., spherical) the surface area can be calculated knowing the mass stripping rate. Alternatively, the heat transfer rate can be determined directly from the mass stripping rate if the heat transfer from the stripped fragments to the coolant is assumed to be instantaneous. Therefore, the ultimate objective of any fragmentation experiment is to determine the mass stripping rate. To determine this rate it is necessary to observe the time history of the drop mass during fragmentation. Due to the opaque appearance of the micromist using regular photography this can only be done using x-ray photography which cuts through the micromist. The only experimentally obtained mass stripping rate was obtained by Reinecke and Waldman (1972), who fit their x-ray data with the following expression,

$$m(T) = \frac{1}{2} m(o) \left\{ 1 - \cos \left(\pi \frac{T}{T_b} \right) \right\}$$
 (1.5)

which yields a mass stripping rate of

$$\frac{dm}{dT} = \frac{1}{2} \frac{\pi \ m(o)}{T_b} \sin\left(\pi \frac{T}{T_b}\right) \tag{1.6}$$

where m(T) is the drop mass at a dimensionless time T and m(0) is the initial drop mass. The expression given In Eqn (1.5) for the drop mass time history is strictly a curve fit of the experimental data and has no theoretical basis. The expression includes a time for total

breakup, T_b , which they found experimentally to correspond to catastrophic breakup of the drop, which in turn correlated with the Weber number as follows

$$T_h = F B_o^{-1/4} (1.7)$$

where the constant F was found to be 65. It is worth noting that Simpkins and Bales (1972) correlated their breakup data with F = 44 and Patel and Theofanous (1981) with F = 1.66.

When using regular photography all that can be seen in the breakup of the drop is the profile of a dark zone which includes both the parent drop and the fragmented particles. The growth of this dark zone characterizes the dispersion of the fragmented particles and cannot be used directly to infer the mass stripping rate. Therefore, most investigators implement Eqn (1.6) and attempt to estimate the time for total drop breakup. However, it is very difficult to set a meaningful criterion for determining this time. This is reflected in the number of different criteria used by different investigators. Because of this arbitrariness in the breakup time criteria used by different investigators there have been many conflicting results.

1.3 Vapor Explosion Modelling

The following is a brief review of vapor explosion modelling as it evolved from the first calculation by Hicks and Menzies (1965). This review is not intended to be a discussion of the details of each model or computational technique used. Rather emphasis is placed on the importance of the fragmentation mechanisms incorporated in the overall vapor explosion models. A more comprehensive review of vapor explosion modelling can be found in Fletcher and Anderson (1990). The numerical models are presented in chronological order as they appeared in the literature.

1.3.1 Parametric Models

Unlike in Hicks and Menzies' (1965) original thermodynamic analysis, parametric models include the transient processes of melt fragmentation and heat transfer. The first parametric model was developed by Padilla (1970) which was followed by numerous other variations (see Corradini et al., 1988) for a complete list of existing parametric models). In a

parametric model it is assumed that the melt fragments into small particles of a given size or distribution of sizes which are uniformly distributed throughout the coolant. The heat is transferred to the coolant leading to an increase in pressure due to the rise in temperature. This is followed by coolant evaporation whereby high pressure vapor is generated and subsequently expands. With appropriate expressions for fragmentation rates and a time varying heat transfer coefficient, parametric models predict heat transfer rates and coolant evaporation rates. By specifying the physical boundary conditions, the pressure time history within an enclosure can be calculated.

The following is a brief description of one of the earlier parametric models proposed by Cho et al. (1970). In this model the heat transfer rate, Q, from the melt fragments to the coolant is assumed to be

$$Q = h A \left(T_f - T_c \right) \tag{1.8}$$

where T is the temperature, h is the transient heat transfer coefficient, A is the surface area, and the subscripts f and c refer to the melt fragments and coolant, respectively. The heat transfer is assumed to be driven through heat conduction and the expression for the heat transfer coefficient is obtained from the 1-D transient heat conduction equation. The rate of surface area enhancement is taken to be exponential in nature,

$$A \sim \left[1 - exp\left(\frac{t}{t_{ff}}\right) \right] \tag{1.9}$$

where t_{fr} is the time for complete fragmentation and is considered a parameter. The drop diameter is also included as a parameter in the expression for the surface area as a function of time. These two parameters are specified by the user based on empirical data. Any calculations obtained using this model are subject to the validity of the values for these external parameters. The main results obtained from this particular model is that the peak pressure decreases and the pressure rise time increases with increasing fragment size and time for complete fragmentation. Although the parametric models are an improvement over the Hicks and Menzies model, the applicability of these models is very limited.

1.3.2 Thermal Detonation Model

Both the Hicks and Menzies (1965) and parametric models do not address the problem of explosion propagation or escalation from a local trigger. If the vapor film surrounding one or a section of drops in a coarse-mixture is destabilized causing liquid-liquid contact, a localized vapor explosion will occur involving only a small region of the coarse-mixture. As a consequence of this interaction, a local high pressure vapor region will result. The expansion of this high pressure vapor will produce pressure waves and coolant flow ahead of it which will cause the collapse of the vapor film around adjacent melt drops. In this way the sequential explosion of neighboring drops can lead to propagation of the interaction throughout the coarse-mixture. If this propagation were to escalate, whereby the pressure wave would steepen forming a shock wave, a self-sustained explosion front may develop. The existence of such an explosion front was first postulated by Board et al. (1975). In the model the explosion front consists of a coupled leading shock wave and reaction zone where the energy released from the melt in the reaction zone goes into sustaining the shock wave. As a result of the direct analogy made with chemical gaseous detonations, the concept of a self-sustained vapor explosion wave is often referred to as a "thermal detonation". Since the thermal detonation model was the catalyst and is the foundation for all present numerical models for vapor explosions it is appropriate to briefly discuss some of the main points involved.

The structure of the explosion front, as shown in Fig. 5 (taken from Fletcher et al., 1990), consists of three distinct zones. Since the front moves supersonically the mixture ahead of the leading shock is undisturbed. Behind the shock is the reaction zone where melt fragmentation occurs and energy is transferred from the melt to the coolant. The reaction zone terminates at the so-called "CJ plane" and is followed by the expansion zone. In order to have a self-sustained complex the transient expansion zone must not be allowed to influence the reaction zone. The only way this can occur is if the flow velocity at CJ plane is sonic relative to the leading shock wave, and this is referred to as the CJ criterion. In this way no perturbations can propagate upstream to the reaction zone. The role of the leading shock wave is to first collapse the vapor film around the drops and secondly to accelerate the drops relative to the coolant. The relative velocity between the coolant and the drops results in the fine fragmentation of the drops due to hydrodynamic effects. The fine fragmentation of the melt leads to rapid heat transfer to the coolant.

For a chemical or hypothetical thermal detonation, the processes which occur in the reaction zone are highly transient. However, globally the detonation is steady because the leading shock wave and the CJ plane are coupled and move at a constant velocity. Therefore, one can do a global equilibrium analysis of the detonation wave where the inflow and the outflow (taken with respect to the detonation wave) corresponds to the state just before the shock wave and at the CJ plane, respectively. By solving the three conservation equations of mass, momentum and energy along with an equation of state, the locus of downstream states can be determined knowing the initial conditions of the mixture. For a gaseous chemical detonation, the stable solution is obtained by invoking the CJ criterion and can be determined graphically by the tangency point between the Rayleigh Line and the equilibrium Hugoniot as shown in Fig. 6. A complete description of the analysis and derivation of the governing equations can be found in Appendix A. Calculations based on this simple one dimensional equilibrium analysis yields results which are in excellent agreement with gaseous chemical detonation experiments.

1

The attractiveness of the equilibrium analysis is that it is based solely on energetics and is independent of nonequilibrium processes which occur within the reaction zone. This was especially attractive for thermal detonations since very little was known about the fragmentation process which occurred in the reaction zone. For this reason, Board et al. (1975) carried out a similar analysis for thermal detonations using mass averaged quantities for the specific volume and enthalpy of the two component three phase mixture. This is valid only if the mixture is in a state of equilibrium at the inflow and outflow boundaries. This then requires that the fragmented melt is in both thermal and mechanical equilibrium with the coolant at the outflow boundary. Board et al. (1975) used the fragmentation data of Simpkins and Bales (1972) to show that complete fragmentation can be reached before mechanical equilibrium between the parent drop and coolant is achieved at the CJ plane. They proposed that fragmentation of the melt drops occurs strictly due to hydrodynamic effects and assumed that the temperature and velocity of the stripped fragments equilibrate with the coolant instantaneously. For equal volumes of tin at 1000°C, water at 100°C and steam the calculations yield a detonation velocity of 300 m/s and a CJ pressure of about 80 MPa. Although these values could not be reproduced by later investigators (Frost et al., 1990; McCann et al. 1991), in general the predicted CJ pressures and velocities far exceed any experimentally observed values.

1.3.3 Steady-state models

The Board et al.(1975) thermal detonation model gave the first clear physical representation of the propagation phenomenon in a vapor explosion. The thermal detonation model enables one to predict detonation properties based on a simple equilibrium analysis. Even if the assumptions used in the analysis were valid and detonation properties could be calculated, it in no way provides the proof for the existence of such a wave in reality. To determine if a thermal detonation can be realized in reality it is necessary to look at the nonequilibrium processes which occur within the reaction zone.

Sharon and Bankoff (1978) and Scott and Berthoud (1978) independently presented the first steady-state models which included a model for the structure of the reaction zone in a thermal detonation. Both models are based on the structure of the detonation proposed by Board et al. (1975). The models used a two-component mixture where one component consisted of unfragmented melt and the other a mixture of fragmented melt and coolant (liquid and vapor phase). By allowing slip between the two components, the key nonequilibrium process of melt fragmentation could be included in the model. Both models assumed that fragmentation would be due to hydrodynamic effects exclusively. Both models used the mass stripping correlation obtained by Reinecke and Waldman (1970) (equation (1.5)) to model the fragmentation process. Sharon and Bankoff (1978) also used the modified boundary stripping model proposed by Ranger and Nicholls (1969). By assuming a shock velocity or pressure and using the shock jump conditions the post shock conditions could be calculated. Using these values as initial conditions the six conservation equations (three for each component), complete with mass, momentum and energy transfer terms between components, could be integrated from the post shock plane to any plane downstream.

Both Sharon and Bankoff (1978) and Scott and Berthoud (1978) noted that for the wave to be self-sustained the reaction zone must be terminated by a CJ plane. They also showed that such a CJ plane would exist where slip between the two components vanished. Scott and Berthoud (1978) also pointed out that reaching a maximum of the entropy within the reaction zone was a necessary condition to have a self-sustained propagation. Based on the no slip argument the reaction zone length could be obtained knowing the distance downstream from the shock where velocity equilibration occurred. Knowing the reaction zone length they could infer if such a wave could exist in a given experimental system. Depending on what fragmentation correlation was used different conclusions could be

made. For example Sharon and Bankoff (1978), using the boundary stripping correlation of Ranger and Nicholls (1969) and an initial shock velocity calculated from equilibrium Hugoniot calculations, and calculated reaction zone lengths which were nonphysical. Nonphysical reaction zone lengths refer to excessively large reaction zones where heat and momentum losses would prevent the possible existence of such a detonation. The same resulted if the Reinecke and Waldman (1970) correlation given in Eqn. (1.5) in conjunction with the breakup time (T_b) with F = 65 (Reinecke and Waldman, 1970) or F = 44 (Simpkins and Bales, 1972). However, if F = 1.5 (Patel and Theofanous, 1981) was employed, physically possible reaction zone lengths could be realized.

Burger et al. (1986) later presented a steady-state model very similar to that just described. It is clear from the discussion of the models that the fragmentation model employed will greatly affect the results. It is the fragmentation model which dictates whether or not physically possible reaction zone lengths are predicted. An accurate representation of the fragmentation process is the key to success of such models. It is also explicitly implied that melt fragmentation through thermal effects is unimportant for propagation of a thermal detonation. Considering the strong flow generated behind the shock wave this assumption is reasonable although it has yet to be proven experimentally.

1.3.4 Transient models

If a thermal detonation can be realized, an escalation process from the initial triggering is required because, in general, a trigger strong enough for direct initiation does not exist in accident scenarios. Consequently, most of the current work in numerical modelling is focused on modelling the escalation process using transient detonation codes (Fletcher et al., 1989; Young, 1989; Medhekar et al., 1988; Burger et al., 1989; Oh and Corradini, 1987). One of the objectives of these codes is to determine whether or not explosion escalation can lead to a steady-state propagation. There is no increase in the complexity of the physical phenomenon when going from a steady-state to a transient modelling approach. However, the computational complexities increases dramatically since the equations solved are partial differential equations as opposed to ordinary differential equations for steady-state models. A good review of the multiphase equations and numerical techniques used in transient detonations codes can be found in Fletcher and Anderson (1990).

In terms of fragmentation correlations used in the codes, there is no difference between the steady-state and transient codes. In the past, with the exception of Oh and Corradini (1987), these numerical codes rely solely on hydrodynamic stripping type fragmentation models. It is now generally accepted that in order to have a reasonable numerical modelling of the escalation process, a simple stripping type hydrodynamic fragmentation mechanism will not suffice (Burger et al., 1989). This is clear since in the escalation process the melt drops ahead of the explosion front would be subjected to a spectrum of coolant flow velocities as the front accelerates. During the early stage of initiation coolant flow velocities of the order of meters per second would be encountered and therefore thermal effects would dominate in the fragmentation process. At the other extreme of the escalation process, for a fully developed steady-state propagating wave, hydrodynamic effects would be expected to dominate due to flow velocities of hundreds of meters per second which would exist behind the leading shock wave.

Burger et al. (1989) attempted to model tin/water experiments performed in the KROTOS facility at ISPRA using their transient detonation code with only a hydrodynamic fragmentation mechanism. The numerical simulation produced much lower pressures as compared to the pressures recorded during the experiments. They postulated that this disagreement was due to the lack of a thermal fragmentation model in their code. By including a simple ad hoc thermal fragmentation model in their code they obtained better agreement with the experimental results.

Although several investigators have investigated the hydrodynamic breakup of a cold liquid drop in a liquid medium as discussed earlier, no experimental results are available showing the effect of flow velocity on the fragmentation of a hot molten drop where thermal effects will also play a role. In particular there exists no experimental results to describe the transition from a thermal to a hydrodynamic type fragmentation mechanism as the flow velocity is increased. In fact none of the existing thermal fragmentation models incorporate the effect of coolant flow, and therefore according to these models, thermal fragmentation is not cut-off at high flow velocities. Whether thermal fragmentation acts independently of the hydrodynamic fragmentation and whether they mutually augment or suppress one another has not been investigated.

1.4 Objectives and Outline of the Present Work

1.4.1 Objectives of the present investigation

In general, the mechanisms involved in the initial mixing, triggering and propagation phases of a vapor explosion are qualitatively understood through large-scale experimental observations. What is not clear is the process of fine fragmentation which occurs in the propagation phase. Small-scale experiments have produced little in terms of direct information on the fragmentation process. This is due to the difficulty of observing the process through the vapor generated during the interaction. Nevertheless there have been many mechanisms proposed to describe the fragmentation of a hot drop in (i) quiescent coolant conditions (i.e., thermally driven mechanisms) or (ii) high coolant flows typical of thermal detonation conditions (i.e., hydrodynamic driven mechanisms). There is no data available for the fragmentation of hot drops for intermediate coolant flow conditions. In recent years there has been a shift in emphasis from large-scale experiments to numerical modelling. In the past, vapor explosion modelling has taken three approaches in dealing with the fragmentation mechanism; (i) in the thermodynamic model (Hicks and Menzies, 1965) and the equilibrium Hugoniot calculations (i.e., Board et al., 1975) the use of a fragmentation model is not required, (ii) in parametric models the fragmentation process is modeled parametrically and therefore an exact representation is not required, (iii) in the later steady-state and transient models the entire model revolves around the fragmentation mechanism since it governs the heat transfer rate. Therefore, in order to model vapor explosions with any degree of confidence it is crucial to have a reliable fragmentation model. To model the escalation process in a vapor explosion, the effect of coolant flow velocity on fragmentation must also be taken into account.

The objectives of the present work are two-fold: (i) to study experimentally the thermally driven fragmentation process of a hot drop-coolant interaction using flash—ray visualization, (ii) to study the influence of coolant flow velocity on the fragmentation process. In particular, emphasis is placed on determining if there is a transition from thermal fragmentation at low flow velocities to hydrodynamic fragmentation at high flow velocities, and if so, what is the nature of this transition. This is accomplished by comparing the fragmentation process of a hot alloy drop with that of a "cold" alloy drop with increasing flow velocities. The term "cold" refers to the case where the drop and coolant are at the same temperature. Data obtained for cold drop breakup will be used to

compare with data of previous work to resolve some of the existing conflicts in data obtained by different investigators in the past.

1.4.2 Outline of the thesis

...

0.0

The present work is an experimental investigation of the fragmentation process in the triggered interaction of a single molten metal drop in water. The experimental facility and instrumentation used in the study are described in Chapter 2. In Chapter 3 experimental results are presented, including the vapor bubble dynamics and drop fragmentation data obtained using regular and flash x-ray photography with a weak trigger. Also, results on the influence of shock pressure on the explosion yield, and the effect of coolant flow velocity on the fragmentation of drops at elevated temperatures and at isothermal conditions are presented. In Chapter 4 a general discussion of the results and implications concerning the present state of vapor explosions is given. A simple model using the Rayleigh equation for bubble dynamics is used to predict the vapor bubble dynamics observed experimentally. A thermal fragmentation model is proposed based on the direct observation of the fragmentation phenomenon using x-ray photography. The possibility of realizing a thermal detonation are investigated using the experimental fragmentation times reported in Chapter 3 in conjunction with an equilibrium one-dimensional Hugoniot analysis. Conclusions and recommendations for future research are summarized in Chapter 5. A statement outlining the original contributions of the present work is given in Chapter 6. Appendix C includes the derivations of detailed equations used in the Hugoniot calculations.

The bulk of the work reported on in this thesis was presented in the following three papers at the thirteenth International Colloquium on Explosive and Reactive Systems held at Nagoya Japan in July 1991.

- Ciccarelli, G. and Frost, D.L., "The Effect of Fluid Flow Velocity on the Fragmentation Mechanism of a Hot Melt Drop."
- Frost, D.L., Ciccarelli, G., and Watts, P., "Flash X-ray Visualizing of the Steam Explosion of a Molten Metal Drop."
- Frost, D.L., Ciccarelli, G., "Implications for the Existence of Thermal Detonations from Equilibrium Hugoniot Analysis."

Chapter 2

EXPERIMENTAL DETAILS

2.1 Experimental Facility

The experimental facility shown in Fig. 7 consists of a rectangular tank with a vertical tube welded to the bottom. The test drop is released into the tank and the interaction is triggered by the passage of a shock wave. The shock wave is generated by a triggering system which is housed inside the vertical tube at the bottom the tube. Windows are located on all four sides of the tank in order to obtain simultaneous flash x-ray photographs in one direction and regular back lighting (shadow) photography in the orthogonal direction. The test section measures 25.5 cm long, 12.5 cm high and 10 cm wide and is constructed of 0.375 cm thick aluminum plates. X-rays are taken in the direction where the tank is the narrowest and the x-ray film is placed up against the outside of the back window. The smaller width of the tank along with the use of very thin Lexan (.625 mm) for the windows enabled low x-ray absorption and optimum contrast on the film. The windows through which regular photography was taken were constructed of 2.54 cm thick pyrex glass. Lexan windows could not be used for the regular photography since the high pressure in the tank following the passage of the shock caused the windows to bow thus distorting the image.

The drop is heated in a furnace which is fastened to the top of the tank. The furnace consists of a central heating coil and four concentric thermal and electrical insulating shells, as shown in Fig. 8. The outer shell measuring 9 cm outer diameter is made of aluminum and acts as a protective cover for the more fragile inner insulating shells. The second outermost shell consists of loose fiberglass type insulating material which minimizes heat losses through the wall. This insulation is wrapped around a hollow graphite cylinder with a bottle neck bottom. The graphite can withstand very high temperatures and has a very high thermal capacity and conductivity which maintains a uniform temperature distribution

within the furnace. A quartz cylinder is used to electrically insulate the graphite cylinder from the internal nichrome heating coils. The temperature in the furnace is monitored by a thermocouple which is embedded inside the central stainless steel rod which plugs the hole at the bottom of the graphite cylinder. An insulating firebrick plug is placed above to reduce any heat that would otherwise be lost through the top. In order to minimize oxidation of the drop surface, it is placed inside the oven when the desired temperature is achieved. The drop comes to rest in the gap between the graphite and central rod and is released into the tank by raising the rod.

The interaction is triggered when the drop falls to a predetermined depth in the water through the use of a low power He-Ne laser and photodiode system. The laser shines horizontally through the center of the tank at the predetermined depth, directly in the path of the descending drop and is directed onto a photodiode. With a simple electrical circuit the triggering system is activated when the photodiode detects a drop in light intensity resulting from the interruption of the beam by the falling drop. Since the drop trajectory through the water can be erratic, often a plastic funnel is used below the exit of the furnace to direct the drop into the path of the laser beam.

The trigger system shown in Fig. 9 consists of a high voltage circuit in which either an exploding wire (i.e., a fine copper wire) or electric detonator (referred to as a blasting cap for the remainder of the report) can be used as the source of the triggering explosion. The blasting cap contains 0.1 g lead azide primary charge and 0.25 g PETN base charge. An 8 µf (30 kV maximum charging voltage) capacitor is used in conjunction with the exploding wire while a smaller 2 µf charged to 3 kV is used to initiate the blasting cap. An EG&G TM-11A trigger module in tandem with an EG&G switching spark gap is used to trigger the discharge of the capacitors across the exploding wire or blasting cap. The exploding wire and blasting cap are located at the bottom of the vertical heavy walled tube 3.8 cm in diameter, 18 cm long, as shown in Fig. 7. The interaction is triggered when the drop is approximately 2 cm above the tube exit. The explosion of the exploding wire or blasting cap generates a vapor bubble within the vertical tube pushing water ahead of it. Thus by varying the amount of trigger energy the drop could be subjected to different water flow velocities.

2.2 Photography

A Scandiflash single head flash x-ray system (model 150) with a maximum discharge voltage of 150 kV was used for some of the experiments. In the experiments where x-ray visualization was employed, the maximum discharge voltage of 150 kV was used. Each x-ray flash delivers a dose of 25 mR of soft x-rays for a duration 35 nanoseconds. The x-ray head is placed directly in line with the drop location at the time of the explosion. The distance between the drop and the x-ray film is roughly 8 cm. The distance from the x-ray head to the drop, 55 cm, corresponded to the distance where maximum contrast could be achieved. Kodak XAR-5 13x18 cm high speed x-ray film was used with a Kodak 18x24 cm Min-R intensifying screen and a Kodak Min-R cassette. The positioning of the high speed camera and x-ray head relative to the water tank can be seen in Fig. 7.

Simultaneous backlighting photography was taken using three different camera/lighting combinations. In order to capture the overall bubble dynamics a Hycam 16 mm camera was used at a framing rate of 4,000 frames per second. The backlighting is provided by a 1,000 watt quartz halogen lamp equipped with reflectors. Kodak high-speed 7292 color movie film (300 ASA) was used. A glass light diffuser was placed between the light source and the back tank window. The Hycam films are convenient because they can be used for projection screening of the filmed event. A Cordin 16 mm rotating drum camera was also used to record the drop/water interaction at a nominal framing rate of 25,000 frames per second for a total of 224 frames. This camera, which gives much better time resolution than the Hycam, is used to study the details of the bubble dynamics. The Cordin camera is operated with the shutter open with back lighting during the event provided by a 5 ms duration Xenon flash tube discharged with about 500 Joules. When operating the camera at 25,000 frames per second the maximum recording time was limited to the finite duration of the flash. Kodak TMAX 100 and 400 ASA 35 mm film were used. High spatial resolution single frame open shutter photographs were taken using a 35 mm camera in conjunction with a Photonics Palflash 500 spark gap flash unit.

2.3 Shock pressure recording

4

The trigger pressure is measured with the use of underwater pressure transducers placed in the water near the drop. Two types of pressure transducers are used: (i) an underwater tourmaline gauge (PCB Piezotronics 138A01, sensitivity 725 mV/MPa, quoted risetime of 1.5 ms) and (ii) an underwater PVDF pressure transducer (Imotec, sensitivity 11 mV/MPa, risetime 70 ns, sensitive diameter 0.5 mm). Signals from the pressure transducers are

recorded with using a LeCroy 9400A oscilloscope recording at 30 MHz or a PC-based data acquisition board operated at 1 MHz.

2.4 Event Timing and Recording

Several delay generators were used in order to film the entire interaction and to obtain an xray at a given time after initiation. Figure 10 is a flow chart indicating the different delays used from when the drop intercepts the laser to when the x-ray is finally taken. In most cases the laser beam is directly below the funnel so as to ensure that the drop breaks the beam. In general this is above the desired depth for the interaction to be triggered. Therefore, the TTL signal which is given out by the photo diode circuit when the beam is broken is delayed (typically 40-50 ms) using DELAY#1 so that the drop falls an additional amount. Since the flash requires about 1 ms to reach full intensity the flash and triggering of the exploding wire must be staggered by this amount. Two outputs are taken from DELAY#1, one goes to a TM11 via a pulse amplifier to trigger the flash and the other goes to DELAY#2 which is set to 1 ms. Again two outputs are taken from DELAY#2. One goes to a TM11 via a pulse amplifier to trigger the exploding wire or blasting cap and the other goes to DELAY#3 which is an integral component of the x-ray system. DELAY#3 is used to set the time after triggering at which the x-ray is to be taken. Note the transit time for the triggering shock to reach the drop (i.e., typically 135 µs) must be accounted for when analyzing the radiographs.

2.5 Description of drop and coolant materials

Three different drop materials were used in the present experiments. Tin was chosen because of its low melting point, availability, and its properties are well tabulated. Tin is one of the most common metals used in vapor explosion research and as a result comparison of results can be made with other investigators. The second drop material used is *cerrolow* alloy (trade name), a low melting point alloy (Tmpt = 49°C) consisting of 45% bismuth, 23% lead, 19% indium, 8% tin, and 5% cadmium. Since the precise surface tension of the cerrolow alloy is not available a value of 0.455 N/m will be used which is based on the mass-weighted average of the surface tension of the components. The attractiveness of the alloy is that both hot and isothermal drop experiments can be carried out with the same drop material. The third type of material used was gallium which is liquid at about 28°C. The size of the drop is often characterized in terms of its "effective"

diameter which corresponds to the diameter of a sphere of equal material and mass (i.e., $d_{eff} = (\frac{6 \text{ M}}{\pi \text{ p}})^{1/3}$.

In the past there have been several different coolants used for small-scale vapor explosion experiments although the most common is water. In the present experiments water was used exclusively due to its availability and nontoxicity. Boiling of the water before each trial or the use of distilled water had no observable effect on the results. Therefore, regular tap water was used for all the experiments reported here.

Chapter 3

EXPERIMENTAL RESULTS

3.1 Explosion of a Single Hot Drop Under Low Flow Conditions (Thermal Fragmentation)

3.1.1 Introduction

It is generally acknowledged in the scientific community that the key to understanding and accurately modelling large-scale vapor explosions lies in obtaining a good representation of the fine-scale fragmentation of the drops in the coarse-mixture. As outlined in the introduction there have been many small-scale single drop experiments performed in the past using various drop coolant pairs and triggering techniques. In general, the results from these experiments were limited to vapor bubble diameter time histories and post debris analysis of the fragmented drop. Based on these experiments, investigators have proposed a number of fragmentation mechanisms by which a single molten drop can be broken up into sub-millimeter sized particles in a time of the order of milliseconds. Due to the limitations of the experimental results one can only consider these proposed mechanisms as speculative. What is required is an experiment where one can observe directly the fragmentation process which occurs within the vapor bubble during the interaction.

In this section, experiments are reported whose purpose was to determine the fragmentation process involved in the interaction of a hot molten metal drop in water under weak triggering conditions. A weak trigger is desired so as to isolate the fragmentation due to thermal effects from any fragmentation driven by purely hydrodynamic effects which may be caused by the flow field in the water generated from the trigger. Regular photography is used to observe the time history of the vapor bubble generated while simultaneous flash x-ray is used to observe the drop fragmentation process which occurs within the vapor bubble. Experiments were carried out using tin and cerrolow alloy drops. For the cerrolow alloy both hot and cold drop experiments were performed to determine if

hydrodynamic effects resulting from the trigger play any role in the drop fragmentation process.

To study the fragmentation of a hot drop solely due to thermal effects, ideally one would seek to use the weakest possible trigger so as to minimize the amount of coolant flow generated by the trigger. Initial experiments using a very weak trigger (4 μ f capacitor charged to 4 kV) proved to be unsuccessful since the resulting interactions were not repeatable. It is well known that the amount of noncondensible gas present in the initial vapor film surrounding the drop has an effect on the film collapse (Buchanan, 1974). It appears that for this weak trigger the overpressure associated with the shock wave is too low to overcome any variations in the amount of air which is dragged down with the drop upon entrance into the water. It was found that using an 8 μ f capacitor charged to 7.5 kV resulted in very reproducible explosions in terms of vapor bubble dynamics and the fragmentation process.

The vapor bubble produced by the drop-water interaction is visualized using high-speed backlighting photography. Two different cameras with different filming rates are used in order to obtain both an overview and a detailed recording of the bubble growth-collapse cycle. The Hycam is used to observe the bubble over its entire lifetime with a time resolution of 250 μ s. These films are meant to give only an overall picture of the bubble dynamics since the filming rate is too slow to make out the exact times of the bubble maxima and minima which are required when comparing with x-ray photographs. These details are obtained from the Cordin camera films which give a time resolution of 40 μ s. Due to the limited flash duration, the bubble could only be tracked to its second maximum.

3.1.2 Fragmentation of a Cold Alloy Drop

A

To determine the relative importance of hydrodynamic and thermal fragmentation effects, experiments were first carried out to subject a cold liquid metal drop (i.e., at the same temperature as the surrounding water) to a blast wave. In this case, since the drop and coolant form an isothermal system, only hydrodynamic effects can play a role in the breakup of the drop. The fragmentation process is best illustrated by considering a series of x-ray photographs at different times. Figure 11 shows a series of x-ray photographs (each photograph corresponds to a different trial) showing the breakup of a 0.5 g drop of cerrolow alloy. The water temperature is 60°C so that the alloy drop remains a liquid at all

times. The times shown are with respect to the time that the shock arrives at the drop location.

Initially the drop has an ellipsoidal shape. Mass is stripped continuously from the drop surface and is convected downstream of the drop into the wake region (the convective flow is from bottom to top). During the first several milliseconds, a surface layer of mass is drawn off producing long distorted filaments extending from the drop downstream. At later times these filaments break up into fine particles as they are accelerated by the flow. The radiograph at 5 ms in Fig. 11 shows an example of the thin filaments extending from the surface of the drop and the micromist of fine particles that form in the wake region. This process continues until at a time of about 7.5 ms when the drop appears to be completely fragmented. The drop remains liquid during the drop breakup, so after the interaction the fragments tend to coalesce at the bottom of the tank. This makes it impossible to determine an accurate distribution of sizes of the fragments generated during the interaction using the post-trial debris.

Since the duration of the pressure waves from the exploding wire trigger is only about 20 μ s (see Fig. 26), it is clear that the fragmentation is a result of the convective flow generated by the expansion of the exploding wire vapor bubble. An estimate of the ambient flow velocity can be obtained by measuring the velocity of the vapor bubble generated by the exploding wire trigger. From regular high-speed photography, the bubble is visible within the test section after about 500 μ s (for example, see Fig. 13). The bubble position and velocity are shown in Fig. 12 (taken from the trial shown in Fig. 13) as a function of time. The bubble rapidly decelerates and eventually reaches a constant velocity of about 2 m/s. Although the convective flow velocity is not constant and it is difficult to determine when the drop is "completely fragmented", an order of magnitude estimate for the nondimensional total breakup time can be made to compare with previous results. For example, if we take the average convective flow velocity of 4 m/s, a total breakup time of 7.5 ms with an initial drop diameter of 6 mm, then the nondimensional breakup time T is 2. This value is consistent with that obtained by earlier investigators (typical values measured for the nondimensional total breakup time range from 2 to 5, Pilch and Erdman, 1987).

3.1.3 Hot Drop Experiments

To illustrate the steam explosion of a single hot melt drop, both regular high-speed photographs and flash x-ray radiographs will be presented. Regular photographs will first

be presented to describe the dynamics of the steam bubble generated during the interaction of a molten tin drop. X-ray radiographs will then be used to illustrate the drop breakup behavior.

3.1.3.1 Vapor Bubble Dynamics

During the steam explosion of a hot drop, a steam bubble is formed shortly after the triggering shock wave initiates collapse of the vapor film. An overall view of the dynamics of the steam bubble is shown in Fig. 13 which includes a series of Hycam photographs from the explosion of a 0.5 g tin drop initially at 700°C immersed in water at 65°C. The exit of the vertical tube containing the triggering system is visible at the bottom of each frame. The dark rectangle at the top of the each frame is the bottom of the funnel which is used to guide the drop to the position of the laser beam. The bright vertical line which can be seen in the center of all the frames is due to a crack in the glass diffuser located outside the tank. At t = 0, the exploding wire is triggered, illuminating the funnel from below and generating cavitation bubbles in the water which are caused by the sharp expansion behind the initial blast wave generated by the exploding wire. The typical lifetime of the majority of the cavitation bubbles is about 300 µs. The bubble generated by the trigger system first appears at the bottom of the frame at a time of about 500 µs, moving upwards. The initial drop shape appears to be slightly elongated indicating the presence of a small amount of air that is trapped around the drop when it first contacts the water surface. The shock arrives at the drop 135 µs later and the steam bubble generated during the interaction grows to a maximum diameter at 750 µs. The vapor bubble at this time is almost perfectly spherical except for a small bulge on the top which is due to the initial entrained air. The bubble overshoots its equilibrium radius and collapses to a minimum at about 1.5 ms. After the collapse of the first bubble a second much larger bubble is produced as the result of a second interaction between the water and the drop. This second bubble collapses asymmetrically at 9.75 ms due to the ambient coolant flow with no significant third bubble generated. Apparently only two bubble cycles are required to release the thermal energy of the drop. At the time of the second bubble collapse the drop is completely broken up and the fragments are uniformly dispersed over a volume roughly equal to that occupied by the second bubble at its maximum.

The initial growth of the steam bubble is illustrated in Fig. 14 which shows several double exposure open shutter photographs of exploding drops. Initiation of the exploding wire trigger system generates a flash that illuminates the drop from below. A preset time later, a

second flash is fired, showing the profile of the steam explosion bubble at that time. At time zero on the photographs, the shock arrives at the drop location. At 95 μ s the expansion of the vapor bubble is clearly evident. This represents a maximum time for film collapse and superheating of the water which contacts the drop surface. An enlargement of the drop at 255 μ s is shown, illustrating the ripples (with a typical scale of about 0.5 mm) that exist on the vapor film surrounding the drop prior to the passage of the shock wave. At 575 μ s, the vapor bubble is near its maximum diameter and drop fragments are visible in the water surrounding the bubble. These fragments are torn from the drop surface during the first interaction stage following the initial melt-water contact and accelerated during the expansion of the vapor bubble. The inertia of the fragments causes them to penetrate the bubble surface when the bubble begins to decelerate near its maximum diameter.

٠٤.٠

To obtain a more accurate measurement of the bubble growth, drop interactions were recorded with the Cordin camera running at 25,000 frames/s for a temporal resolution of 40 us. An example is shown in Fig. 15 for a drop with the same conditions as the trials described above. Shown in Fig. 16 is a plot of the horizontal bubble diameter versus time taken from every second frame from the high-speed film. The bubble diameter is normalized with the effective initial drop diameter, $d_{eff} = 5.1$ mm. The solid circles correspond to the frames shown in Fig. 15. Time t = 0 identifies the frame before the shock wave arrives at the drop location. The initial drop shape appears to be almost spherical except for a small bulge on the top right indicating the presence of a small amount of entrapped air. By 240 µs the vapor bubble has expanded to more than double the initial drop diameter. The bubble surface appears very smooth at this point in the expansion phase. Also visible in this frame are cavitation bubbles in the bulk of the water. At 560 µs the vapor bubble reaches its maximum horizontal diameter of about three times the initial drop diameter and melt fragments are visible in the water surrounding the bubble. Due to the upward water flow generated by the trigger bubble the steam explosion bubble is displaced upwards and the fragments first appear on the upstream side of the bubble.

At 800 and 960 µs the bubble is collapsing and leaves behind a trail of fine fragments. The vapor bubble collapses until a time of about 1.2 ms at which point the bubble is obscured by the fragments within the interaction region. The rebound and expansion of a second vapor bubble is first visible at a time of 1.28 ms. No vapor production is evident around the small fragments in the water indicating that the small fragments have solidified. The second vapor bubble expands reaching a diameter of 4 times the initial drop diameter at 1.760 ms and reaches a maximum of about 6.5 times at a time of about 4 ms. Again, as in

the first bubble maximum, fragments emerge from the vapor bubble as it approaches its maximum. The bubble then collapses to a minimum and no further bubble oscillations are observed.

Although there are small variations in the drop shape and vapor film thickness from one trial to the next, the overall shape of the bubble diameter—time profile is quite repeatable. Figure 17 shows a composite of 7 trials illustrating the variation in the details of the normalized growth of the bubble diameter for the same initial drop conditions. The first vapor bubble maximum is typically about three times the initial drop diameter. Collapse of the first bubble occurs between 1.1 and 1.6 ms. There is more scatter in the growth of the second bubble which depends on the complex heat transfer and fragmentation processes that occur during the first collapse.

To investigate the influence of melt fragmentation on the initial explosion and size of the first bubble maximum, experiments were carried out in a system in which no fragmentation was possible. In particular, a solid steel sphere with a similar diameter (5 mm) and initial temperature (700°C) as the hot tin drops, was dropped into water and subjected to the same triggering shock conditions. Figure 18 shows an example of a solid hot sphere interacting with a shock and the growth of the vapor bubble around the drop. After the shock passes the drop, the vapor film surrounding the sphere collapses and a steam bubble is generated that grows to a maximum diameter about twice the initial sphere diameter about 500 µs later. The presence of a small bubble of gas or vapor on the top of the sphere (visible in the photograph at time t = 0), leads to an asymmetry in the bubble shape. The cavitation of the water in the tank generated by the passage of the triggering blast wave is most intense in the wake of the sphere because of the hot wake region of the sphere itself. When the steam bubble collapses, it collapses asymmetrically and appears to peel away from the drop from the bottom. This effect is due to the vertical convective flow generated by the steam bubble associated with the exploding wire trigger at the base of the tank. Note that after collapsing, the bubble rebounds slightly then disappears after about 1 ms. In the absence of fragmentation, the heat due to conduction from the center of the drop to the surface is insufficient to form a second steam bubble.

For a hot solid sphere, most of the thermal energy contained near the surface of the sphere is transferred following the initial collapse of the vapor film surrounding the sphere. The steam bubble that is generated grows to a maximum size in a similar time as that for a molten drop, although the maximum bubble diameter attained is smaller. The similarity in

the dynamics of the first bubble generated between a molten drop and solid sphere suggests that the energy transfer is limited to a thin surface layer of the drop and that significant fragmentation of the molten drop does *not* take place during the short time that the water is in contact with the drop prior to the generation of vapor and expansion of the first bubble.

3.1.3.2 Fragmentation of a Molten Tin Drop

With regular photography, very little information can be extracted concerning the dynamics of the drop fragmentation that occurs within the vapor bubble. In order to observe the fragmentation process, flash x-ray radiography (with simultaneous high-speed photography) was used in the present study to see through the vapor bubble. Since only one x-ray photograph can be taken per experiment, to obtain a time history of the drop breakup it is necessary to take a number of x-rays at different times during different experiments. Figure 19 shows such a composite of trials where the x-ray photograph is shown on the right and the regular photograph (taken simultaneously but in a perpendicular direction) is shown on the left. The times shown are normalized relative to $t_{\rm C}$, the time for the first bubble collapse estimated from the high-speed film record for each trial. In this way, the fragmentation behavior can be compared at different stages in the bubble growth cycle. Figure 20 shows a representative trial with the solid circles representing the times shown in Fig. 19.

At a time of $t/t_C = 0.22$, the vapor bubble has grown to twice its initial size. From the x-ray photograph, the surface of the drop appears highly perturbed with thin filaments of metal extending radially out from the drop symmetrically around the drop. At $t/t_C = 0.4$ the bubble has almost reached its maximum diameter. At this time, growth of the protruding spikes of metal is apparent and close inspection of the x-ray photograph shows that a thin "shell" of fragments is present inside the bubble near the bubble surface. At $t/t_C = 0.63$ the drop surface is highly convoluted and the vertical displacement of the vapor bubble is evident. Fine fragments are visible near the spikes probably due to freezing and shattering of the smallest filaments of metal. Note that the distortion of the drop occurs *inside* the vapor bubble where there is little drag to impede the breakup. This can be compared with the breakup of a cold drop where in the absence of vapor it takes considerably more energy (and time) to disperse the drop fragments in a *liquid* medium. At bubble collapse the regular and x-ray photographs look similar. The impact of the incoming water with the drop shatters the fine spikes and the subsequent heat transfer and turbulent motion of the vapor generated leads to total fragmentation of the drop. At a nondimensional time of 1.11,

the second high-pressure steam bubble is expanding and from the x-ray photograph, the orderly melt fingers evident at early times have been completely destroyed. What remains is an expanding compact region containing fragments, water droplets and vapor. As the bubble grows the fragments are carried out with the expanding vapor. At a time of $t/t_C = 1.47$, the fragments are dispersed throughout the bubble and continue to move radially outwards as the bubble decelerates. As the bubble approaches the second maxima ($t/t_C = 2.73$) the inside of the bubble is largely void of particles.

3.1.4 Fragmentation of a Molten Cerrolow Alloy Drop

To study the effect of drop properties on the drop fragmentation behavior, a second series of experiments was carried out with 0.5 g drops of cerrolow alloy with the same trigger conditions and initial conditions (i.e., $T_{drop} = 700^{\circ}\text{C}$, $T_{water} = 65^{\circ}\text{C}$) as for the molten tin drops. The properties of the alloy differ from tin in that it is heavier (density = 9.2 g/cm³ vs. 7.0 g/cm³ for tin), has a lower heat capacity ($c_p = 154 \text{ J/kg}^{\circ}\text{K}$ vs. 223 J/kg $^{\circ}\text{K}$ for tin) and remains liquid throughout the interaction.

Figure 21 shows the horizontal bubble diameter time history for five trials with cerrolow alloy drops (cf. Fig. 17 for tin drops). The overall shape of the curves is similar to that obtained for tin drops. The first bubble maximum is a similar size as for the tin drops although the second bubble reaches a smaller maximum size ($d/d_{eff} \sim 4-6$) as compared to tin ($d/d_{eff} \sim 6-9$).

Figure 22 shows a series of trials for alloy drops showing simultaneous regular (on the left) and x-ray (on the right) photographs (cf. Fig. 19 for tin drops) and Fig. 23 shows the characteristic bubble growth history with the solid circles again representing the trials shown in Fig. 22. At the time of the arrival of the shock ($t/t_C = 0$) the initial drop has an ellipsoidal shape as compared with the more spherical tin drops (due to the higher surface tension of tin). At $t/t_C = 0.25$, the drop surface appears highly distorted, with filaments of melt again extending radially from the surface of the drop. At $t/t_C = 0.375$ the drop appears elongated in the horizontal direction relative to the initial drop diameter. The x-ray photograph taken with the bubble at its maximum diameter ($t/t_C = 0.5$) shows that the drop is highly deformed. The highly turbulent motion of the vapor within the bubble plays a role in the large deformation of the melt fingers and parent drop. The absence of any freezing effects is in contrast with molten tin drops where freezing of the surface of the melt filaments probably limits the extent of deformation. As the bubble collapses ($t/t_C = 0.688$)

the drop appears very elongated forming thin strands. Shortly after the collapse of the bubble, the hydrodynamic impact appears to have shattered the distorted drop into fine fragments and the surface no longer appears continuous. As the bubble expands the fragments are dispersed and eventually penetrate the water as the bubble decelerates.

3.2 Effect of Flow Velocity on the Fragmentation of a Single Hot and Cold Drop

3.2.1 Introduction

₹.

120

Photographic results from large-scale spill experiments carried out at Sandia National Laboratory (Mitchell et al., 1981) demonstrate that a vapor explosion occurs as the result of a propagating front. If the explosion front propagates at a subsonic velocity (relative to the sound speed in the multiphase upstream mixture), it will push the fluid ahead accelerating the coolant and melt drops at different rates. Since the sound speed in the mixtures is very low the front usually moves at a supersonic speed (Mitchell et al., 1981), in which case the leading shock wave will accelerate the coolant and melt drops at different rates. In most existing numerical models it is this differential acceleration (hydrodynamic effect) which causes fine fragmentation and hence governs the energy release rate. During the initial stages of the explosion escalation process where the induced flow ahead of the front is low, hydrodynamic effects alone cannot account for the drop fragmentation. It is clear that a thermal fragmentation mechanism, as observed in the previous section, must be present. If one considers the escalation process of a large-scale vapor explosion, the drops ahead of the accelerating explosion front are subjected to a spectrum of flow velocities.

In this section the effects of the water flow velocity on the fragmentation of both a hot and cold drop are presented. Two series of experiments are performed using an alloy drop, one with the drop heated to 700°C and the other under isothermal conditions with the water at 60°C. In the isothermal drop experiments the drop is released from below the water surface so that the drop and water are at the same temperature during the entire fragmentation process. Therefore, the fragmentation process is completely driven by the relative motion between the drop and the water (i.e., hydrodynamic effects). By comparing the fragmentation of the cold and hot alloy drop under exactly the same triggering conditions one can determine the relative importance of hydrodynamic and thermal fragmentation effects.

3.2.2 Flow velocity measurement

The same tank used in the experiments just described, shown in Fig. 7, was used for these experiments. The flow is generated by the expansion of a exploding wire vapor bubble confined within the trigger tube. Since the inner diameter of the tube is fairly small, the bubble interface rapidly becomes planar as it propagates up the tube. High-speed photographs show that the bubble interface is planar after it emerges from the tube. If we assume that evaporation and condensation of the bubble interface is negligible during the time of interest it can be treated as a massless piston. In this case due to the planar nature of the interface and the proximity of the drop to the tube exit the flow velocity which the drop would be subjected to will be very close to the interface velocity. By varying the capacitor voltage one can obtain a range of flow velocities with a maximum of about 60 m/s for the case of the blasting cap. As the bubble surface emerges from the tube it decelerates reaching a steady-state velocity. The time required to achieve steady-state velocity varies depending on the strength of the trigger. The bubble surface position as a function of time could be obtained from the high-speed film and is shown in Fig. 24. Only a few points are shown and a line is drawn in to show the steady-state portion of the bubble trajectory. For the strongest trigger, the blasting cap, a steady-state velocity of 53.9 m/s is achieved almost immediately after the bubble emerges from the tube. In the case of a 3 kV discharge across an exploding wire, the weakest trigger, the final steady-state velocity of 0.53 m/s is achieved after 1.5 ms. For the intermediate triggers the deceleration times lie between these two limits. The steady-state value will be used to characterize the flow velocity in the remainder of this thesis.

The distance travelled with time for a sphere subjected to a drag force by a stream of liquid is well known. The following expression describes the distance travelled by the drop as a function of time.

$$\frac{x}{d} = \frac{T}{\sqrt{\rho_d \rho_d}} \cdot \frac{4}{3C_D(\rho_d \rho_d)} \ln \left\{ 1 + \frac{3C_D}{4} \sqrt{\frac{\rho_f}{\rho_d}} T \right\}$$
(3.1)

where C_D corresponds to the drag coefficient for a sphere at a given Reynolds number (see Appendix A for the details of the derivation). In order to verify that the bubble interface velocity corresponds to the water flow velocity at the drop location the following simple experiment was performed. A 6 mm steel sphere was released into the flow (~45 m/s) generated by a blasting cap, corresponding to a Reynolds number of about 270,000. From

the high speed film taken of the interaction a distance-time graph can be plotted for the sphere's ensuing motion. This plot is shown in Fig. 25 where the solid circles represent the experimental data. The solid line on the graph corresponds to the analytical solution using equation (3.1) with the experimental conditions as input and a drag coefficient of 0.35. The experimental data follows this curve very closely. Note equation (3.1) does not consider the initial velocity of the falling drop (~1 m/s) which may be considered negligible compared to the generated flow velocity. In the literature the drag coefficient for a sphere in a flow with a Reynolds number of 270,000, which corresponds roughly to the critical Reynolds number where the so called "drag crisis" occurs, is between 0.2 and 0.4 (Daugherty and Franzini, 1977). Therefore, the experimentally measured value of 0.35 for the drag coefficient is reasonable, confirming the fact that the flow velocity is equal to the velocity of the bubble surface.

3.2.3 Effect of shock overpressure on maximum bubble size

Fig. 26 shows a typical pressure-time history recorded at the drop position for the case of an exploding wire (15 kV capacitor charge) and a blasting cap in the tank shown in Fig. 7. The peak pressure and positive phase duration are 12.8 MPa and 16 µs for the exploding wire and 37.5 MPa and 18 µs for the blasting cap. Although the positive phase duration of the shock wave remains short and fairly independent of the trigger strength it is clear that the shock overpressure is greatly influenced by the trigger strength. In order to attribute the observed fragmentation phenomenon solely to the flow velocity produced by the expanding trigger vapor bubble it must first be shown that the shock overpressure has no effect on the explosion phenomenon.

In this section experiments investigating the effect of the shock overpressure on the explosion of a single melt drop, quantified by the variation of the first vapor bubble maximum, are reported. In order to separate the shock overpressure effect from the trigger bubble flow effect, a series of experiments using 0.5 g tin drops at 750°C were performed in a square tank measuring 18 cm x 18 cm x 27 cm high, shown in Fig. 27. Since there is no trigger tube to confine the exploding wire vapor bubble, the flow generated is very low and varies very little with trigger energy. By filming the bubble growth rate and calculating the bubble surface velocity it was estimated that the flow velocity at the drop location was less than 3 m/s for a capacitor charging voltage of 10 kV and only slightly higher for a voltage up to 15 kV. The shock wave strength was varied by varying the charging voltage of the 8 µf capacitor up to a maximum of 15 kV which yields shock overpressures of 17.8

MPa. This was found to be the maximum pressure which the apparatus could withstand without damage to the windows. Due to the short duration of the shock wave and the low flow velocity generated by the trigger explosion thus any effect that the shock overpressure would have on the explosion of the drop would be detected in the maximum size of the first vapor bubble.

Fig. 28 shows a typical pressure trace (the trace is shown twice with two different time scales) recorded at the drop location for a 12 kV capacitor charge. The first spike on the bottom trace is the noise which is generated by the TM-11 trigger module at time zero. The blast wave arrives at the drop location 60 µs later corresponding to a drop-electrode distance of 9 cm. From the higher magnified upper trace the shock peak pressure measures 12.7 MPa with a duration of about 5 µs. The pressure trace is relatively clean except for a second pressure pulse due to shock reflection off the tank base which arrives at the drop about 70 ms later.

Fig. 29 shows a compilation from many experiments using tin drops and solid spheres illustrating the variation in the first bubble maximum (scaled by the initial effective drop diameter) estimated from high speed film records from each trial as a function of the shock overpressure. Due to the difference in heat capacity between the tin and the steel sphere one cannot make a direct correspondence between the two results, except for comments on the general trend of the data. For shock pressures above about 2.0 MPa the maximum size of the first vapor bubble produced by the explosion of the tin drop is approximately 4 times the initial drop diameter. Above this shock pressure, taking into account the scatter in the data, the bubble maxima appear to have a very weak dependence on the shock pressure. For shock pressures below this value the first bubble maximum decreases dramatically to a low of 0.6 MPa where no interaction could be triggered in the tin drop. This sudden drop off in the size of the first bubble maximum at low pressures is due to the incomplete collapse of the vapor film surrounding the drop. The added presence of noncondensible gas in the film acts as a cushion preventing film collapse. The maximum bubble diameter produced by the hot solid sphere shows a similar slight increase with increasing shock pressure. Since there is no difference in trend of the maximum bubble diameter data for the cases of an exploding tin drop and a nonfragmenting sphere with shock overpressure the shock pressure, one can conclude that shock overpressure has negligible effect on the fragmentation process for overpressures up to 18 MPa.

3.2.4 Effect of flow velocity on the fragmentation of cold alloy drops

Before considering the effect of flow velocity on a hot drop, it is useful to first characterize the influence of flow velocity on the fragmentation of a cold drop. Since the same drop material is used in both the hot and cold drop experiments (i.e., cerrolow alloy) a direct comparison of the two can give insight into the relative importance of thermal and hydrodynamic fragmentation mechanisms during the explosion of a hot drop. For the cold drop experiments the drop is released from below the water surface so that the drop and water are in thermal equilibrium (the water temperature is maintained at 60°C). This method of drop release eliminates the possibility of a trailing gas bag which is characteristic of above-surface drop release. Nevertheless it was observed that a trailing gas bag had no noticeable effect on drop breakup. In general, the drop takes on an ellipsoidal shape as it descends in the water. Since the drop is usually slightly tilted to one side as it falls, its shape appears different in the photographs from one trial to the next, depending on the drop orientation.

Figures 30a-d show a sequence of photographs illustrating the fragmentation process of a 0.5 g cold alloy drop at four different water flow velocities. The protrusion which is visible in the lower portion of the first photograph in each sequence is the head of a bolt which is attached to the top of the vertical tube. The dark region at the bottom of the photographs corresponds to the bubble generated by the trigger system. The photographs are arranged to show the time history of both the drop and bubble surface position. The variation of bubble position with time shown in Fig. 24 corresponds to the trials shown in Figs. 30a-d. For the lowest flow velocity of 0.5 m/s which corresponds to a Weber number of 14.5 (note the terminal velocity of the drop is about 1 m/s, and this value is added to the flow velocity to calculate the Weber number), obtained using an exploding wire with a 3 kV capacitor charge (Fig. 30a) it is apparent that on the time scale of milliseconds the drop undergoes little fragmentation. Since the Weber number is just below the critical Weber number of about 17 when drop breakup begins (Tan and Bankoff, 1986), the drop undergoes simple oscillatory motion. Fig. 30b shows the fragmentation process for a flow velocity of 3.8 m/s (We = 94). After 3 ms the projected area of the fragmentation zone has nearly quadrupled compared to the initial drop area. During the first 2 ms the drop surface is drawn off producing long filaments extending from the drop on the downstream side. After about 3 ms fine particles can be seen to form downstream of the drop as a result of the breakup of the long filaments. This type of behaviour was observed by Tan and Bankoff (1986) using mercury drops in water and Kim et al. (1983) with gallium drops in a water flow. The upstream surface of the drop shows only minimal signs of roughness caused by the growth of instabilities. There is also very little lateral expansion of the drop as a result of drop deformation. Fig. 30c shows the drop breakup in a 18.4 m/s (We = 2,440) flow. Shortly after the initiation of the exploding wire (up to $640 \text{ }\mu\text{s}$), cavitation bubbles can be seen to form throughout the bulk of the water as a result of the sharp expansion behind the blast wave generated by the exploding wire. The breakup is again characterized by a drawing off of the drop surface at the equator, only in this case there is little evidence of the filament structure downstream of the drop. Instead the drawn off surface material quickly breaks up into small fragments. At this Weber number the upstream surface roughening is much more pronounced.

For the maximum flow velocity in this series of experiments of 53.9 m/s (We = 13,442), obtained using a blasting cap (Fig. 30d), the breakup is much faster and more violent. Fine fragments are immediately tom off the drop surface. The fragmentation rate is so high that the fragment mist behind the drop appears opaque on the photographs. Due to the initial flat shape of the drop the lateral growth observed in this trial is a result of fragments from the upstream surface being convected parallel to the surface rather than due to the deformation of the parent drop. An indentation appears to grow on the upstream surface of the drop near the center of the drop dividing the parent drop into two sections. This behaviour is usually referred to as "catastrophic breakup" and was also observed by Reinecke and Waldman (1970) for Weber numbers above 30,000 for water droplets in an air stream. The catastrophic breakup can be attributed to the growth of large wavelength waves on the upstream surface of the drop. The drop is severed when the amplitude of these waves becomes comparable to the drop width.

3.2.5 Correlation of Cold Drop Data

In order to obtain more quantitative information a second series of cold drop experiments was carried out using smaller 0.25 g drops of gallium in order to have a more spherical and reproducible initial drop shape. For this series of experiments only high-speed regular photography was used to record the fragmentation process. The photographic results for the gallium drops are similar to those obtained for the alloy drops shown in Figs. 30a-d. .

Drag Coefficient

It is of interest to calculate the effective drag coefficient, CD, exhibited by the drop. The drag coefficient will be different from that of a solid since the drop continually deforms and fragments as a result of the water flow. The Reynolds number in all the gallium drop experiments was between 60,000 and 200,000. The drag coefficient of a sphere in this Reynolds number range is about 0.4-0.5 (Daugherty and Franzini, 1977). Fig. 31 shows the displacement of the drop, x, normalized with the initial drop diameter perpendicular to the flow, d, as a function of a nondimensional time, T, for several experiments. The graph shows that all the curves for the different experiments collapse approximately to a single curve with the nondimensional parameters chosen. The experimental data can be fit approximately using the expression given in equation (3.1) with a drag coefficient of 4 (see Fig. 31). Using early times (up to a nondimensional time of 1), when drop deformation and breakup are not as advanced, a constant drag coefficient between 2 and 3 is more representative. This value is higher than that of a solid sphere because the drop more closely resembles an oblate spheroid as a result of aerodynamic drop flattening and also the effective projected area of the drop increases with time as a result of drop flattening. This value of 2-3 for the drag coefficient for early times is in agreement with that reported by Simpkin and Bales (1972) who fit their water drop/air data with a drag coefficient of 2.5 as well as Patel and Theofanous (1981) who fit their mercury drop/water data with a drag coefficient slightly less than 2.5.

Nondimensional Breakup Time

Since regular photography was used to film the drop breakup, direct observation of complete drop fragmentation was not possible. The only information which can be obtained from the high speed film concerns the size and shape of the silhouette or profile of the cloud of fine fragments stripped from the drop surface. In the past there have been various criteria used to define the size of the silhouette corresponding to the time of total drop breakup. For example, Patel and Theofanous (1981) used the doubling of the initial drop diameter and Kim et al. (1983) used the quadrupling of the silhouette area along with several other criteria to define the total fragmentation time of the drop. To compare with past results, we have calculated the time history of the silhouette area for each trial by digitizing the photographs and using image analysis software to calculate the projected area. Fig. 32 shows the nondimensional time for quadrupling of the initial drop projected area as a function of the Weber number for each experiment. The two solid circles represent the

time for total fragmentation estimated from x-ray radiographs. The solid circle for the lower Weber number case corresponds to the experiment from Fig. 11 and the higher Weber number experiments were done using 0.4 g alloy drops from Fig. 35. The x-ray points fit well with the trend of the quadrupling of the projected area obtained from the gallium experiments. Overall, the nondimensional time for quadrupling of the area is between 1 and 2.5 but there does appear to be a decreasing trend with Weber number.

An inverse dependence of the nondimensional drop breakup time with Weber number has been observed experimentally by Patel and Theofanous (1981), Simpkins and Bales (1972), and Reinecke and Waldman (1970). Reinecke and Waldman (1970) pointed out that a similar Weber number dependence results from the characteristic amplification time for the fastest growing Rayleigh-Taylor instability wave. They consequently attributed their observed drop breakup to catastrophic drop breakup caused by drop piercing of long wavelength Rayleigh-Taylor instability waves. Different proportionality constants have been obtained by the different investigators due to the different criteria used to define total breakup. Patel and Theofanous (1981) obtained a constant of proportionality of 1.66 based on the doubling of the initial drop diameter, Simpkin and Bales (1972) obtained a value of 22 based on the first appearance of waves on the upwind surface of the drop and 65 for total fragmentation, and Reinecke and Waldman (1970) fit their x-ray data for total fragmentation with a constant of 45. However, other investigations of drop fragmentation have found no clear dependence of breakup time with Weber number. For example, Kim et al. (1983) found $T_{A=4A_0} \sim 2$ for gallium drops and Baines and Buttery (1979) reported a breakup time of about 4 independent of Weber number.

The present data can best be fit with the following Weber number dependence

$$T_{A=4Ao} = 12 We^{-1/4}$$
 (3.2)

which is plotted in Fig. 32 along with the experimental data. Equation (3.2) should only be considered as a curve fit to the data to show the slight dependence with Weber number and for comparison with previous work. The scatter in the data is large so that an accurate correlation cannot be found. The constant F in equation (3.2) is 12 and does not match any of the other values reported in the past.

3.2.6 Effect of flow velocity on the interaction of a hot drop

A series of experiments was carried out to investigate the interaction of a hot alloy drop, initially at 700°C, immersed in water at 60°C and subject to different flow velocities. Figs. 33a-d show a sequence of photographs taken during four such experiments. For a flow velocity of 0.5 m/s (We = 14.5) the interaction results in the formation of a vapor bubble centered at the drop. The vapor bubble expands to a maximum size after about 1 ms. The dispersed fragments from the initial interaction obscure the bubble collapse. The degree of fragmentation is extensive at 2 ms when the vapor bubble has collapsed leaving fine scale fragments dispersed in the surrounding liquid. From Fig. 30a it is apparent for a cold drop under similar flow conditions at the same time, that fragmentation is minimal. Based on this comparison, it is evident that the fragmentation mechanism in a hot drop interaction, under this flow condition, is dominated by thermal effects with little contribution from hydrodynamic fragmentation resulting from the incident flow.

For a higher flow velocity the vapor bubble formed around the drop as a result of the interaction is displaced upwards relative to the drop in the direction of the flow. This bubble migration can be seen in the interaction shown in Fig. 33b for a flow velocity of 4.8 m/s (We= 186). Although the upward displacement of the bubble is much more pronounced in Fig. 33b as compared to 33a, the bubble collapse times are similar. This indicates that the increased flow velocity has little effect on the dynamics of the vapor bubble. A comparison of the time scales for hydrodynamic fragmentation of a cold drop (see Fig. 30b) with the hot drop shows that hydrodynamic fragmentation is too slow to account for the breakup of the hot drop. Even at this moderate velocity the presence of the vapor bubble surrounding the drop negates any contribution from the hydrodynamic stripping process which is present for the cold alloy drop at the same flow velocity.

Fig. 33c shows the interaction of a hot alloy drop with a flow velocity of 17 m/s (We= 2,654). From the photographs there is no evidence of vapor formation on the upstream surface of the drop, although, a vapor bubble does form in the wake region. The vapor bubble grows to a maximum size after about 800 µs and then collapses. The asymmetric collapse of this bubble causes further fragmentation at the downstream surface of the drop. From the sequence of photographs it is not clear if the evaporation is completely suppressed at the bottom of the drop or if the high pressure vapor is restricted from expanding as a result of the high flow velocity and swept into the downstream wake region. At 400 µs the bottom of the dark cloud is fairly smooth but by 800 µs the bottom

surface becomes highly corrugated indicating the penetration of the drop surface or stripped mass into the water. A comparison of the hot drop interaction in Fig. 33c with the cold drop breakup at a similar flow velocity reveals that the fragmentation of the upstream surface of the drop is very similar to that of a cold drop (see Fig. 30c) for times later than 400 µs. The growth of the vapor bubble above the drop also disperses the fragments stripped from the front of the drop further downstream than would be possible without a vapor bubble due to the low viscosity of vapor compared to water. The combined fragmentation of the drop due to the stripping of the upstream surface and the fragmentation of the back surface due to rapid evaporation and bubble collapse leaves the wake region littered with fragments at later times not shown in the figure.

Figure 33d shows the interaction of a hot drop with a flow velocity of 57 m/s (We = 14,760). The behaviour of the drop is very similar to the breakup of the cold alloy drop at the same flow conditions, as shown in Fig. 30d. There is strong lateral expansion due to the stripping of fragments from the upstream surface of the drop and the drop appears to be in the process of dividing into several smaller drops.

A similar series of hot drop experiments was carried out using tin as the drop material. Figs. 34a and 34b show the results for the two extreme flow velocity cases. For a flow velocity of 0.5 m/s the tin drop interaction is unaffected by the flow. Characteristically a vapor bubble is formed which expands to a maximum and then collapses. This bubble expansion and collapse is very similar to that observed in the hot alloy experiments. For the case of a 51 m/s flow velocity, shown in Fig. 34b, a large gas bag is dragged down behind the drop. However, the flow strips the bag away and the drop fragmentation appears to be unaffected by its presence. The tin drop rapidly fragments in a fashion similar to the hot and cold alloy drops at this flow velocity.

3.2.7 X-ray Visualization of Fragmentation Process

Flash x-ray was used in a series of experiments using blasting caps to generate flows of the order of 40 m/s. Both hot and cold drop conditions were studied in order to determine if the fragmentation mechanism in both cases was the same, as suggested by the high speed regular photographs presented in Figs. 30d and 33d. Shown in Fig. 35 is a series of x-ray radiographs taken at different times in the fragmentation process of a 0.4 g cold alloy drop. Shown below each photograph is the dimensional and nondimensional (in brackets) time after the arrival of the triggering shock wave at the drop location. The nondimensional time

(see equation (1.4)) is calculated using the average velocity of the flow up to the time at which the x-ray was taken. The average Weber number for these trials is about 8,500.

At time zero the drop takes on an ellipsoidal shape which is characteristic of the cold drop alloy trials. The initial drop shape can vary from experiment to experiment and thus the resulting shape of the fragment cloud behind the drop will vary accordingly. The sequence of photographs shows that the fragmentation of the drop is a result of mass being stripped from the drop surface and carried downstream. Typically there is a darker region upstream which contains the parent drop and a lighter region downstream which is comprised of the stripped fragments. Using regular photography it is not possible to distinguish between these two regions. By 640 µs there is no distinguishable sign of a parent drop upstream and thus fragmentation can be assumed to be complete. An insufficient number of experiments were carried out using x-ray photography to obtain an accurate nondimensional total breakup time. However, based on the limited data a value between 1.5 and 2 is most representative and is included in Fig. 32.

Fig. 36 shows a sequence of x-ray radiographs taken of a 0.5 g tin drop initially at 700°C interacting in a water flow velocity of about 40 m/s (similar to the cold drop experiments shown in Fig. 35). The photographs show that up to a time of 185 µs a vapor bubble is present which forms around the drop following the initial contact between the drop and the water. However, the vapor bubble does not undergo the characteristic growth and collapse cycle which is observed under low flow conditions (e.g., see Fig. 33a and 33b). As was observed in the x-ray records taken for low flow velocity hot drop experiments (see section 3.1.3), melt spikes protruding radially outwards from the drop surface are evident. There appears to be a substantial number of fine fragments located at the surface of the vapor bubble creating a ring around the drop. At later times the vapor bubble is displaced upwards by the oncoming water flow, as observed at 320 µs. At this time the vapor bubble region above the drop is fairly free of fragments. At later times, 440 µs, the bubble region behind the drop becomes increasingly dark as more and more melt is fragmented and carried into the wake. By 560 µs the vapor bubble has collapsed and only a cloud of fine fragments remain. The subsequent dispersion of these fragments due to the water flow can be seen at 720 µs. Several x-ray photographs were taken at each time and the phenomena described above was found to be quite repeatable from one experiment to the next.

Chapter 4

3

DISCUSSION

4.1 Phenomenological Model for Thermal Fragmentation

Models proposed in the past to describe the fragmentation process for a hot drop interaction were based on *indirect* evidence from regular high-speed photography. Flash x-ray radiography allows the fragmentation of the melt drop to be observed *directly*. The fragmentation mechanisms described earlier in the introduction will now be reconsidered in light of the experimental data and a new phenomenalogical model for the fragmentation process will then be described based on the flash x-ray results.

From a direct comparison between the fragmentation of cold and hot cerrolow alloy drops, it is clear that direct hydrodynamic fragmentation of the drop by the relative flow of the ambient water cannot account for the breakup of a hot drop. Even for the higher flow velocities a vapor bubble forms immediately following film collapse. This vapor bubble acts as a physical barrier deflecting the flow, preventing direct contact between the water and the drop surface. From the x-ray photographs, there is also no evidence that the impact of the water with the drop following film collapse directly causes fragmentation of the drop. Therefore the energy required to break up the drop must be derived from the thermal energy of the drop itself, i.e., heat transfer during liquid-liquid contact leads to the rapid generation of high-pressure vapor that expands doing mechanical work on the drop surface. The x-ray photographs do not show any evidence that water is injected into the drop by the formation of water jets formed during asymmetric film collapse as proposed by Kim (1985). If the formation of coolant jets is the primary mechanism for drop fragmentation, then the explosion process should be quite sensitive to the initial shape of the vapor film (i.e., thickness and asymmetry) as well as the strength of the triggering shock wave which will determine the amount of coolant injected into the drop. However, the results presented in Section 3.2.3 indicate a very weak dependence on the triggering strength for shock pressures up to 20 MPa and that the triggering process serves only to

collapse the vapor film and initiate the subsequent explosion. It was also found that the explosion of a drop with a large attached air bag was qualitatively similar to the explosion of a drop with only a thin vapor film surrounding the drop.

Based on the experimental observations the fragmentation of a hot drop can be divided conceptually into three stages: (i) collapse of the initial vapor film and formation of the melt spikes $(t = 0-100 \mu s)$, (ii) growth of perturbations on drop surface and distortion of drop by turbulent vapor flow inside bubble ($t = 100 \,\mu s - 1 \,ms$), and (iii) collapse of bubble, impact of the water with the drop and fine fragmentation of the bulk of the drop (t > 1 ms). Figure 37 shows a schematic of a scenario for the events that occur following film collapse. Prior to film collapse, small-scale (~ 0.5 mm) ripples are present on the vapor film surrounding the drop (see Fig. 14d) that are caused by Kelvin-Helmholtz instability of the vapor-water interface as the drop descends in the water. During shock-induced film collapse (picture b of Fig. 37) of the vapor film, these perturbations will grow on the film surface due to Rayleigh-Taylor instability. The instability occurs in the later phase of the film collapse when the vapor-water interface decelerates due to the increased pressure in the vapor film. After the passage of the triggering shock, the collapsing film will first contact the drop at a series of local points (picture c). Rapid heat transfer and the formation of high-pressure vapor bubbles at these points will lead to a nonuniform pressure distribution on the surface of the drop. The local generation of high-pressure vapor at the drop surface will cause the formation of a surface wave and a small crater or indentation on the drop surface (pictures d and e). Some initial fragmentation occurs as a result of the cratering process. The metal squeezed between the indentations form thin filaments of metal that are ejected radially from the surface at high speed (picture f in Fig. 37). The filaments then break up into small fragments. The shape of the drop surface at early times (see Figs. 19 and 22) suggests that the drop surface is distorted by strong localized forces much as a ball of putty is deformed when squeezed sharply by hand, extruding the putty between the fingers. The mechanism of melt jet formation by rapid bubble growth at the melt surface has been explored further in experiments in an analogous system which will be described later.

The filaments of melt that extend from the drop surface continue to grow as the vapor bubble expands. During the expansion of the bubble, although the drop surface appears severely distorted and some fine fragments are present within the bubble and near the bubble surface, the parent drop appears to be largely intact. As the vapor bubble decelerates as it reaches its maximum diameter, the inertia of the fine fragments cause them

to impact and penetrate the bubble surface as shown in picture g in Fig. 37. These fragments are eventually left behind the collapsing bubble. When the bubble collapses and contact between the water and the drop is re-established, a second melt/water interaction occurs. The hydrodynamic force associated with the inrush of the water and the subsequent rapid boiling effectively shatter the remainder of the drop. The melt fragments are then dispersed by the expansion of the vapor.

4.1.1 Formation of Melt Jets

To gain insight into the mechanism of the formation of the jets of melt that are visible at early times in the interaction, further experiments were carried out in a stratified water/liquid metal system. The experiments were used to qualitatively investigate the behavior of a liquid metal surface following the generation of local high pressure vapor bubbles on the surface. The apparatus, as shown in Fig. 38, consists of a narrow channel (5 cm wide and 1.2 cm thick) filled to a height of 5 cm of liquid metal with an equal height of water above the metal. A low melting point alloy was used (Wood's metal) and the apparatus was heated above the melting point of the alloy with a surface heater. Two exploding wires were placed less than a millimeter above the metal surface in the water and located 2.5 cm apart. The exploding wires were connected in parallel to a 8 µF capacitor charged to 4 kV and discharged simultaneously, generating two line sources of high-pressure vapor just above the liquid metal surface. The subsequent vapor bubble growth and growth of the surface perturbations were recorded with regular and x-ray photography.

Figure 39 shows four x-ray radiographs (from different experiments) at different times, illustrating the growth of waves on the liquid metal surface. At t = 0, prior to triggering the exploding wires, the tips of the electrodes holding the wires are just visible above the metal surface. At t = 1 ms, the metal surface has become highly perturbed with cavities forming at the locations of the electrodes. By 2 ms a definite structure has emerged. Four distinct surface waves have formed on the metal surface, two between the electrodes moving towards each other and one on either end moving towards the side walls. There are also three very fine filaments of metal which form at the exploding wire locations and one at the midpoint between the exploding wires. After 5 ms the two surface waves between the exploding wires have merged forming one large spike at the midpoint. The surface waves on the sides have collided with the walls and have also formed spikes. The three large spikes are remarkably symmetric. The two fine filaments at the exploding wire locations

are still present and appear to have grown vertically and spread laterally slightly. At later times, the spikes break up into fine particles.

The initial waves formed on the liquid metal surface by the impulsive disturbances are reminiscent of the waves observed by Naugolnykh et al. (1989) during the local generation of high-pressure vapor on a liquid surface with a laser beam. The formation of liquid metal jets has also been observed by Greene et al. (1983) in film boiling experiments with a stratified water/liquid metal system. Greene postulated that the metal jets were the result of local liquid-liquid contact between the melt and water caused by local film collapse. The similarity in appearance between the jets formed in Fig. 39 and the surface perturbations in the hot drop experiments suggests that the local generation of high-pressure vapor at an interface is a plausible explanation for the spike formation observed in Figs. 19 and 22.

4.1.2 Influence of External Flow on the Thermal Fragmentation Process

From the high speed regular photography it is evident that the external flow plays an increasingly important role with increasing flow velocity. For flows up to about 20 m/s the vapor bubble which is produced following film collapse is simply displaced in the direction of the flow. The process of melt spike formation and its rate of growth remains the same as at lower flow velocities. At flows above 40 m/s the bubble dynamics and fragmentation change significantly, as can be seen in Fig. 36. As in the low flow case, a vapor bubble is produced shortly after the passage of the shock and melt spikes form at the drop surface. The main difference is in the lifetime of the vapor bubble and the fragmentation rate of the drop inside the vapor bubble. From Fig. 36 it is clear that the complete fragmentation of the drop does not require the collapse of the vapor bubble as observed in low flow experiments. The majority of the drop fragmentation occurs within the vapor bubble. Since the contact time between the water and drop surface following film collapse is very short, the additional fragmentation cannot be attributed to hydrodynamic stripping caused by the initial high flow associated with the shock wave. At later times the bubble effectively shields the drop from the oncoming flow, so the increased fragmentation is not the result of direct stripping of the drop surface by the water flow from the expansion of the triggering bubble. There also appears to be more initial fine fragments near the bubble surface, as compared to that observed in the low flow fragmentation. It is possible that the large shock overpressure (~30 MPa) generated with the blasting cap does have some influence on the initial fragmentation caused by the contact of the water and drop surface. Under the higher shock overpressure the vapor film will collapse at a faster rate, and thus the deceleration of the interface as it approaches the drop surface must also be higher. Since the wavelength of Rayleigh-Taylor instability is inversely proportional to the square root of the acceleration one would expect more contact points between the water and drop surface to result. Therefore more mass can be stripped during the initial local explosions on the drop surface. However, this cannot account for the large increase in fragmentation of the drop observed at later times.

Figure 40 shows a schematic of a scenario for the events that occur following the initial formation and expansion of the vapor bubble. As the bubble is displaced downstream one would expect that the eventual contact between the water and the upstream surface of the drop would result in a second explosion. Since there is no evidence of such an explosion this indicates that evaporation at the vapor-bubble interface prevents direct contact between the water and drop surface. The vapor produced by the evaporation cannot expand upstream due to the high stagnation pressure produced by the oncoming water flow. Therefore, the vapor is forced to flow around the drop (Corradini, 1980), as shown in Fig. 40c. The enhanced fragmentation can be attributed to the vapor flow which tears away the melt spikes that are initially formed and then continues to strip the drop surface. The vapor then carries the fragments into the bubble downstream from the drop which explains the increasing amount of fragments in the vapor bubble with time observed in the x-ray radiographs. The circulation of the vapor within the bubble provides for excellent heat exchange between the parent drop and fragments to the vapor. This energy is then transferred through the bubble surface and convected downstream by the external water flow. Since the vapor bubble appears to totally condense by 560 µs with no further interaction between the fragmented drop and water one can conclude that energy transfer is complete. This is followed by the subsequent dispersion of the fragments downstream by the water flow. In the fragmentation of the cold drop under similar flow conditions (see Fig 35), complete fragmentation and hence energy transfer occurs by a time of 640 μs. One can conclude that although the process of fragmentation in the hot and cold drops are very different the overall time for complete energy transfer from the drop to the water is about the same.

4.2 Model for Bubble Dynamics

j.

The experimental results demonstrated that for a hot drop under low flow conditions (i.e., <20 m/s), drop fragmentation is driven by thermal effects and direct hydrodynamic

fragmentation by the surrounding flow of coolant plays no role. The production of vapor during the interaction has two effects on the overall heat transfer from the drop to the water. The low thermal conductivity of the vapor, relative to that of water, greatly reduces the heat transfer coefficient and thus the overall heat transfer from the drop that would otherwise be possible if no vapor bubble was present. The vapor bubble also acts as a physical barrier against any additional fragmentation due to direct stripping of the drop surface by the water flow around the drop. For flows as high as 40 m/s, x-ray radiographs have shown that thermal effects are still important in that a vapor bubble is generated during the early stages of the interaction.

In light of the important role that the vapor bubble plays in the interaction it is of interest to develop an analytical model to predict the lifetime and dynamics of the bubble generated from a single drop interaction. Further insight into the drop fragmentation and explosion propagation processes can also be obtained by such an analysis. In the following sections a simple parametric model is developed to predict the time history of the bubble diameter generated from the interaction of a hot drop under low flow conditions. The model predictions are compared with the hot tin drop experimental results reported in Chapter 3.

4.2.1 Formulation of model

The initial collapse of the vapor film, following the passage of the shock wave, leads to liquid-liquid contact between the drop and water. Due to the sudden increase in the water temperature at the interface (i.e., typically supercritical) the pressure also shoots up due to thermal expansion. The pressure at the interface is relieved by the formation of a shock wave which propagates away from the interface into the water. The pressure at the interface relaxes with a characteristic time $\tau = \alpha/c^2$ where α is thermal diffusivity and c is the speed of sound (Cooper and Blewett, 1978). The characteristic relaxation time for water is about 10^{-13} seconds. During the time the water is in a supercritical state rapid heat transfer to the water occurs. When the pressure at the interface drops below the critical pressure, the water at the interface flashes into vapor and an evaporation wave is generated which propagates into the water. In the present model the evaporation process is not modeled, instead it is assumed that the water and drop surface come in contact and after a certain amount of "contact" time, the water which remains above the superheat limit flash evaporates. The vapor produced forms a high pressure bubble enclosing the drop. As the bubble expands, energy is transferred to the bubble by the distorting drop surface. The

contact time and the extent of the growth in the drop surface area are the two parameters in the model.

Since the initial energy deposited in the bubble following film collapse occurs in a time that is short relative to the time for bubble expansion (<40 µs compared to 1 ms for bubble expansion) then a good approximation to the subsequent bubble growth will be given by the solution to the classical Rayleigh equation for bubble dynamics(see Appendix B for details),

$$R\ddot{R} + \frac{3}{2}\dot{R}^2 = \frac{1}{\rho} \left\{ (P_B - P_\infty) - \frac{2\sigma}{R} - \frac{4\mu\dot{R}}{R} \right\}$$
 (4.1)

where R, R, ρ , P_B , P_∞ are the bubble radius, radial velocity, radial acceleration, liquid density, and pressure in the bubble and at infinity and σ and μ are the interface surface tension and the viscosity of the water, respectively. The Rayleigh equation is derived from conservation of mass and momentum applied to the surrounding water and does not consider any mass flux across the bubble surface due to evaporation or condensation. Condensation may play a minor role in the later stages of the bubble expansion when the bubble growth slows down and the bubble pressure and temperature drop. The added complexity of including evaporation and condensation effects in the present model is not considered justifiable. Following the initial superheating of the water, the net heat transfer to the vapor is incorporated through an expression for the conservation of energy for the steam inside the bubble, which assuming a closed system can be written as,

$$\frac{dU}{dt} = \dot{Q} + P \frac{dV}{dt} \tag{4.2}$$

where U and V are the internal energy and volume of the bubble. Figure 41 shows a schematic of the control volume used in the analysis consisting of only the steam inside the bubble. The net heat transfer, Q, includes heat transfer into the bubble from the distorting drop surface, Q_{DS} , and heat transfer out of the bubble through the vapor bubble surface, Q_{BS} , such that $Q = Q_{DS} - Q_{BS}$. If an estimate for the net heat transfer is made, then equations (4.1) and (4.2) together with an appropriate equation of state U = U(P, V) and initial conditions can be solved for the time history of the bubble growth, R(t).

To estimate the heat transfer rate from the drop to the vapor, the following expression was employed,

$$Q_{DS} = h A_0 K(R) (T_d - T_v)$$
 (4.3)

where h is the heat transfer coefficient, A_o is the initial drop surface area based on the effective drop diameter, K(R) is a growth factor accounting for the increase in drop surface area due to the formation of melt spikes from the drop surface, and T_d and T_v correspond to the drop and vapor temperatures, respectively. A heat transfer coefficient of 10^3 was used based on previous investigators (e.g., Fletcher and Thyagaraja, 1989), and it was assumed that the area available for heat transfer increases by an order of magnitude by the time the bubble reaches its maximum. From the x-ray results it was observed that the length of the melt spikes grew proportionally with the bubble radius. If we assume that the cross sectional area of the spikes remains constant, then the growth of the spike surface area also grows proportionally with the bubble radius. Therefore, during the bubble growth and collapse, the surface area is taken to increase proportionally with the bubble radius (i.e., $K(R) = 10(R/R_{max})$).

Heat transfer through the vapor bubble surface is assumed to be through conduction. Assuming a linear temperature profile between $(R-R_o)/2$ and R, the heat transfer rate is expressed as follows

$$Q_{BS} = 4\pi R^2 \left\{ \frac{k_v (T_V - T_I)}{0.5(R - R_0)} \right\}$$
 (4.6)

where k_V and T_V are the vapor thermal conductivity and temperature and T_I is the saturation temperature of the vapor corresponding to the bubble pressure.

With the assumption of ideal gas behavior for the steam, the internal energy is given by

$$U = \frac{PV}{\gamma - I} = \frac{4\pi}{3(\gamma - I)} PR^3 \tag{4.5}$$

where γ is the ratio of the specific heats at constant pressure γ in dvolume (c_p/c_v). Replacing the internal energy in equation (4.2) by the expression given in equation (4.5) an explicit expression for the time derivative of pressure, P, as a function of bubble radius, R, can be derived



$$\frac{dP}{dt} = \frac{3(\gamma - 1)}{4\pi} (R^3 - R_o^3) \ \ \ \ \ \ - \frac{3\gamma P \dot{R}}{(R - R_o)}$$
 (4.6)

4.2.2 Estimation of Vapor Bubble Initial Conditions

To estimate the initial conditions in the vapor bubble (i.e., pressure and volume) we must first determine the drop temperature just before the shock wave reaches it. This requires calculating how much the drop cools as it falls through the water to the depth where it is triggered. Because of the small drop size and poor heat transfer characteristics through the vapor film one can treat the cooling drop as a lumped-heat capacity system (i.e., a uniform temperature exists in the drop at all times). This treatment of the problem is applicable since the Biot number is about 0.01, which is well below the critical value of 0.1. The heat loss through the vapor film results in a decrease in the internal energy of the drop, and thus

$$m c_p \frac{dT}{dt} = q_o A (4.7)$$

where m and c_p is the mass and heat capacity of the drop, A is the drop surface area, and q_o is the average heat flux. An estimate for q_o can be obtained from data obtained by Walford (1969) who measured the average heat loss experienced by a 6.35 mm diameter nickel sphere, at different temperatures, dragged in water at various temperatures. There will be a small error in using Walford's data due to the difference in drop material and size (recall the effective drop diameter in the present experiments is 5.1 mm). The sphere velocities used in Walford's experiments varied between 1.2 and 1.5 m/s which is comparable with the 1 m/s terminal velocity measured in the free falling tin drops. In any case, Walford showed that the average heat flux was almost completely independent of velocity, for the velocity range used in his experiments. Walford's data shows that a value $q_o = 4 \times 10^6 \text{ W/m}^2$ is appropriate for a sphere and water temperature of 700°C and 60°C, respectively. Integrating equation (4.7), taking q_o to be constant (Walford's data shows that q_o is fairly constant for the drop and water temperature range used in the present experiments), and assuming that the drop reaches terminal velocity, u_T , instantaneously, the drop temperature at any depth, L, is given by

$$T = T_o - \frac{4\pi \ q_o \ r^2 \ L}{m \ c_p \ u_T} \tag{4.8}$$

Taking an initial drop temperature of 700°C, tin drop mass of 0.5 g, and 6 cm to be a typical water depth where the interaction is triggered, equation (4.8) yields a drop temperature of 527°C.

Experimental results show that after about two frames from the high-speed camera (i.e., \sim 80 μ s) the growth of the vapor bubble is first visible. When the triggering shock first arrives at the drop location, film collapse and superheating of the water occurs within this time of 80 μ s. The exact time for film collapse or superheating is not known, therefore, for the purpose of these calculations it will be assumed that the time during which there is liquid-liquid contact and rapid heat transfer is on the order of one frame duration, or about 40 μ s. It will also be assumed that the water perfectly wets the drop surface following film collapse and that heat transfer is through conduction only. As discussed in the section (4.1), the problem is more complex since only local points of contact between the water and drop surface result following film collapse. Considering the above assumption and neglecting curvature effects, the interface temperature, T_I , can be calculated using equation (1.1). For a drop and water temperature of 527°C and 60°C, respectively, the interface temperature is estimated to be 460°C. The temperature profile of the water near the drop surface can be derived from the one-dimensional diffusion equation, and is given by

$$\frac{T(x,t) - T_I}{T(x,0) - T_I} = erf\left(\frac{x}{2\sqrt{\alpha}t}\right)$$
 (4.9)

where erf is the error function, x is the distance from the drop surface into the water, T is the water temperature at a distance x, and α is the thermal diffusivity of water. As mentioned earlier, we will consider that all the water which is heated to a temperature above the superheat limit (~300°C) in a time of 40 μ s will evaporate. Equation (4.9) predicts that a 1.87 μ m thick layer of water will be superheated above the superheat limit, which corresponds to a mass of 0.15 μ g. If this mass of water is assumed to vaporize at the superheat limit, then the initial pressure in the bubble will be about 8.6 MPa and the density will be about 46 kg/m³ corresponding to the saturated vapor conditions at 300°C. Based on this density the thickness of the vapor layer will expand to about 40 μ m during the evaporation process.

4.2.3 Estimation of y for Ideal Gas Assumption

Equations (4.1) and (4.6) were solved numerically using a fourth-order Runga-Kutta method with a time step of 1 μ s. Before any calculations could be performed an appropriate value of γ for steam was sought. Since the steam is initially in a state of saturated vapor one would expect that as the bubble grows, and the steam pressure and temperature drop, steam would condense. Therefore, a γ representative of wet steam must be incorporated in the ideal gas model.

A value of γ was found by comparing bubble diameter time histories calculated using different values of γ with the bubble diameter time histories obtained using a real gas equation of state under the same conditions. The equation of state for the steam was based on the equations given by Reynolds (1979) which are a fit to the steam table data of Keenan et al. (1969). The solution was obtained by solving equation (4.1) and (4.2) along with the real gas equation of state. The bubble diameter growth curves for $\gamma = 1.09$, 1.25 and 1.4 are shown together with the predictions using the steam tables in Fig. 42. Note these curves were calculated for the case of no net heat transfer to the bubble (i.e., adiabatic process), $\dot{Q} = 0$ in equations (4.2) and (4.6). From Fig. 42 it is evident that the bubble growth is fairly sensitive to the choice of γ . The ideal gas bubble behavior predicted using a value of $\gamma = 1.09$ fits very well with the initial growth of the bubble predicted by the steam table calculations. After the bubble maximum diameter is reached the steam table calculation predicts a faster collapse of the bubble. The reason for this can be seen in the calculated bubble pressure time histories shown in Fig. 43. For the ideal gas predictions the bubble pressure increases during the collapse phase (t > 0.7 ms) whereas in the case of the calculations using the steam table, the pressure remains constant and the steam condenses. Therefore, the reason for the slower collapse of the ideal gas bubble is because the increased bubble pressure retards the bubble collapse.

Figure 44 shows the steam bubble expansion-compression process predicted by the real gas equation of state on the P-V plane. Also shown in the figure is the saturation dome which is depicted by a dotted line. The steam, initially saturated vapor at 8.6 MPa, expands to a minimum pressure of 0.012 MPa at the bubble maximum diameter. At this state the steam quality is about 70%. The bubble then collapses with no change in pressure until all of the vapor has condensed. Since the steam tables are based on equilibrium states, the real gas equation of state solution is valid only if the bubble grows or collapses very slowly so that the steam has time to equilibrate. Another way of looking at it is that in the

use of steam tables it is assumed that condensation can occur at an infinite rate. This is clearly not the case and therefore the remainder of the calculations were performed assuming ideal gas behaviour for the steam with a γ value of 1.09.

4.2.4 Numerical Results for First Bubble cycle

Taking the estimated initial conditions for the vapor bubble, the bubble dynamics were calculated for adiabatic and nonadiabatic cases. The calculated bubble diameter time histories are shown in Fig. 45 superimposed on the experimental data from the hot tin drops taken from Fig. 17. The actual data points for the seven trials are shown so as to better distinguish the predicted curves. The numerical predictions for the adiabatic expansion and compression of the steam reproduces fairly well the period of the bubble cycle but underestimates the maximum diameter observed experimentally. The added heat only slightly increases the bubble maximum and correspondingly increases the time for bubble collapse. Shown in Fig. 46 is a graph showing the total energy added from the drop to the bubble and lost through the bubble surface. The heat lost to the water is negligible compared to the heat added from the drop surface which totals about 0.175 J by the time the bubble collapses. A plot of the bubble pressure and internal energy as a function of time for the nonadiabatic case is shown in Fig. 47. This curve indicates that the bubble pressure drops very rapidly in the first 200 µs and remains overexpanded for most of the bubble lifetime. As a result of the added heat from the drop, the internal energy and pressure of the bubble starts increasing before the bubble reaches its maximum diameter at about 0.8 ms. Although the amount of energy added to the bubble is significant compared to the initial energy of the bubble, since it is ramped up from time zero there is not much increase in the bubble maximum diameter compared to the adiabatic case.

The largest uncertainty in the model lies in the estimation of the initial contact time between the drop surface and the water and the increase in drop surface area during the bubble expansion. A parametric study was performed in order to determine the sensitivity of the predicted bubble dynamics to these two parameters.

The effect of the initial contact time on the subsequent bubble dynamics can be seen in Fig. 48. Recall 80 µs was the time observed experimentally when the vapor bubble just began to show signs of expanding. Therefore, this represents an upper limit for the contact time. Based on diffusive heat transfer the thickness of the thermalized layer of water is proportional to the square root of time. Therefore, a doubling of the time used in the

previous calculations (i.e., $80 \mu s$) corresponds to an increased layer thickness factor of 1.414 and a quarter of the contact time (i.e., $10 \mu s$) corresponds to half the thickness. From Fig. 48 it can be seen that there is a noticeable change in the resulting bubble dynamics even for these small changes in contact time. Increasing the contact time has the same effect as adding additional heat through increased surface area only in this case the added heat occurs very quickly at the beginning of the bubble cycle. It is clear from the results that the model is very sensitive to the contact time.

4

Figure 49 shows three bubble diameter time histories for three different drop surface area growth factors, K(R) where K is the total increase of the drop surface area when the bubble reaches its maximum size. These three cases include no surface area growth (K = 0) during the bubble growth and an area growth of one (K = 10) and two (K = 100) orders of magnitude compared to the initial drop surface area. In effect, the case where K equals zero is the same as the adiabatic case since heat loss to the water is negligible. Increasing the surface area by two orders of magnitude does not have a significant effect on the predicted results. In general the bubble dynamics are not as sensitive to the choice of K as compared to the initial drop surface-water contact time.

Upon close observation of the curves in Fig. 45 it is apparent that the general shape of the bubble growth curves for the numerical and experimental results are not consistent. The bubble growth curve calculated using the Rayleigh equation is much broader than the experimental curves. This can clearly be seen in Fig. 50, which shows the same two numerical bubble diameter growth curves from Fig. 45, under adiabatic and nonadiabatic conditions, and one of the experimentally measured bubble diameter growth curves. As stated earlier, the numerical curves predict well the period of the experimental curve, although, they underpredict the value of the maximum diameter. If the initial contact time or the amount of additional heat added are adjusted so as to match the bubble maximum diameter, the predicted curves will overshoot the experimentally observed collapse time. This indicates that the experimentally observed bubble diameter time history are not governed solely by the inertia of the water as is modeled by the Rayleigh equation.

The apparent difference in the numerical and experimentally measured bubble trajectories can be attributed to the presence of hot melt fragments which migrate to the bubble surface during the bubble expansion phase. These fragments are generated from the cratering of the drop surface following film collapse and from the breakup of the filaments extending from the drop surface. As the bubble surface decelerates as a result of overexpansion, the

inertia of the fragments, with the help of the low resistance offered by the vapor, carry the hot fragments into the cooler vapor which exists just inside the bubble surface, eventually penetrating the bubble surface (see Fig. 14c). This provides a mechanism by which energy can be transported from the drop surface directly to the water even with a vapor bubble present. These hot fragments cause more water to evaporate at the bubble surface and thus increase the maximum diameter surpassing that which is possible through normal bubble dynamics. In addition, it is often very difficult to distinguish the bubble surface from the surface formed by the fragments as they penetrate the bubble surface. Therefore, the experimental curves also include a certain degree of error in measuring the true bubble diameter.

It is beyond the scope of this study to implement the details of the fragmentation mechanism into the present model. This would require developing a detailed analytical model for the fragmentation process. It would also require a nonequilibrium phase transition model to taken into account evaporation due the injection of the hot fragments into the surrounding water. The present model, considering its many assumptions, does provide a first order approximation for the bubble dynamics. More importantly, it brings to light the important role which the fragmentation process plays in the resulting bubble dynamics.

4.2.5 Estimation of the Interaction Efficiency

At the end of the first bubble cycle the water outside the collapsing bubble contacts the already severely distorted drop which has retained much of its initial thermal energy. The subsequent energy transfer from the drop to the vapor bubble produces an even larger second bubble. It is of interest to estimate numerically the amount of energy which must be deposited into the bubble at the time of collapse so as to reproduce the observed growth of the second bubble. To estimate the second bubble cycle without including too many new parameters it will be assumed that the energy is deposited at a constant rate over a time of 200 µs. This time corresponds roughly to the time it takes for the second bubble to emerge from the cloud of fragments after reaching its minimum size. Additional heat added from the drop and lost through the bubble surface will be neglected for this second bubble cycle. Shown in Fig. 51 is the model prediction with heat added between the times of 1.5 and 1.7 ms at a rate of 10,000 J/s superimposed on the experimental data. This adds an additional 2 J of energy into the bubble at the time of collapse. Fig. 52 shows the cumulative amount of energy transferred from the drop to the bubble starting at the time of film collapse at time

zero. Initially about 0.3 J of energy goes into superheating of the water, and during the bubble expansion and collapse about 0.17 J of energy is transferred to the bubble from the distorting drop surface. The most significant amount of energy (i.e., 2 J) is deposited at the time of bubble collapse giving a total of 2.5 J of the drop energy which is required to reproduce the experimental curves. Note, although the initial phase of the explosion (i.e., the evaporation process) is not modeled, it turns out that the energy transferred during this time (0.3 J) is a very small portion of the overall energy transfer from the drop (2.5 J).

One of the main objectives of steam explosion studies is to determine what fraction of the melt's thermal energy could be converted into mechanical work done by the expanding vapor. This fraction is often referred to as the "conversion ratio". For a 0.5 g drop at 527°C (corresponding to the state of the drop just before the interaction is initiated) the total available thermal energy is 82 J of which 63% is sensible heat and the rest is in the form of latent heat given off when the drop freezes. Since the energy loss to the water through the bubble surface in the first bubble cycle is negligible (see Fig. 46), all the energy transferred from the drop goes into PdV type work done by the bubble. Therefore the conversion ratio is determined by the total energy transferred from the drop and the total initial available thermal energy of the drop. The conversion ratio based on the total energy transferred to the bubble (see Fig. 52) as a function of time for the predicted bubble diameter curve is shown in Fig. 53. Only 3% of the initial available energy of the drop is spent on generating the experimentally observed bubble dynamics. Based on thermodynamic considerations there is a limit on the amount of the available thermal energy that can be converted into mechanical work. Hicks and Menzies (1965) considered a process which the melt and coolant are mixed at constant volume and allowed to come to thermal equilibrium and then this mixture is allowed to expand isentropically from this compressed state to the ambient pressure. The work done for this process is calculated by the area under the isentrope on the P-V diagram or by the change in internal energy of the mixture between the compressed state and the final state. For this type of calculation the amount of work done depends on the ratio of the volumes of coolant and melt which participate. For the case of 0.5 g of tin at 527°C and water at 60°C a maximum work output of 27 J occurs at a water to tin volume ratio of 0.27, as shown in Fig 54. This corresponds to 34 % of the initial thermal energy of the tin drop. Compared to the work done by the modeled vapor bubble, from Fig. 52, the total work output from the exploding drop is about 9.5 % of the Hicks and Menzies calculated maximum work output. In place of the Hicks and Menzies process the true maximum efficiency would be obtained if a Carnot engine is used where the drop is the hot reservoir and the water is the cold. Based on the temperature of the drop and water this yields an efficiency of about 58 %.

Some of the unaccounted for energy is radiated outwards from the interaction zone in the form of shock waves which are produced at the time of initial film collapse and bubble rebound. Additional energy is lost to the water during the initial contact between the drop and the water. In the model it is assumed that the water which is heated above the superheat limit evaporates, therefore, the energy associated with the remainder of the heated water does not contribute to the work done by the bubble. However, the largest portion of the energy goes into the fragmentation of the drop. As discussed by Cho et al. (1976), the majority of the energy for drop fragmentation goes into work done against the hydrodynamic drag force exerted on the fragments as they are dispersed. In an idealized view of a single drop interaction it is assumed that the drop breaks up and the fragments are dispersed in the water where they lose their thermal energy. The present study shows that the fragmentation process is much more efficient than this. First only a small amount of the drop's energy is used up to generate a first bubble. At the same time the steam inside the bubble provides a less dissipative environment, in terms of work done to overcome drag, for the growth of the melt spikes and dispersion of the initial fragments which are formed after film collapse. This process of drop surface distortion is very important since it preconditions the drop for the eventual inrush of water which occurs as the result of the bubble collapse. The generation of the spikes allows the inrushing water to penetrate deep into the drop as opposed to the initial film collapse where the interaction is restricted to the drop surface. The final fragmentation of the drop is due to the hydrodynamic forces imparted on the drop by the inrushing water and the violent evaporation of additional water. The contribution from the first of these two factors requires no additional energy from the drop since the initial energy transferred following film collapse is returned to the drop in the form of kinetic energy of the inrushing water. Therefore, even though the conversion ratio appears to be low (i.e., 3 %), the observed thermal fragmentation process is a very efficient means of fragmenting the drop. However, the time required for total fragmentation by this mechanism is long since it is dependent on the characteristic bubble collapse time which is of the order of milliseconds.

4.3 The Use of Hugoniot Analysis for Predicting the Existence of a Thermal Detonation

In the field of combustion it is well established that a gaseous detonation can occur depending on the boundary conditions, initiation energy and mixture properties. In the field of vapor explosions it is not clear if a "thermal detonation" can occur and there is no concrete experimental evidence to support its existence. This is because it is very difficult to control the initial conditions of the coarse-mixture (i.e., void fraction and drop size). As a result of these experimental difficulties, one must turn to analytical techniques to obtain some insight into the existence of a thermal detonation.

Board et al. (1975) first proposed that a self-sustained steadily propagating "thermal detonation" may exist making a direct analogy with the well established theory of chemical detonations. If steadily propagating vapor explosion waves do exist, they must satisfy the one dimensional conservation laws of mass, momentum and energy. Without any knowledge of the nonequilibrium mechanical and thermodynamic processes in the "reaction" zone of the thermal explosion wave, it is possible to determine the possible downstream equilibrium states on the basis of the conservation laws and an equation of state. Such calculations are referred to as Hugoniot analysis and since the calculations are essentially based on the energetics and not the kinetics of the energy release process, they can be made even with total ignorance of the mechanism of propagation of the wave. Valuable insights into the properties of vapor explosion waves can be deduced from these energetics considerations.

Hugoniot analysis predicts the properties which a thermal detonation would exhibit if it were to exist but it in no way guaranties that such a steady-state wave can exist in reality. This is determined by the detailed rate processes which occur in the reaction zone. The governing relations for the Hugoniot analysis are outlined in Appendix C and in this chapter detonation properties are calculated for some typical initial coarse-mixture conditions. Fragmentation data reported in Chapter 3 are then used to comment on the possible existence of such a wave based on the estimated reaction zone length.

4.3.1 Results for Tin/Water/Steam Mixtures

The Hugoniot curve for equal volumes of tin at 1000°C and water and steam at 100°C, shown in Fig. 55, illustrates several features that are common to Hugoniot curves for low

energy melts. The initial mixture state is denoted by an O on the graph. The Hugoniot curve has two distinct sections separated by a sharp discontinuity or "kink" at the saturation boundary: a lower region, inside the saturation dome, that is nearly flat, and an upper region, in the compressed liquid region, that is quite steep. For the case in which equal volumes of tin, water, and steam are present initially, the Rayleigh line shown in the figure contacts the Hugoniot curve at the "kink" in the Hugoniot curve at the phase boundary (at a pressure of 14.8 MPa). This point represents a minimum in the mass flux, but it is not a true CJ point in the sense that the slope of the Hugoniot as well as the isentrope at this point is indeterminate.

In Fig. 56, the Hugoniot curve for 1000°C tin (with equal volumes of tin, water and steam) is replotted on a semi-log scale to show the other thermodynamic points of interest. The horizontal displacement of the Hugoniot curve at a pressure of about 3 MPa inside the saturation boundary is a result of the contribution of the latent heat of the melt when the melt freezes. Although a CJ detonation does not exist for this Hugoniot curve (since the Rayleigh line intersects the Hugoniot at the "kink"), a CJ deflagration point exists which is located within the two-phase saturation region. The constant volume and pressure points are also located inside the saturation region, denoted by CV and CP, respectively.

As the thermal energy of the melt increases, the Hugoniot curve shifts up. This is illustrated in Fig. 57 which shows the Hugoniot curve for 1250°C tin (equal volumes of tin, water and steam). The Hugoniot still lies partially within the saturation region, but in this case both CJ solutions exist and are located outside the saturation region. Figure 58 shows the entropy change across the reaction zone as a function of specific volume for points on the Hugoniot curve shown in Fig. 57, illustrating that the CJ points are entropy extrema. Note that the entropy change in the supercritical region near the CJ detonation point is very small, so that the Hugoniot and the isentrope are virtually indistinguishable in this region. The Hugoniot curve for tin at 1500°C, shown in Fig. 59, just intersects the saturated vapor curve. For higher temperature melts, the Hugoniot curve falls entirely outside the saturation region.

4.3.2 Effect of Mixture Properties on the Detonation State

Hugoniot calculations are useful for studying the effect of varying different thermodynamic parameters on the predicted CJ detonation state. In particular, for the case of tin at 1000°C, the effect of varying the void fraction and tin/water volume ratio on the detonation pressure

and velocity have been investigated. Figure 60 shows the effect of void fraction on the predicted detonation state for mixtures that contain equal initial volumes of tin and water. When the initial void fraction is changed, keeping the relative volume fractions of tin and water the same, the Hugoniot curve changes only slightly. However, the initial mixture specific volume (denoted by O in Fig. 56) changes considerably when the void fraction changes. As a result, the CJ solution changes substantially with a change in void fraction. For void fractions above 26%, a CJ detonation state does not exist, since the Rayleigh line intersects the Hugoniot curve at the discontinuity at the saturation boundary (see, for example, Fig. 56). For void fractions below 26%, the detonation pressure and velocity increase rapidly with decreasing void fraction, ranging from 20 MPa and 370 m/s at 25% void to 370 MPa and 1360 m/s at 10% void, respectively.

The effect of varying the melt/water volume ratio is illustrated in Fig. 61 for tin at 1000°C, with the initial void fraction equal to 33.3% in each case. Note that both the detonation velocity and pressure increase with tin/water volume ratio and reach a maximum at some point. In particular, the detonation pressure reaches a maximum when the tin/water volume ratio is about 4. This graph can be used to determine the effective "sensitivity" for a fuel-coolant mixture, where a more sensitive mixture will yield a higher pressure detonation state.

4.3.3 Estimation of Reaction Zone Length Based on Experimental Drop Breakup Data

In order for a thermal or chemical detonation to propagate, the reaction zone length must be sufficiently short so that heat and momentum losses in the reaction zone are not significant. From the work that has been done in gaseous chemical detonations it has been found that in order for a detonation to propagate in a tube it must accommodate at least one detonation cell (i.e., single head spin detonation) and for a detonation to propagate in a tube without being affected by the tube boundaries the tube must accommodate at least 13 detonation cells (i.e., this diameter is referred to as the critical tube diameter). A cell is a diamond shaped pattern which is inscribed on a soot coated tube wall by a detonation. The detonation cell size characterizes the reactivity of a mixture where the cell size decreases with increasing reactivity. Typically the size of a cell varies from 30 to 60 reaction zone lengths, where 30 is representative of most hydrocarbons. Therefore, if we extend this theory to thermal detonations the coarse-mixture size must be at least 30 reaction zone lengths in size and over 400 reaction zone lengths for it to propagate independent of the

mixture boundaries. The applicability of this criterion for thermal detonations is uncertain and therefore it must be treated as a first order estimate.

In a thermal detonation the flow generated behind the shock wave collapses the vapor film around the drops creating more favorable conditions for heat transfer between the hot melt and the water. The convective flow behind the leading shock causes the melt drops to fragment and thus enhance the surface area available for heat transfer. If one assumes that the fragments are so small that they give up their thermal energy to the water instantaneously, the reaction zone length can be estimated by the distance downstream from the leading shock where drop fragmentation is complete. Therefore, with information on the flow velocity and an estimate of the time for complete fragmentation of the drop the reaction zone length can be readily estimated.

The flow velocity relative to the detonation wave at the CJ plane can be obtained from the Hugoniot analysis. From the calculated detonation velocity the flow velocity directly behind the leading shock wave can also be calculated. In this calculation the flow velocity at the CJ plane will be used since it is one of the outputs from the Hugoniot analysis. This is not the most conservative estimate because the flow velocity directly behind the leading shock wave is higher than that at the CJ plane. A nondimensional breakup time, T, of 1.75 was estimated from the x-ray radiographs taken of the fragmenting cold drop at the higher flow velocities. We will consider this value to be independent from the Weber number even though data obtained through regular photography showed a small dependence.

As an illustrative example we will consider a coarse-mixture of equal volumes of tin at 1500°C, water and steam at 100°C. The Hugoniot curve and CJ state for this mixture is given in Fig. 59. The predicted detonation velocity and flow velocity at the CJ plane relative to the detonation wave are 647 m/s and 547 m/s, respectively. This gives a CJ plane flow velocity relative to a fixed observer of 100 m/s. Based on a nondimensional breakup time of 1.75, the corresponding dimensional breakup time for this flow velocity and a drop size of 1 cm is about 66 µs. This yields a reaction zone length of 3.6 cm. Note that the breakup time is proportional to the drop size and therefore longer reaction zone lengths will result for larger drops. If we employ the criterion described earlier that the coarse-mixture size must be at least 30 times the reaction zone length to support a detonation, this yields a minimum mixture size of 1.08 meters and the critical tube criterion requires a 14.4 meter coarse-mixture size. A typical nuclear reactor vessel is meters in size

and therefore the first criterion is met and therefore the possibility of a thermal detonation cannot be ruled out.

4.4 Comments on the Initiation of a Thermal Detonation

The Hugoniot calculations along with the experimental drop breakup data demonstrated that a thermal detonation under the right coarse-mixture conditions could possibly be realized. In order for such a thermal detonation to be initiated directly, a minimum trigger pressure of the order of the CJ pressure is required. For the example discussed, this corresponds to a pressure of 180 MPa. Clearly a trigger pressure of this magnitude is not possible in most industrial plants. Therefore, the detonation must develop through an escalation process initiated from a weaker trigger.

In vapor explosion waves observed experimentally, the propagation of the coherent interaction is driven by the production of high-pressure vapor in the reaction zone which compresses the mixture ahead of the front. For example, Frost and Ciccarelli (1988a) used high-speed photography to study the propagation of a steam explosion through a linear array of molten tin drops confined within a narrow channel. They observed that the explosion propagates (at a speed of about 60 m/s) as a result of the expansion of the high pressure vapor generated by a single drop causing the sequential explosion of adjacent drops. The present hot drop experimental results indicate that as the flow generated ahead of the propagating front increases, the production of vapor will be inhibited and possibly suppressed altogether for high enough flow velocities. In the absence of vapor generation, the work required to sustain the propagation of the wave must come from the expansion of the water heated within the reaction zone. If there is insufficient expansion due to the limited heat transfer to the water (e.g., in the case of low temperature melts and small melt/coolant volume ratios) then the explosion front would be retarded and the propagation velocity would decay. As a result there would exist a maximum velocity for the propagation of a self-sustained vapor explosion wave. This is a possible explanation why in most intermediate scale experiments (e.g., Fry and Robinson (1979); Burger et al. (1989); Baines (1984)) there appears to be an upper limit on the explosion propagation velocity (of the order of 200 m/s), well below the velocities predicted by Hugoniot calculations based solely on energetics considerations. It is likely for the low temperature melt mixtures studied extensively experimentally, that a transition mechanism (analogous to deflagration-to-detonation transition in a combustible gas) does not exist by which a local interaction will escalate to a self-sustained super-critical thermal "detonation" wave. In vapor explosions, the escalation mechanism is intimately linked to the fragmentation mechanism which determines the rate of energy release that drives the propagation of the explosion.

4.5 Comments on the Experimental Techniques used to Determine Drop Breakup Times

A brief discussion on the estimation of breakup time from past and present results using regular photography was given earlier. There is considerable scatter in the reported breakup times arising from the different criteria used by the various investigators. The present investigation highlights the limitations of using regular back lighting photography to estimate fragmentation rates. In the low flow cold drop experiments, regular photography proved to be adequate and x-ray radiographs did not provide any additional information. In this case the fragmentation process was relatively slow and was characterized by the formation of melt filaments which could be resolved using regular photography. For the high flow cold drop experiments the fragmentation was much faster producing a cloud of fine fragments that obscure the visibility of the parent drop. Regular photography proved to be inadequate in this case since it is impossible to resolve the extent of fragmentation of the parent drop. As a result investigators using regular photography techniques are forced to analyze the fragmentation process in terms of the growth of this opaque cloud of fragments. Ultimately any criterion for drop breakup based on the size of the cloud is inaccurate since the size is directly proportional to the extent of the dispersion of the fragments once they detach from the parent drop and not on the degree of fragmentation. To obtain quantitative information concerning the fragmentation rate or time for complete fragmentation, visualization with x-ray radiography is necessary. From the xray photographs the fragmentation rate could be determined by measuring the rate of change in the volume of the parent drop. To obtain such information the x-ray must be of sufficient strength to penetrate the fragment mist and not the parent drop. This technique was effectively used by Reinecke and Waldman (1978). The energy of the soft x-rays used in the present experiments was not ideally suited for this purpose. In the radiographs, the parent drop could be discerned from the fragment mist as a darker area superimposed on a larger grayer region. In some cases one could interpret the disappearance of this darker area as the time of complete fragmentation but in most cases a certain amount of subjectiveness in the interpretation is inevitable.

In the hot drop experiments regular photography is not useful for observing the fragmentation process since in general a vapor bubble forms which obscures the view of the parent drop. For the high flow velocity the regular photography proved to be misleading since the rate of growth of the cloud appeared similar for both the hot and cold drop experiments. X-ray radiographs showed that the phenomenon was quite different at early times with vapor being formed in the hot drop experiment which could not be observed using regular photography. In conclusion, caution must be used in interpreting data on hot and cold drop fragmentation when using regular photography.

Chapter 5

CONCLUSIONS

In the present study, x-ray radiography as well as regular photography was used to investigate the fragmentation process during the vapor explosion of single drops of melt. For cold liquid metal drops, fragmentation of the drop occurs as mass is stripped off the surface due to the relative motion of the coolant. The hydrodynamic fragmentation process is relatively slow with complete fragmentation of the drop evident only after about 7.5 ms. For hot drops, the induction time for the initiation of the explosion is on the order of 40 μ s after film collapse. A first vapor bubble is generated which grows to a maximum diameter in about 600 µs (for 0.5 g drops) and then collapses X-ray photographs show that significant distortion of the drop occurs during the growth of the first vapor bubble. Fine filaments of metal are ejected from the drop surface and break up into small fragments. Since the dispersion of the fine fragments occurs in a vapor phase medium with little drag, the dispersion process is quite efficient (as compared with the dispersion of fine fragments in a liquid medium). At the time of the collapse of the first bubble, the drop surface is highly convoluted and a second interaction is initiated. For molten tin drops, the second bubble generated is always larger than the first bubble. For hot cerrolow alloy drops, a similar interaction occurs although the second bubble is not as large as for tin. A phenomenological model for the fragmentation mechanism has been proposed based on direct observation of the drop breakup with flash x-ray visualization. Additional experiments in a stratified liquid metal/water system show that the generation of highpressure vapor bubbles at the metal/water interface leads to the formation of jets of liquid metal similar to that observed during the initial stages of the explosion of a hot drop.

From the experimental results it is clear that the vapor explosion of a hot drop is influenced by the magnitude of the flow velocity of the surrounding water. For the lower flow velocity (<5 m/s) the interaction of the drop takes on the characteristic vapor bubble growth and collapse cycle. The global fragmentation time for the hot and cold drops under high flow conditions (> 45 m/s) is the same, however, the mechanism of fragmentation is very

different in each case. In the cold drop experiments the fragmentation was through stripping of the drop surface. In the hot drop interactions there was no evidence of any vapor bubble oscillations and there was no noticeable difference in the cold and hot drop interactions using regular high speed photography. However, x-ray radiographs taken during the hot drop interactions showed that at early times a vapor bubble forms around the entire drop and is later displaced downstream. It is also evident that the rate of fragmentation inside the bubble is faster than that observed in the low flow case. It is proposed that shear on the drop surface generated by vapor flow (produced by evaporation at the upstream surface of the bubble) around the drop allows fragmentation to occur while the drop is still inside the vapor bubble. The experiments looking at the effect of external flow indicate that as the flow velocity increases the amount of vapor produced by the explosion decreases. It is proposed that the decrease in the expansion work done by the vapor bubble may explain the maximum propagation velocities observed in intermediate scale experiments to date. It is clear that any attempt at numerical modelling of the escalation of a vapor explosion must consider the effects of flow velocity on the fragmentation behavior of the melt drops within the reaction zone.

The dynamics of the vapor bubble were modeled using a simple parametric model incorporating the Rayleigh equation for bubble dynamics and an energy equation for the vapor. The two parameters in the model were the initial contact time between the drop surface and the water following film collapse and the growth factor describing the surface area enhancement resulting from the generation of melt spikes. It was found that the predicted results were very sensitive to the choice of the contact time. The experimental bubble diameter time history curves could not be reproduced exactly. The predicted curves were found to be broader than the experimental curves. It was postulated that this inconsistency could be attributed to the migration of hot fragments to the bubble surface. The penetration of these fragments causes additional evaporation at the bubble surface resulting in a larger vapor bubbles. It was found that only 3% of the initial drop thermal energy was required to reproduce the experimentally observed bubble dynamics.

It was also estimated using a Hugoniot analysis along with an experimentally determined drop breakup time that for the case of equal volumes of tin at 1500°C, and water and steam at 100°C a reaction zone thickness of about 3.6 cm would exist. Employing the critical tube criterion for gaseous detonation yields a value of 1.08 m to be the minimum mixture size which can support a detonation. This implies that the possibility of a thermal

detonation occurring in most accident scenarios where typical coarse-mixture sizes of the order of meters are envisioned cannot be ruled out

The present experiments show that the energy required for fragmentation of a hot drop is derived from the thermal energy of the drop rather than the kinetic energy of the ambient flow or direct shattering of the drop by the triggering shock or film collapse. The majority of current models for the escalation and propagation stages of a vapor explosion include fragmentation models based on hydrodynamic fragmentation mechanisms (e.g., Rayleigh-Taylor instability or boundary layer stripping). It is likely in the initial escalation stage of a coherent vapor explosion, when system pressures are still relatively modest (i.e., subcritical), that thermal fragmentation effects will dominate, particularly for low-energy melts. More information is required on the fragmentation, heat transfer and momentum exchange mechanisms before significant improvement in the state of the art models can be made.

CONTRIBUTIONS TO ORIGINAL KNOWLEDGE

į

Based on the findings of experiments carried out in several apparatus and photographic techniques along with some analytical modelling, the author has made original contributions to knowledge by:

- i) employing x-ray radiography to study the fragmentation of a hot molten drop following the passage of a shock wave. The x-ray visualization was used to "see through" the vapor bubble which in the past prevented any direct observation of the fragmentation process using regular photography. X-ray radiographs showed for the first time the creation of thin melt filaments protruding from the drop surface during the growth of the vapor bubble. These observations permitted the author to propose a physical model to describe the fragmentation process of a hot drop under both low and high flow conditions.
- ii) obtaining data on the breakup of a cold drop under varying flow conditions using x-ray and regular photography. The author obtained a breakup correlation (i.e., $T_b = 12 \text{ We-}^{1/4}$) using the quadrupling of the micromist cloud criterion, support for the results was obtained by including two x-ray data points at the lowest and highest Weber numbers. The Weber number dependence in the correlation could not be attributed to the onset of catastrophic breakup since there was little evidence for this.
- observing the fragmentation of a cold drop in a water flow and the fragmentation of the same drop heated to a high temperature under the exact same flow conditions. By direct comparison of the results the author could obtain an estimate of the relative importance of hydrodynamic effects from the water flow on the explosion of a hot drop under varying flow conditions.
- estimating the amount of energy released by the drop during the explosion using a parametric model. It was found that only 3% of the initial available thermal energy of the tin drop was converted into mechanical work done by the bubble dynamics. It was found that the majority of this fraction of the thermal energy (about 2/3) is released at the time of the first bubble collapse.

REFERENCES

- Baines, M. and Buttery, N. E., "Differential Velocity Fragmentation in Liquid-Liquid Systems," Report RD/B/N4643, Berkeley Nuclear Labs, UK, 1979.
- Baines, M., "Preliminary Measurements of Steam Explosion Work Yields in a Constrained System," First U.K. National Conference on Heat Transfer, *Institution of Chemical Engineers Symposium Series*, No. 86, 1984, pp. 97-108.
- Board, S.J., Farmer, C.L., Poole, D.H., "Fragmentation in Thermal Explosions," Int. J. Heat and Mass Transfer, Vol. 17, 1974, pp. 331-339.
- Board, S.J., Hall, R.W., Hall, R.S., "Detonation of Fuel Coolant Explosions," *Nature*, Vol. 254, 1975, pp. 319-321.
- Buchanan, D. J., "A Model for Fuel-Coolant Interactions," J. Phys. D., App. Phys., Vol. 7, 1974, pp. 1441-1457.
- Bürger, M., Kim, D.S., Schwalbe, W., Unger, H., Hohmann, H., Schins, H., "Two Phase Description of Hydrodynamic Fragmentation Process Within Thermal Detonation Waves," ASME J. Heat Transfer, Vol 106, 1984, pp. 728-734.
- Bürger, M., Miller, K., Buck, M., Cho, S.H., Schatz, A., Schins, H., Zeyens, R., and Hohmann, H., "Analysis of Thermal Detonation Experiments by Means of a Transient Multiphase Detonation Code," *Proc. 4th Topical Meeting on Nuclear Reactor and Thermal Hydraulics*, Karlsruhe, K.F.G. 10-13 October 1989, Vol. 1.
- Bürger, M., Carachalios, C., Kim, D.S., Unger, H., "Theoretical investigations on the Fragmentation of Drops of Melt with Respect to the Description of Thermal Detonations (Vapor Explosions) and Their Application in the Code FRADEMO," Commission of the European Communities Report EUR 10660 EN, 1986.

- Buxton, L.D. and Benedick, W.B., "Steam Explosion Efficiency Studies; part I," SAND79-1399, NUREG/CR-0947, Sandia National Laboratories (Nov. 1979).
- Cho, D.H., Ivins, R.O., Wright, R.W., "Pressure Generation by Molten Fuel-Coolant-Interactions under LMFBR Accident Conditions," *Proc. of New Development in Reactor Mathematics and Applications*, CONF-710302, Vol. 1, 1971, pp. 25-49.
- Cho, D.H., Fauske, H.K., and Grolmes, M.A., "Some Aspects of Mixing in Large-Mass, Energetic Fuel-Coolant Interactions," *Proc. Int. Mtg. Fast Reactor Safety and Related Physics*, Vol. 4, p. 1852, Chicago, Illinois (Oct. 1976).
- Ciccarelli, G., Frost, D.L., Zarafonitis, C., "Dynamics of Explosive Interactions Between Molten Tin and Water in Stratified Geometry," *Proc 12th ICDERS*, Ann Arbor, Michigan, 1989.
- Cole, R.H., "Underwater Explosions," Princeton University Press, Princeton, NJ, 1948.
- Cooper, F., and Blewett, P., "Pressure Generation Due to a Temperature Discontinuity at Liquid-Liquid Plane Interface," *Phys. of Fluids*, 21(3), 1978, pp. 334-346.
- Corradini, M. L., "Analysis and Modelling of Steam Explosion Experiments," Sandia National Laboratory Report, SAND80-2131, 1981.
- Corradini, M. L., Kim, B. J., and Oh, M. D., "Vapour Explosions in Light Water Reactors: a Review of Theory and Modelling," *Prog. Nucl. Energy*, Vol. 22, 1988, pp. 1-117.
- Daugherty, R.L. and Franzini, J.B., "Fluid Mechanics with Engineering Applications," McGraw Hill Inc., 1977.
- Drumheller, D. S., "The Initiation of Melt Fragmentation in Fuel-Coolant Interactions, "Nucl. Sci. Eng., Vol. 72, 1979, pp. 347-356.

- Dullforce, T.A., Buchanan, D.J., and Peckover, R.S., "Self-Triggering of Small- Scale Fuel Coolant Interactions: I Experiments," J. Phys. D.: Appl. Phys. 9, pp. 1295-1303, 1976.
- Engel, O.G., "Fragmentation of Water Drops in the Zone Behind an Air Shock," *Journal Research Nat. Bur. of Stand.*, Vol. 60, No. 3, 1958.
- Fletcher, D. F., and Anderson, R. P., "A Review of Pressure-Induced Propagation Models of the Vapour Explosion Process," *Prog. in Nucl. Energy*, Vol. 23, 1990, pp. 137-179.
- Fletcher, D.F., and Thyagaraja, A., "A Mathematical Model of Melt/Water Detonations," Appl. Math. Modeling, Vol.13, 1989, pp. 339-347.
- Fröhlich, G., and Anderle, M., Experiments for Studying the Initiation Mechanisms for Steam Explosions, Institute für Kernenergetik und Energiesysteme report IKE2-51, Universität Stuttgart, Stuttgart, FRG (1980).
- Frost D.L., and Ciccarelli, G., "Propagation of Explosive Boiling in Molten Tin-Water Mixtures," *Proc. of ANS National Heat Transfer Conference*, Houston, 24-27 July 1988a, Vol.2.
- Frost, D.L., Ciccarelli, G., Dynamics of explosive interactions between multiple drops of tin and water. In: Kuhl AL, Bowen JR, Leyer J-C, Borisov A (eds) Progress in Astronautics and Aeronautics, AIAA, Washington, 1988b, pp. 451-473
- Frost, D. L., and Ciccarelli, G., "Propagation Mechanisms of Molten/Fuel Moderator Interactions," Atomic Energy Control Board of Canada Report, project #2.148.1, 1991.
- Fry C. J., and Robinson C. H., "Experimental Observations of Propagating Thermal Interactions in Metal/Water Systems," Proc 4th CSNI specialist meeting on fuel-coolant interaction in nuclear reactor safety, Bournemouth, UK, 1979.

- Greene, G. A., Park, N. A., Burson, S. B., Klages, J., Klein, J., Sanborn, Y., and Schwarz, C. E., "Some Observations on Simulated Molten Debris-Coolant Layer Dynamics," *Proc. Int. Meeting on LWR*, Severe Accident Evaluation, Vol. 2, Cambridge, Mass., Aug. 28-Sept. 1, 1983.
- Harper, E.Y., Grube, G.W., and Chang, I., "On the Breakup of Accelerating Liquid Drops," *Journ. of Fluid Mech.*, Vol. 52, pp. 565-591 (1972).
- Hicks, E.P., and Menzies, D.C., "Theoretical Studies on the Fast Reactors in Maximum Accident," Proc. Conf. Safety, Fuels, and Core Design in Large Fast Power Reactors, p. 654, ANL-7120, Argonne National Lab, 1965.
- Keenan, J.H., Keyes, F.G., Hill, P.C., Moore, J.G., "Steam Tables," John Wiley and Sons, Inc., New York, 1969.
- Kim, B. J., "Heat Transfer and Fluid Flow Aspects of a Small-Scale Single Droplet Fuel-Coolant Interaction," PhD Thesis, University of Wisconsin, Madison, WI, USA, 1985.
- Kim, D. S., Bürger, M. Fröhlich, G. and Unger, H., "Experimental Investigation of Hydrodynamic Fragmentation of Gallium Drops in Water Flows," *Proc. Int. Meeting on LWR Severe Accident Evaluation*, Cambridge, Massachusetts, Aug. 28 Sept. 1, 1983, Vol. 1, TS-6.4.
- McCahan, S. and Shepherd, J.E., "Models of Rapid Evaporation in Non-equilibrium Mixtures of Tin and Water," Presented at 13th ICDERS, 1991.
- Mitchell, D. E. and Corradini, M. L., "Intermediate Scale Steam Explosion Phenomena: Experiments and Analysis," SAND81-0124, NUREG/CR-2145, Sandia National Laboratories (Sept. 1981).
- Medhekar, M., Abolfadl, M., and Theofanous T.G., "Triggering and Propagation of Steam Explosions," *Proc. of ANS National Heat Transfer Conference*, Houston, July 24-27, Vol. 2, 1989, pp. 244-251.

- Naugolnykh, K. A., Rybak, S. A., Puchenkov, O. V., and Zosimov, V. V., "Laser Stimulated Instabilities of Waves in a Subsurface Layer of a Liquid," in Nonlinear Waves in Active Media, Ed. J. Engelbrecht, Springer-Verlag, Berlin, 1989.
- Nelson, L. S. and Duda, P. M., "Steam Explosion Experiments With Single Drops of Iron Oxide Melted With a CO₂ Laser, *High Temperatures-High Pressures*," Vol. 14, pp. 259-281, 1982.
- Ochiai, M., and Bankoff, S. G., "Liquid-Liquid Contact in Vapor Explosions," Proc. Int. Conf. on Fast Reactor Safety, Am. Nucl. Soc., Chicago, IL, October 5-8, 1976.
- Oh, M. D., and Corradini, M. L., "A Propagation/Expansion Model for Large-Scale Vapor Explosions," *Nucl. Sci. Eng.*, Vol. 95, 1987, pp. 225-240.
- Padilla, A., "Transient Analysis of Fuel-Sodium Interactions," Trans. Am. Nucl. Soc., Vol.13, 1970, pp.375-376.
- Patel, P.D., and Theofanous, T.G., "Hydrodynamic Fragmentation of Drops," J. Fluid Mech., Vol. 103, 1981, pp. 207-223.
- Pilch, M., Erdman, C.A., "Use of Break Up Time Data and Velocity History Data to Predict the Maximum Size of Stable Fragment for Acceleration-Induced Break Up of a Liquid Drop," Int. J. of Multiphase Flow, Vol. 13, No. 6, 1987, pp. 741-757.
- Plesset, M.S. and Chapman, R.B., Journ. of Fluid Mech., pp. 283-290, 1971.
- Ranger, A.A., and Nicholls, J.A., "Aerodynamic Shattering of Liquid Drops," *AIAA Journal*, Vol. 7, No. 2, 1969.
- Reid, R. C., "Rapid Phase Transitions From Liquid to Vapor," Adv. Chem. Eng., Vol. 12, 1983, pp. 105-208.

- Reinecke, W. G., and Waldman, G. D., "An Investigation of Water Drop Disintegration in the Region Behind Strong Shock Waves," *Proc. 3rd Intl. Conf. on Rain Erosion and Associated Phenomena*, Vol. 2., 1970, pp. 629-667.
- Reynolds, W.C., Thermodynamic Properties in SI. Stanford University Press, Stanford, CA, 1979.
- Scott, E., Berthoud, G.J., "Multiphase Thermal Detonation," Bankoff SG (ed)
 Topics in Two-phase Heat Transfer and Flow, ASME, 1978.
- Sharon, A., Bankoff S.G., "Propagation of Shock Waves in a Fuel-Coolant Mixture. Part A: Boundary Layer Stripping Mechanism. Part B: Taylor Instability," Reports coo-2512-12 and coo-2512-14, Chem, Eng. Dept., Northwestern University, Evanston, Il., 1978.
- Simpkin, P.G., and Bales, E.L., "Water Drop Response to Sudden Acceleration" J. of Fluid Mech., Vol. 55, 1972, p. 629.
- Tan, M.J., and Bankoff, S.G., "On the Fragmentation of Drops," Transactions of the ASME J. of Fluids Eng., Vol.108, 1986, pp. 109-114.
- Taylor, G.I., "The Shape and Acceleration of a Drop in a High Speed Air Stream," The Scientific Papers of G.I. Taylor, ed. by G.K. Batchelor, Vol.III, University Press, Cambridge, 1963, pp. 457-464.
- Theofanous, T.G., Saito, and Efthiniadis, Fuel Coolant Interactions and Hydrodynamic fragmentation, *Intl. Meeting on Fast Reactor Safety Tech.*, Aug. 19-23, 1979, Seattle Washington.
- Vogel, A., Lauterborn, W., and Timm, R., "Optical and Acoustic Investigations of the Dynamics of Laser produced Cavitation Bubble Near a Solid Boundary," J. of Fluid Mechanics, Vol. 206, 1989, pp. 299-338.
- Young M.F., "The TEXAS Code for Fuel-Coolant Interaction Analysis," *Proc. of LMFBR Safety Topical Meeting*, Lyon, France, Vol. III, 19-23 July, 1989, pp. 567-575.

- Walford, F. J., Transient Heat Transfer From a Hot Nickel Sphere Moving Through Water, Int. J. Heat Mass Transfer, Vol.12, pp. 1621-1625 (1969).
- Whitaker, S., "Forced Convection Heat-Transfer Correlations for Flow in Pipes, Past Flat Plates, Single Cylinders, Single Spheres, and Flow in Packed Beds and Tube Bundles," AIChE J., Vol. 18, 1972, p361
- Zyskowsky, W., "Study of Thermal Explosion Phenomenon in Molten Copper-Water Systems," Int. J. of Heat and Mass Transfer, Vol. 19, 1975, pp. 849-868.

Appendix A

- 🗹

DERIVATION FOR THE TRAJECTORY OF A SOLID SPHERE IN A STREAM OF FLUID.

Let us consider a sphere of density ρ_d and radius R in a flow of constant velocity U and density ρ_f . Taking a force balance on the sphere in the direction of the flow and neglecting buoyancy and virtual mass and taking a constant drag coefficient gives

$$\left(\frac{4}{3}\pi \rho_{\rm d} R^3\right) \frac{{\rm d}V}{{\rm d}t} = \frac{1}{2} \rho_{\rm f} (U-V)^2 C_{\rm D} (\pi R^2)$$
 (A-1)

or, the acceleration is given by

$$\frac{dV}{dt} = \frac{3}{8} \frac{\rho_f}{\rho_d} \frac{C_D}{R} (U - V)^2 = \beta (U - V)^2$$
 (A-2)

where

$$\beta = \frac{3}{9} \frac{\rho_f}{\rho_d} \frac{C_D}{R}$$
 (A-3)

Integrating Eqn. (A-2) and taking the initial velocity to be zero yields the following expression for the time history of the sphere velocity

$$\frac{\mathrm{dx}}{\mathrm{dt}} = U - \frac{U}{\beta U t + 1} \tag{A-4}$$

where x is the sphere displacement. Integrating Eqn. (A-4) yields the sphere displacement x at a time t,

$$x = Ut - \frac{1}{\beta} \ln (\beta U t + 1)$$
 (A-5)

or in dimensionless form where $X = \frac{x}{2R}$ and $T = \frac{Ut}{2R} \left(\frac{\rho_f}{\rho_d}\right)^{1/2}$

$$X = T \left(\frac{\rho_d}{\rho_f}\right)^{1/2} - \frac{4}{3C_D} \left(\frac{\rho_d}{\rho_f}\right) \ln \left\{\frac{3}{4} \left(\frac{\rho_f}{\rho_d}\right)^{1/2} C_D T + 1\right\}$$
 (A-6)

Appendix B

3

DERIVATION OF RAYLEIGH'S EQUATION FOR BUBBLE DYNAMICS

The radial motion of a gas bubble in an inviscid and incompressible fluid was first studied by Rayleigh (1917). The following is a derivation of the so called Rayleigh equation for bubble dynamics. We consider a gas bubble with a radius R and pressure P_B in an infinite fluid of density ρ and pressure P_{∞} , see Fig. B-1. We take the motion of the fluid outside the bubble to be irrotational, thus the velocity potential is given by

$$\phi = \frac{R^2 R}{r} \tag{B-1}$$

where r is the radial distance from the center of the bubble. Using Bernoulli's unsteady irrotational flow equation the pressure outside the bubble is given by

$$P = \rho \left\{ \frac{P_{\infty}}{\rho} + \frac{\partial \phi}{\partial t} + \frac{(\nabla \phi)^2}{2} \right\}$$
 (B-2)

where a large distance from the bubble we have noted that $(\nabla \phi) = 0$ and the fluid pressure is P_{∞} . The pressure in the fluid just at the bubble surface, P_{BS} , is determined by setting r = R. This yields

$$P_{BS} = \rho \left\{ \frac{P_{\infty}}{\rho} + \frac{3}{2} \dot{R}^2 + R \ddot{R} \right\}$$
 (B-3)

Regrouping Eqn. (B-3) gives the classical Rayleigh equation.

$$R\ddot{R} + \frac{3}{2}\dot{R}^2 = \frac{1}{\rho} \{P_{BS} - P_{\infty}\}$$
 (B.4)

If surface tension at the bubble surface is neglected $P_{BS} = P_B$, if surface tension is included $P_{BS} = P_B - 2\sigma/R$ and the Rayleigh equation becomes

$$RR + \frac{3}{2}R^2 = \frac{1}{\rho} \left\{ (P_B - P_\infty) - \frac{2\sigma}{R} \right\}$$
 (B-5)

$$R\ddot{R} + \frac{3}{2}\dot{R}^2 = \frac{1}{\rho}\left\{ (P_B - P_\infty) - \frac{2\sigma}{R} \right\}$$
 (B-5)

<u>.</u>

Plesset (1949) further modified Rayleighs equation by taking into account the viscosity of the fluid, μ ,

$$R\ddot{R} + \frac{3}{2}\dot{R}^2 = \frac{1}{\rho}\left\{ (P_B - P_\infty) - \frac{2\sigma}{R} - \frac{4\mu\dot{R}}{R} \right\}$$
 (B-6)

REFERENCES

Plesset, M.S., J. Appl. Mech., Vol. 16, 1949, p. 277.

Rayleigh, L., Philos. Mag., Vol. 34, 1917.

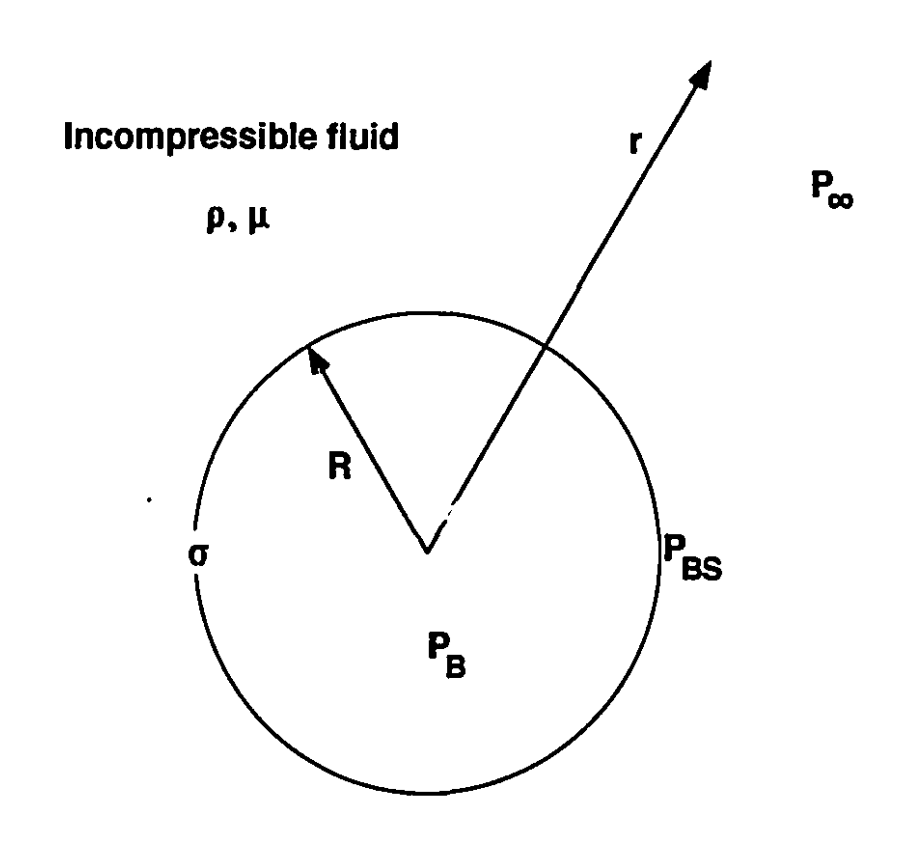


Figure B-1: Schematic showing parameters and notation

Appendix C

GOVERNING RELATIONS FOR HUGONIOT ANALYSIS

It is beneficial to first go through the derivation of the equations used for single-component single-phase mixtures to set the ground work for the more complicated two-component two-phase mixtures encountered in thermal detonations.

First the conservation equations are written for a propagating, steady-state, reaction zone moving at a velocity D into a mixture at rest. Shown in Fig. C-1 is a schematic of a steadily propagating energy release zone in the reference frame moving with this steady zone. Note that the details of the reaction zone are left out. Knowledge of the processes inside this zone is of no consequence as long as this zone is steady and equilibrium conditions prevail at the boundary planes of the zone itself. With subscript o denoting upstream conditions and subscript 1 denoting downstream conditions, application of mass, momentum and energy conservation across the zone yields

$$\rho_1 U_1 = \rho_0 D \tag{C-1}$$

$$P_1 + \rho_1 U_1^2 = P_0 + \rho_0 D^2$$
 (C-2)

$$h_1 + \frac{1}{2}U_1^2 = h_0 + \frac{1}{2}D^2$$
 (C-3)

Combining Eqs. (1) and (2) we obtain the so-called Rayleigh Line

$$D = V_0 \sqrt{(\frac{P_1 - P_0}{V_0 - V_1})}$$
 (C-4)

which relates the velocity, D, of this propagating zone (or wave) to the change in pressure and specific volume, V, across the wave. Eq. (C-4) gives a straight line on a P-V diagram where the slope is proportional to the square of the wave velocity. Therefore, for a given initial condition (P_0, V_0) and wave velocity, the downstream state (P_1, V_1) must lie on this line. If we eliminate the wave velocity from Eq. (C-4) using Eqs. (C-3) and (1) we get the Hugoniot equation as follows.



$$h_1 - h_0 = \frac{1}{2} (P_1 - P_0)(V_0 + V_1)$$
 (C-5)

Replacing enthalpy by h = e + PV we get another form of the Hugoniot with internal energy, e, instead of enthalpy

$$e_1 - e_0 = \frac{1}{2} (P_1 + P_0)(V_0 - V_1)$$
 (C-6)

The Hugoniot curve together with the Rayleigh line are shown schematically in Fig. C-2.

If no chemical changes occur, then the reactant species and product species are identical and Eq. (C-5) denotes the so-called shock Hugoniot or shock adiabat. It should be emphasized again that the validity of Eqs. (C-4) and (C-5) places no restriction on the thickness of the transition zone between the upstream and downstream boundaries of the zone. A normal shock may or may not be present. The flow may even be transient and three dimensional inside the zone. Eqs. (C-4) and (C-5) apply to the steady one dimensional flow and equilibrium conditions that must prevail upstream and downstream of the boundaries of the zone only. If we assume the existence of a normal shock as in the classical ZDN model for detonation structure, then since transition across a shock takes a few molecular collisions and chemical equilibration takes 10⁴ to 10⁵ collisions, it is reasonable to assume that in a chemical detonation the transition to the equilibrium Hugoniot must go via the shock Hugoniot, i.e., from the initial state to the shock adiabat first via the Rayleigh line prior to any reaction, then proceed from the shock adiabat to the equilibrium Hugoniot. Furthermore, if it can be assumed that intermediate states are quasi-equilibrium and the onedimensional conservation laws of mass and momentum are valid, then the intermediate states from the shock to the final equilibrium Hugoniot must also follow the Rayleigh line. However, it should be emphasized, on the basis of the one-dimensional conservation laws valid for a steadily propagating wave, that although the initial state and the final state on the Hugoniot are connected by the Rayleigh line, intermediate states cannot be defined and it is not necessary that a shock must be present at the transition zone.

In Fig. C-2 the points denoted CV and CP represent the final states after constant volume and constant pressure processes, respectively. It is immediately evident from Eq. (C-4) that points between CV and CP are inaccessible (because the wave velocity, D, becomes imaginary). The intersection of the Rayleigh Line and the Hugoniot defines the downstream state. As we can see from Fig. C-2, for a given wave velocity (slope of Rayleigh

line) in general there exist two solutions, the strong solution given by point 2 and the weak solution given by point 1 on the diagram. According to classical theory in chemical detonation, the choice for the detonation velocity is the unique minimum velocity corresponding to the tangency of the Rayleigh line to the Hugoniot curve. The criterion for choosing this tangency solution in classical detonation theory is based on the fact that the weak detonation solution violates the 2nd law of thermodynamics, if we adopt the ZDN model for this structure of a normal shock transition prior to energy release by chemical reactions. The overdriven detonation solution is ruled out on the basis of stability. The increase in density across the wave necessitates the formation of an expansion wave behind the detonation. Since the flow behind the overdriven detonation is subsonic, the expansion can overtake the reaction zone and quench the reaction. However, we must emphasize, within the framework of the Hugoniot calculations, that there exists, a priori, no criterion for the choice of the appropriate detonation solution for given initial conditions.

The unique points at which the Rayleigh lines are tangent to the Hugoniot curve are denoted as CJ (Chapman-Jouguet) points and several additional conditions are associated with these points. Consider the detonation (or upper) branch of the Hugoniot curve. From Eq. (C-4) we see that the slope of the Rayleigh Line is proportional to the square of the mass flux j (j = ρ_0 D) through the wave. The point of tangency of the Rayleigh line and Hugoniot curve therefore represents a minimum in the mass flux. The following expression can be derived giving the change in entropy along the the Hugoniot curve,

$$\frac{dS}{d(j^2)} = \frac{(V_o - V_1)^2}{2T_1} > 0$$
 (C-7)

Since the CJ point represents a minimum in the mass flux, it follows from Eq. (C-7) that the entropy must also be stationary (i.e., dS = 0) at this point, and in fact the entropy is a minimum at this point. Therefore, at the CJ point, the Rayleigh line is tangent to both the Hugoniot and the isentrope going through that point. As a result it can be shown that the downstream flow velocity is sonic relative to the shock wave, which is denoted as the CJ condition. Note that there is a second CJ point in which the Rayleigh line is tangent to the Hugoniot curve, which is referred to as the lower branch solution, or the deflagration mode of propagation. In the present report we will be concerned primarily with the upper branch solution where the wave is supersonic relative to the mixture ahead of the wave.



One can eliminate the complexities of two-component mixtures by treating the mixture as being homogeneous. Homogeneous refers to a mixture which can be treated as a pseudo fluid (with all the appropriate averaging of properties) that obeys all the equations for single component fluids. In order for the homogeneous approximation to hold there can be no slip between the components, hence mechanical equilibrium. The initial temperatures of the components may be different, so that the mixture may not be initially in thermal equilibrium. For a homogeneous mixture the properties are obtained by mass averaging, as follows:

$$V_{mix} = \sum_{i} x_i V_i$$
 (C-8)

$$h_{mix} = \sum_{i} x_i h_i \tag{C-9}$$

where x_i is the mass fraction of the ith component. The caloric equation of state for each component is given by

$$dh = c_p dT + [V - T (\frac{\partial V}{\partial T})_p] dP$$
 (C-10)

In the case of a thermal detonation the components are the melt and the coolant (liquid and vapor). In the present study the melt is taken to be incompressible, so the change in enthalpy is

$$dh = c_D dT + V dP + [h_{sf}]$$
 (C-11)

where h_{Sf} is the latent heat of fusion which vanishes if the final temperature of the melt is below its melting temperature. McCahan and Shepherd (1991) performed a similar Hugoniot analysis taking the compressibility of the melt into account.

In chemical detonations the temperature of the products is fixed because the mass fractions depend on the equilibrium constants which in turn are a function of the temperature. In thermal detonations the final mixture temperature can be fixed by imposing the condition of thermal equilibrium between the melt and coolant. However, since diffusive heat transfer is slow, thermal equilibrium between the melt and the coolant can only be realized in practice if fine fragmentation of the melt occurs.

Using the Hugoniot equation given by Eq. (C-5) in conjunction with the mass averaged specific volume and enthalpy, Eqs. (C-8) and (C-9), and taking Eq. (C-11) to be the caloric equation of state for the melt along with an appropriate equation of state for the coolant (e.g., steam tables if coolant is water) one can obtain the Hugoniot curve on a P-V diagram.

Criteria for Selection of Solution

I

As mentioned earlier, the Hugoniot curve gives a locus of possible downstream states. For example, different slopes of the Rayleigh Lines intersect the Hugoniot curve at different points, giving different downstream states. Many previous investigators have assumed that when a thermal detonation occurs, it is a CJ detonation corresponding to the unique solution of the tangency of the Rayleigh line to the Hugoniot (or the minimum velocity solution). The tangency solution is obtained, like in the single component case, by drawing the tangent to the Hugoniot curve from the initial state. At the CJ point, the entropy along the Hugoniot curve will be a minimum, and so the isentrope as well as the Rayleigh line will be tangent at this point. This ensures that the velocity relative to CJ plane will equal the sonic velocity (as determined from the slope of the isentrope). As in single-component Hugoniot theory, without some knowledge of the structure of the reaction zone (e.g., existence of a leading shock wave, etc.), we cannot use stability or entropy arguments to determine if this solution is the appropriate choice. However, as in the case of chemical detonations, it appears reasonable that nature would choose a solution in which a choking or sonic condition applies as energy addition always drives a flow toward the sonic condition.

Tangency of the Rayleigh line with the Hugoniot gives the unique CJ solution which has the property of sonic conditions at the downstream plane. However, other authors have used a separate equation for computing the sound speed and obtain the CJ solution formally by requiring that the particle velocity be equal to the sound speed at the CJ plane. In a two-component mixture it is difficult to define a unique sonic velocity. Wallis (1969) points out that transient drag forces between the components would probably be both amplitude and frequency dependent and therefore the wave velocity would be a function of these variables as well as the properties of the components. Nevertheless, if we assume homogeneous flow (no slip between the components) one can derive an expression for the homogeneous mixture speed of sound (cH) based on the void fractions of the components (Wallis, 1969)

$$\frac{1}{\rho_{\rm m} c_{\rm H}^2} = \frac{\alpha}{\rho_1 c_1^2} + \frac{1 - \alpha}{\rho_2 c_2^2}$$
 (12)

where a is the voice fraction of component 1, c is the speed of sound, and ρ_m is the mixture density, where $\rho_m = \alpha \rho_1 + (1-\alpha) \rho_2$. Note that since the adiabatic compressibility of a substance is given by $\beta_s = -\frac{1}{V}(\frac{\partial V}{\partial p})_s = \frac{1}{\rho c^2}$ we can see that the above expression (C-12) for

the homogeneous sound speed just expresses the adiabatic compressibility (and hence the sound speed) of the mixture as a (volume fraction) weighted sum of the adiabatic compressibility of the components. One can use this expression to find the point on the Hugoniot curve where the downstream flow velocity equals this homogeneous speed of sound, thus satisfying the sonic condition $U_1 = c_H$. This criterion is not equivalent to drawing a tangent to the Hugoniot (this will be shown later by example) because of the incompatibility of the assumptions used in Eq. (C-12) and in obtaining the Hugoniot itself. So this method of determining the solution is not self-consistent thermodynamically in the sense that the CJ point determined in this manner does not correspond to a minimum in entropy (so that the Rayleigh line is not tangent to the isentrope at this point).

Another method of choosing the solution, assumed by Sharon and Bankoff (1981), is based on a separated flow choking condition. The CJ solution is determined by requiring that the particle velocity is equal to the stratified flow sonic velocity, c_S, given by (e.g., see Wallis, 1969)

$$c_{S} = \frac{\alpha_{d} \rho_{f} + (1 - \alpha_{d}) \rho_{d}}{\alpha_{d} \rho_{f} c_{f}^{2} + (1 - \alpha_{d}) \rho_{d} c_{d}^{2}}$$
(C-13)

Here subscript d refers to the unfragmented drop component and the subscript f refers to the homogeneous mixture consisting of the fragments plus the coolant (vapor and liquid). It can be easily shown that the stratified sonic velocity is higher than the homogeneous speed of sound calculated using Eq. (C-12).

So in summary, there are three possible methods which can be used to determine the final CJ state on the Hugoniot:

- (i) Finding tangency of the Rayleigh Line to the mass averaged Hugoniot curve (analogous to what is done for single component mixtures).
- (ii) Setting the downstream flow velocity equal to the homogeneous speed of sound given by Eq. (C-12).
- (iii) Setting the downstream flow velocity equal to the stratified speed of sound obtained from by Eq. (C-13).

In principle, all three methods should yield the same solution. However, since the expressions for the sound speed imposed differ, each of the three conditions above gives a different solution for the CJ point in practice. A priori, from the basic Hugoniot theory, it is not possible to choose which method is correct. However only the first method above gives a solution that is thermodynamically self-consistent in that at the determined CJ point the Rayleigh line is tangent to the Hugoniot curve as well as the isentrope. In addition, without a detailed knowledge about the structure of the reaction zone in a thermal detonation, there does not appear to be any compelling reason to choose the latter two conditions over the classical tangency solution. Therefore, in the present calculations, the CJ point solution was obtained by constructing the tangent to the mass-weighted Hugoniot curve (which corresponds to the point of minimum entropy change).

<u>REFERENCES</u>

e.

Æ.

- Sharon, A. and Bankoff, S.G., "On the Existence of Steady Super-critical Plane Thermal Explosions," Int. J. Heat Mass Transfer, Vol. 24 1981, pp. 1561-1572.
- McCahan, S. and Shepherd, J.E., "Models of Rapid Evaporation in Non-equilibrium Mixtures of Tin and Water," Presented at 13th ICDERS, 1991.
- Wallis G.B., One-Dimensional Two-Phase Flow, McGraw-Hill, Toronto, 1969.



Figure C-1: Schematic of a steadily propagating energy release zone in a moving reference frame

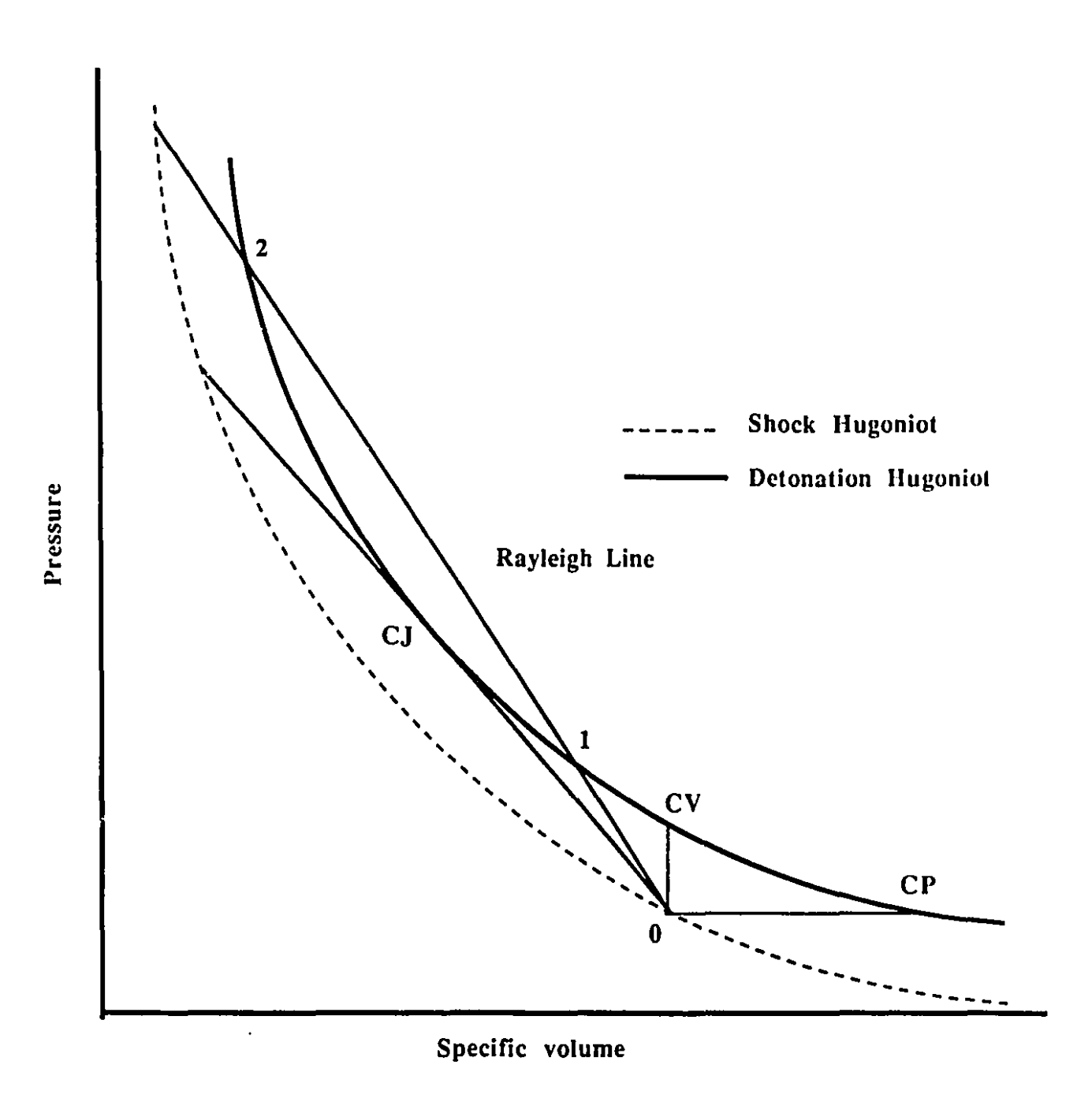
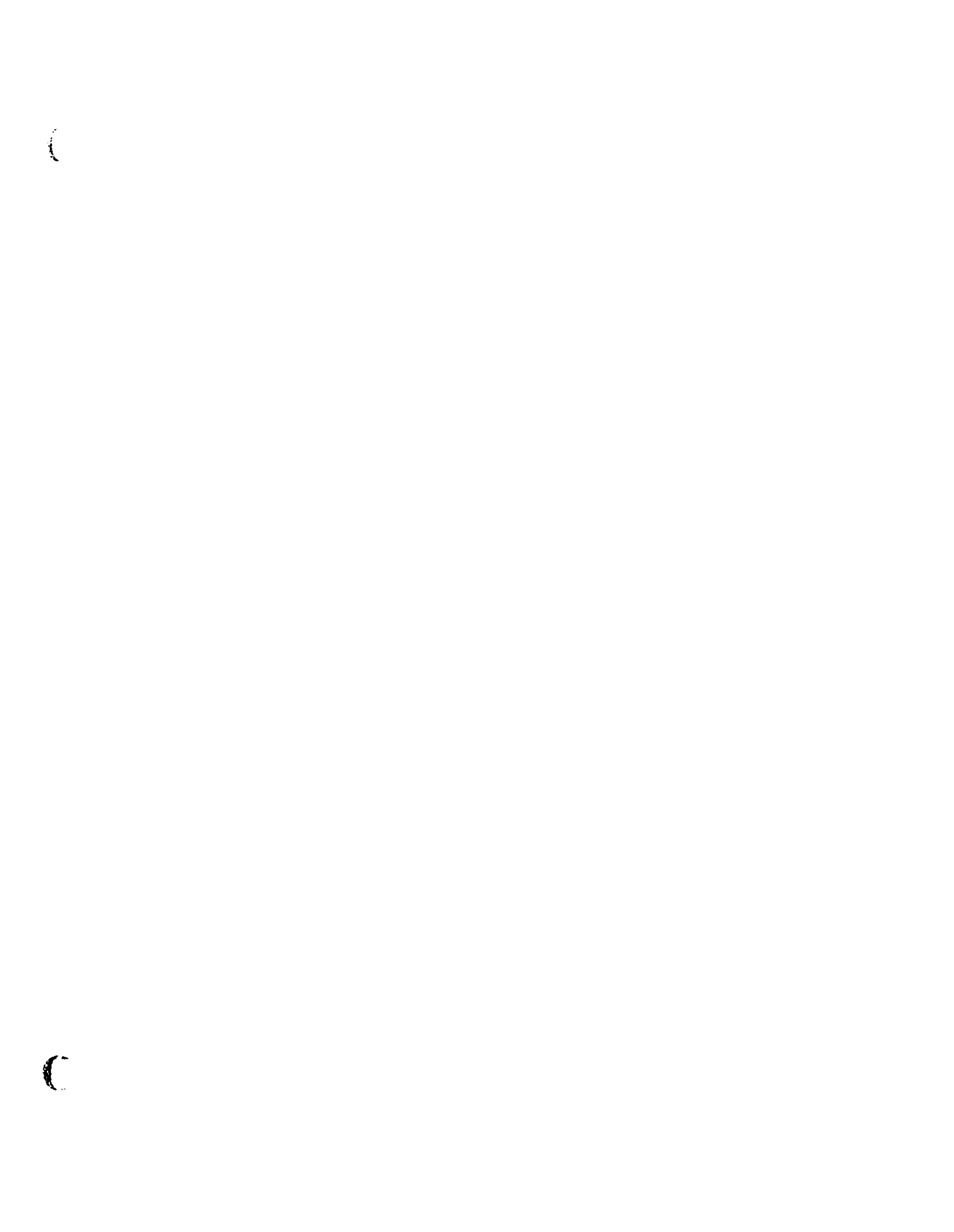


Fig. C-2: P-V diagram showing the CJ detonation downstream state at the tangency point between the Hugoniot curve and the Rayleigh line.



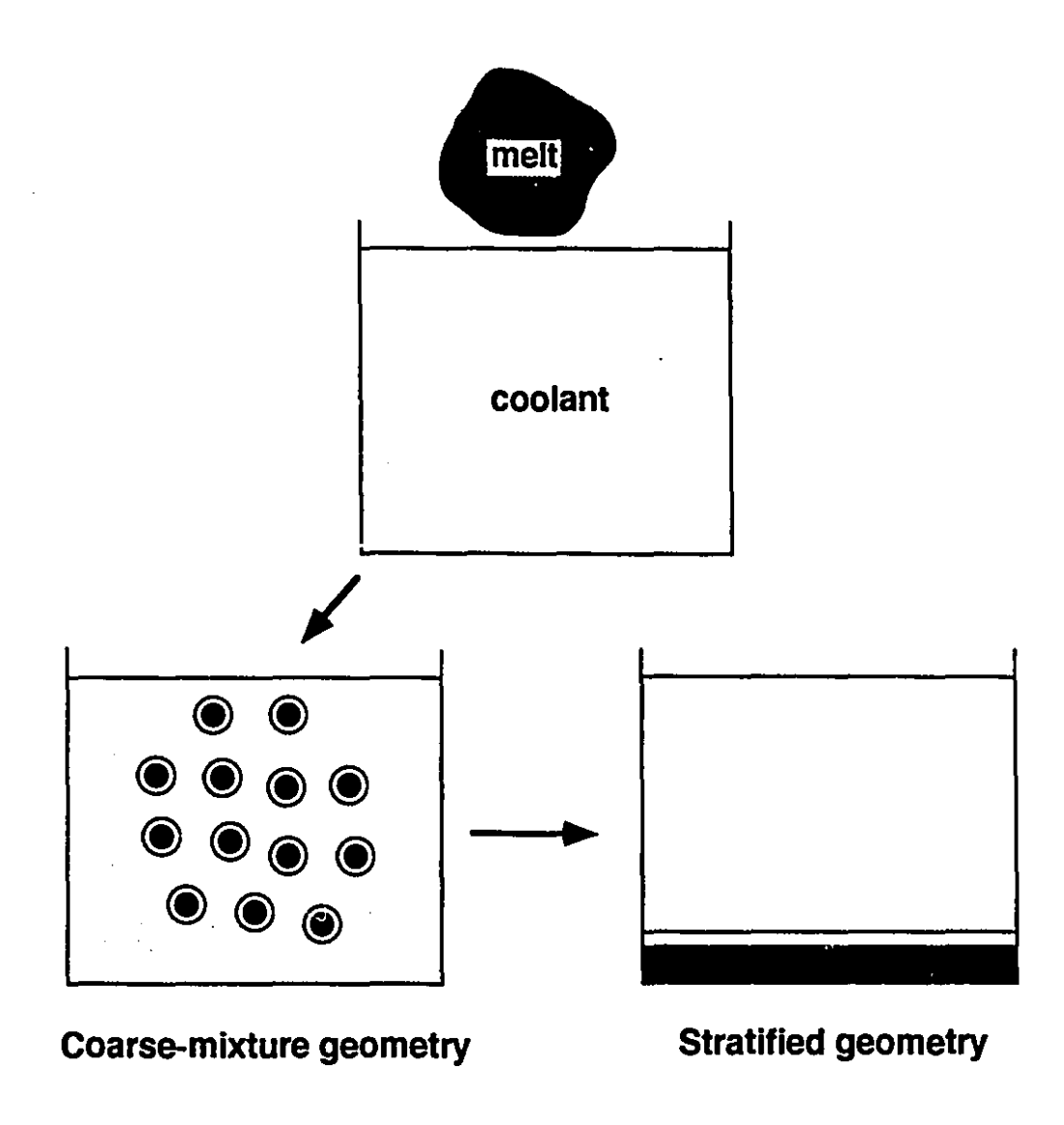


Figure 1: Schematic showing the formation of coarse-mixture and stratified geometry as initial conditions for a large-scale vapor explosion



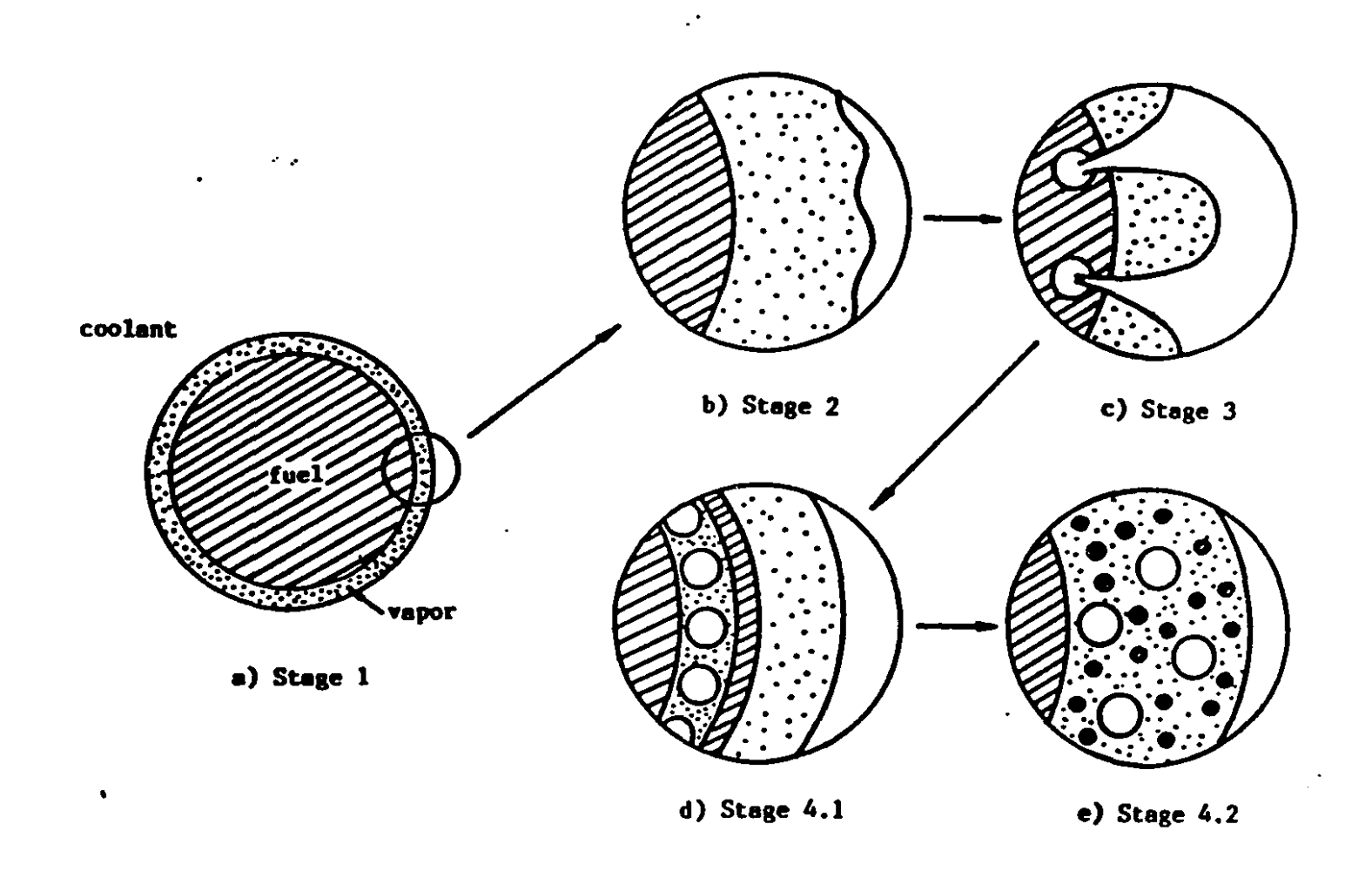


Figure 2 Schematic of Kim's (1985) coolant entrapment thermal fragmentation model

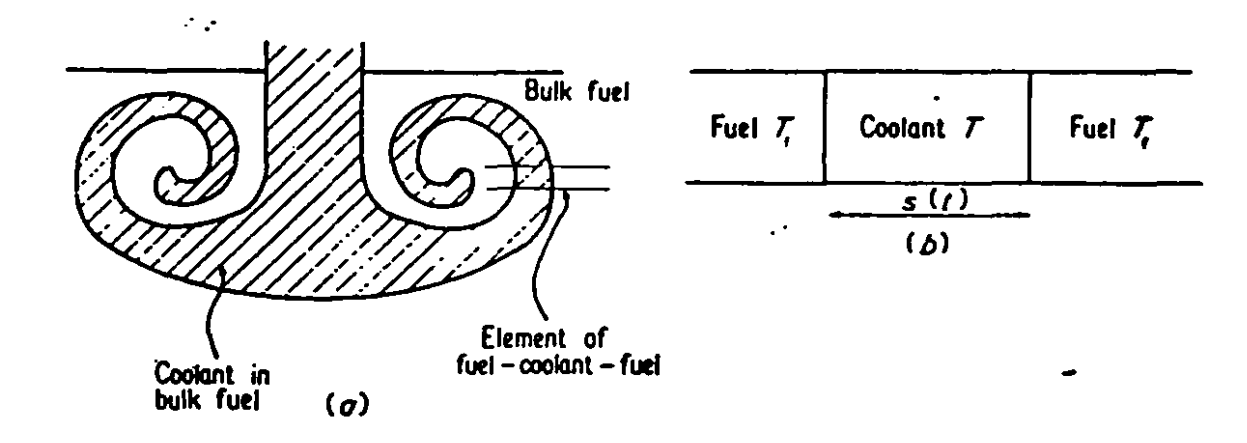
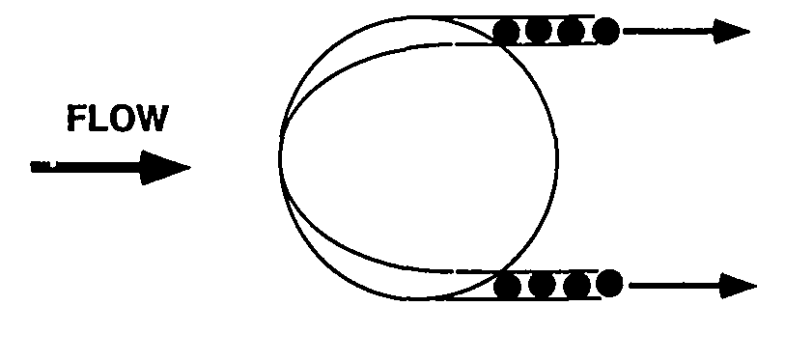
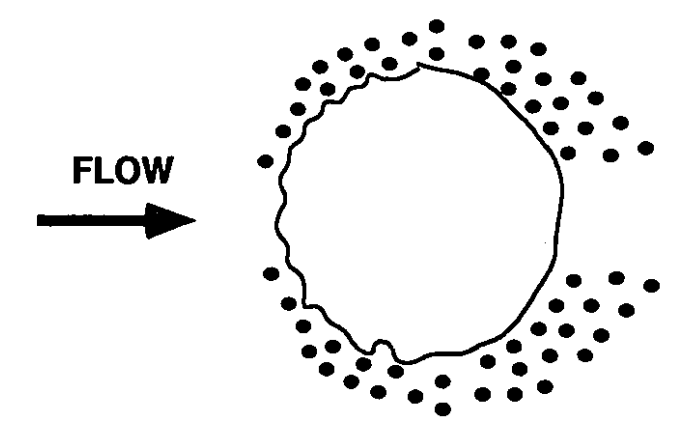


Figure 3 Schematic of Buchanan's (1973) vortex mixing thermal fragmentation model. (a) cross section of jet of coolant after penetration, (b) Element of fuel-coolant-fuel in which heat transfer occurs one-dimensionally

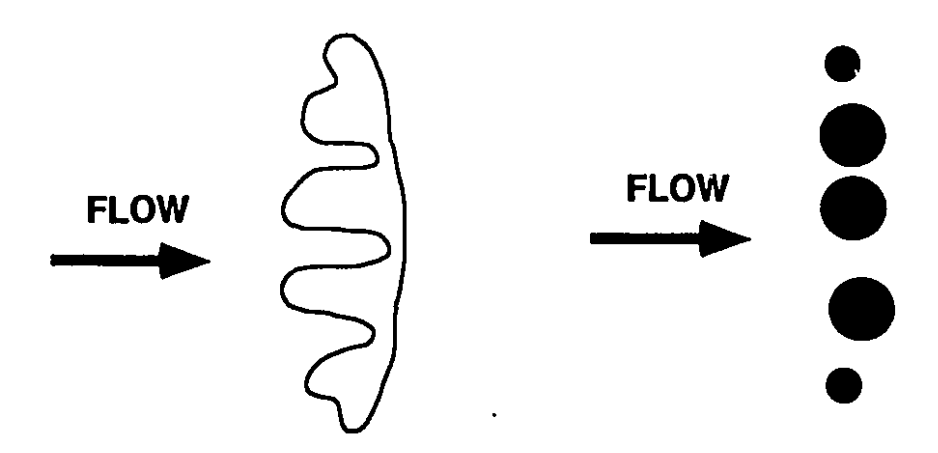
2



Boundary layer stripping



Wave crest stripping



Catastrophic breakup

Figure 4: Schematic showing three different hydrodynamic fragmentation models

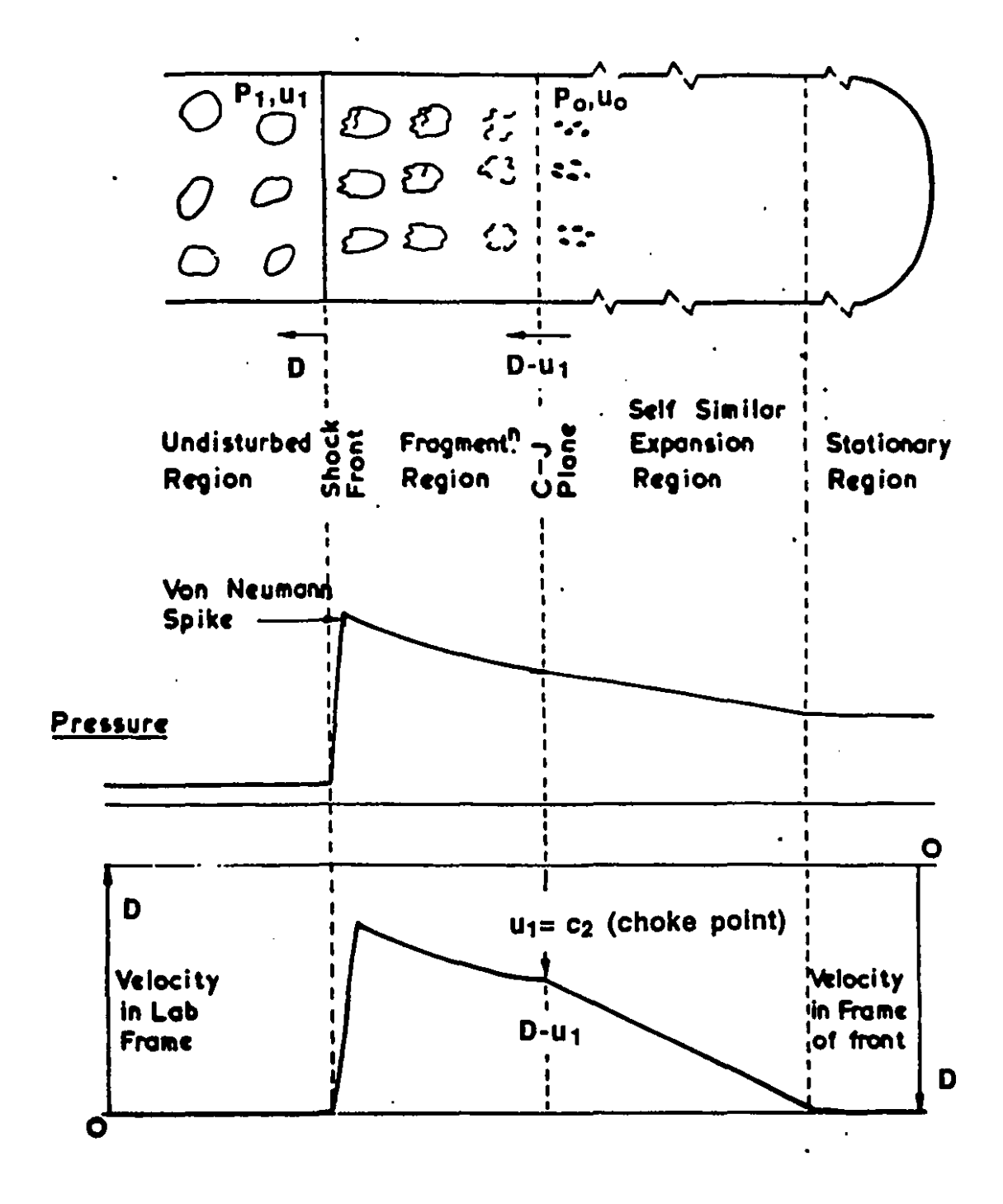


Figure 5 Schematic showing the structure of Board and Hall's (1975) thermal detonation model

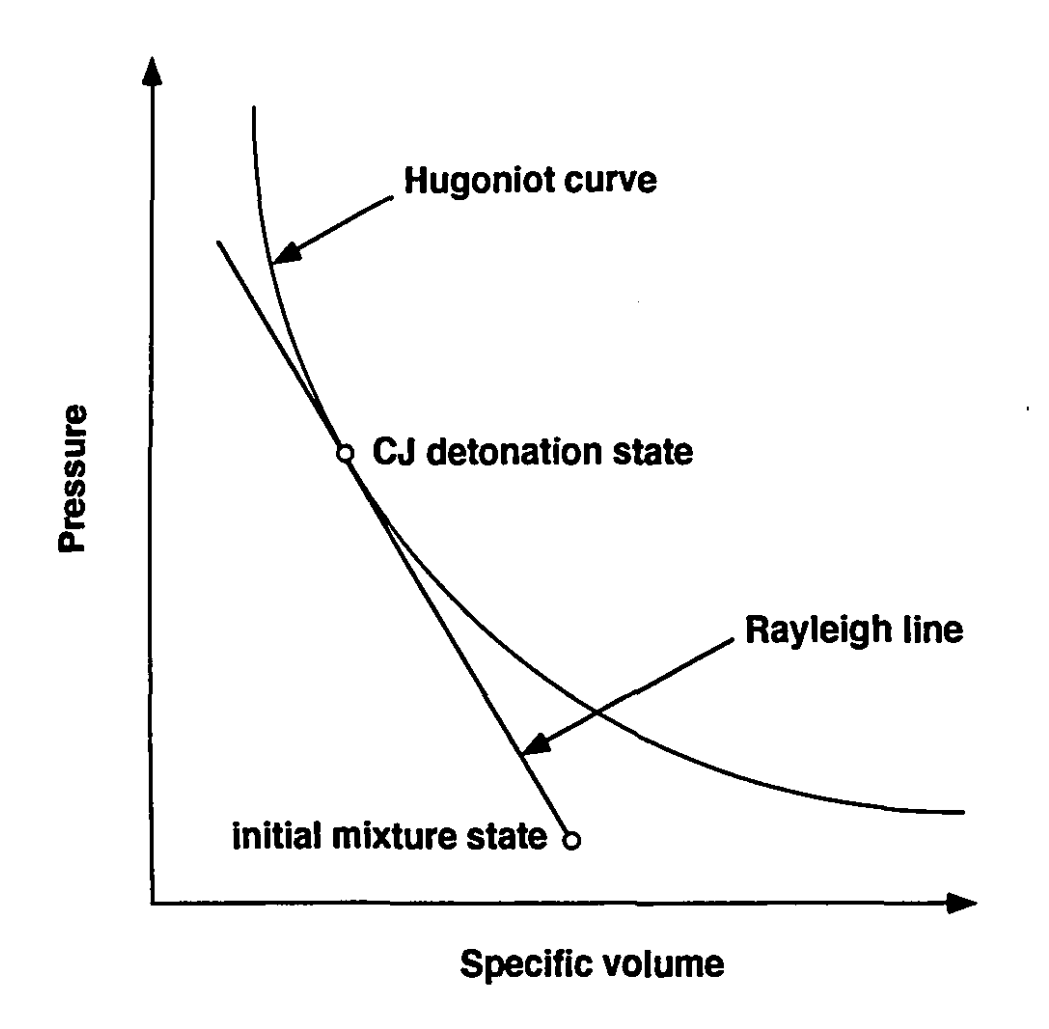
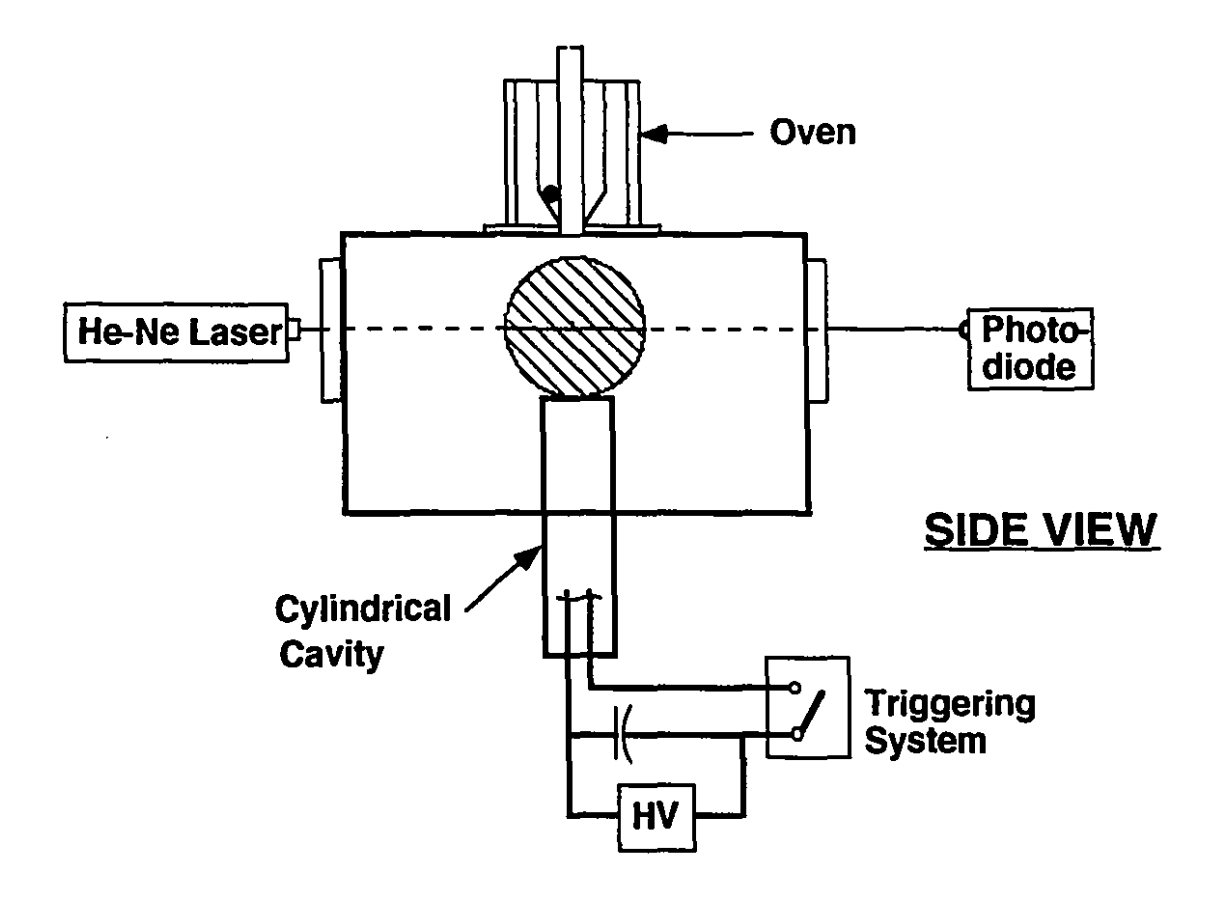


Figure 6: P-V diagram showing the CJ detonation downstream state at the tangency point between the Hugoniot curve and the Rayleigh line.



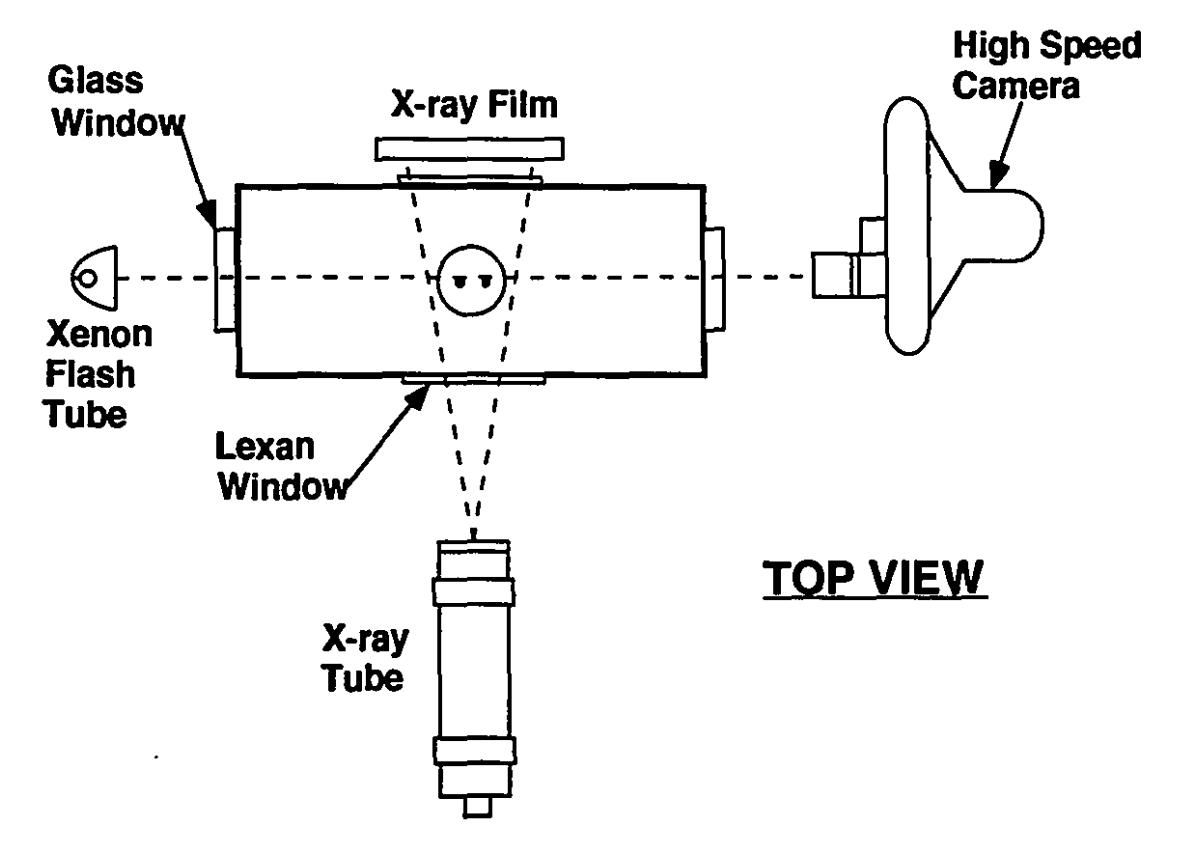


Figure 7: Schematic of experimental facility



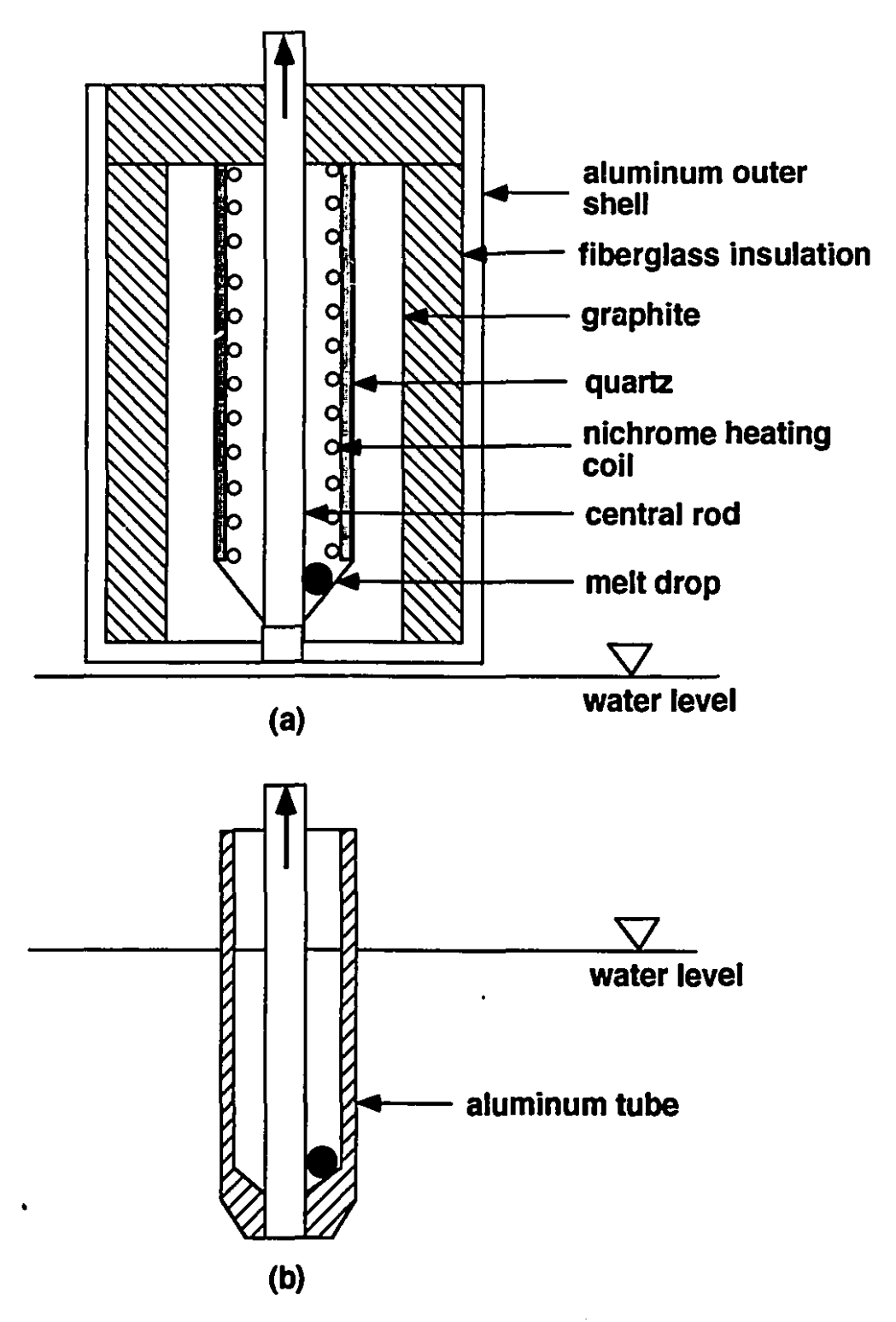


Figure 8: Schematic of (a) furnace used to heat up and release drops and (b) subsurface dropping mechanism for cold drop experiments

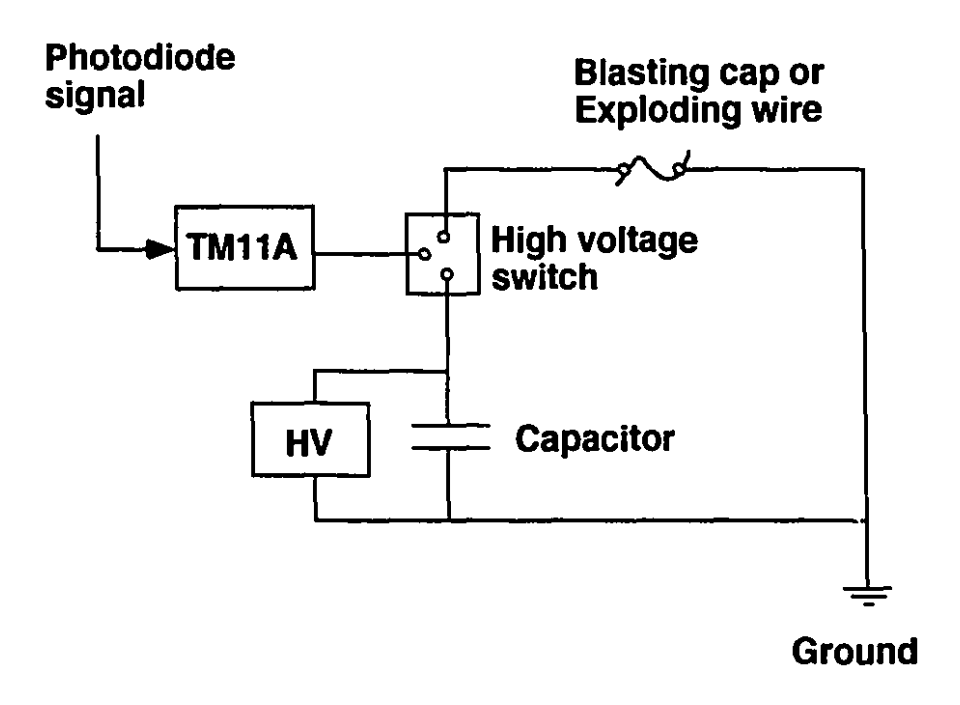


Figure 9: Schematic of high-voltage ciruit used for triggering system

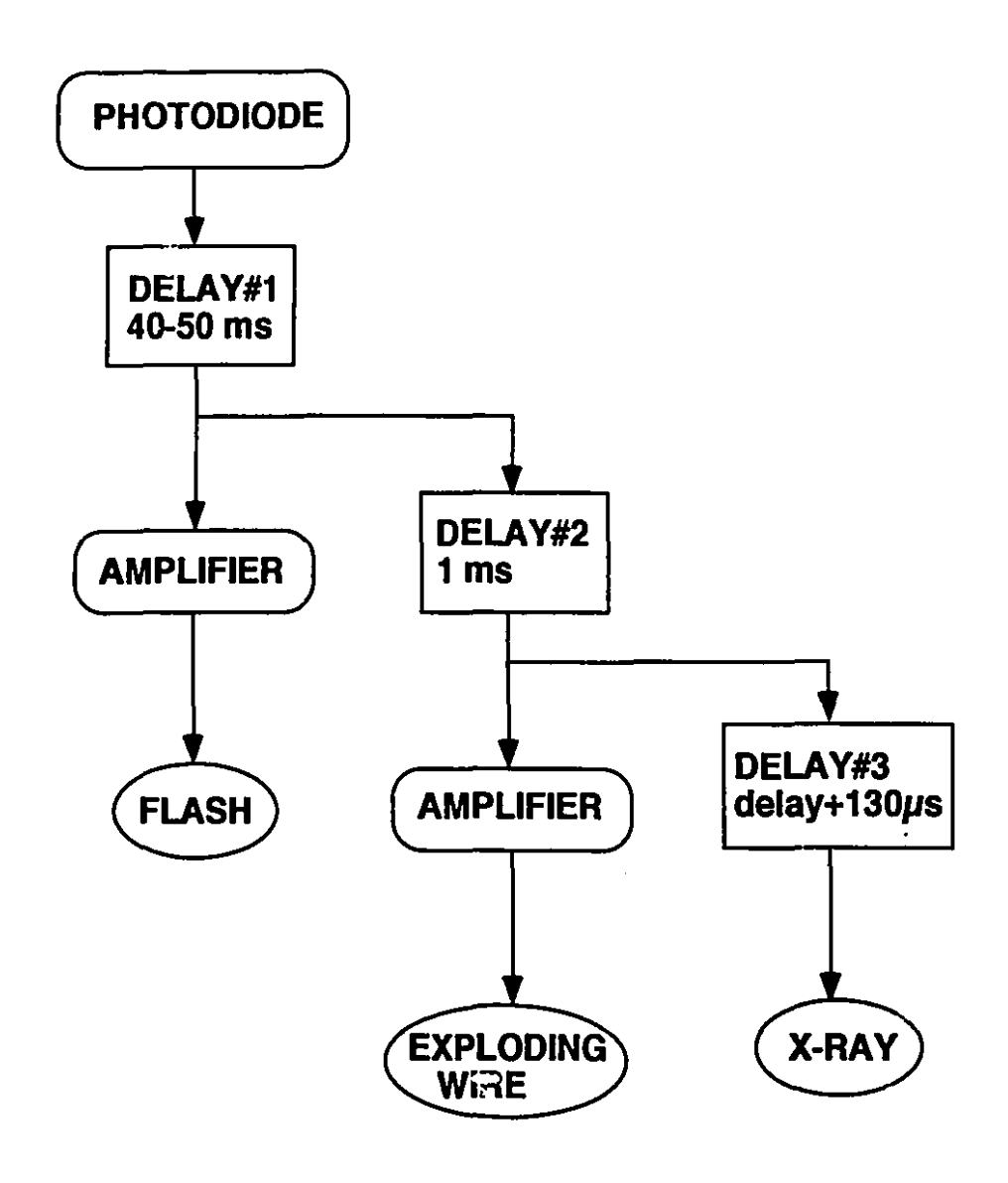


Figure 10: Flow chart indicating the difference delays used in taking simultaneous x-ray and regular highspeed photography



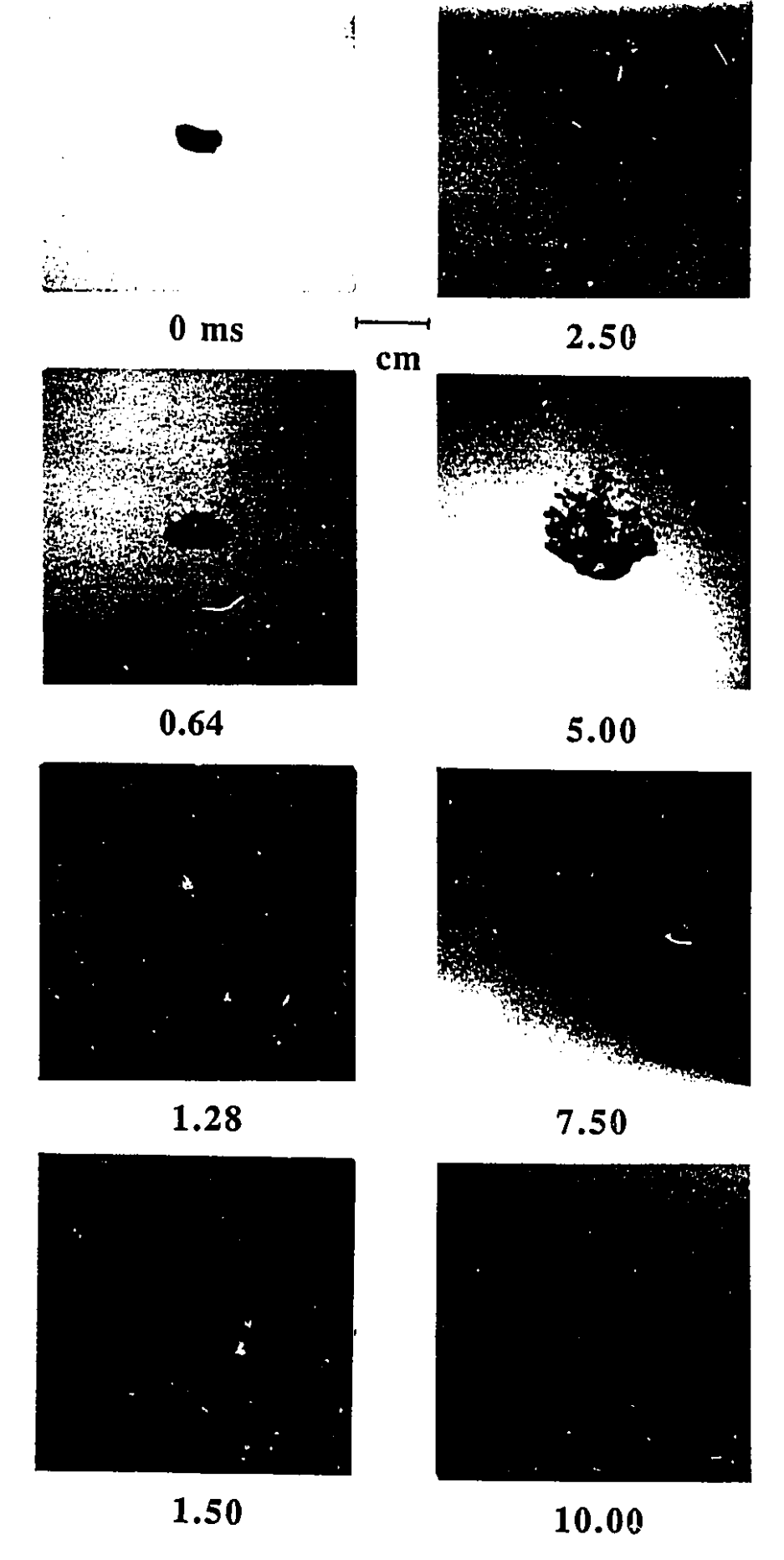


Figure 11: X-ray photographs of the hydrodynamic fragmentation of 0.5 g drops of cerrolow alloy in thermal equilibrium with surrounding water (at 65°C).

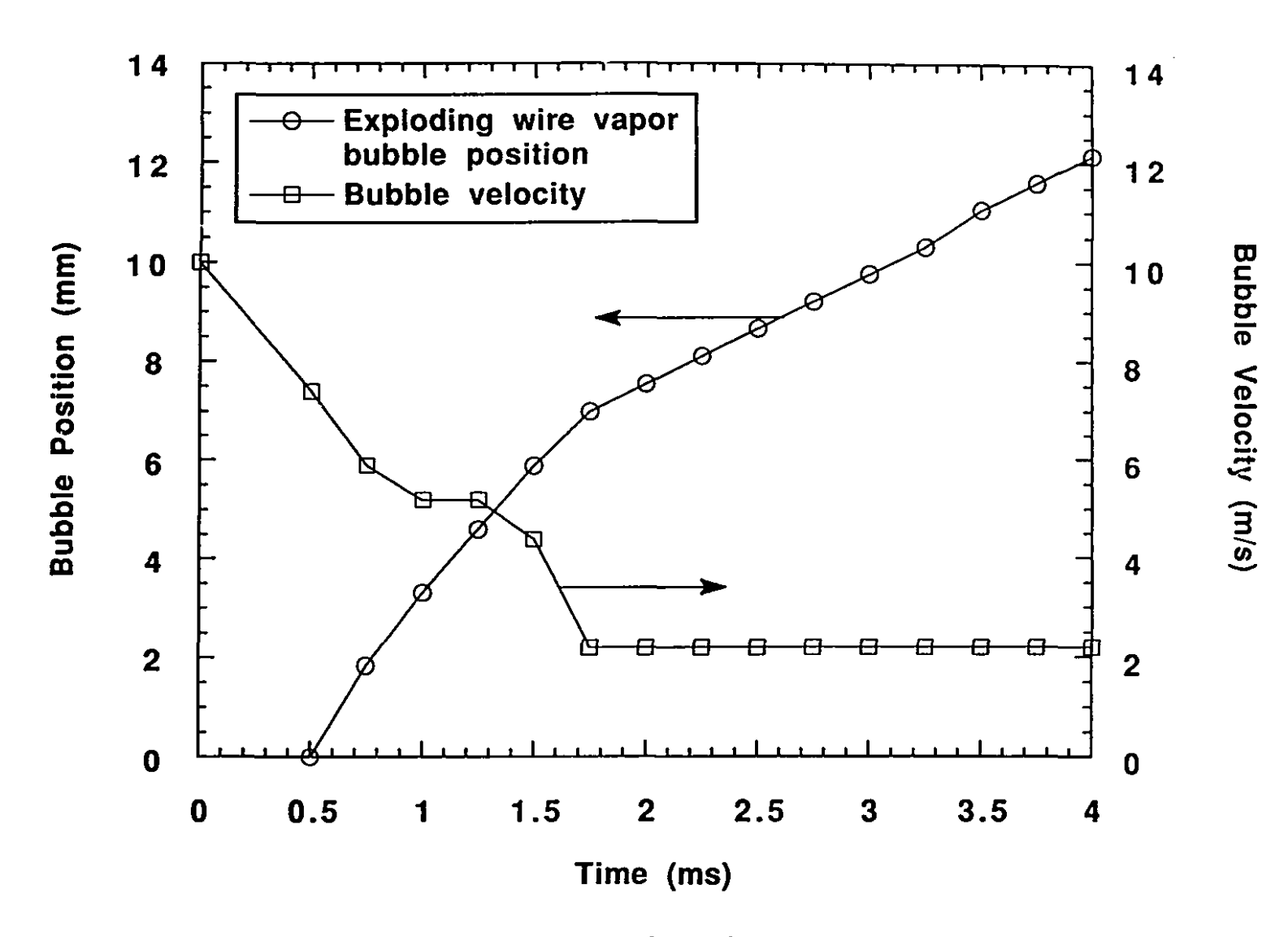


Figure 12: Position and velocity of vapor bubble generated by trigger system

Figure 13: High-speed photographs of the fragmentation of a 0.5 g drop of tin (at 700°C).

0.75

3.00

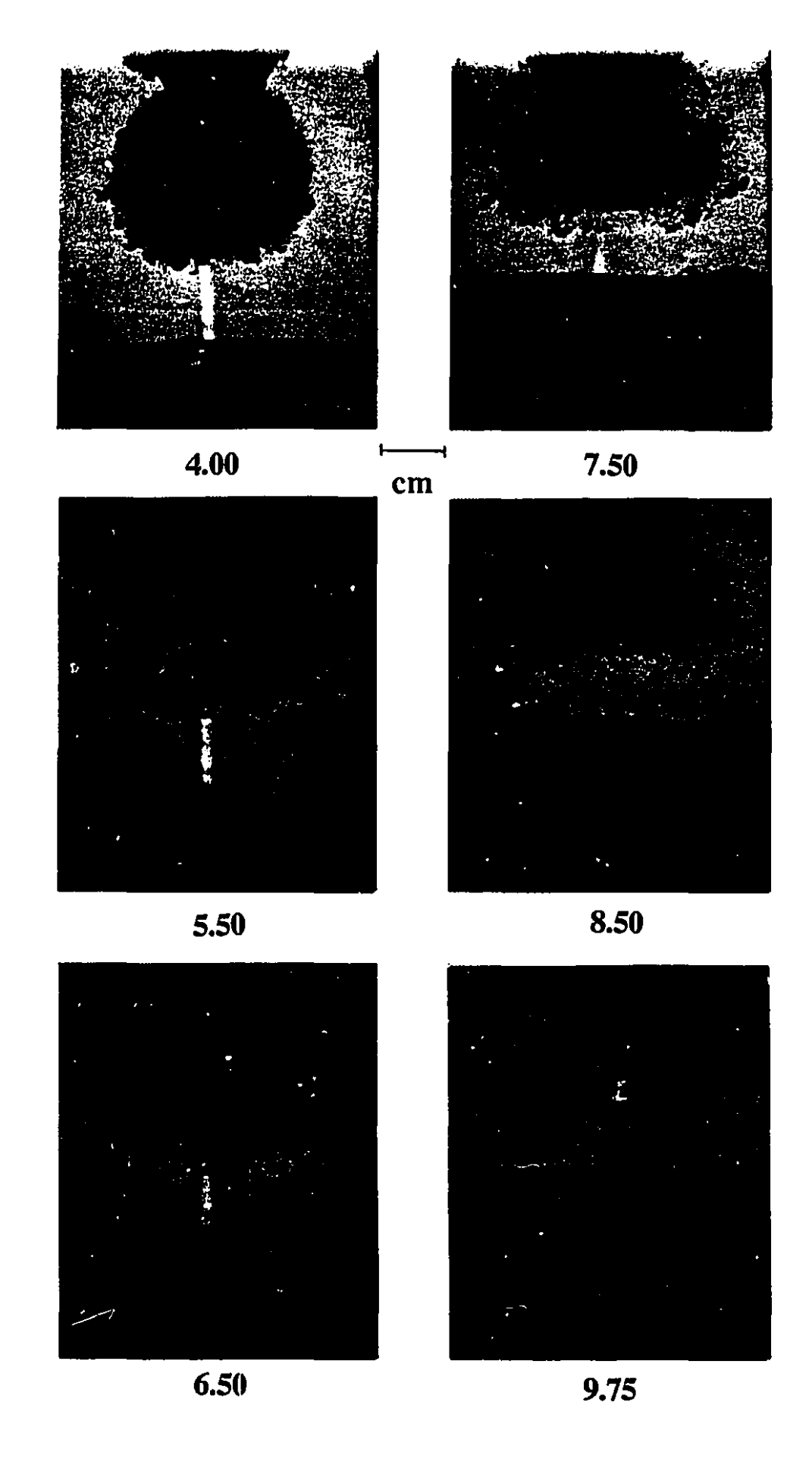


Figure 13 continued

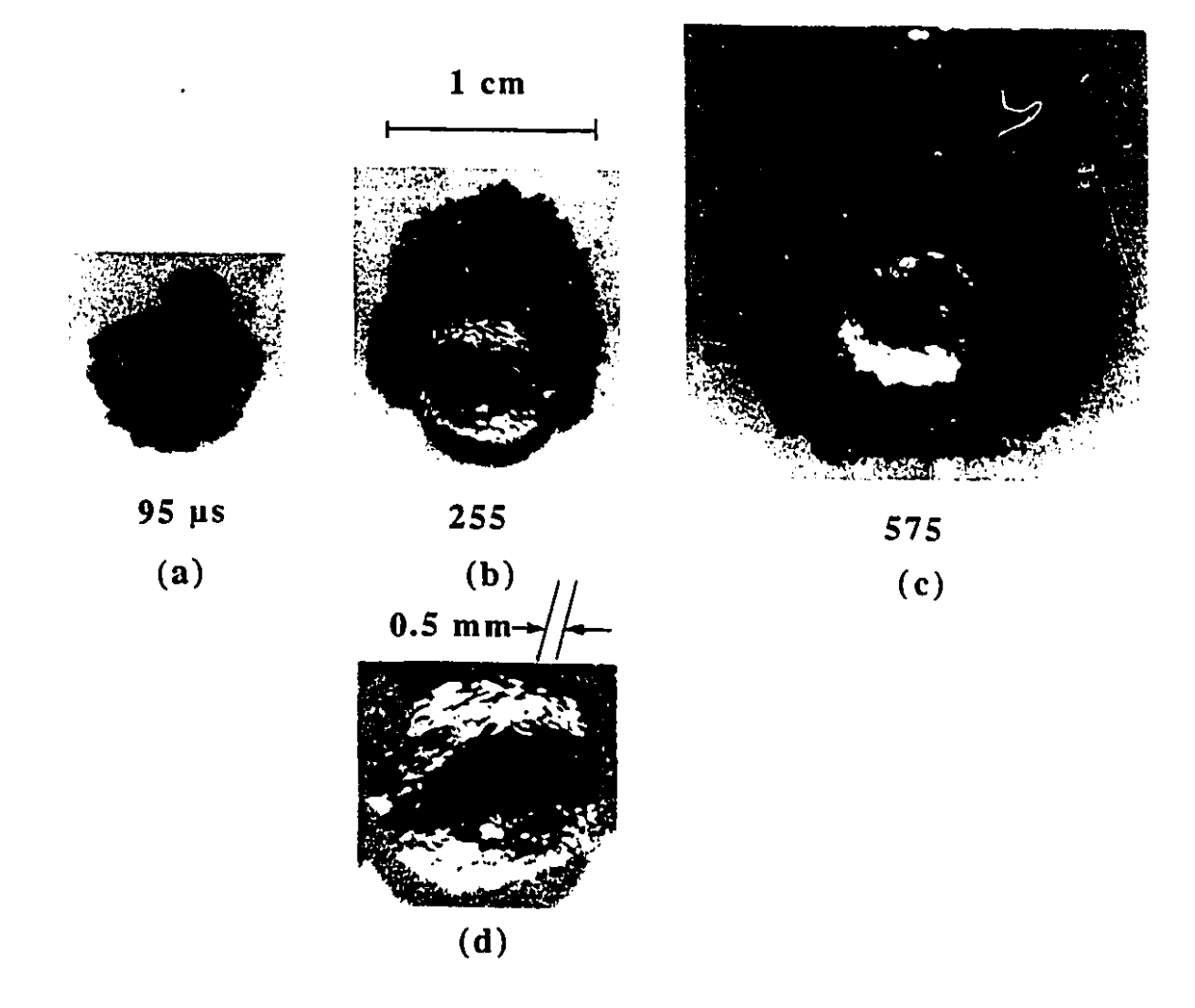


Figure 14: Double exposures of explosion of 0.5 g tin drops at 700°C. Initial drop shape illuminated by exploding wire. Enlargement of drop in center shows surface ripples on initial vapor film.

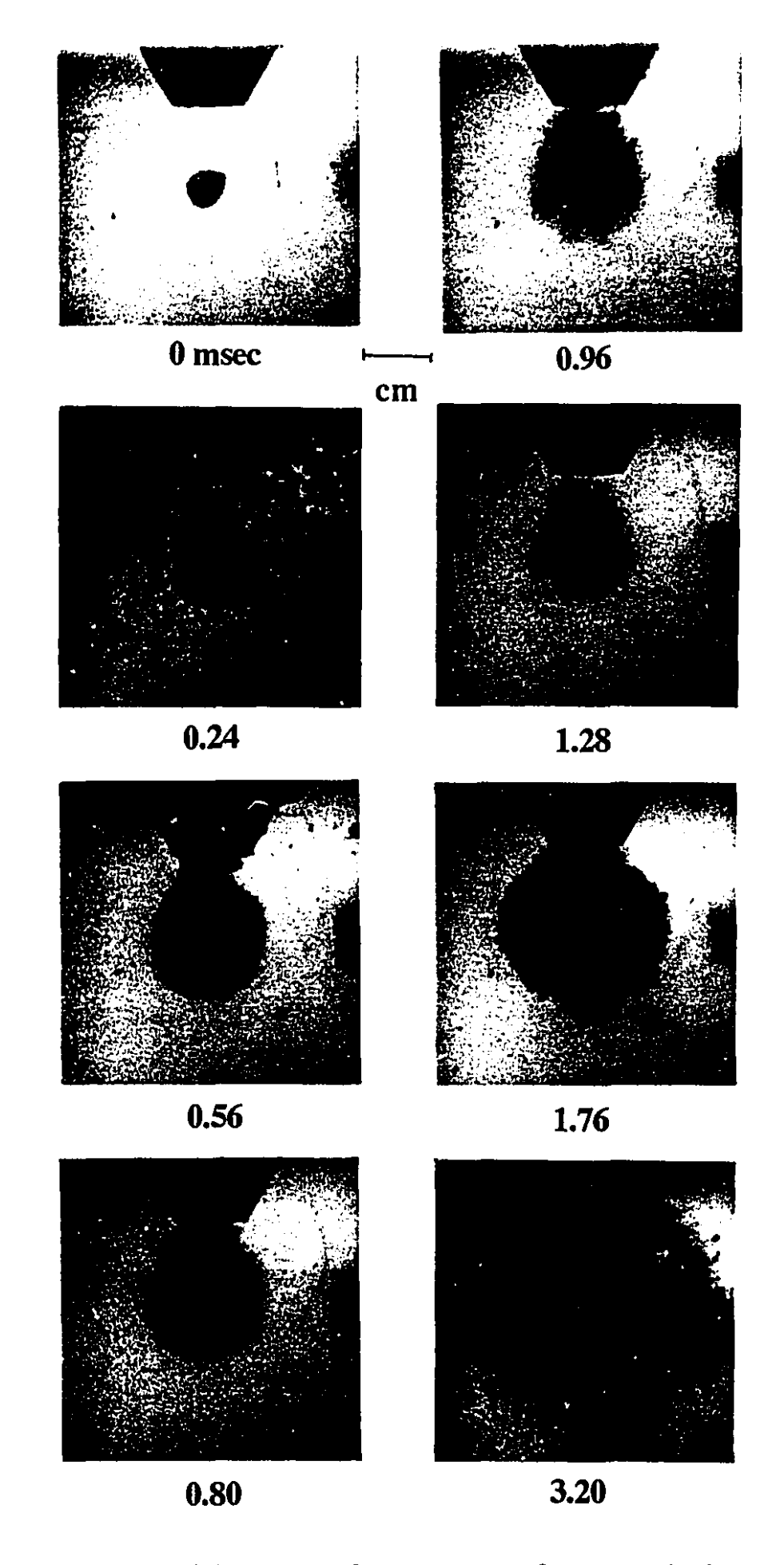


Figure 15: High-speed photographs of the explosion of a 0.5 g drop of tin at 700°C immersed in water at 65°C.

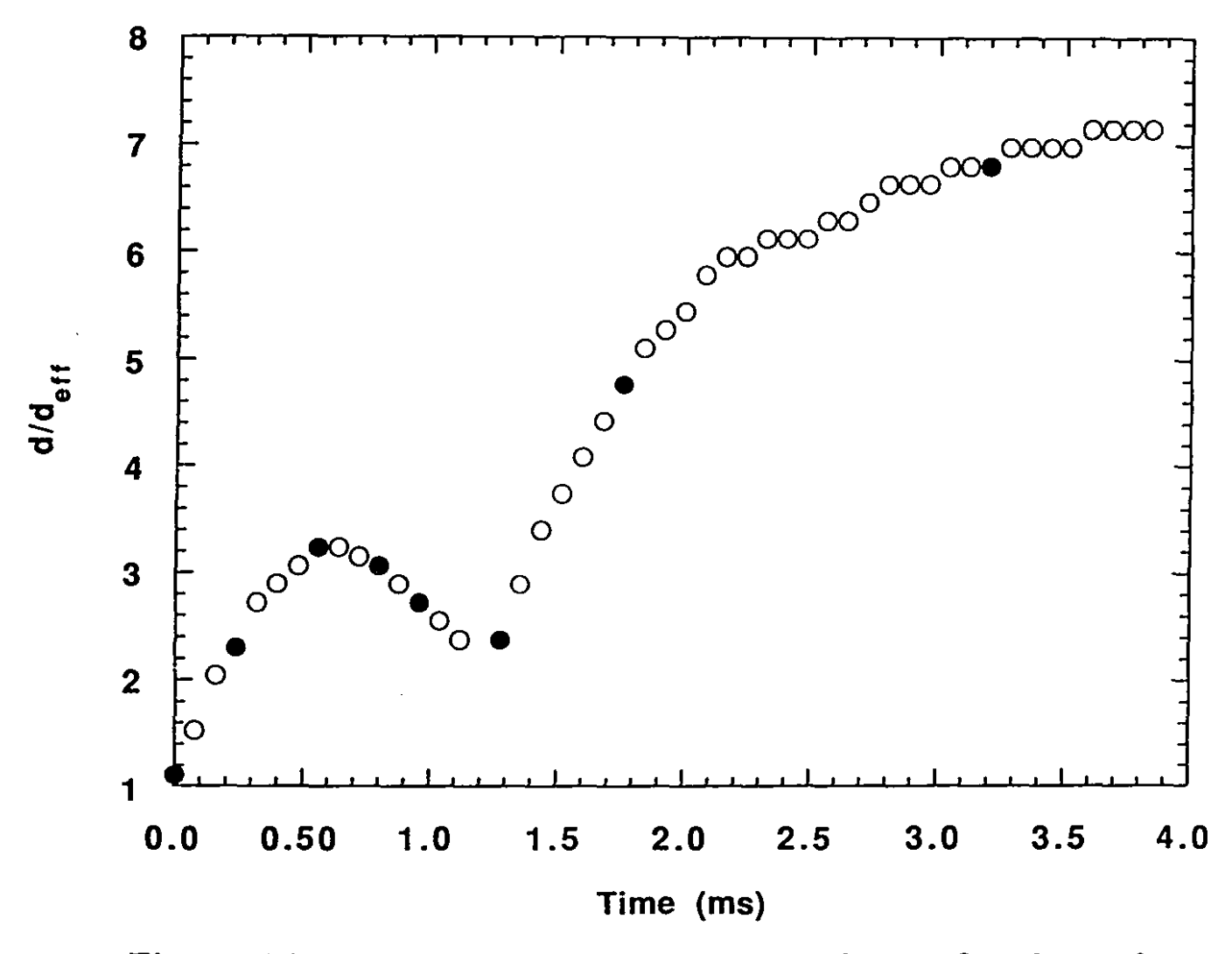


Figure 16: Radial bubble growth time history for drop shown in Fig. 15. Diameter normalized with effective diameter of drop. Solid circles indicate frames shown in Fig. 15

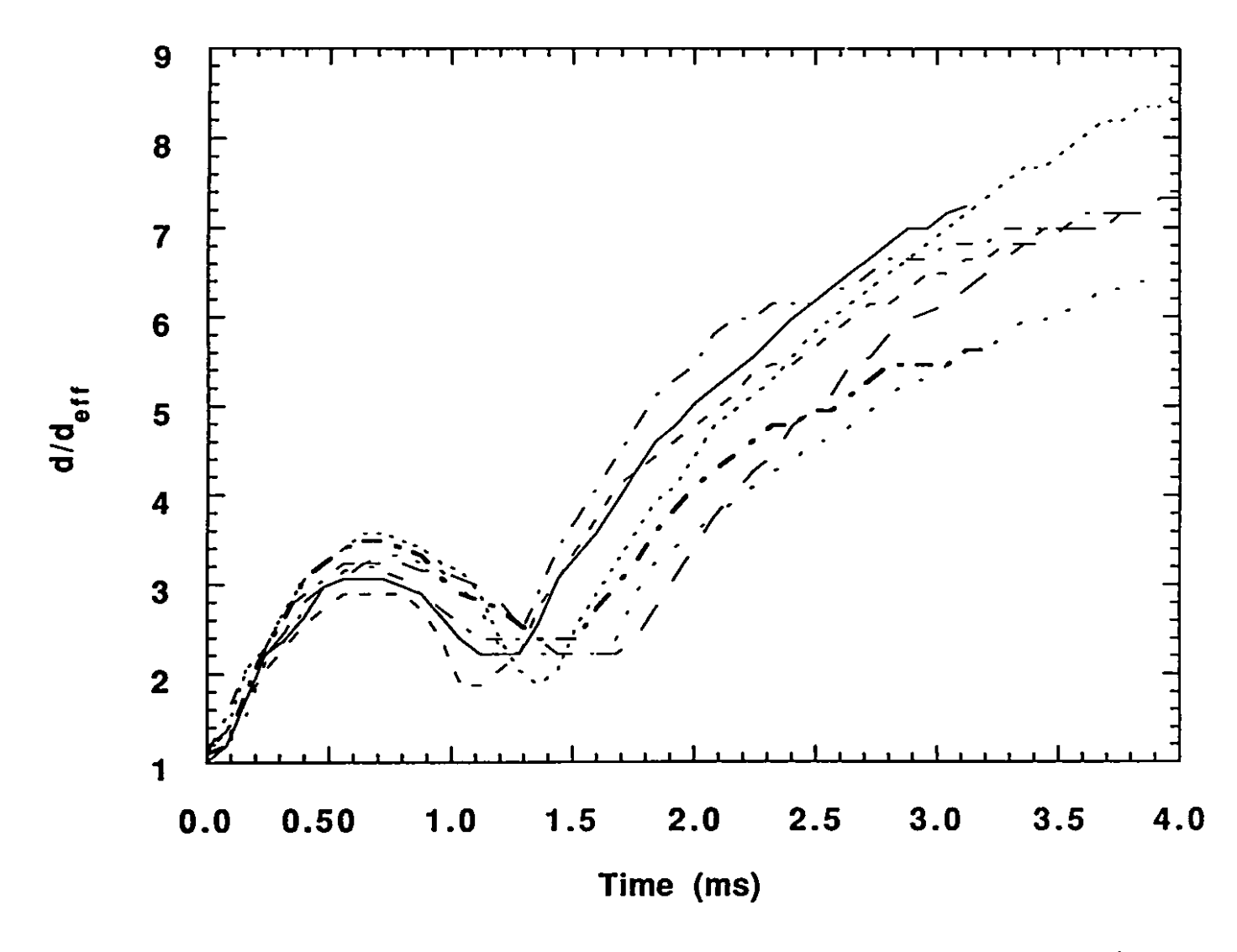


Figure 17: Bubble growth curves for seven different trials with 0.5 g tin drops at 700°C

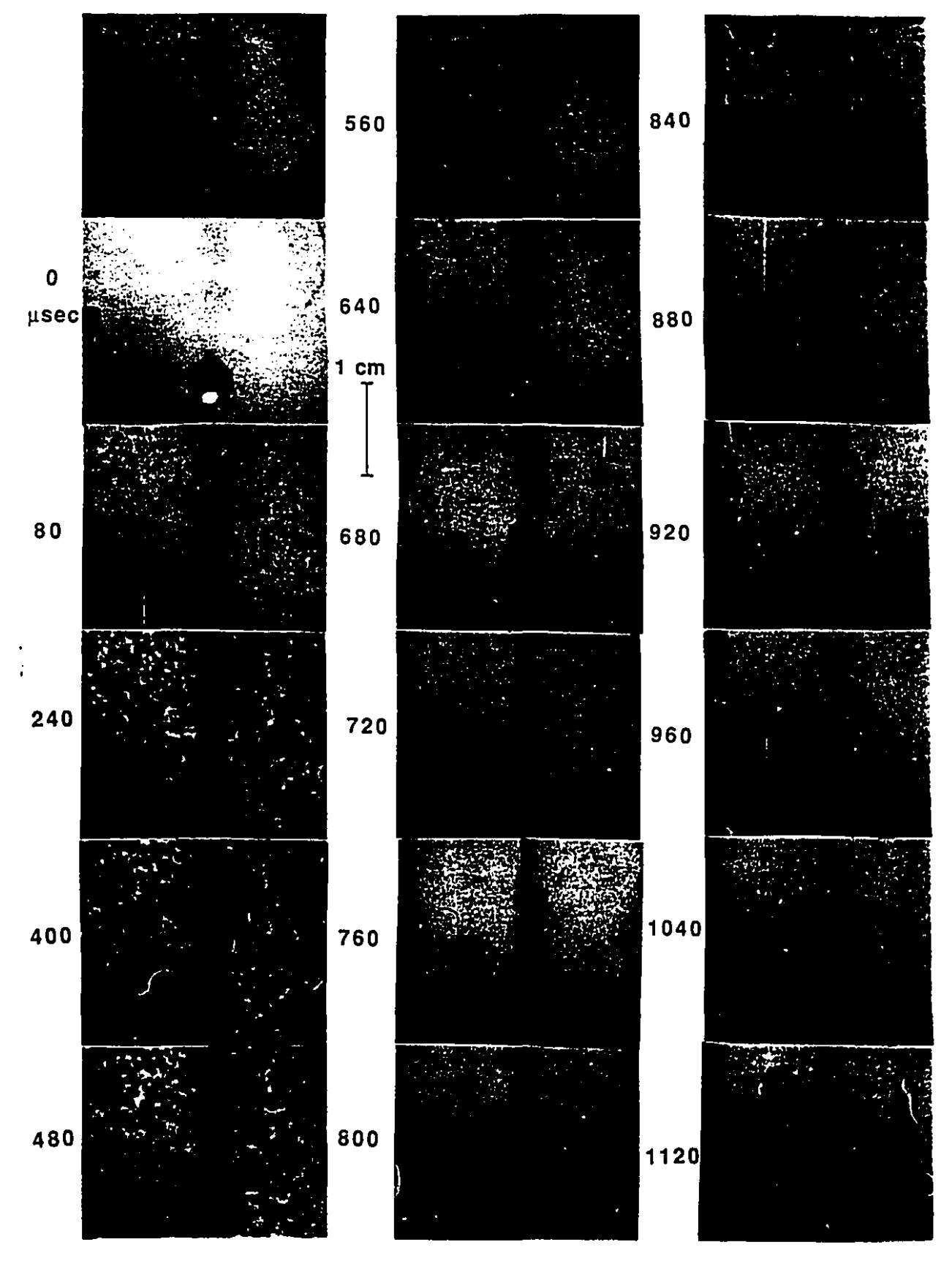


Figure 18: High-speed photographs of a the interaction of solid steel sphere at 750°C with a shock.



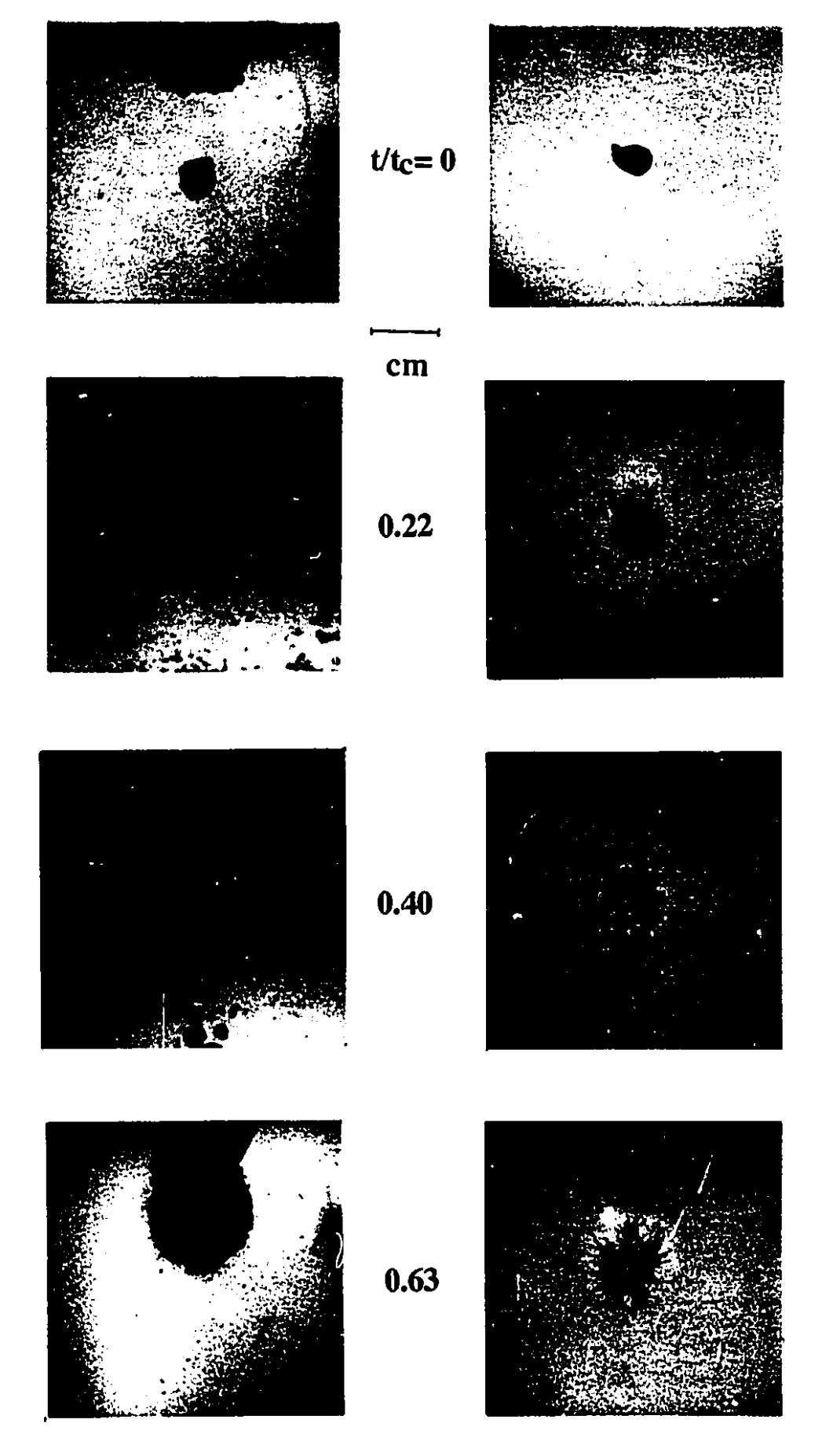


Figure 19: Simultaneous x-ray radiographs (on the right) and regular photographs (on the left) of the vapor explosion of 0.5 g tin drops initially at 700° C. The times given are normalized with $t_{\rm C}$, the time required for the collapse of the first bubble.

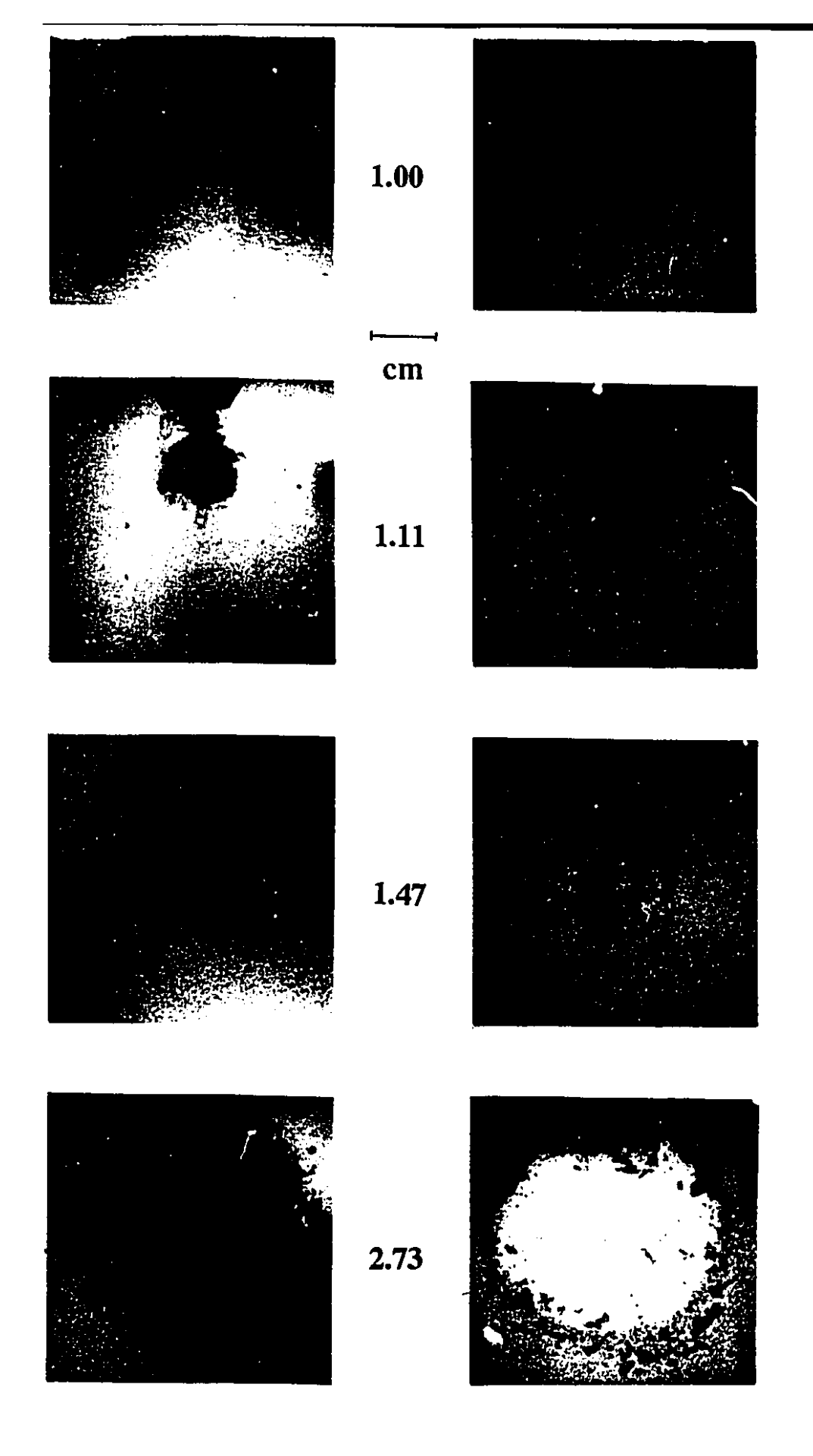


Figure 19 continued

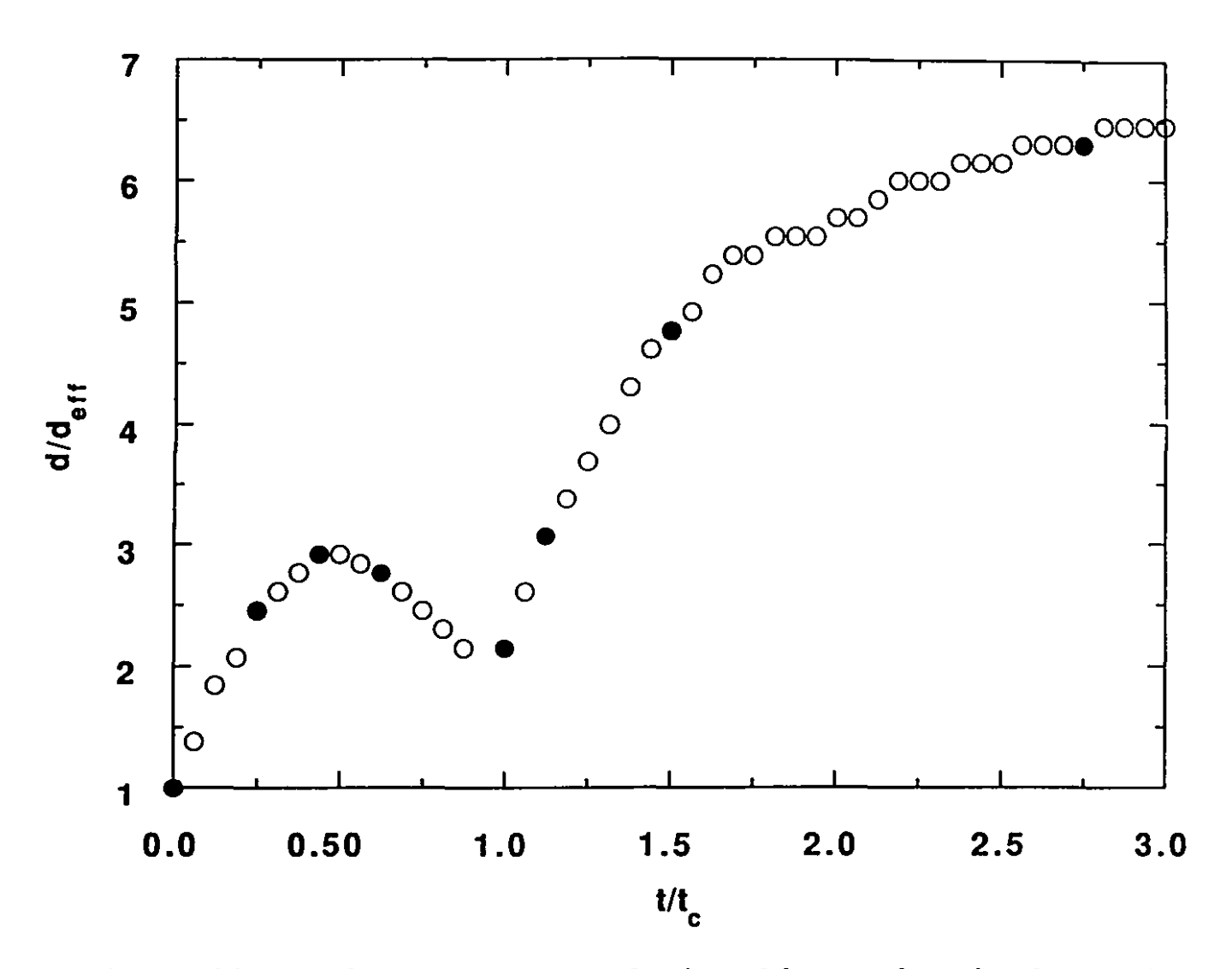


Figure 20: Radial bubble growth time history for tin drops shown in Fig. 19. Solid circles indicate photographs shown in Fig. 19

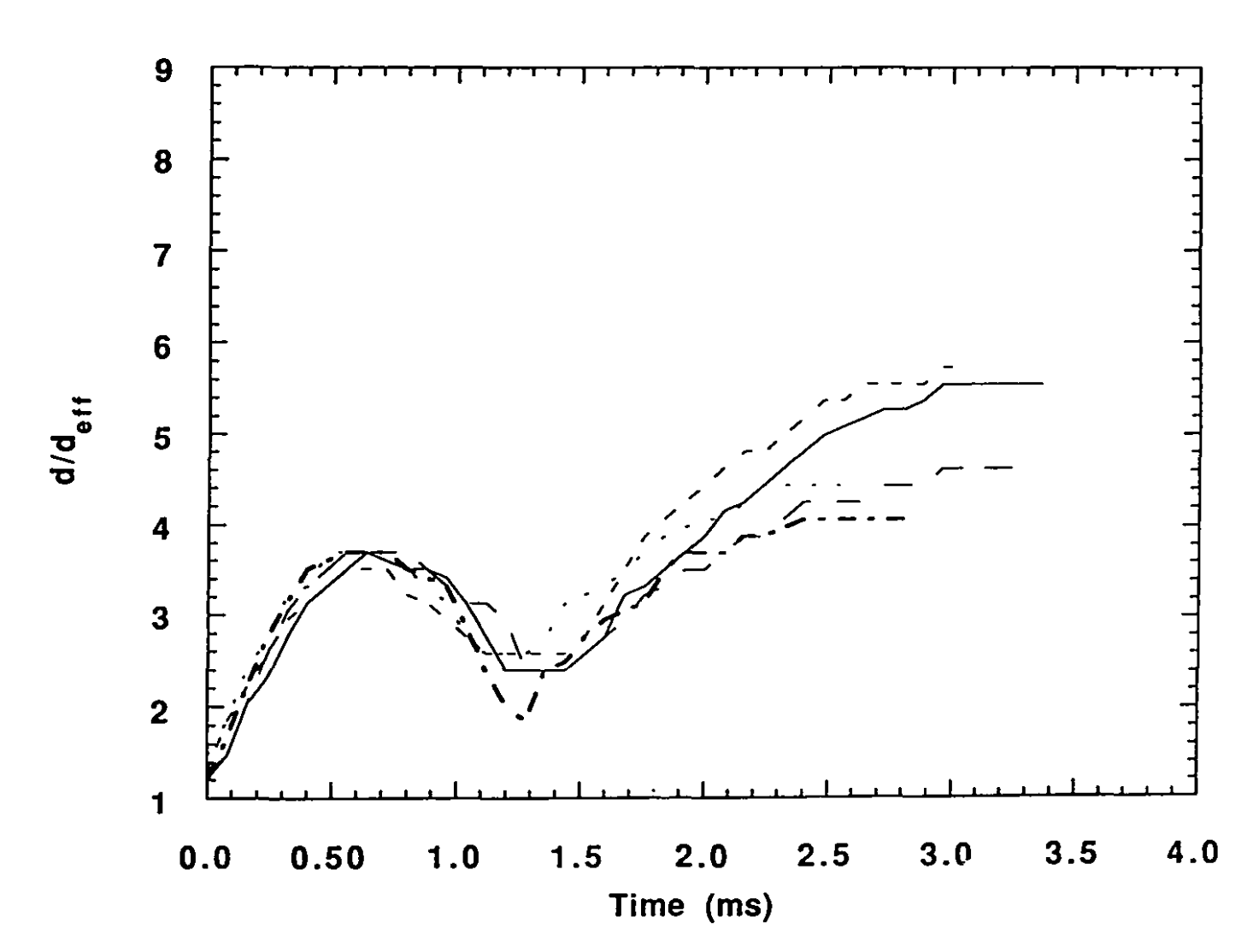


Figure 21: Bubble growth curves for 5 different trials with 0.5 g cerrolow alloy drops at 700°C

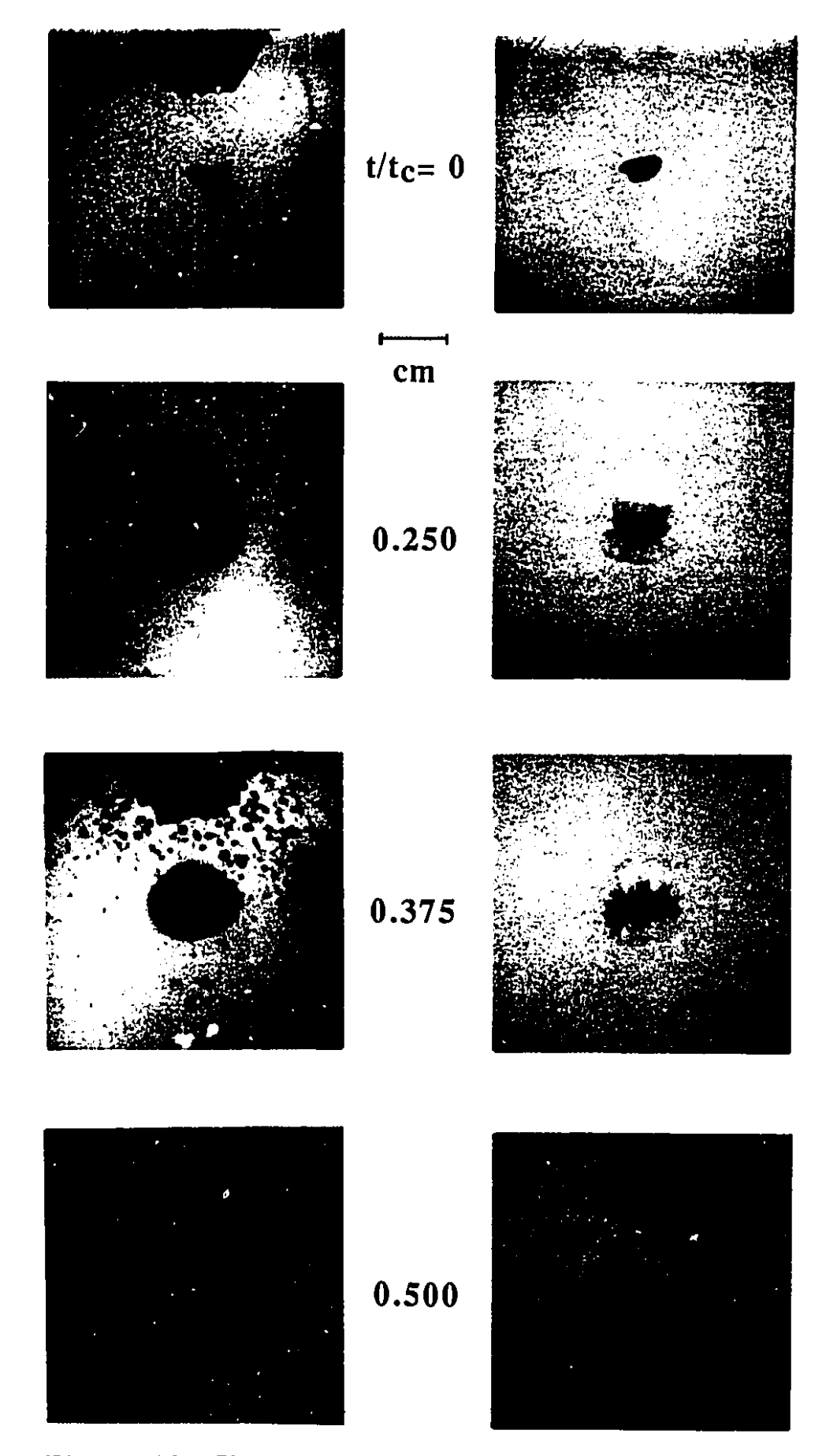
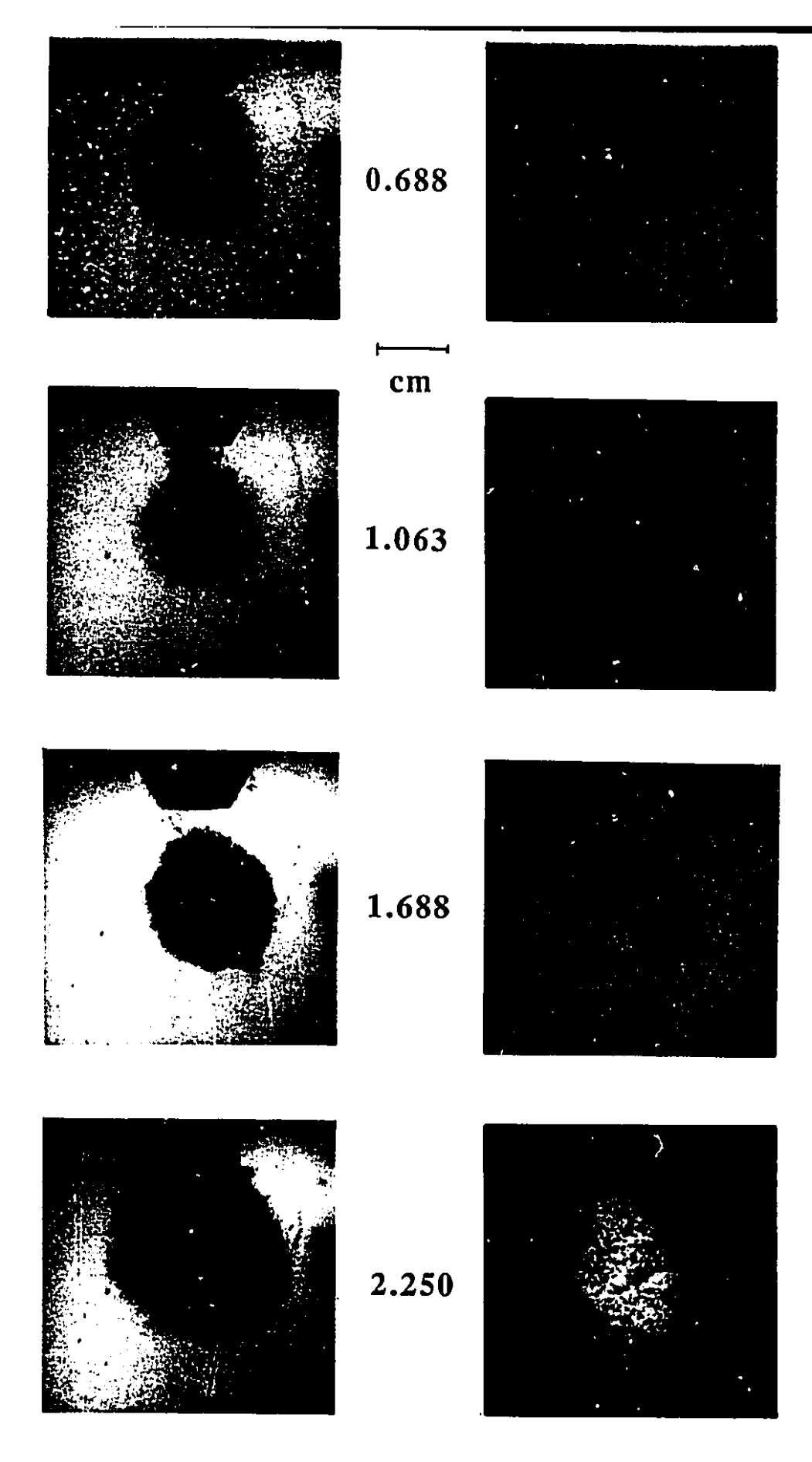


Figure 22: Simultaneous x-ray radiographs (on the right) and regular photographs (on the left) of the vapor explosion of 0.5 g alloy drops initially at 700° C. The times given are normalized with $t_{\rm C}$, the time required for the collapse of the first bubble.



1

Figure 22 continued

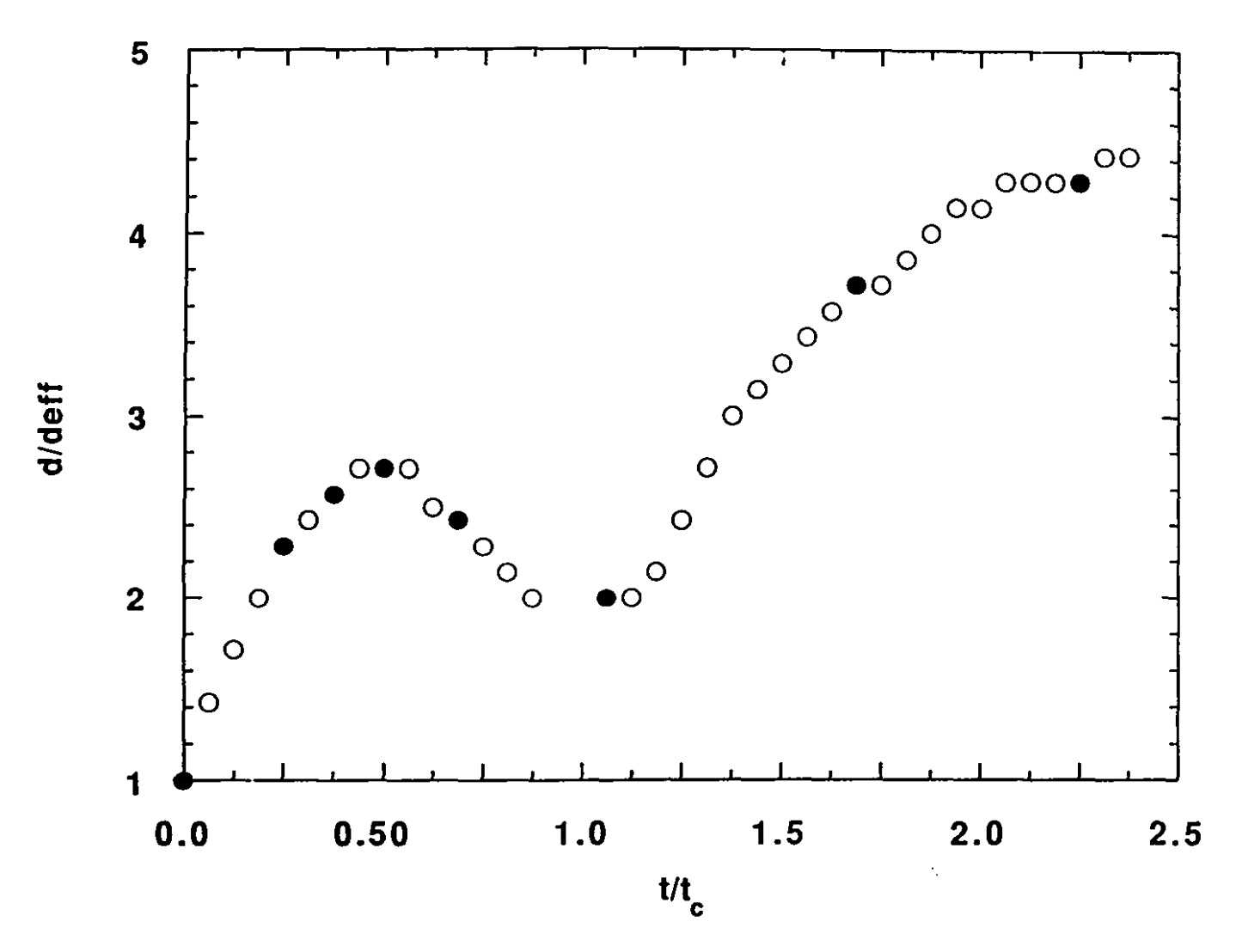


Figure 23: Radial bubble growth time history for alloy drops shown in Fig. 22. Solid circles indicate photographs shown in Fig. 22

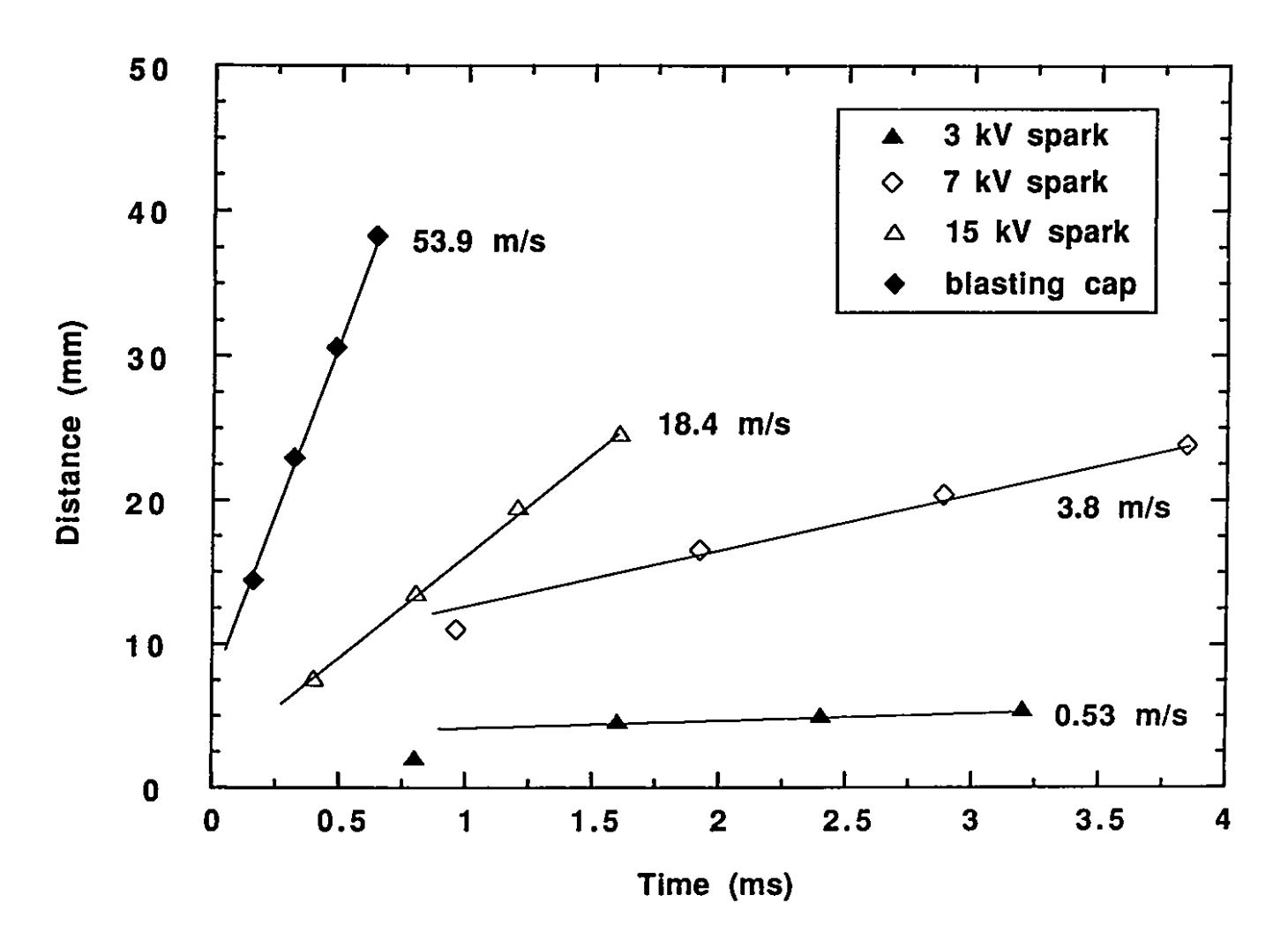


Figure 24: Trigger bubble surface position time history for different trigger strengths

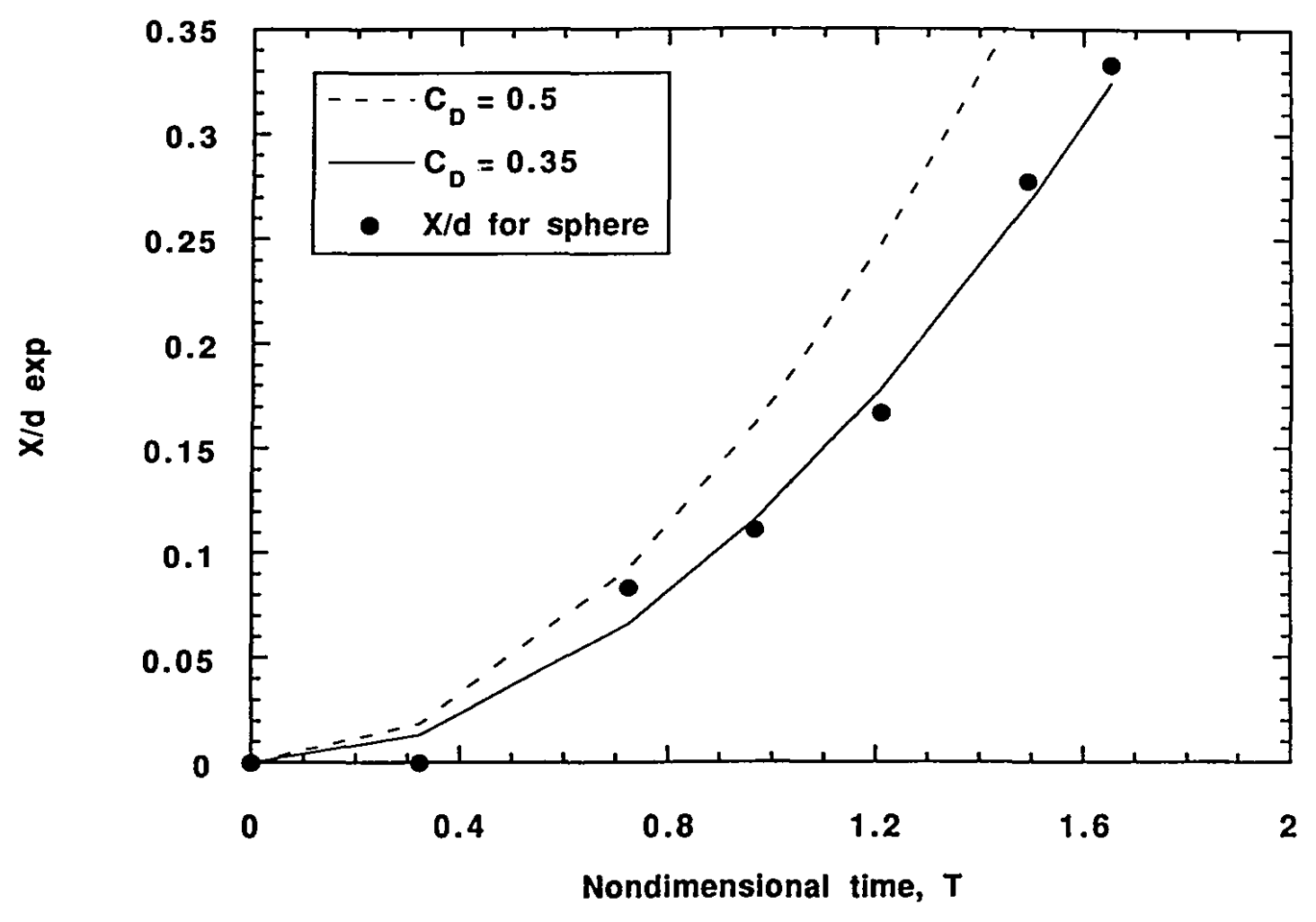
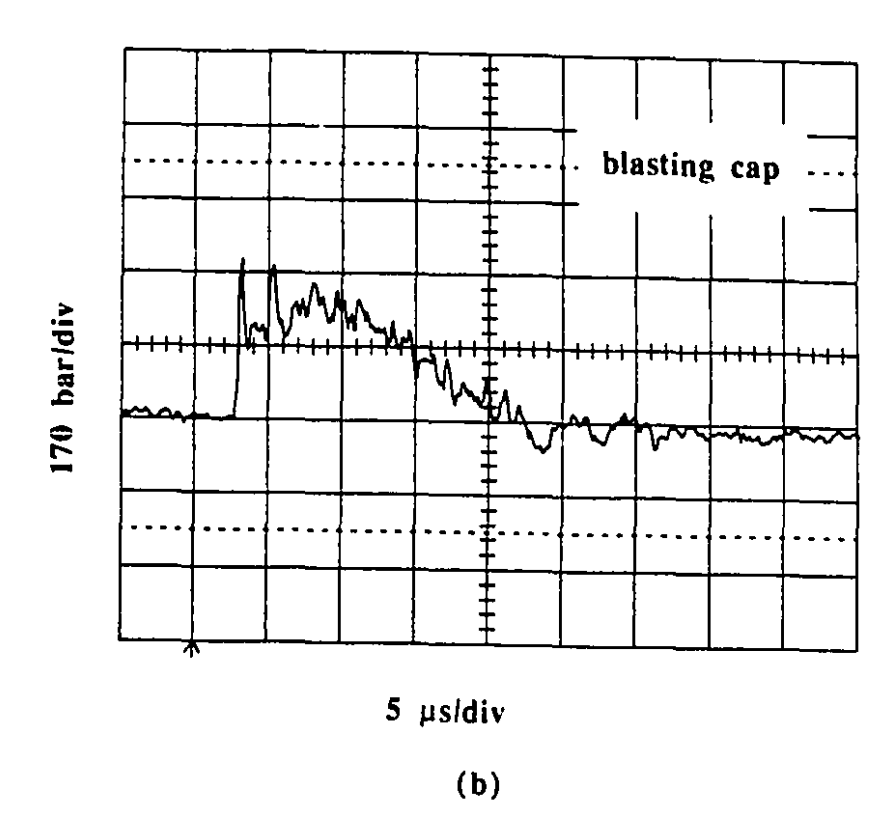


Figure 25: Experimentally measured solid sphere displacement versus normalized time and calculated sphere trajectory for a drag coefficient of 0.35 and 0.5, shown as solid lines



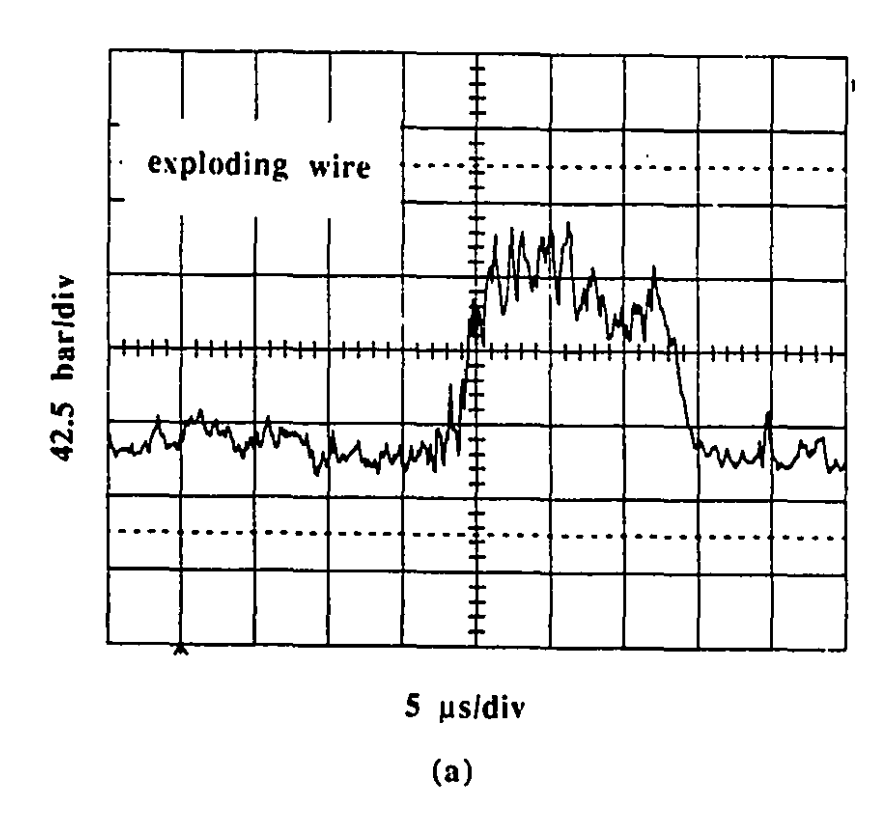


Figure 26: Pressure traces obtained at drop location for (a) exploding wire discharge, $8\mu f$ capacitor charged to 12~kV (b) blasting cap

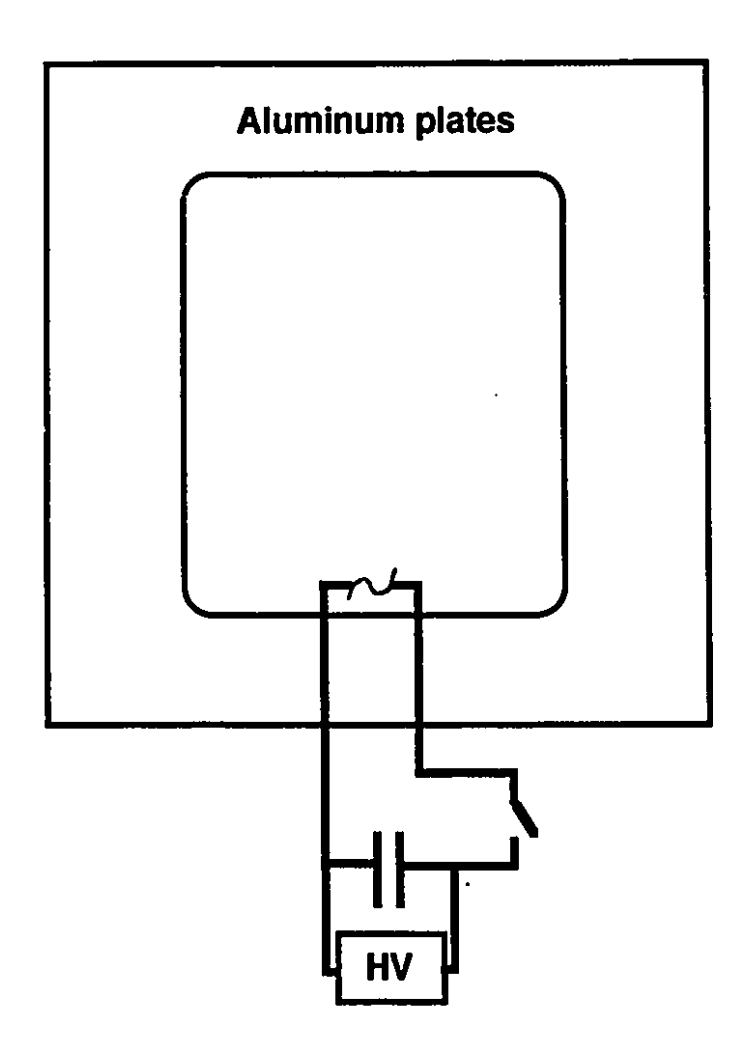
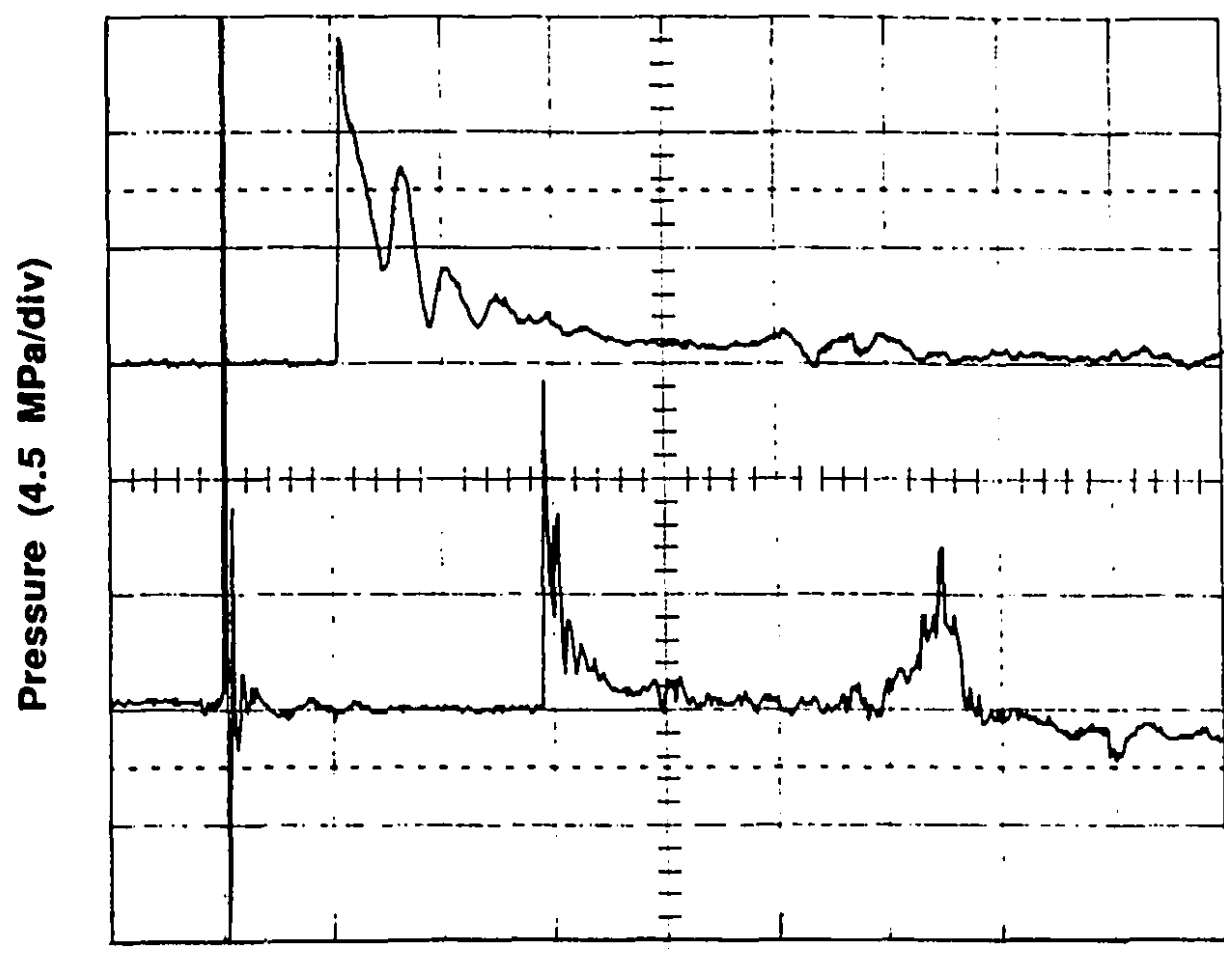


Figure 27: Schematic showing experimental set up for experiments looking at the effect of shock overpressure



Time (upper trace: 5 μ s/div, lower trace: 20 μ s/div)

Figure 28: Pressure trace (the trace is shown twice with two different time scales) recorded at the drop location for a 12 kV charge of an 8 μ f capacitor charge

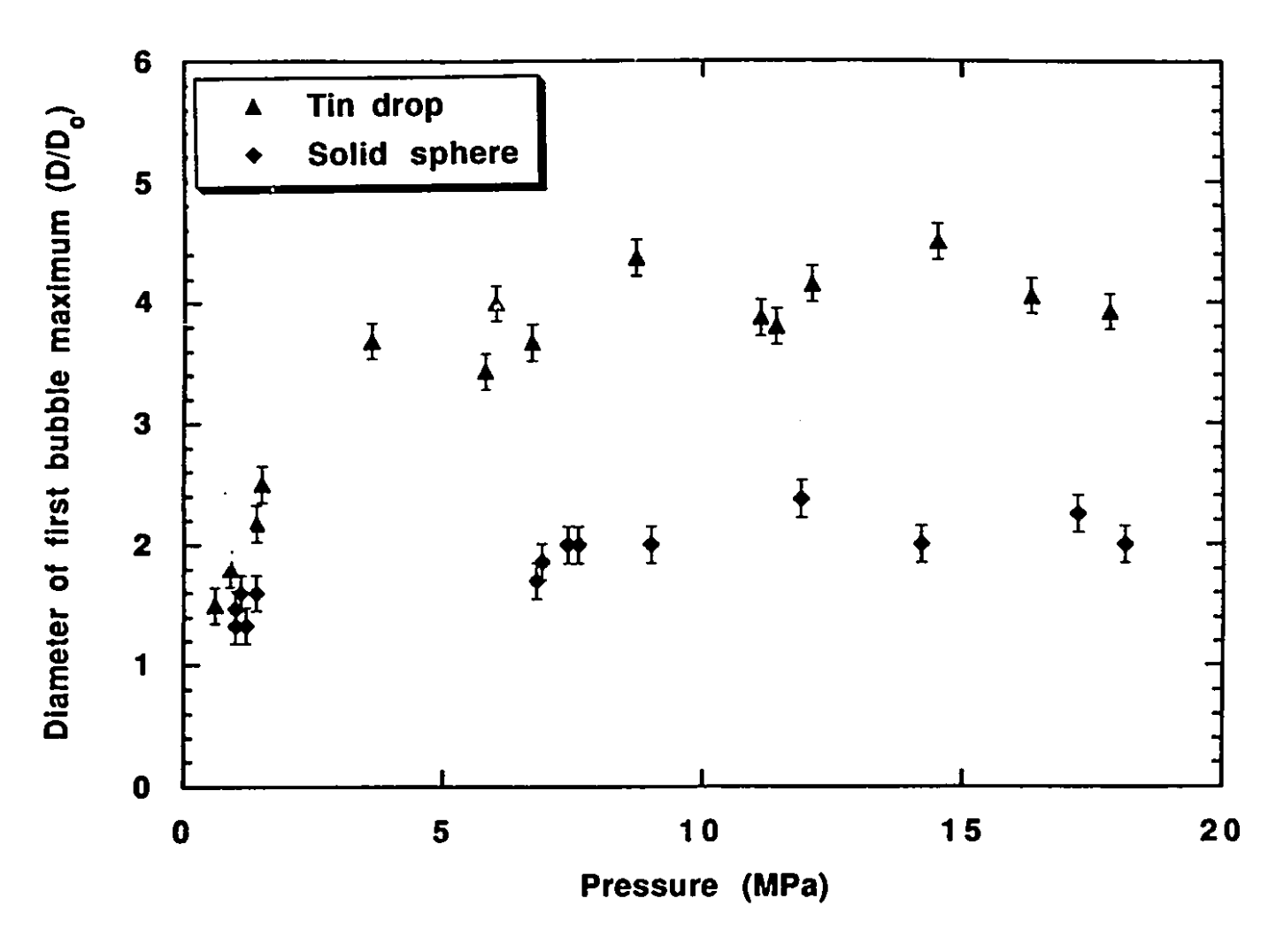


Figure 29: Variation in the first bubble maximum estimated for tin drops and a solid sphere as a function of the shock overpressure



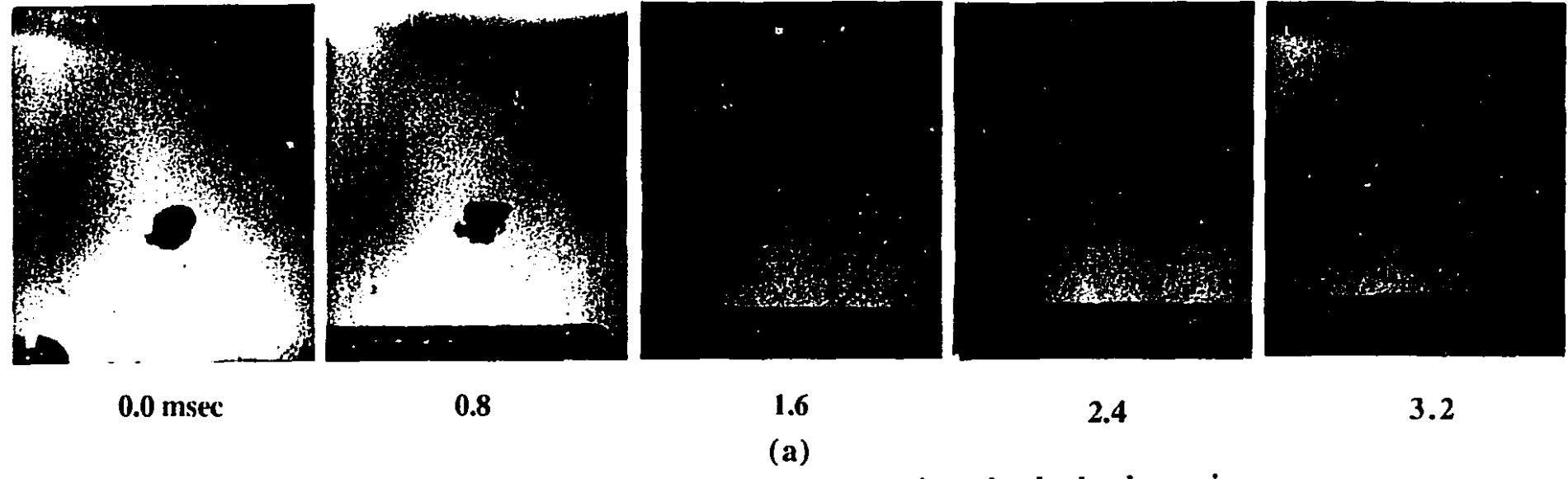
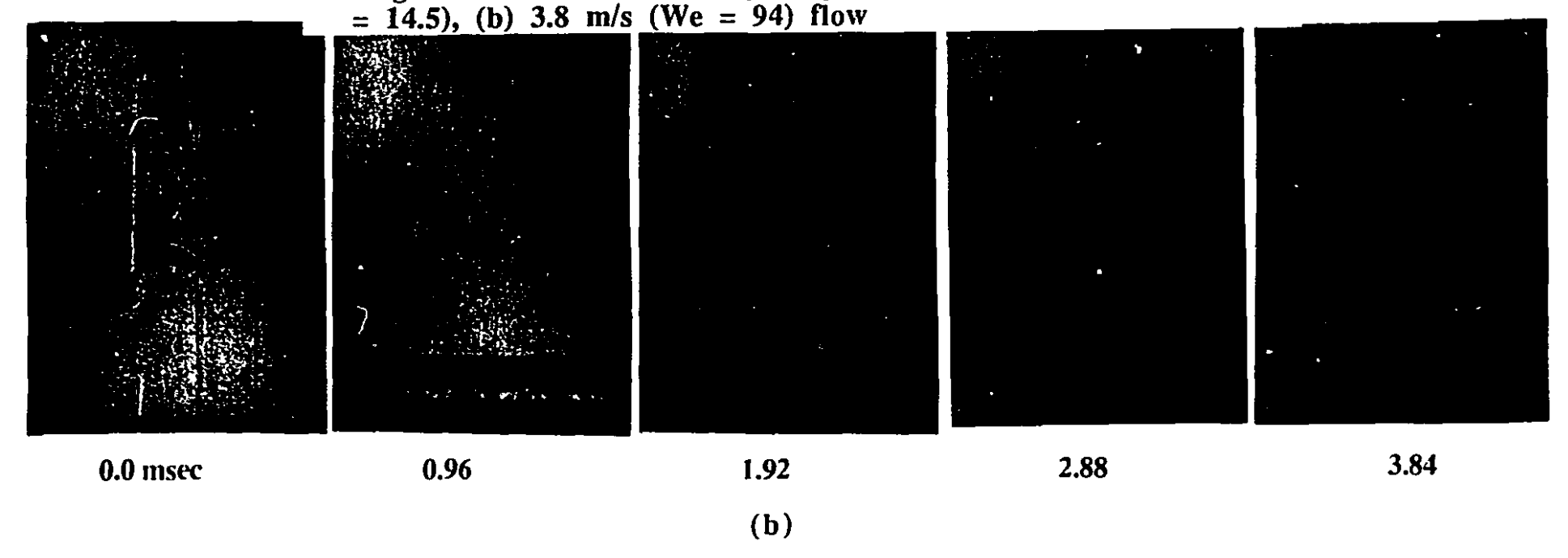
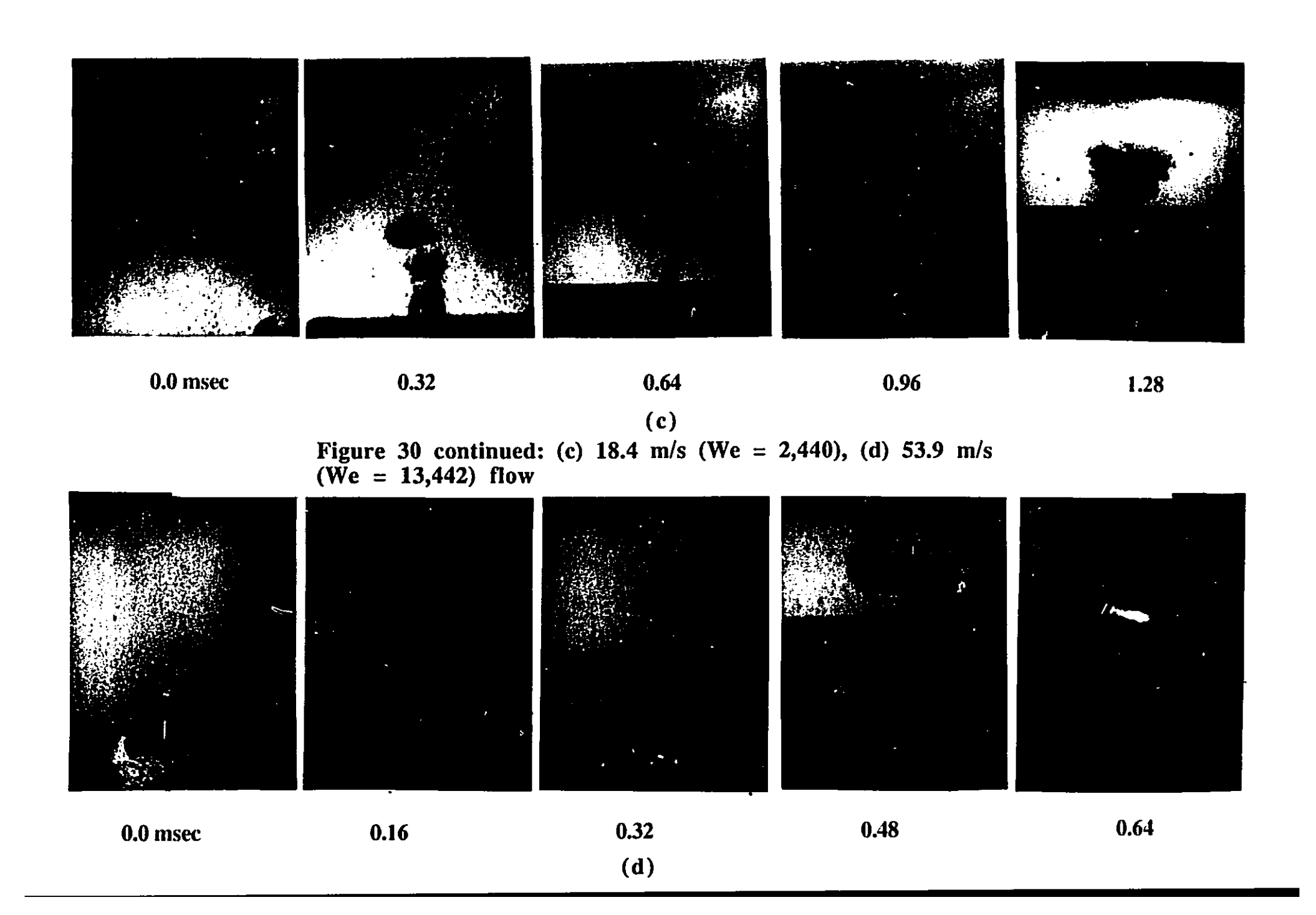


Figure 30: Photographic sequence showing the hydrodynamic fragmentation of a cold alloy drop at 60° C in a (a) 0.5 m/s (We = 14.5), (b) 3.8 m/s (We = 94) flow









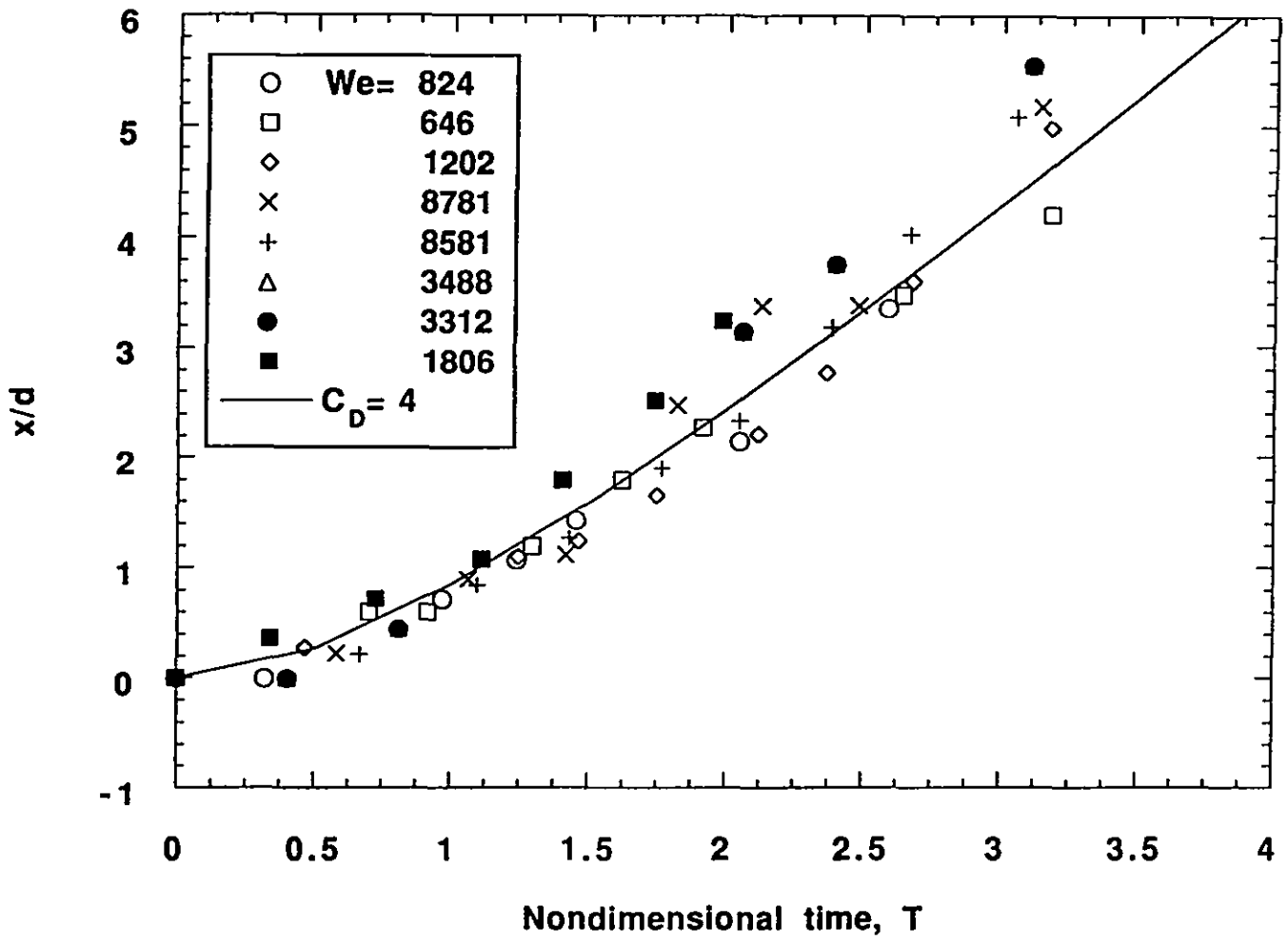


Figure 31: Dimensionless drop displacement versus nondimensional time for cold gallium drop experiments and calculated trajectory for a drag coefficient of 4, shown as a solid line

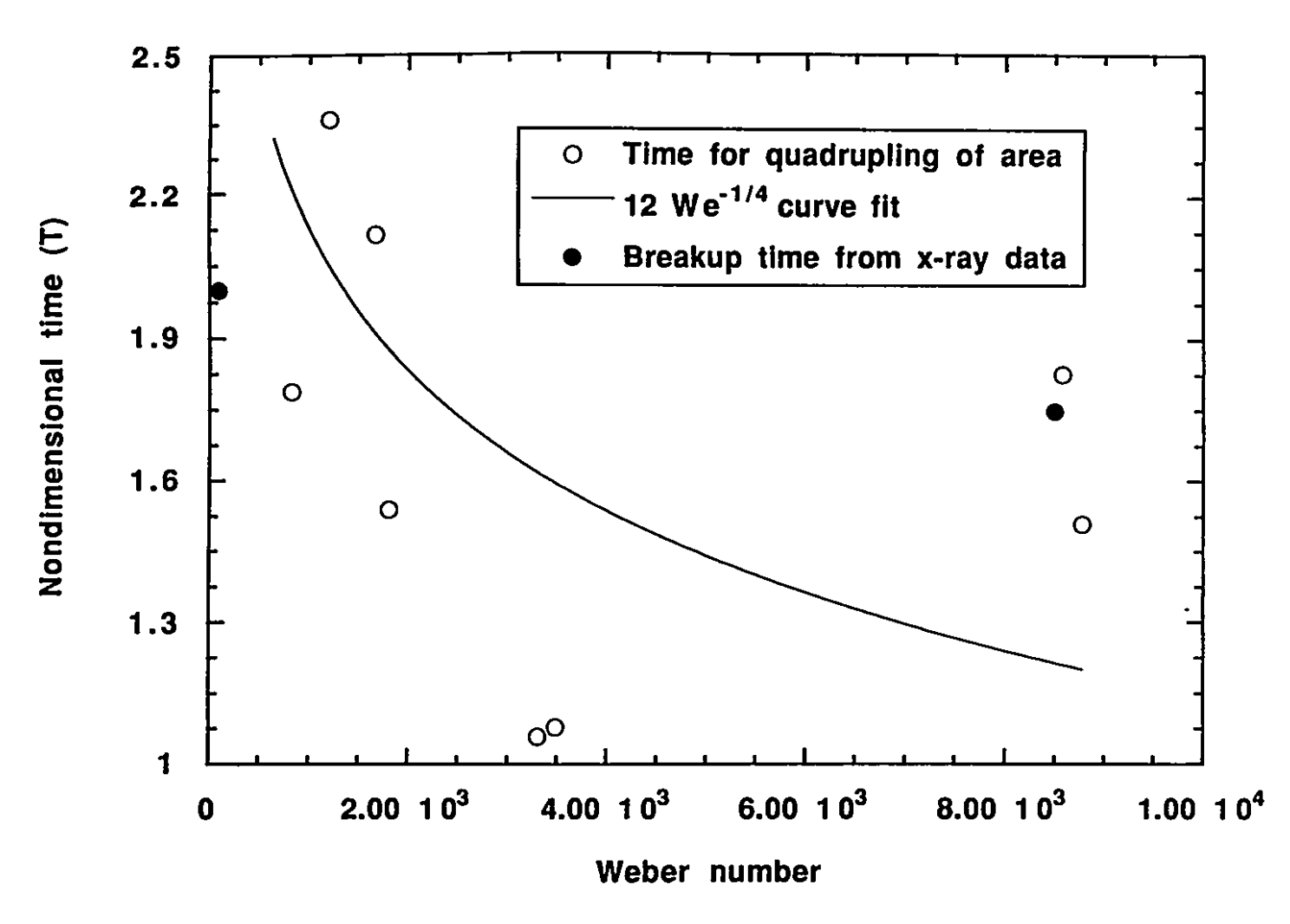


Figure 32: Nondimensional time for the quadrupling of the fragmentation cloud projected area from the photographic results of the cold drop gallium experiments

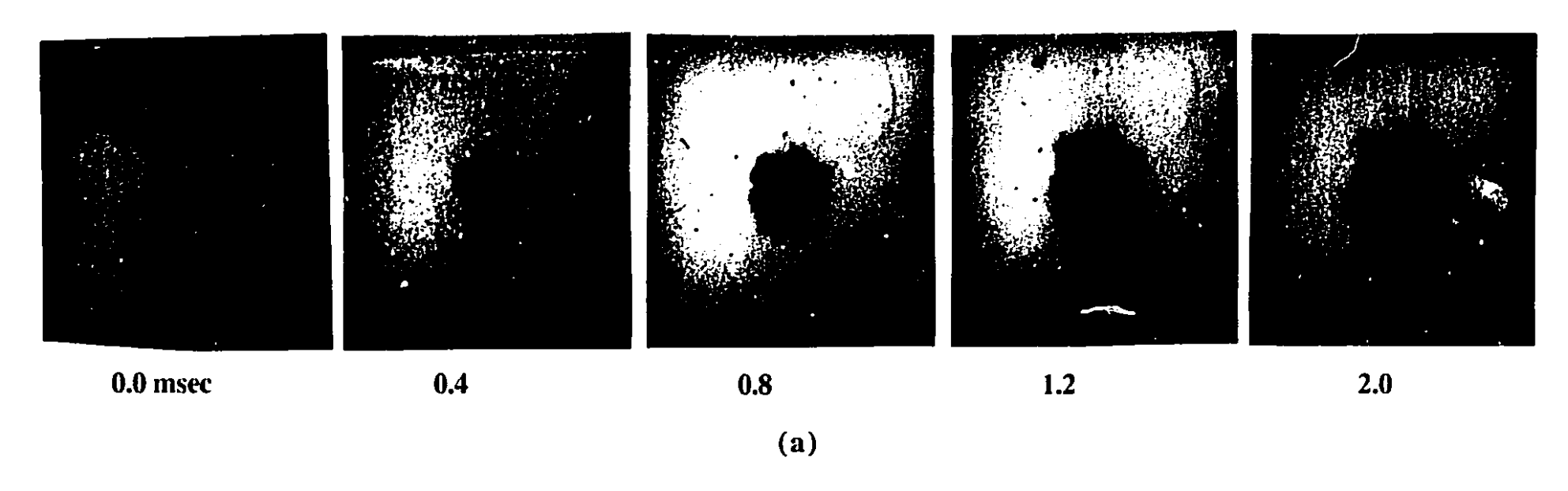
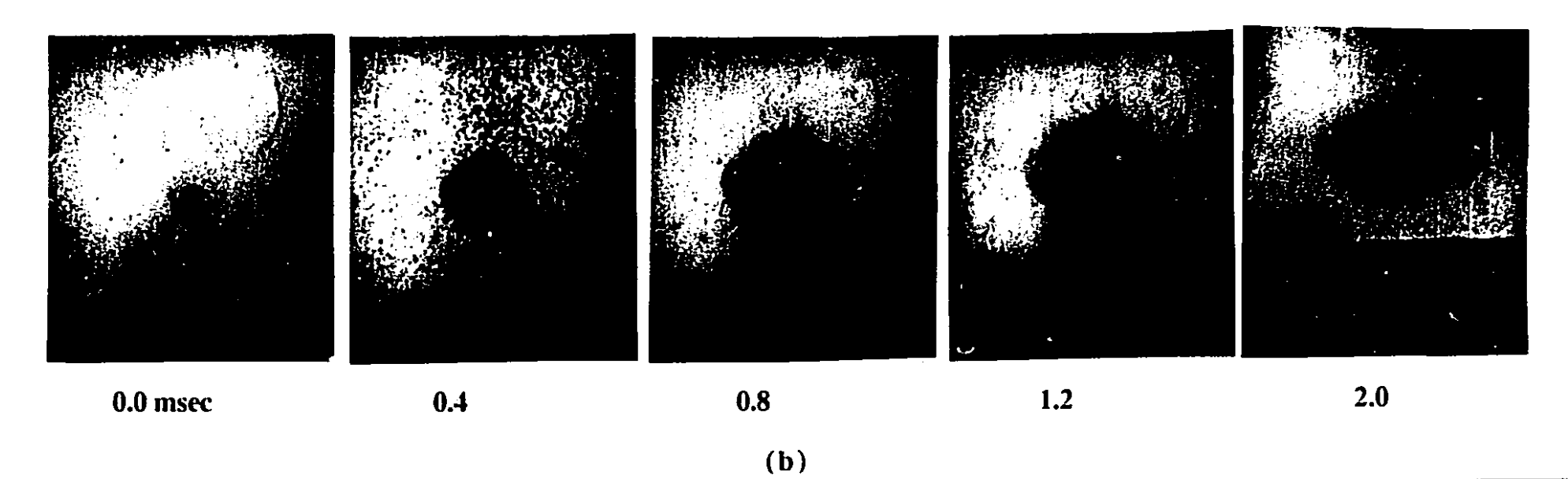
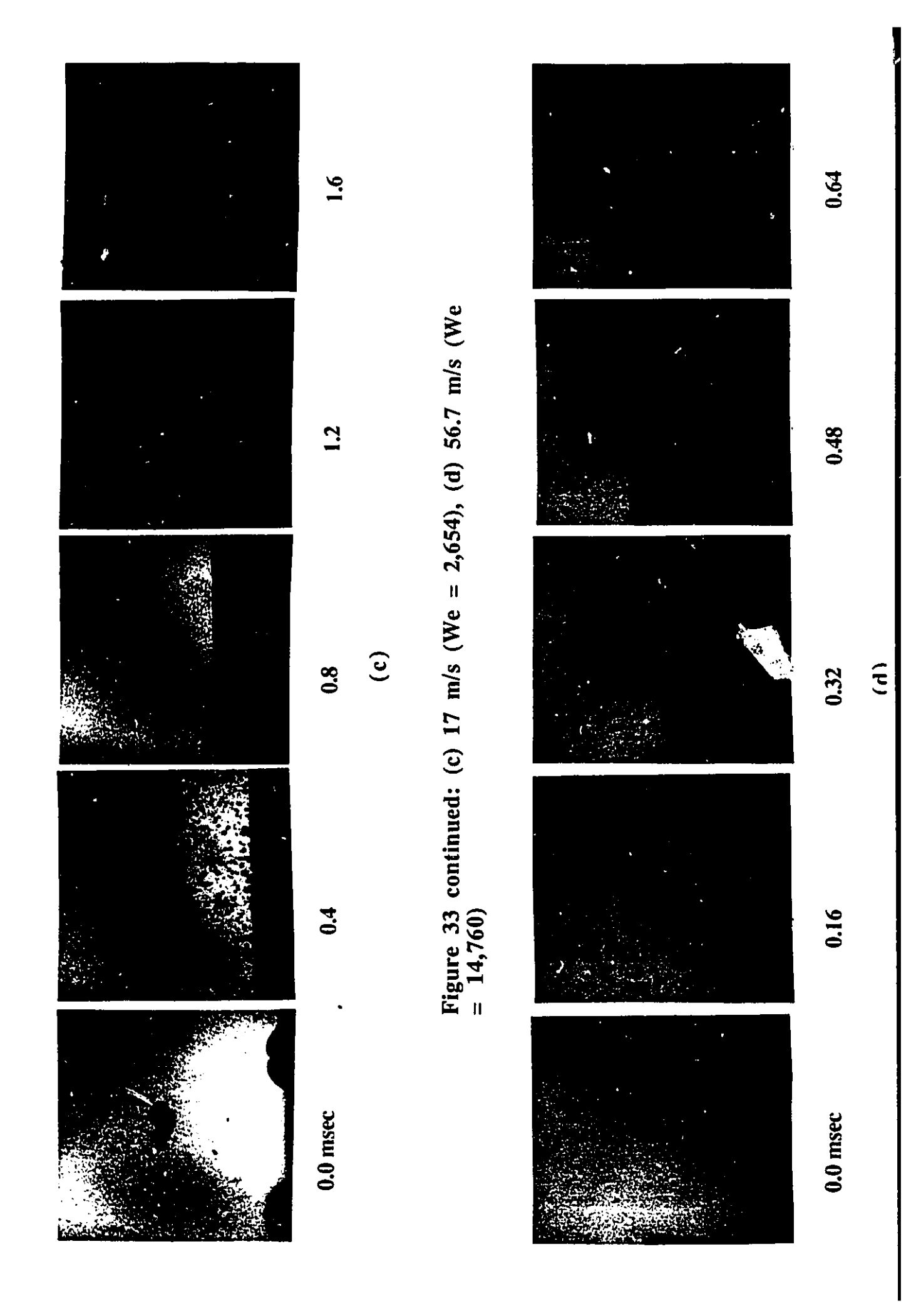


Figure 33: Photographic sequence showing the interaction of an alloy droplet at 700° C in water at 60° C. Water flow velocity is (a) 0.5 m/s (We = 14.5), (b) 4.8 m/s (We = 186)





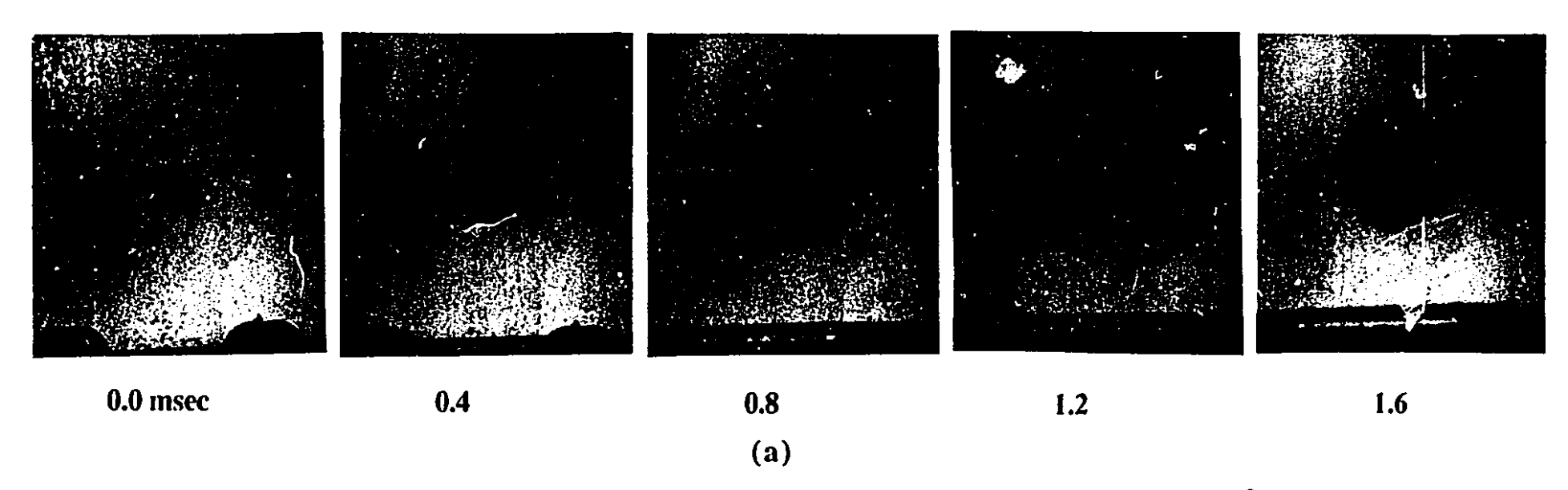
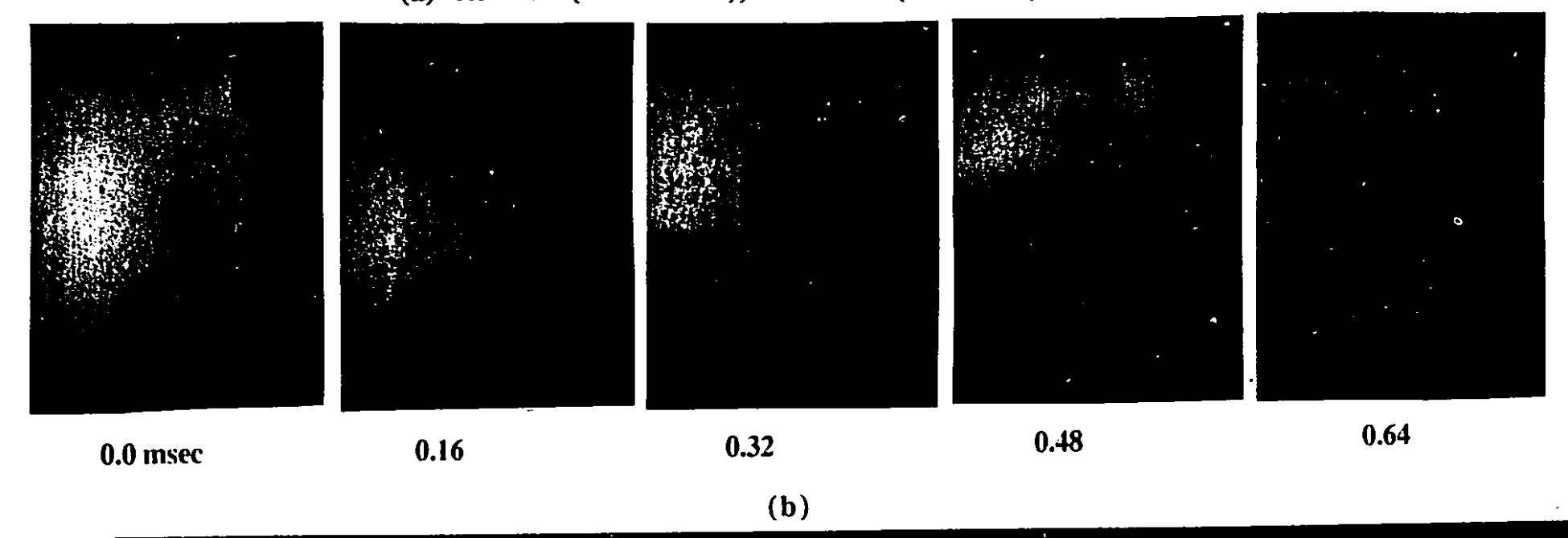


Figure 34: Photographic sequence showing the interaction of a tin droplet at 700°C in water at 60°C. Water flow velocity is (a) 0.5 m/s (We = 14.5), 51.4 m/s (We = 18,500)



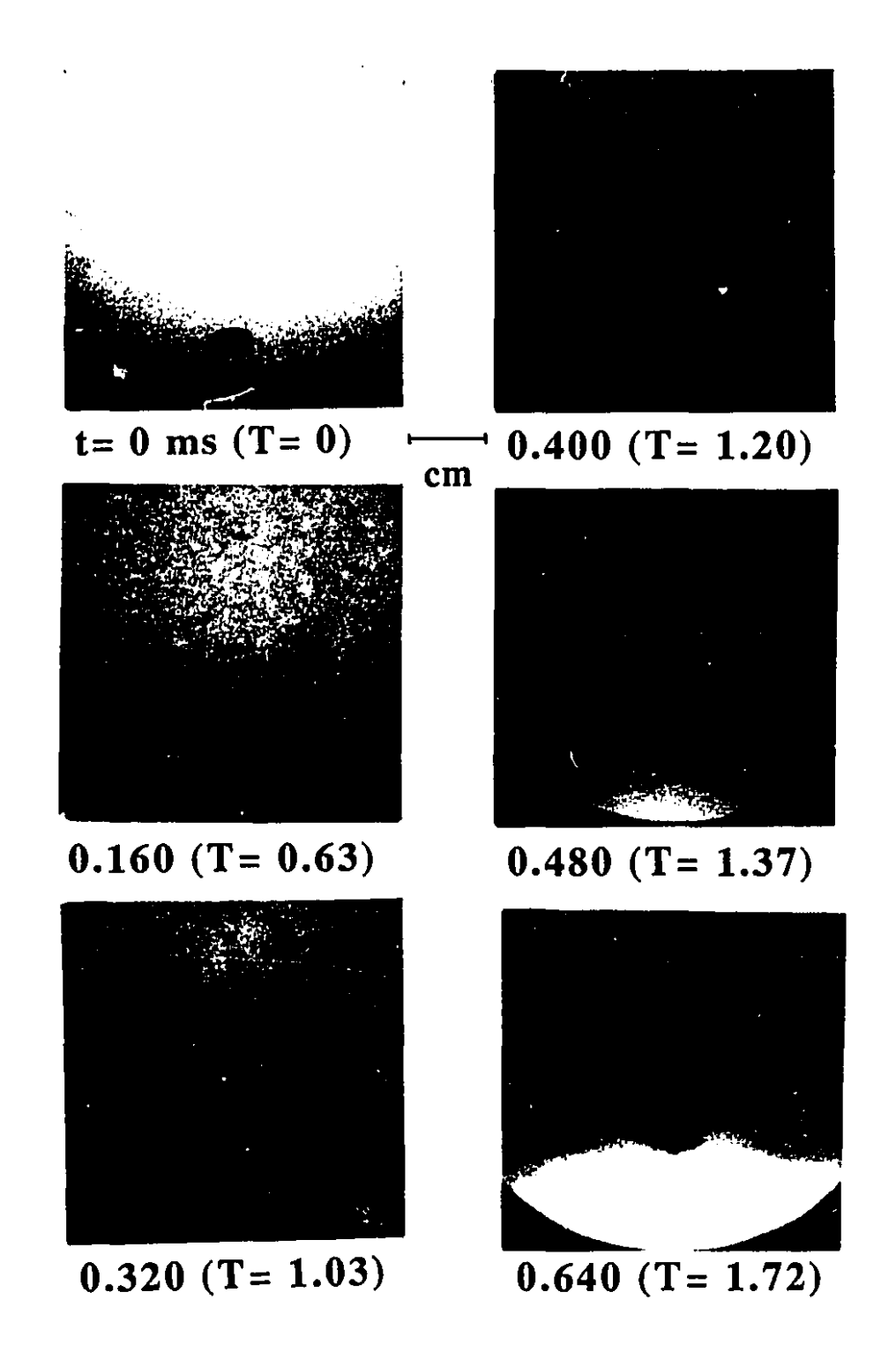


Figure 35: Sequence of radiographs showing the interaction of a cold alloy drop at 60° C in 40 m/s (We = 8,500) flow.

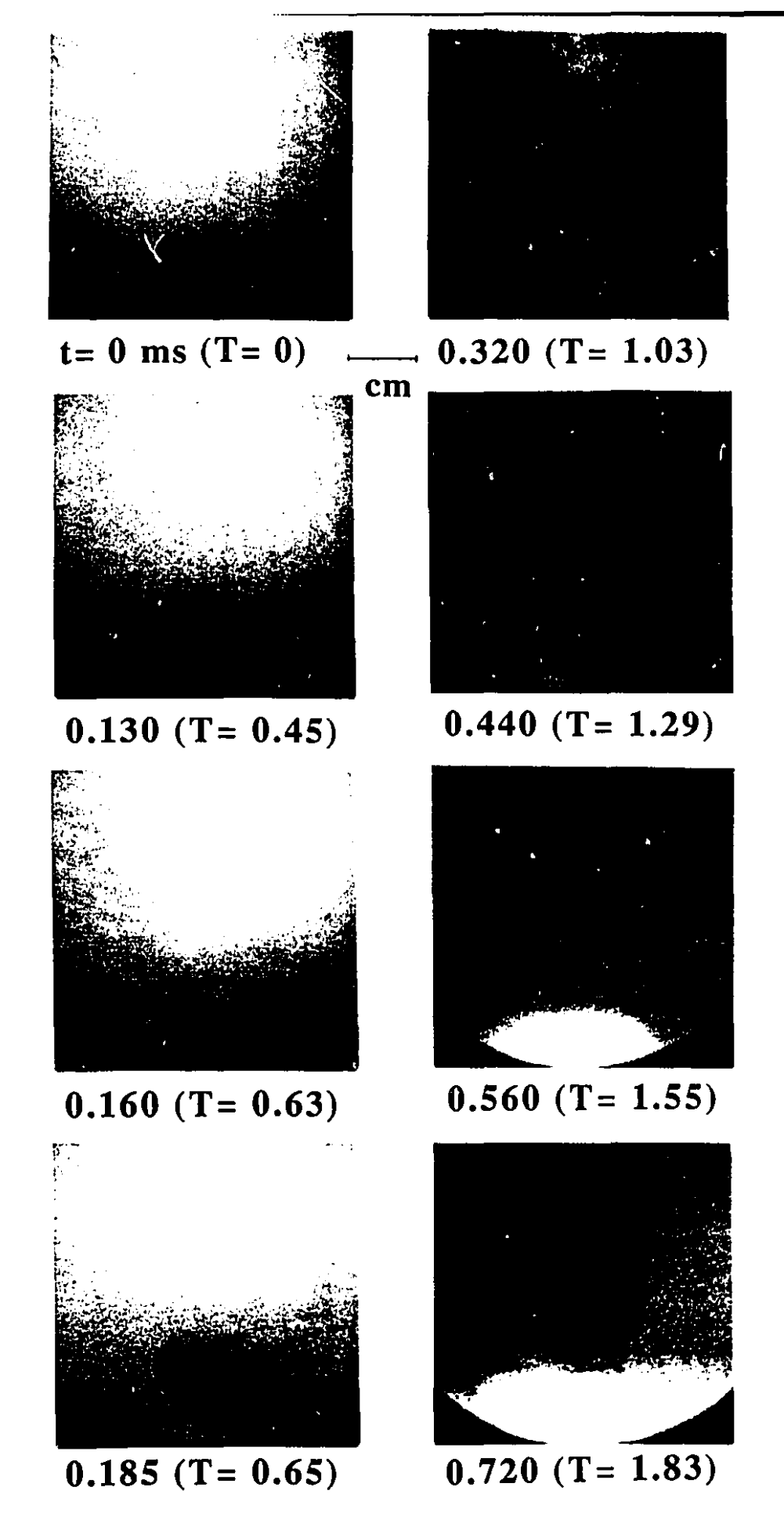
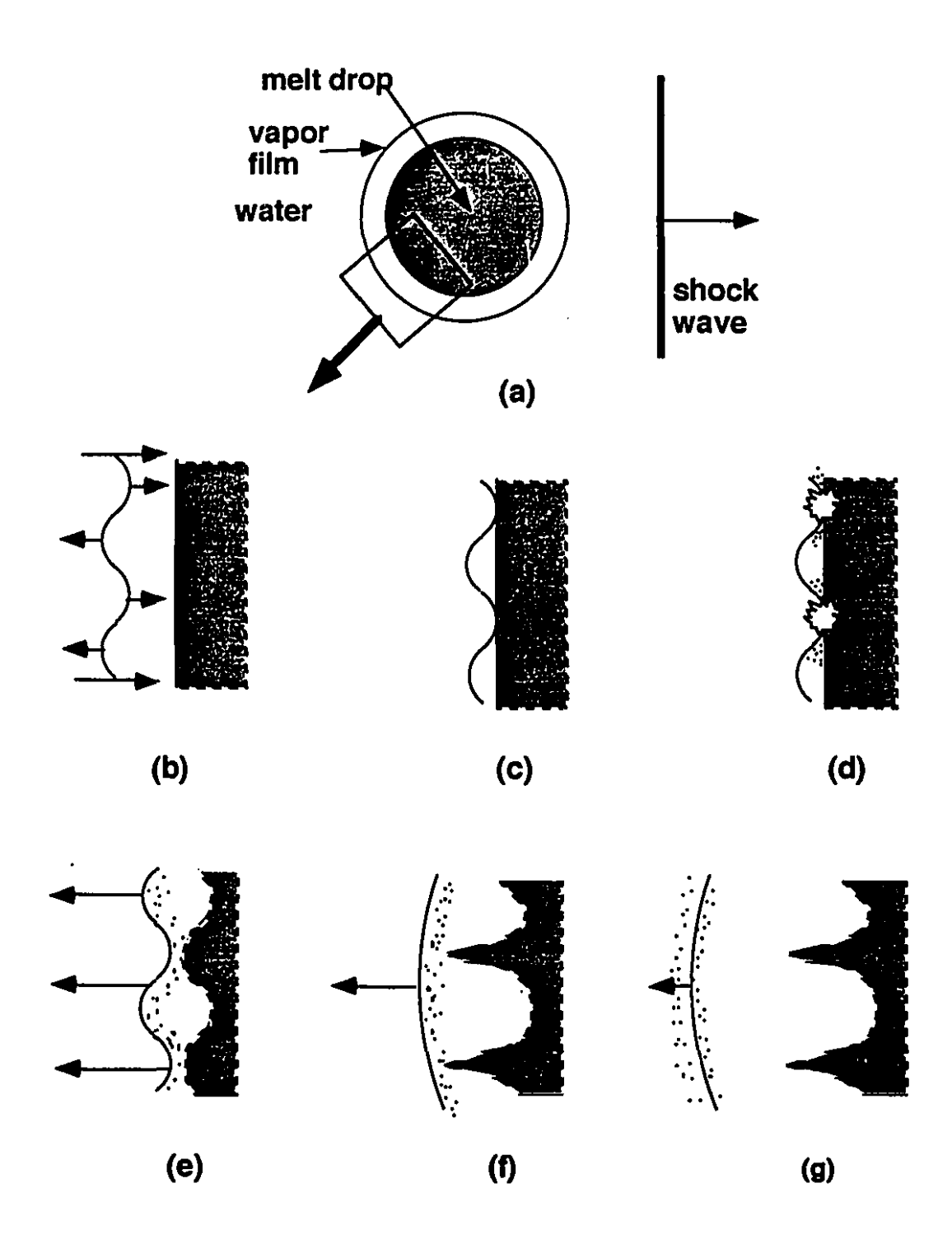
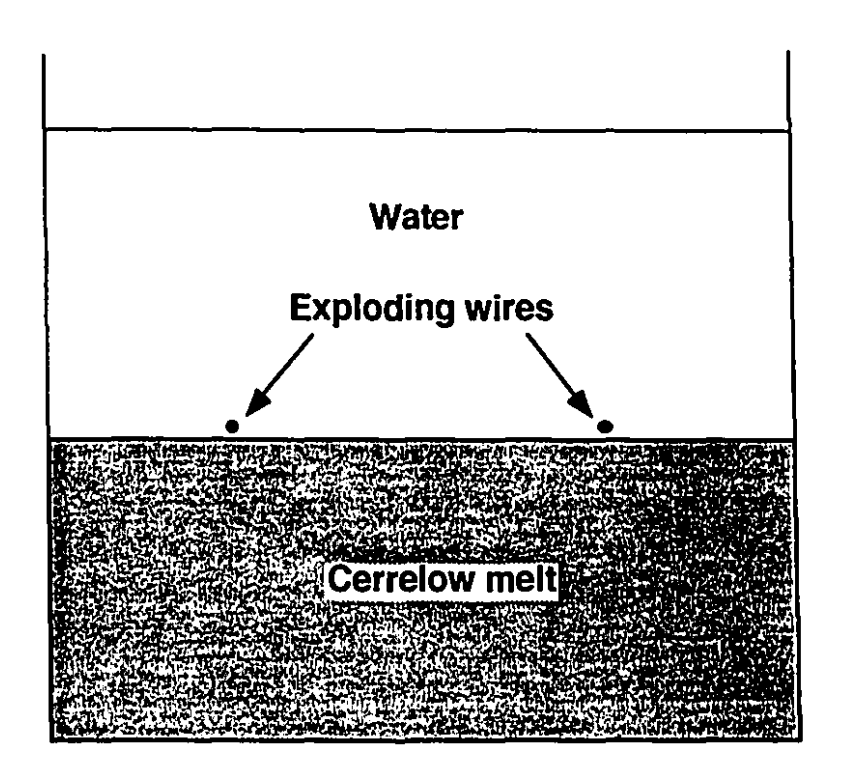


Figure 36: Sequence of radiographs showing the interaction of a tin droplet at 700°C in water at 60°C. Water flow velocity is 40 m/s (We = 8,500).

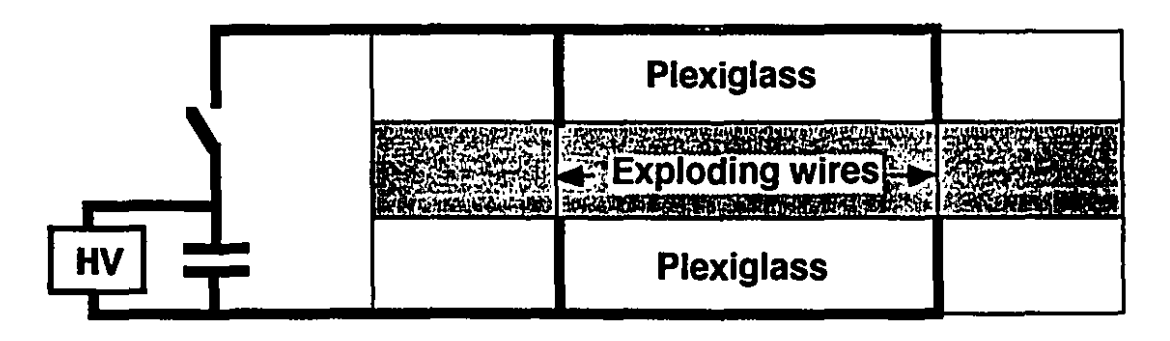


7 #3

Figure 37: Schematic of scenario for fragmentation of melt drop following film collapse.



Side view



Top view

Figure 38: Shematic of apparatus used in stratified layer experiments with local line pressurization

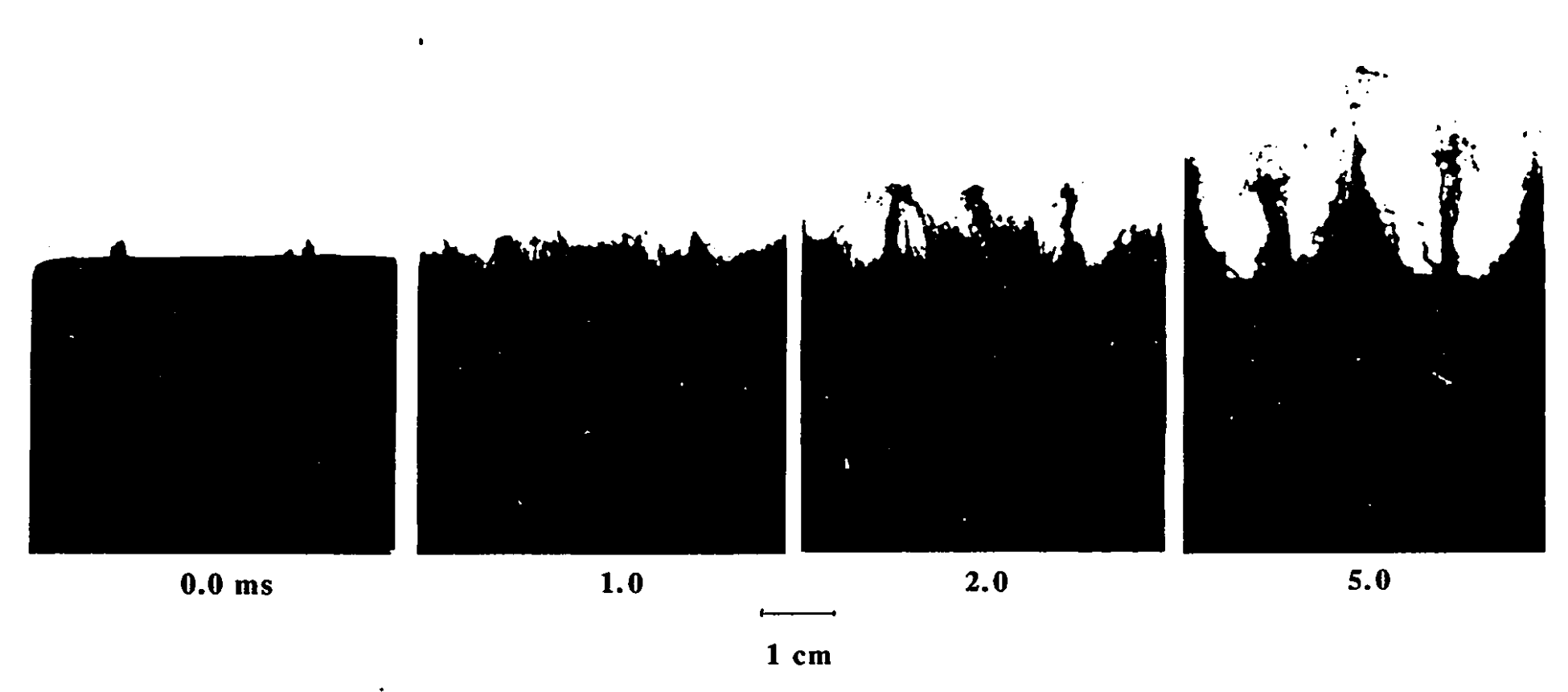
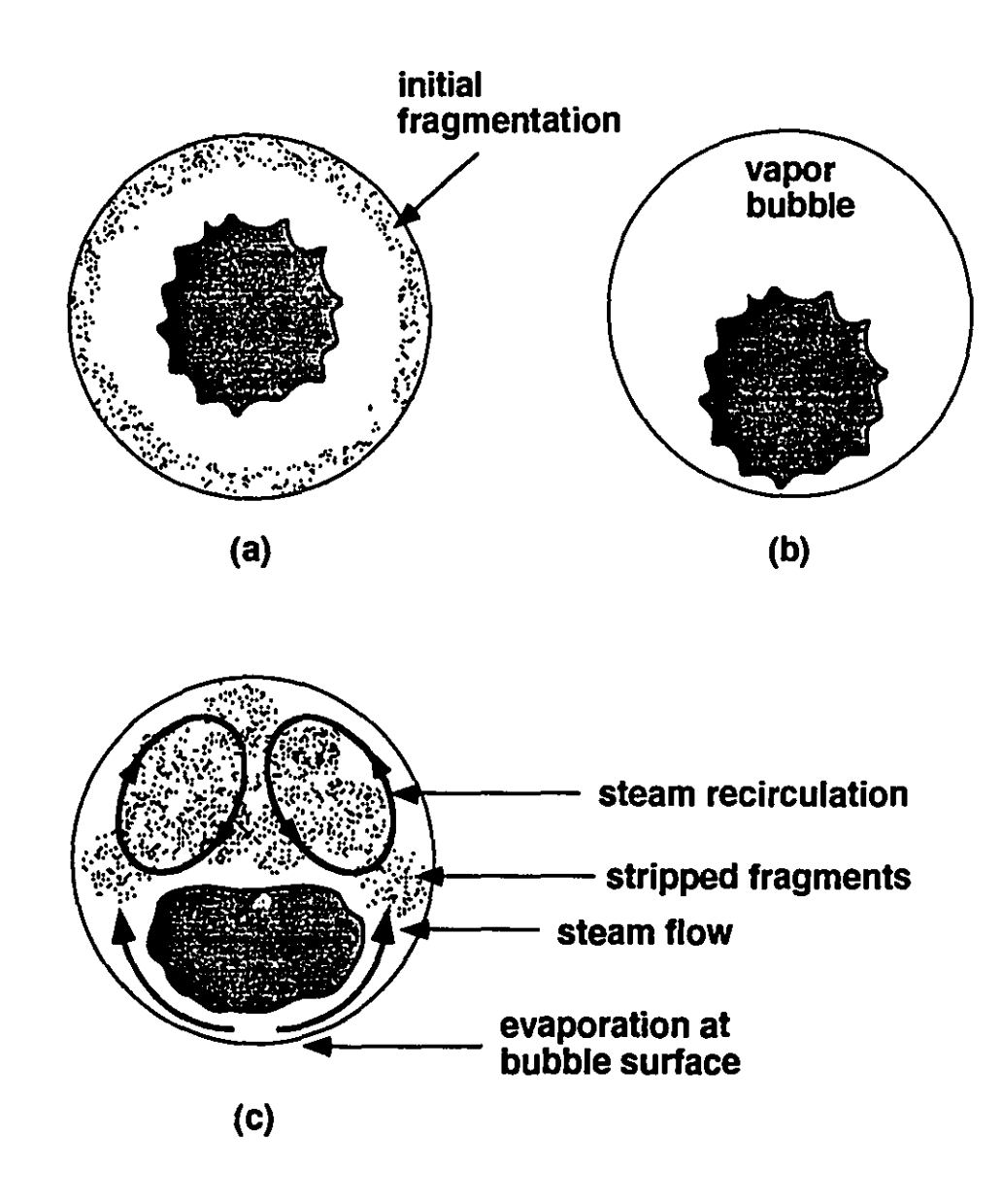


Figure 39: X-ray radiographs of the growth of disturbances at a liquid metal/water interface subject to rapid bubble growth at the interface at two locations. Two exploding wires, located 2.5 cm apart, are visible just above the surface of the metal in the first radiograph.



٦,

Figure 40: Physical picture showing the hot drop fragmentation process in the presence of a strong external flow

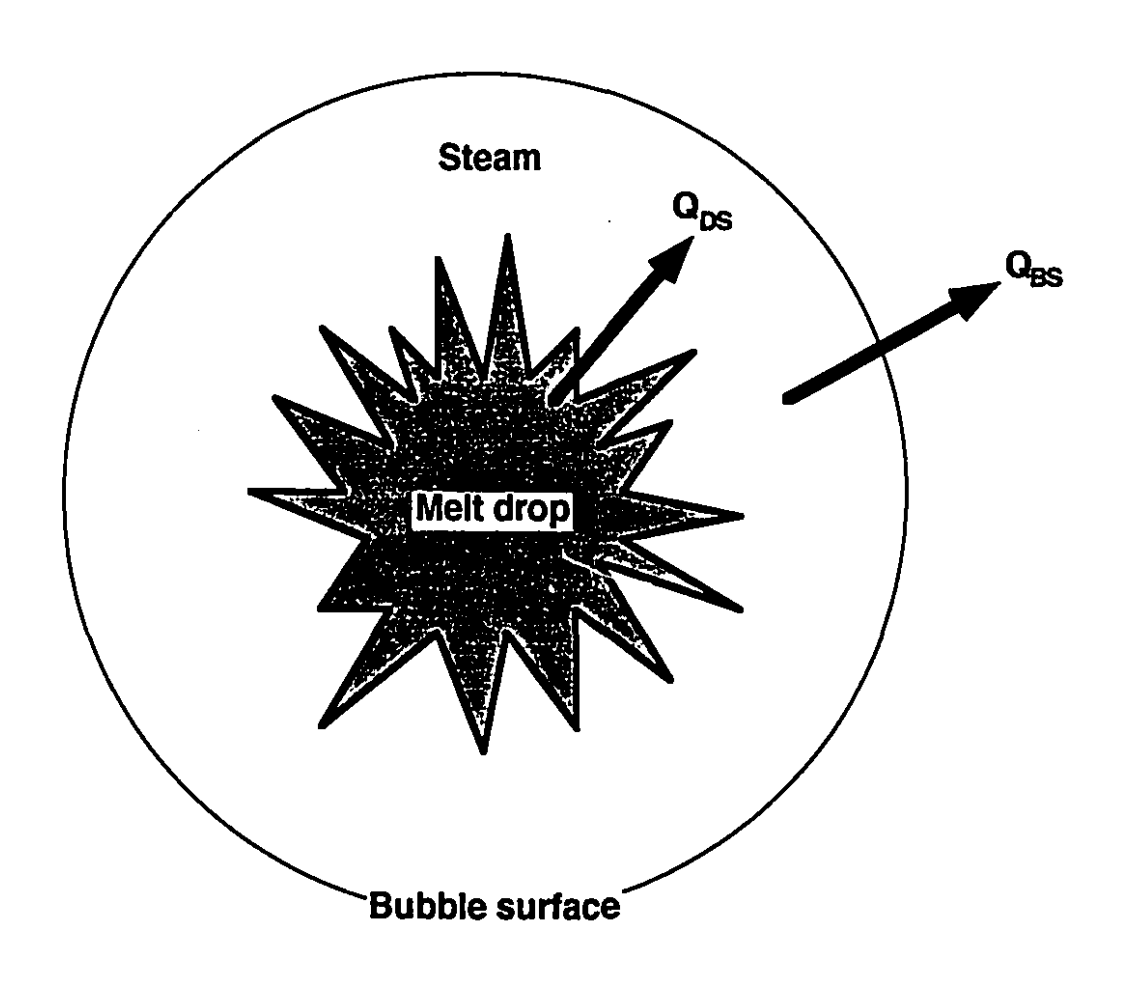


Figure 41: Control volume used in bubble dynamics model

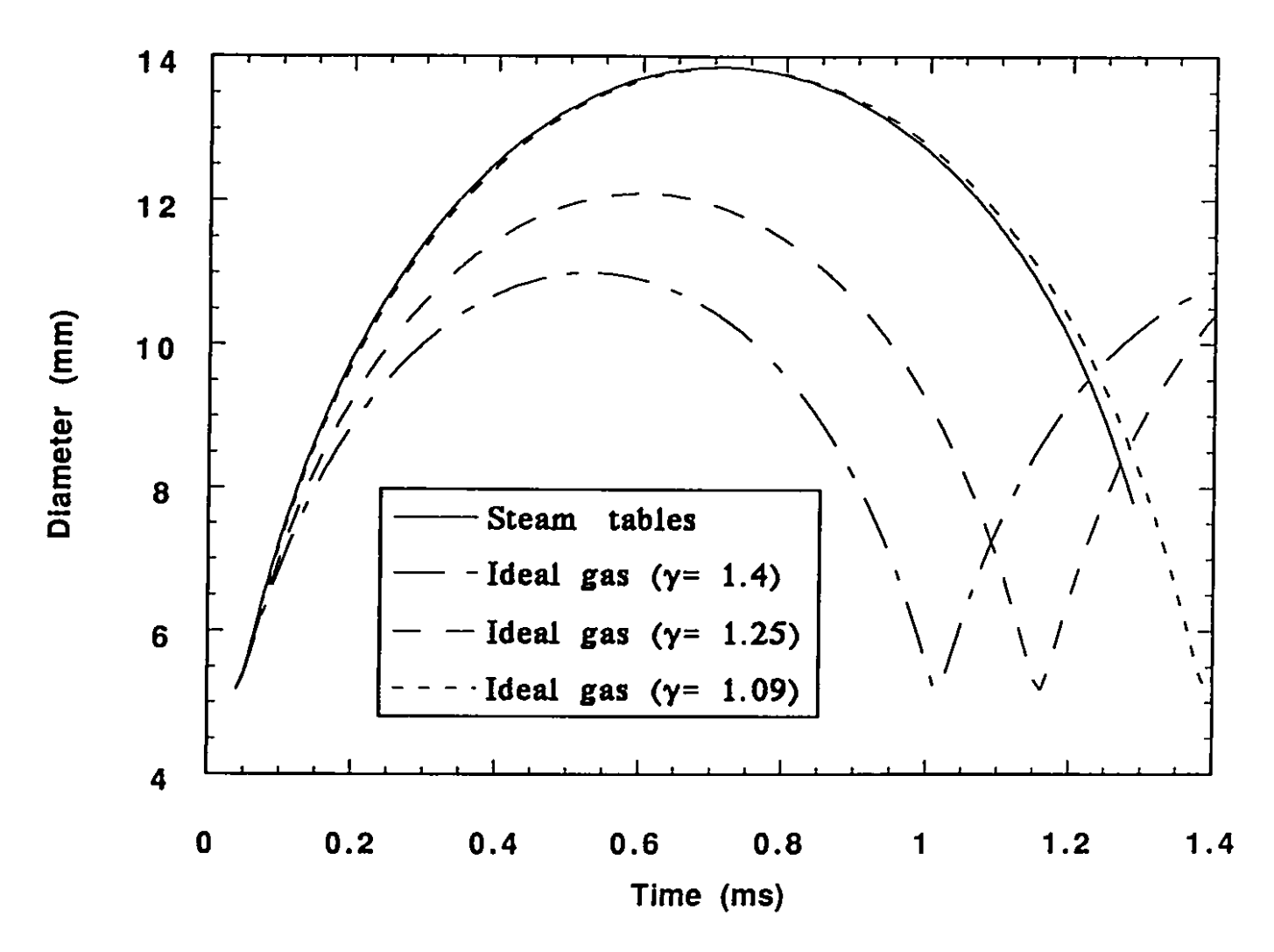


Figure 42: Numerically predicted bubble diameter growth curves with ideal gas assumption and real gas equation of state

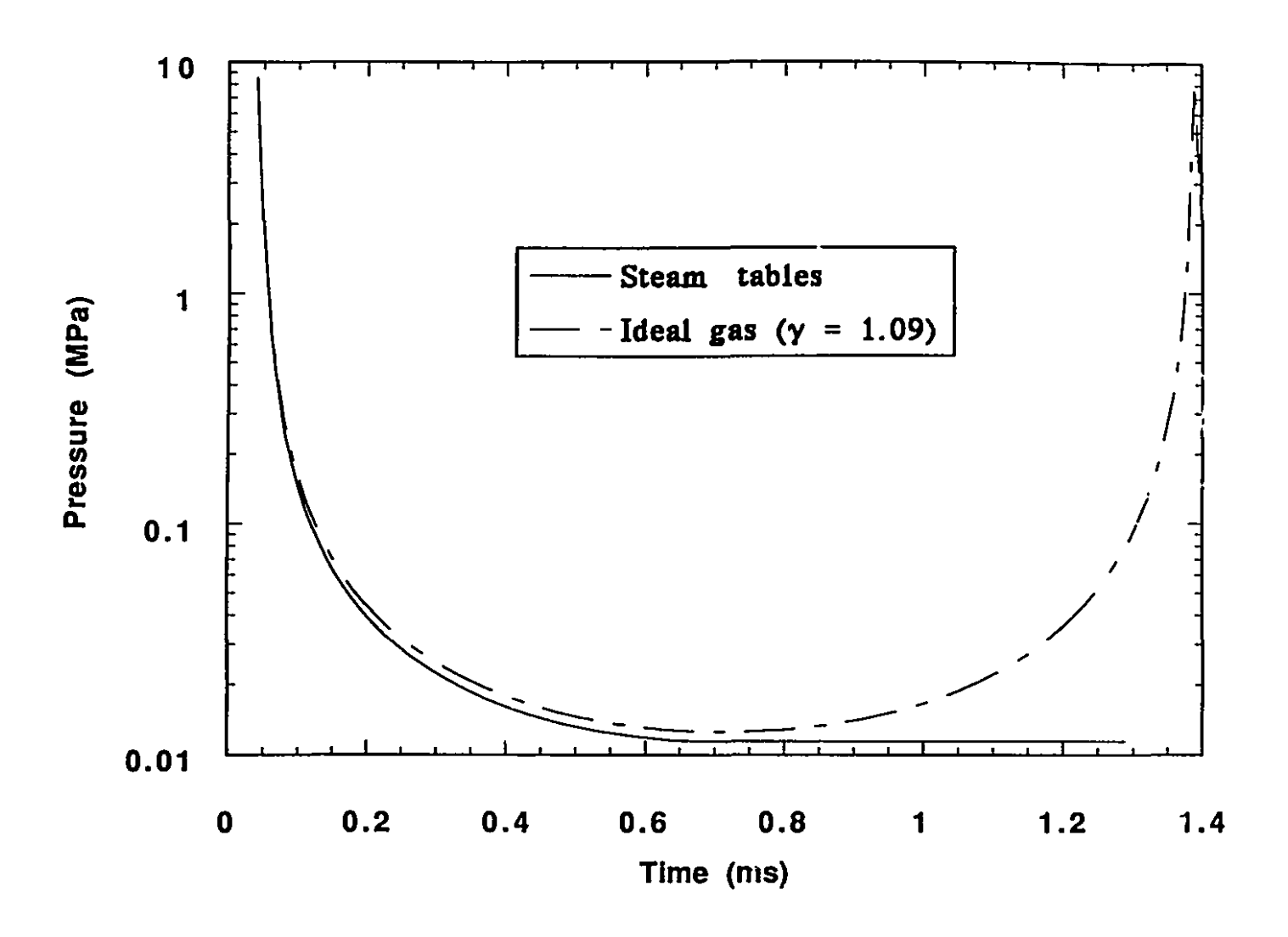


Figure 43: Bubble pressure time history for ideal gas and real gas



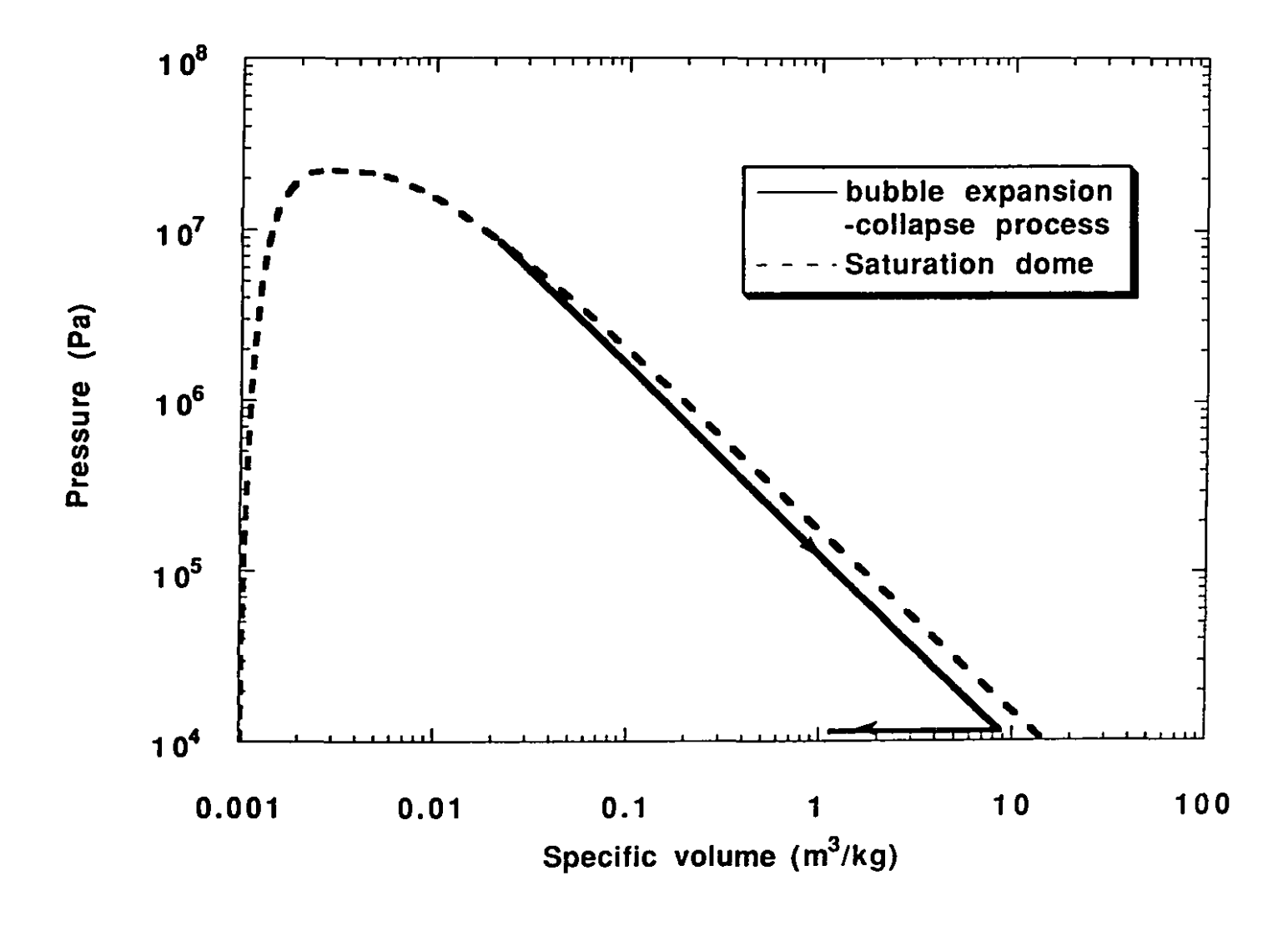


Figure 44: Steam bubble expansion and compression process predicted using real gas equation of state on a P-V plane

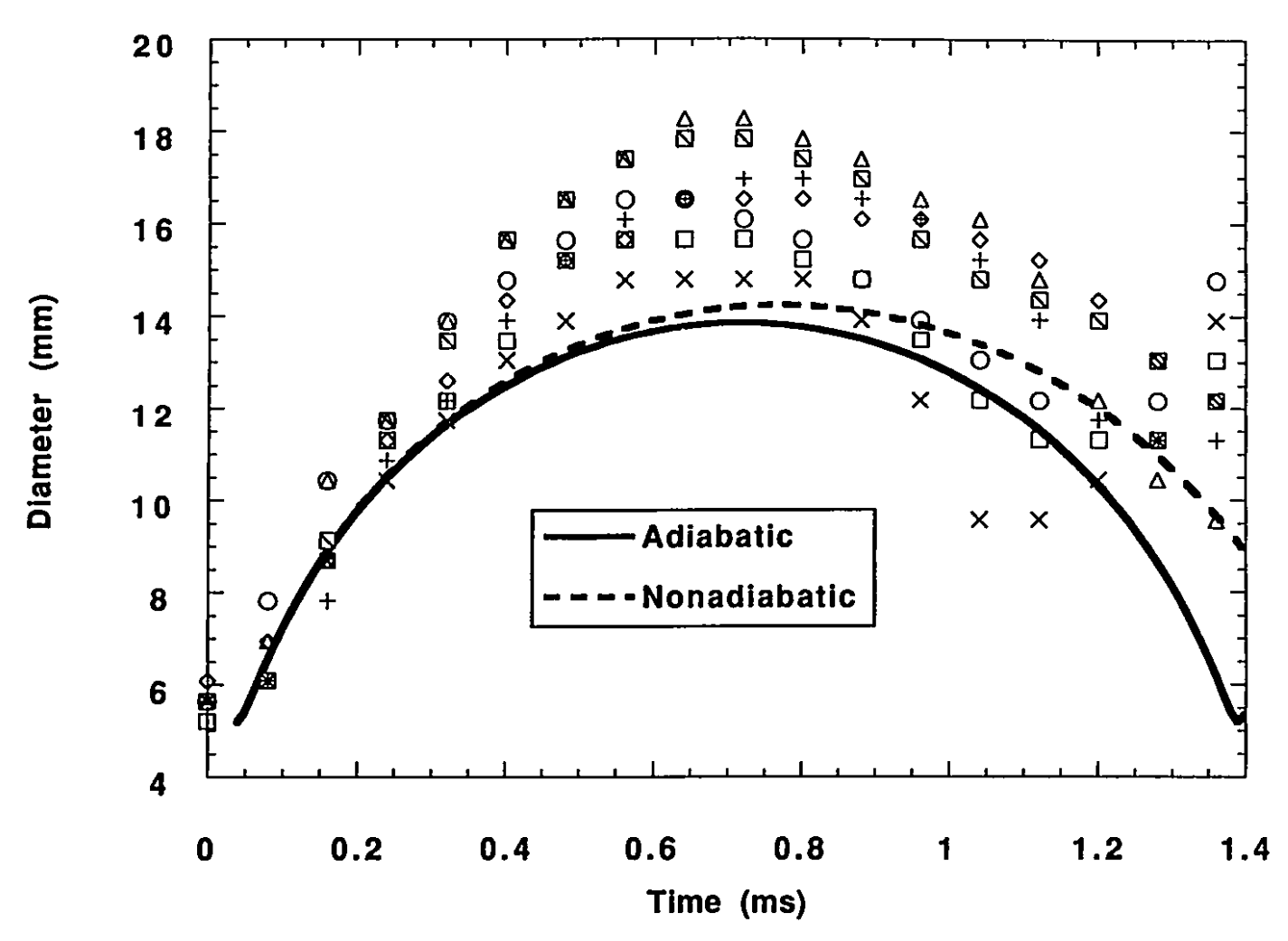
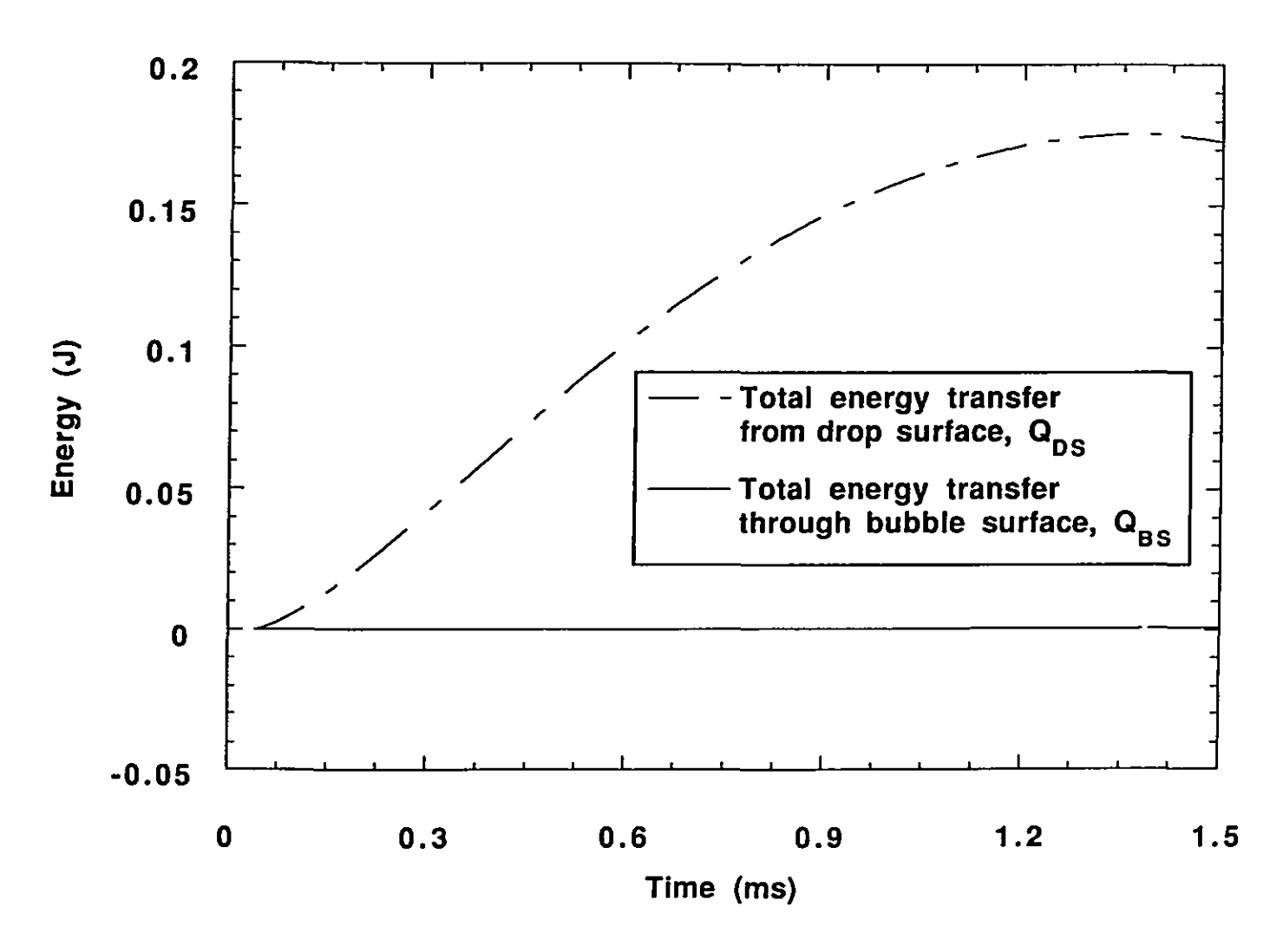


Figure 45: Numerically predicted bubble diameter growth curves for adiabatic and nonadiabatic cases using ideal gas assumption, superimposed on experimental data from Fig. 17



()

Figure 46: Graph showing the total heat added to and lost from the bubble as a function of time

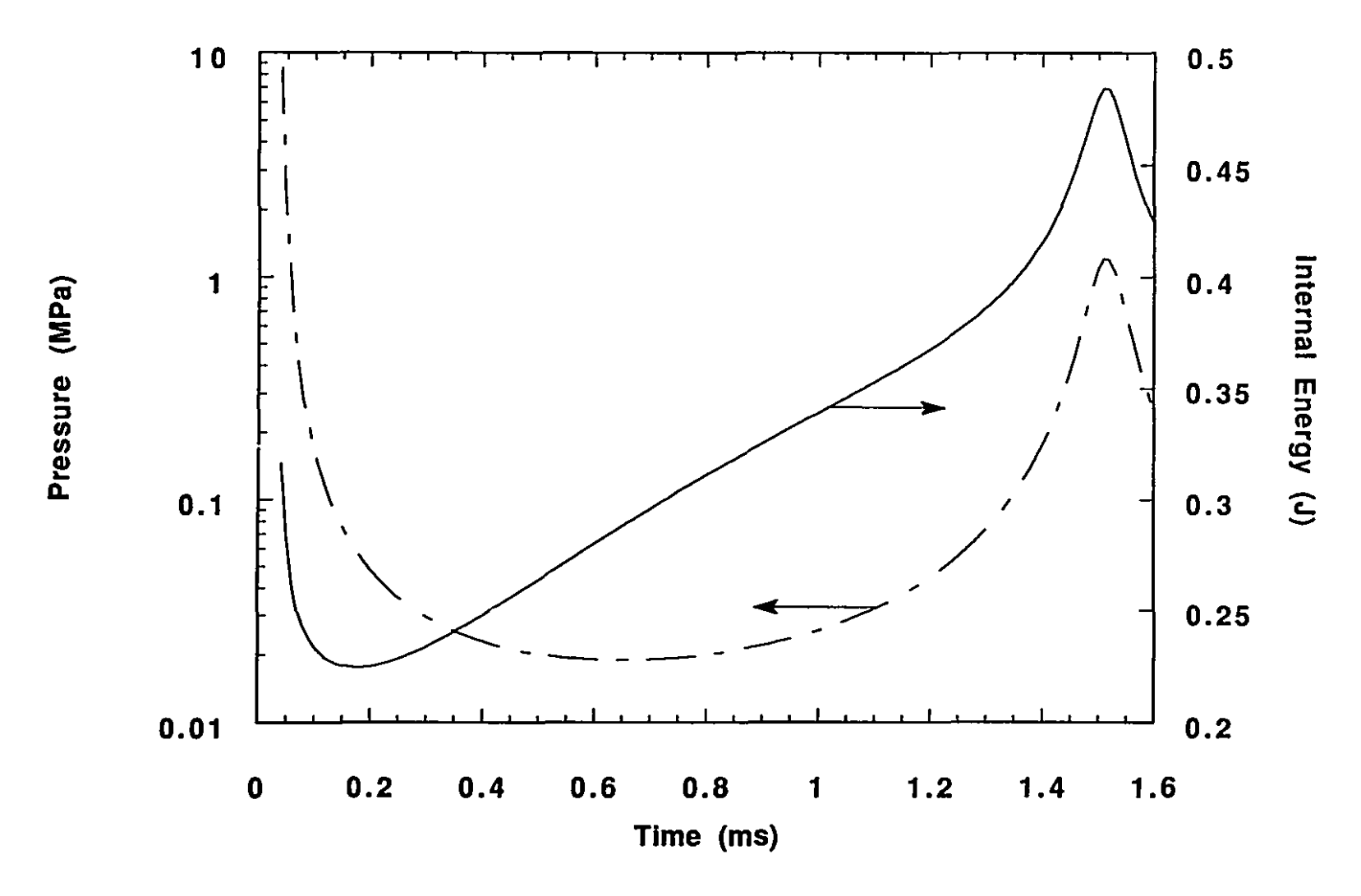


Figure 47: Bubble pressure and internal energy as a function of time for the nonadiabatic case

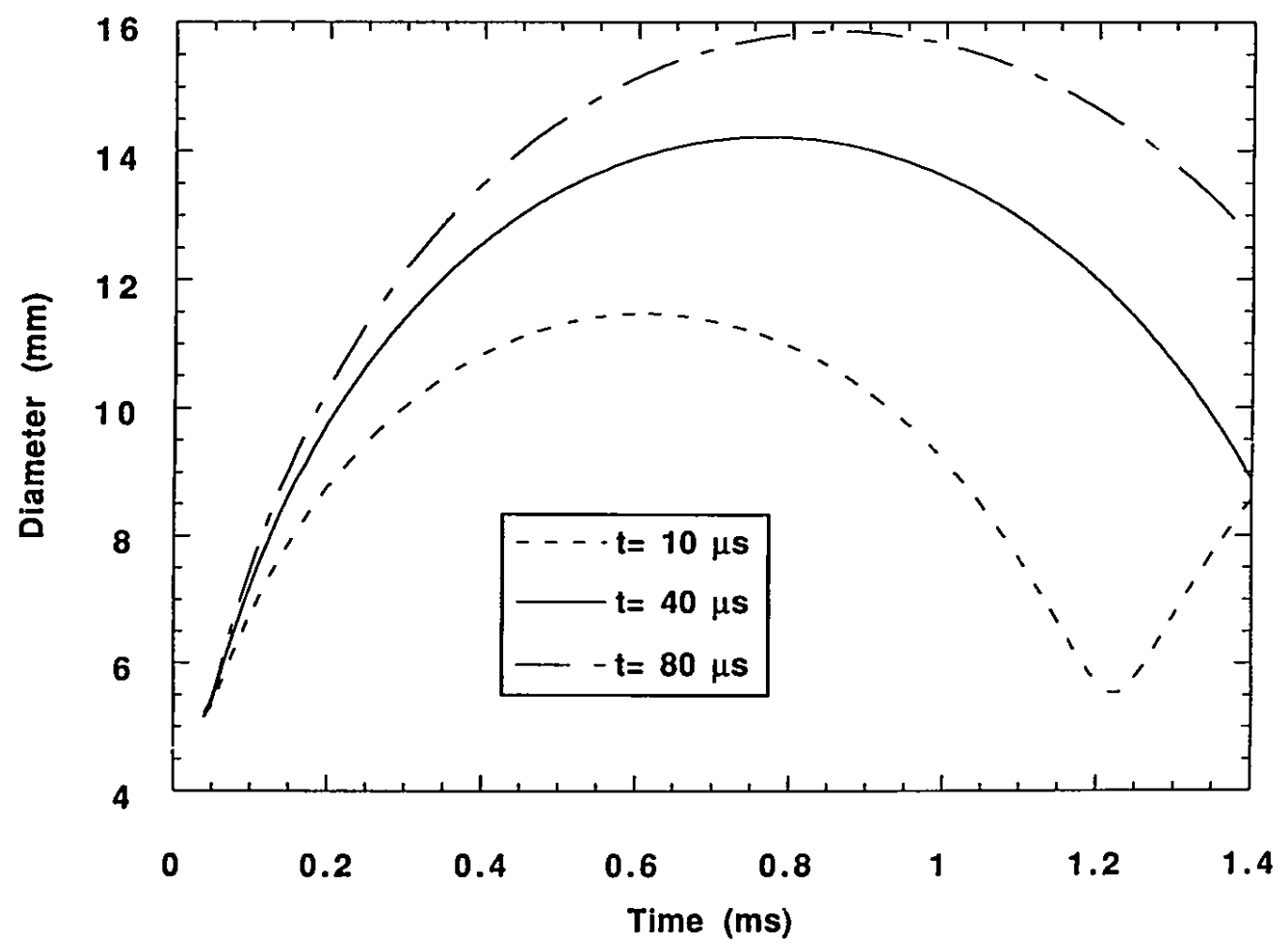


Figure 48: Numerically predicted bubble diameter growth curves for three initial drop water-surface contact times

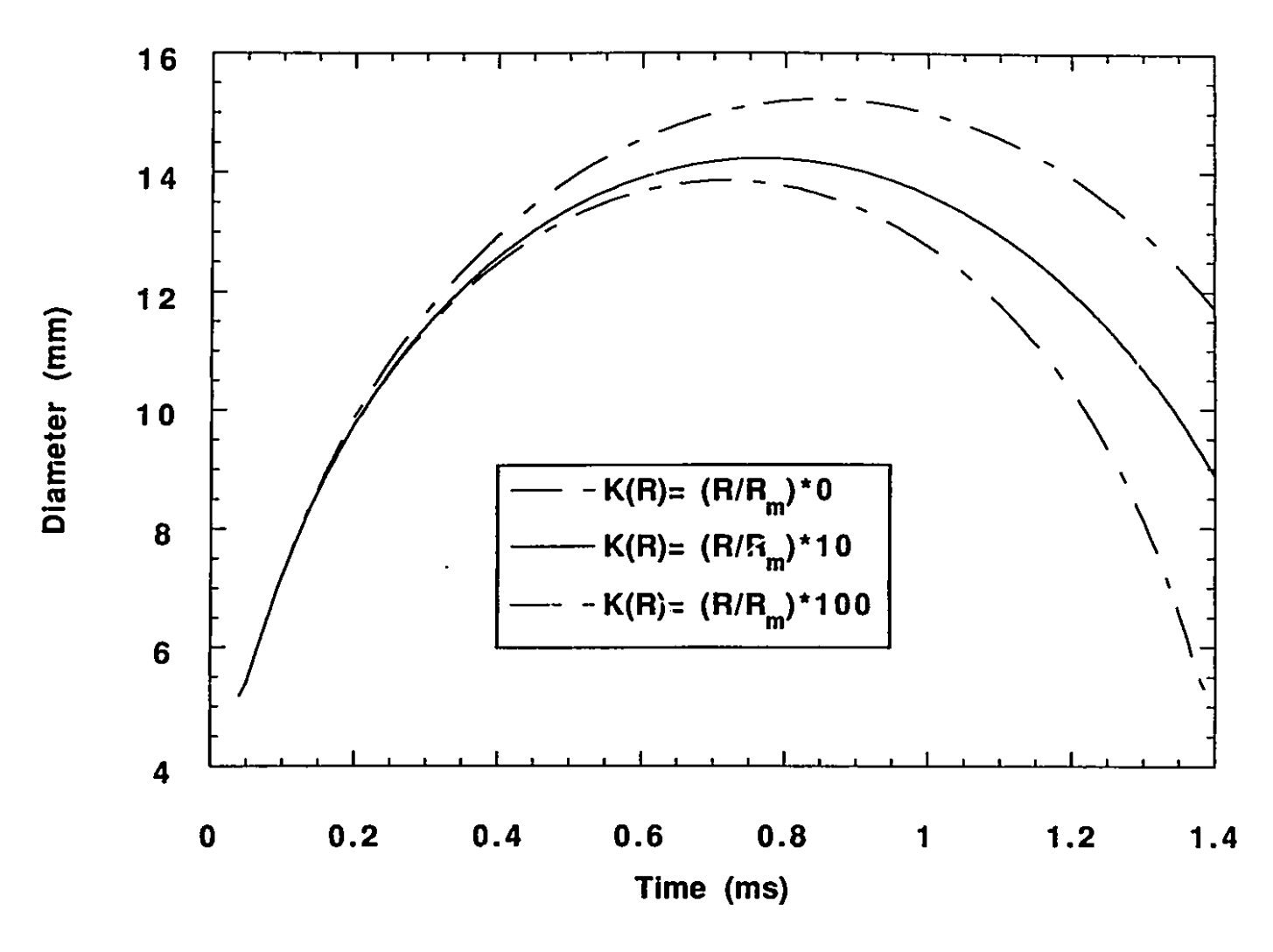


Figure 49: Numerically predicted bubble diameter growth curves for three different drop surface area growth factors

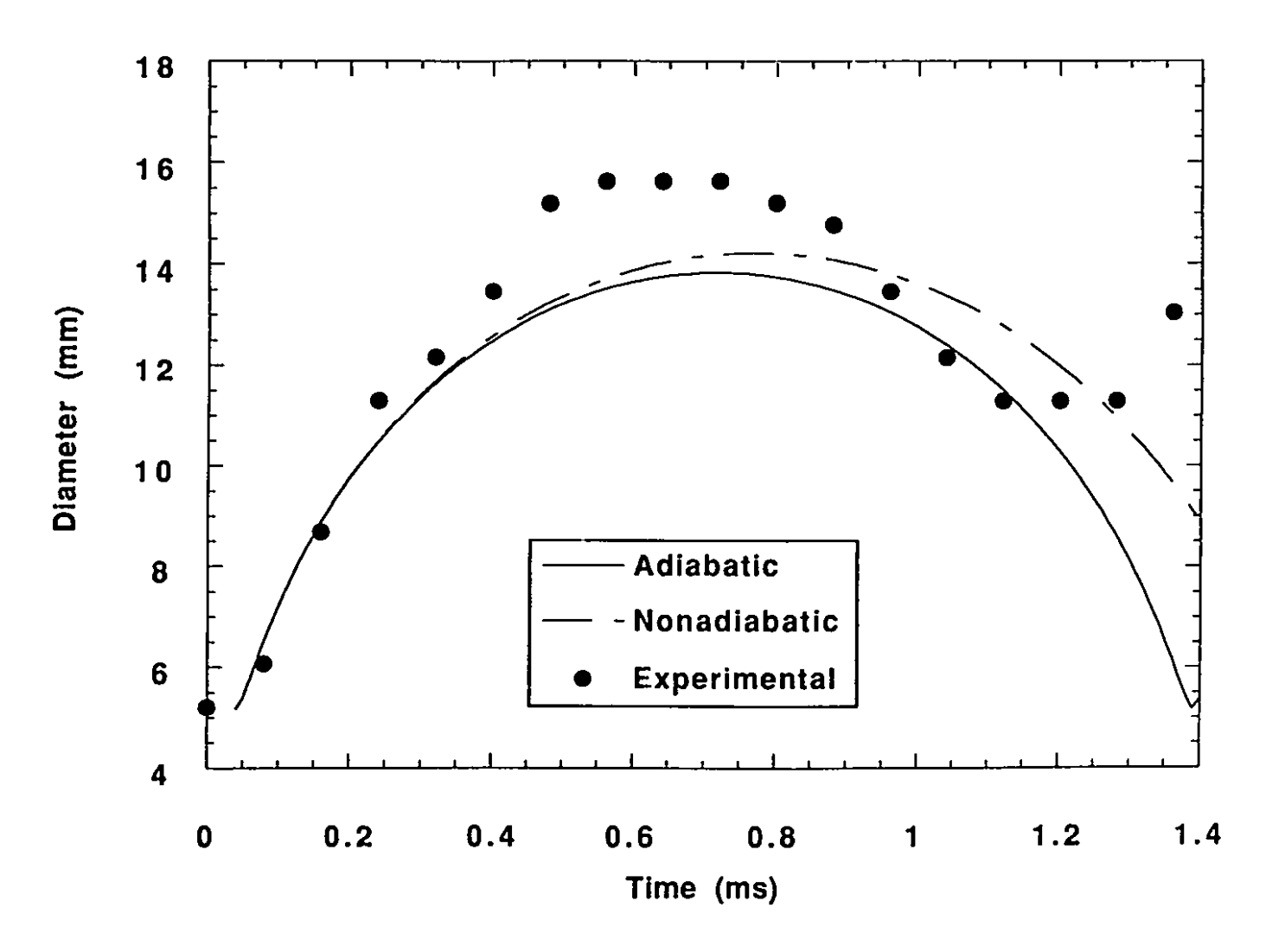


Figure 50: Experimental bubble diameter time history superimposed on two predicted curves for adiabatic and nonadiabatic cases

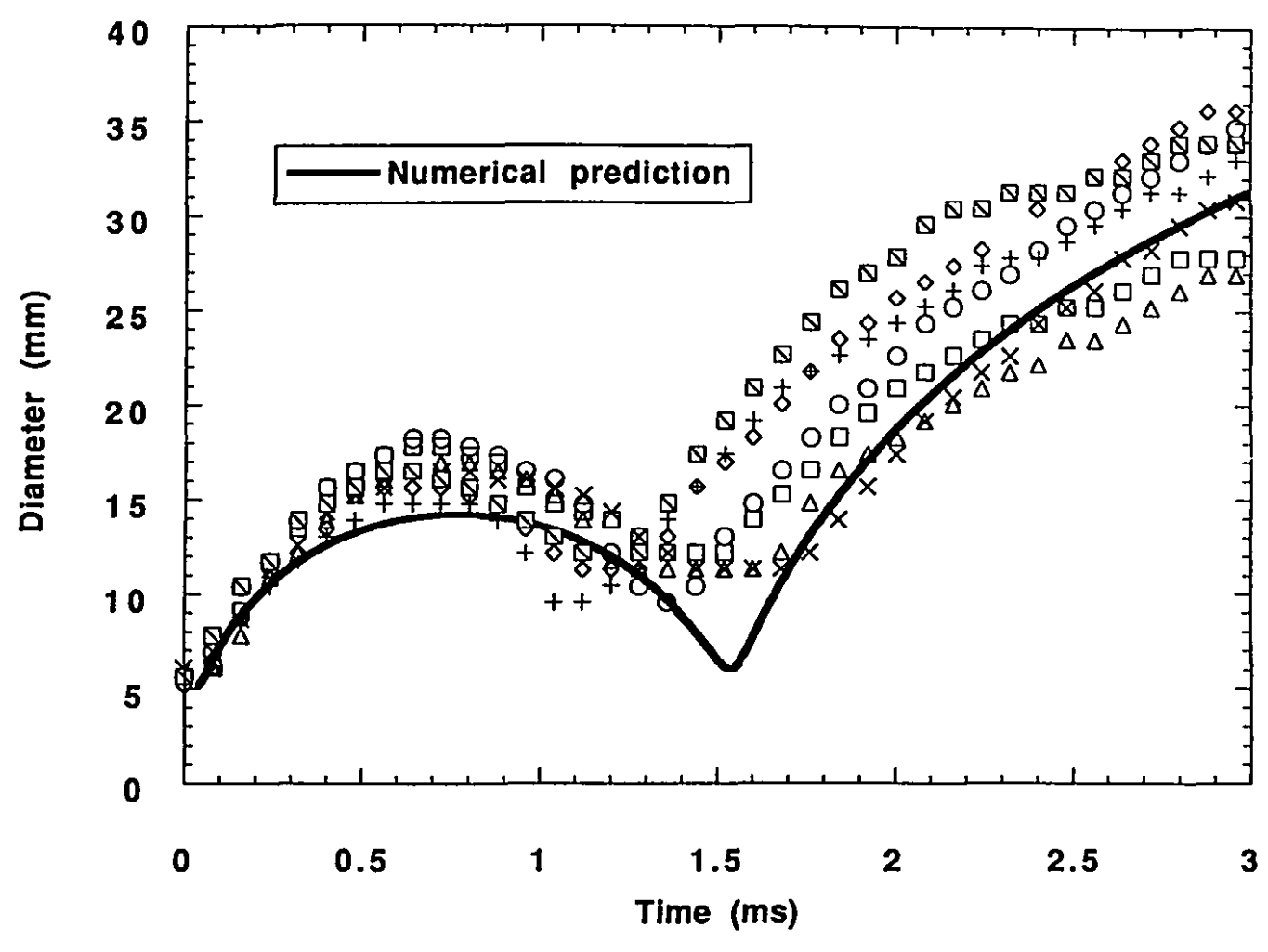


Figure 51: Numerical prediction of the first bubble cycle and the expansion phase of the second bubble superimposed on the experimental data from Fig. 17

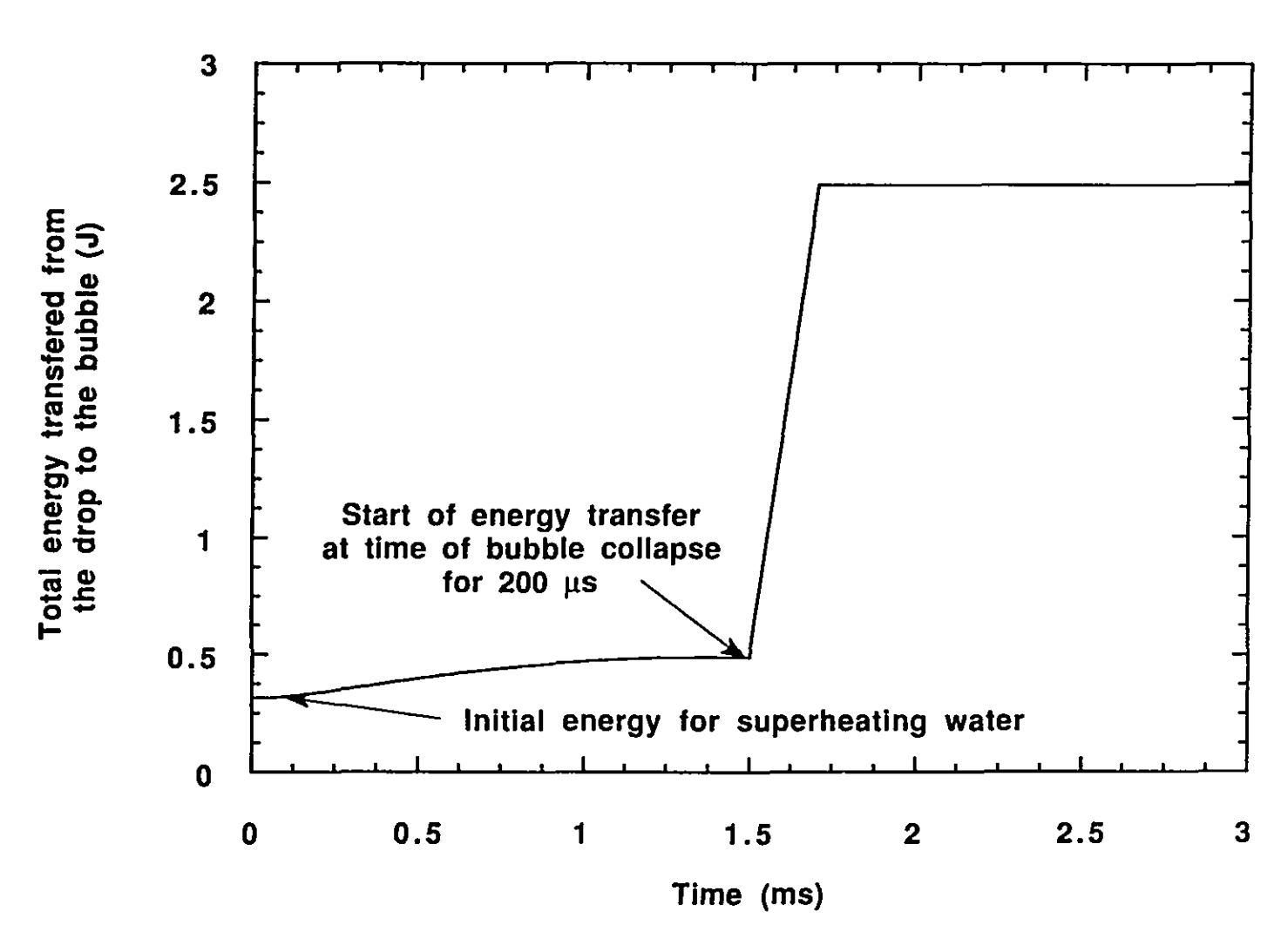


Figure 52: Total amount of energy transferred from the drop to the bubble, starting at the time of film collapse

work obatinable using contant volume mixing

Predicted work done by the bubble over the maximum

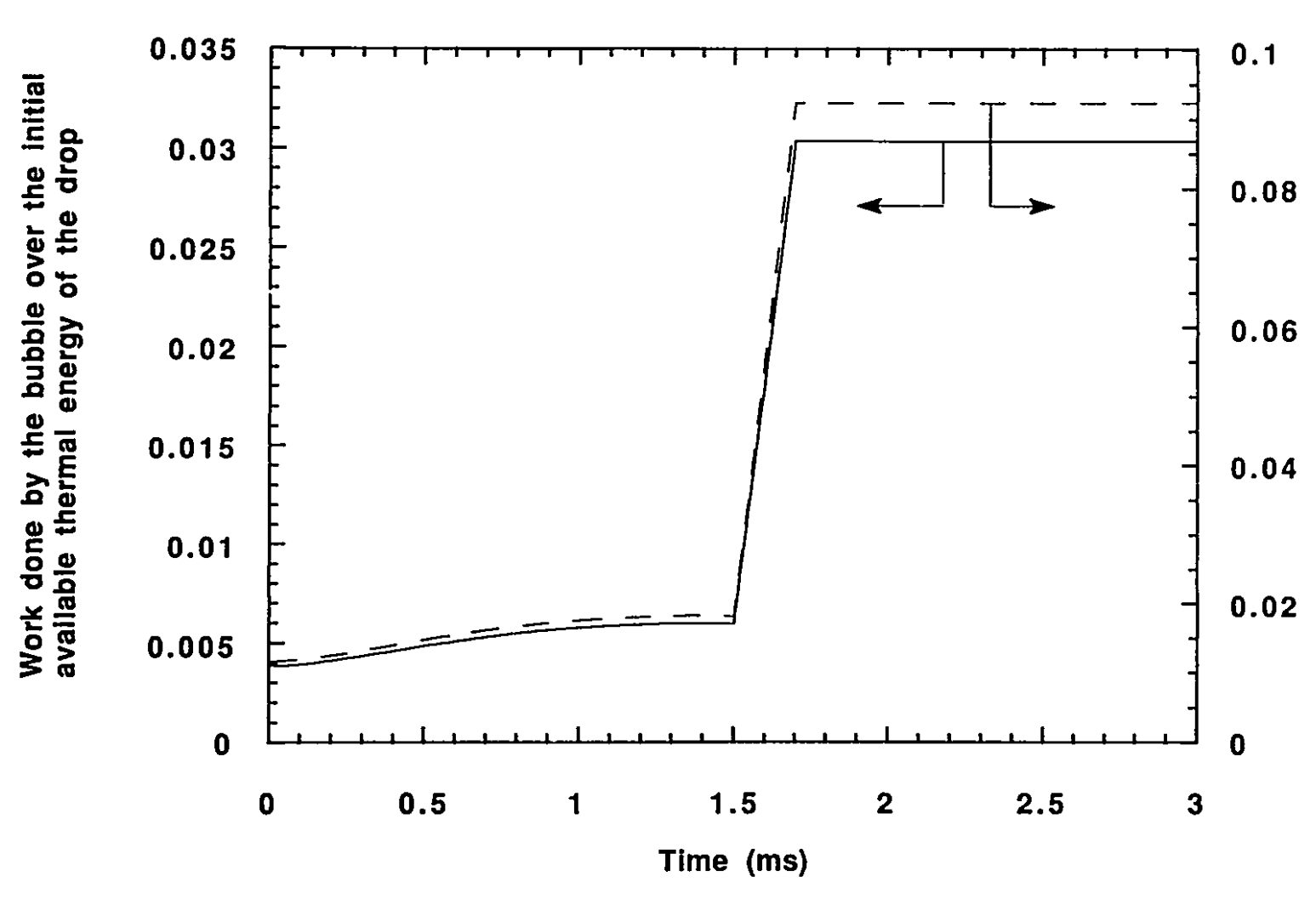


Figure 53: Work done by the vapor bubble over the work done by constant volume mixing and the initial thermal energy of the drop



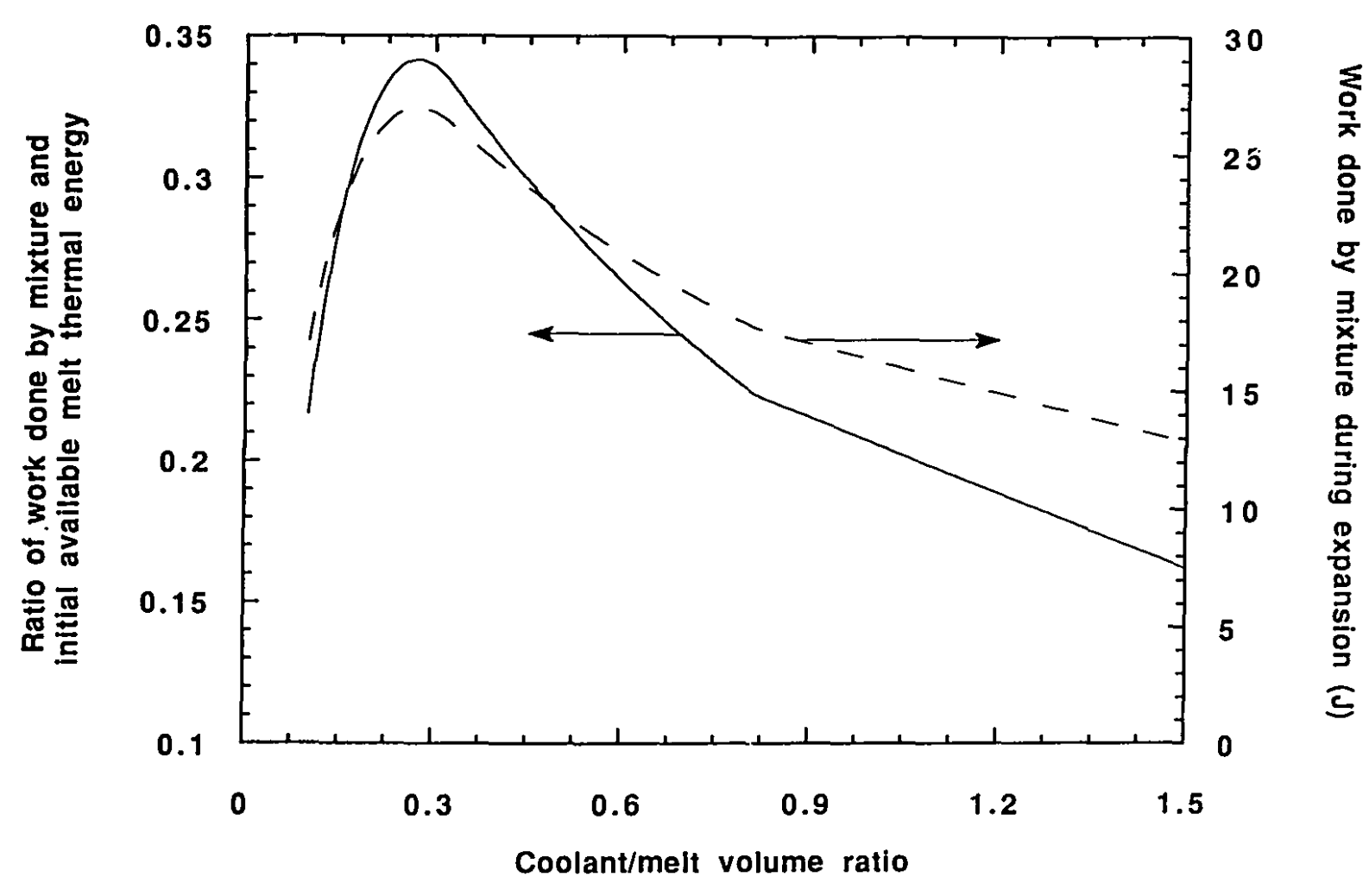
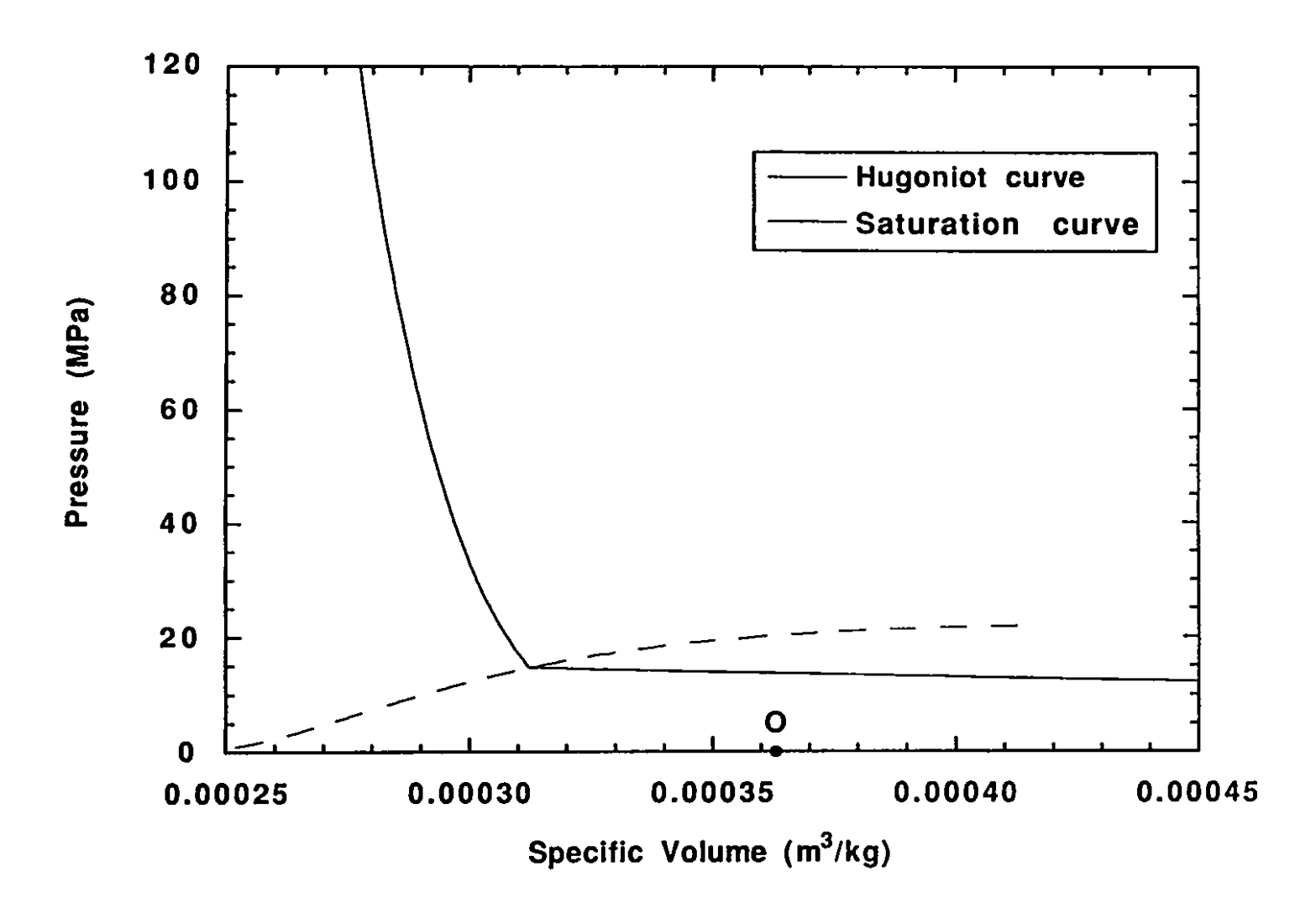
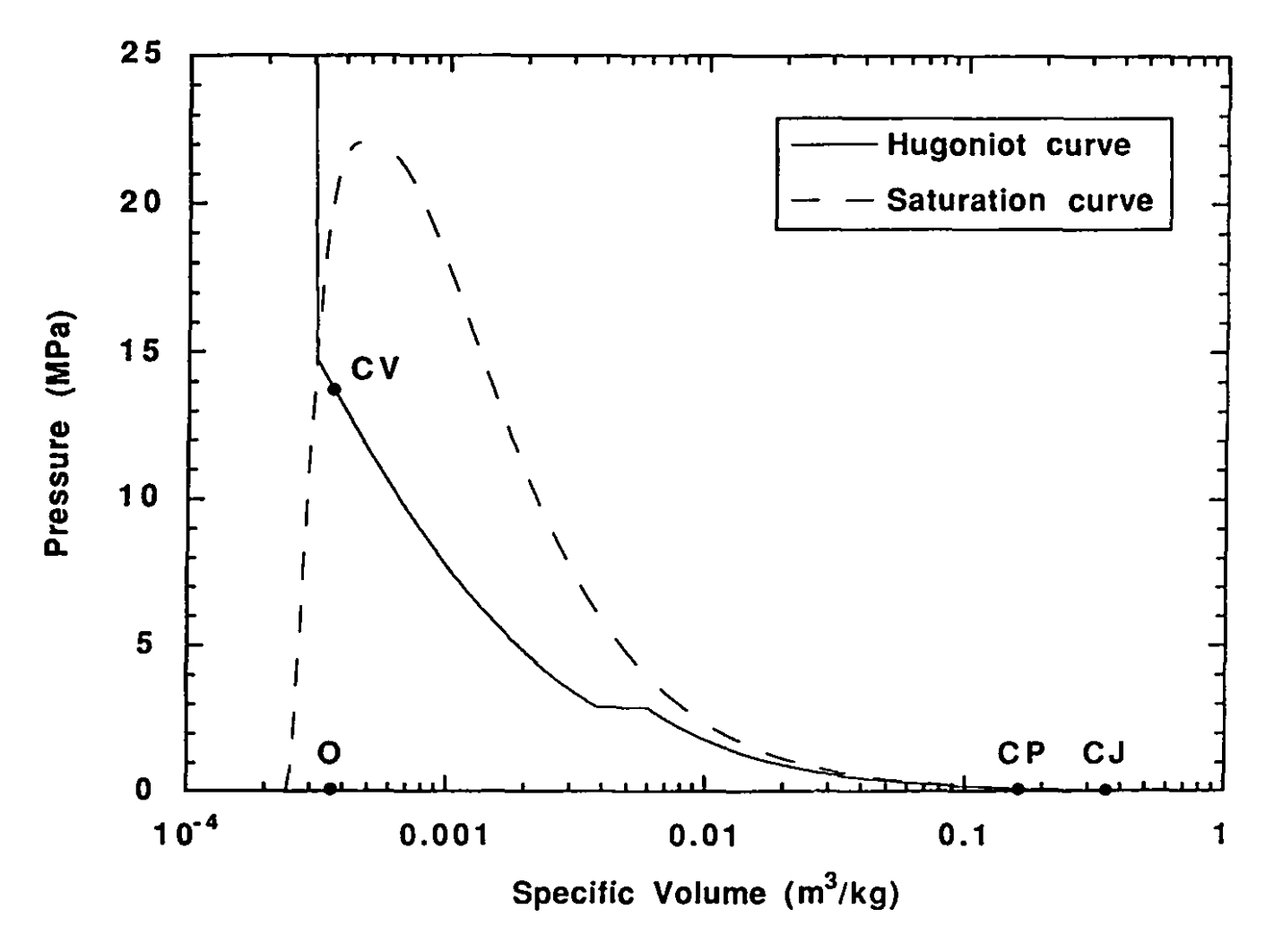


Figure 54: Work done by constant volume mixing of the tin and water until thermal equilibrium followed by isentropic expansion, and the ratio of this work and the initial thermal energy of the drop



eris.

Figure 55: Hugoniot curve for a mixture containing equal initial volumes of tin, water and steam. Tin temperature is 1000°C



1 24

Figure 56: Hugoniot curve for tin at 1000°C. Points denoted O, CV, CP, and CJ refer to initial conditions, constant volume process, constant pressure process and Chapman Jouget deflagration, respectively

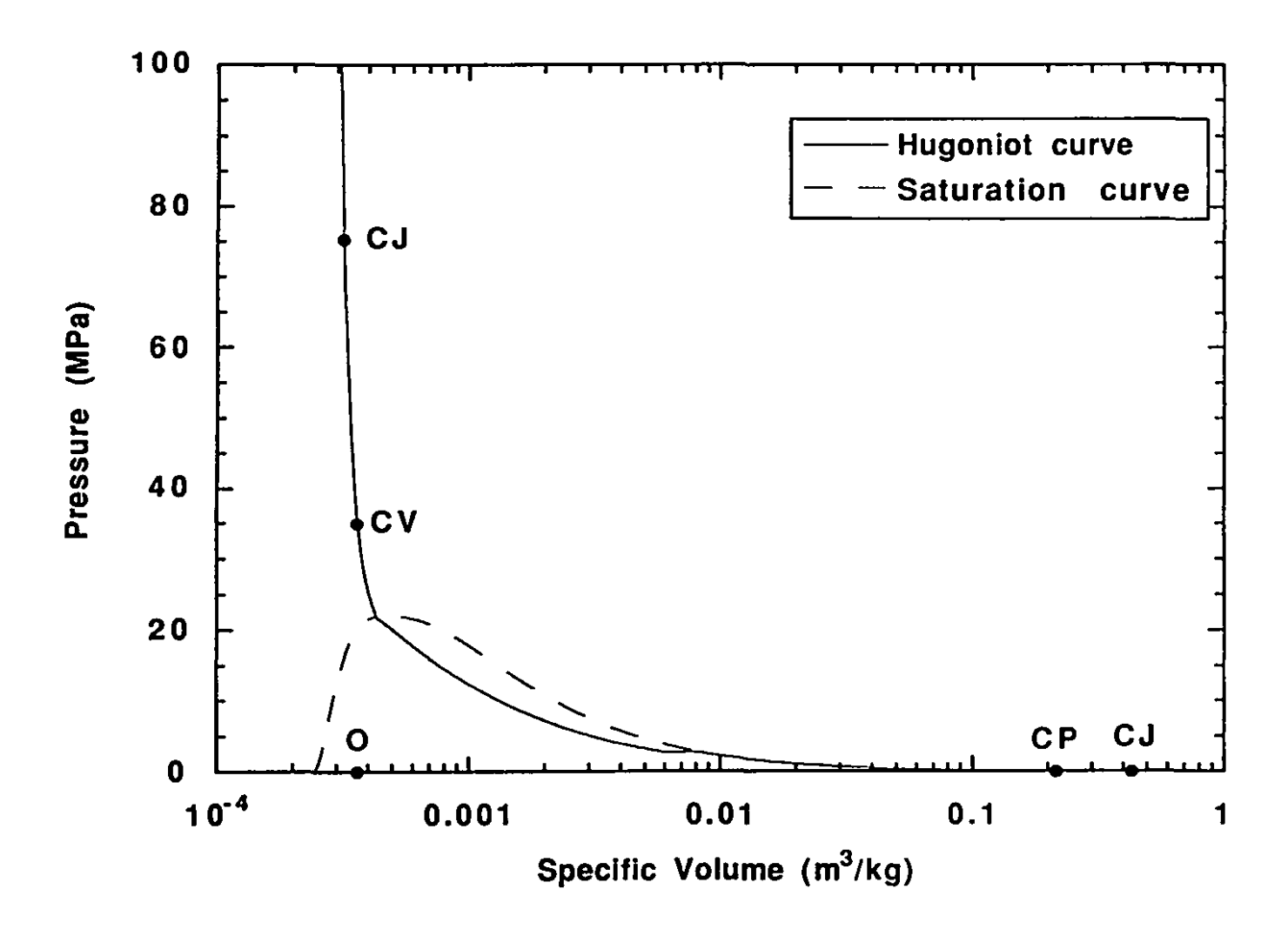


Figure 57: Hugoniot curve for tin at 1250°C (equal volumes of tin, water and steam)

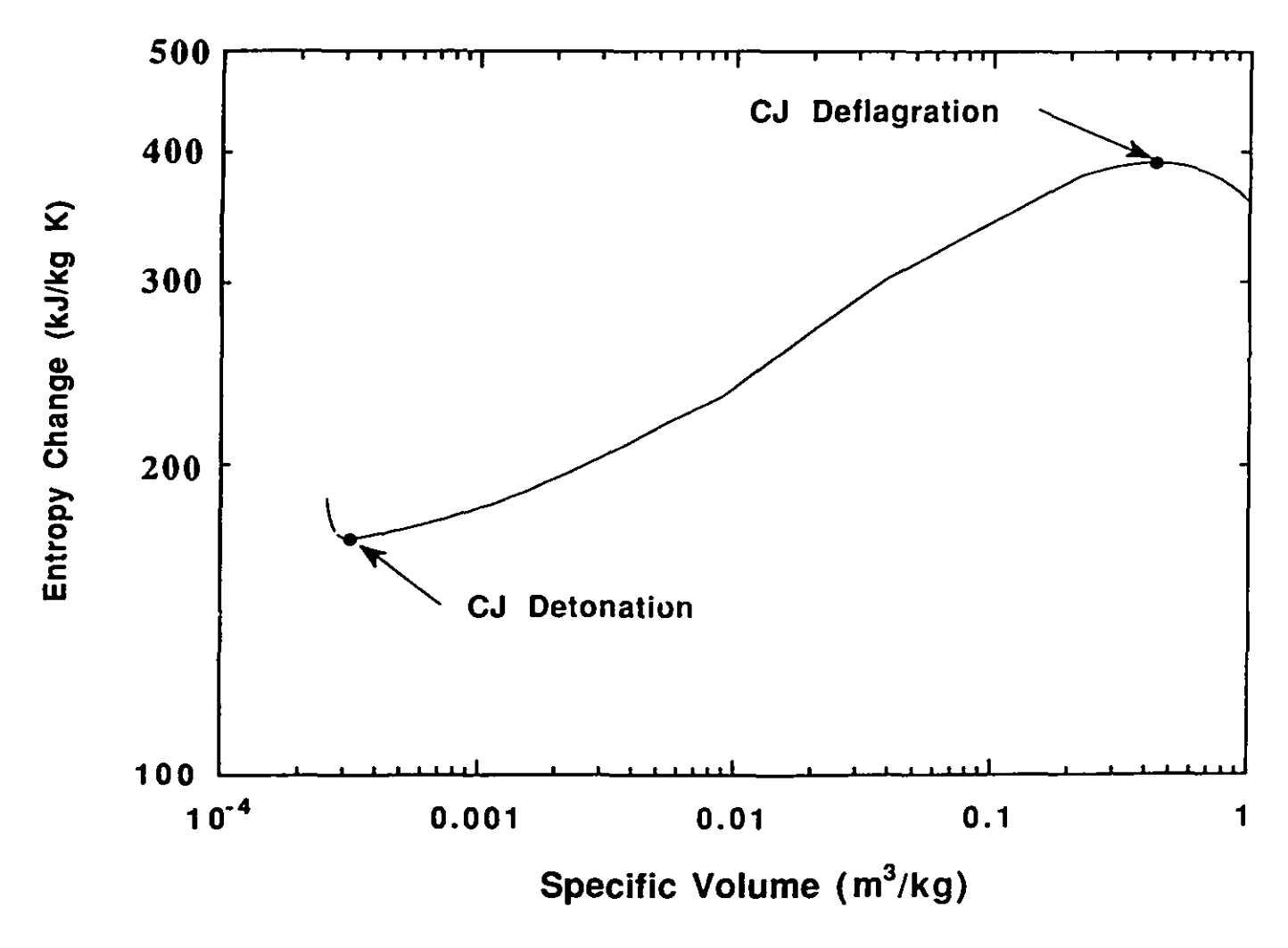


Figure 58: Variation of entropy change across reaction zone along the Hugoniot curve shown in Fig. 57

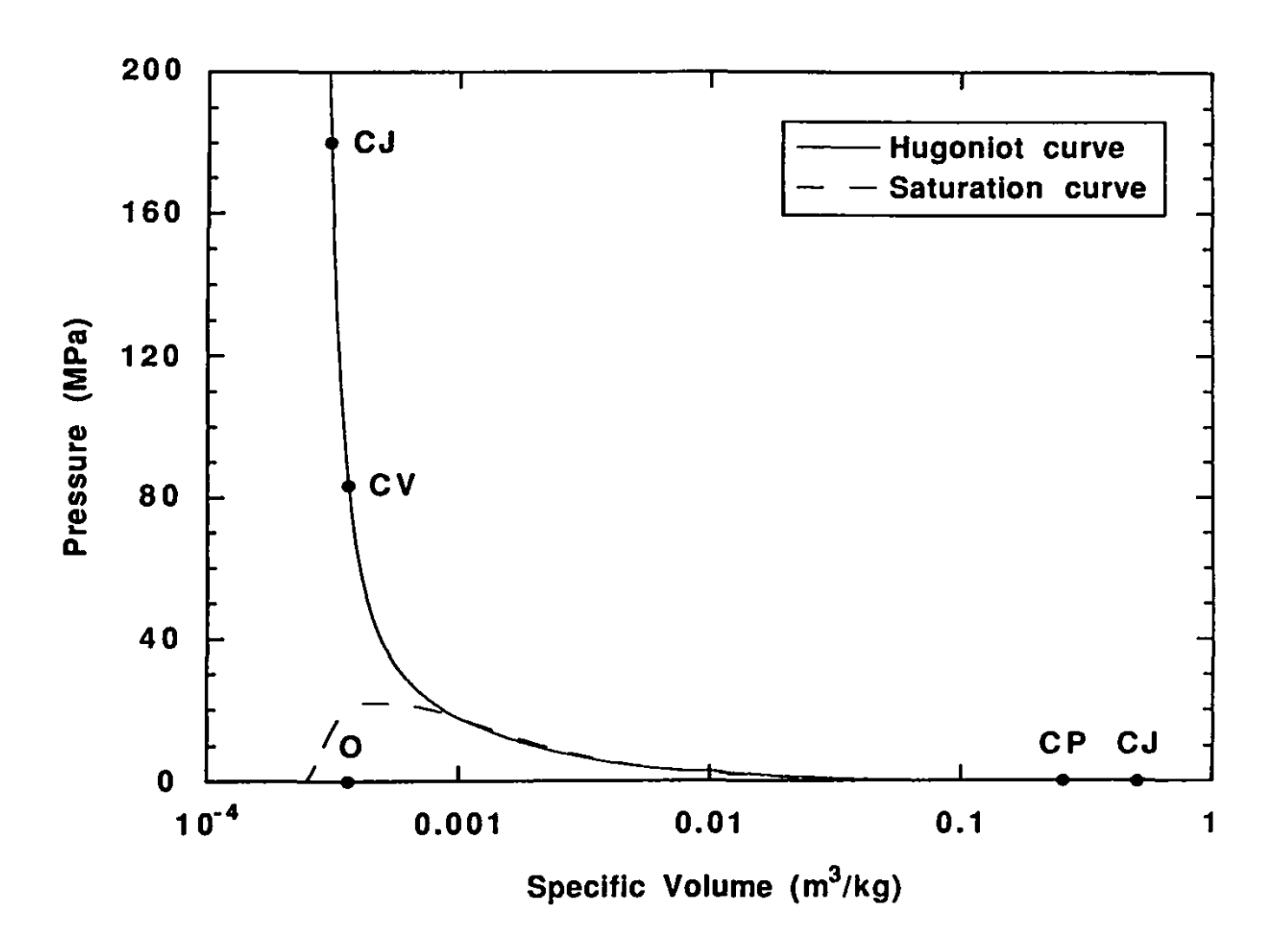
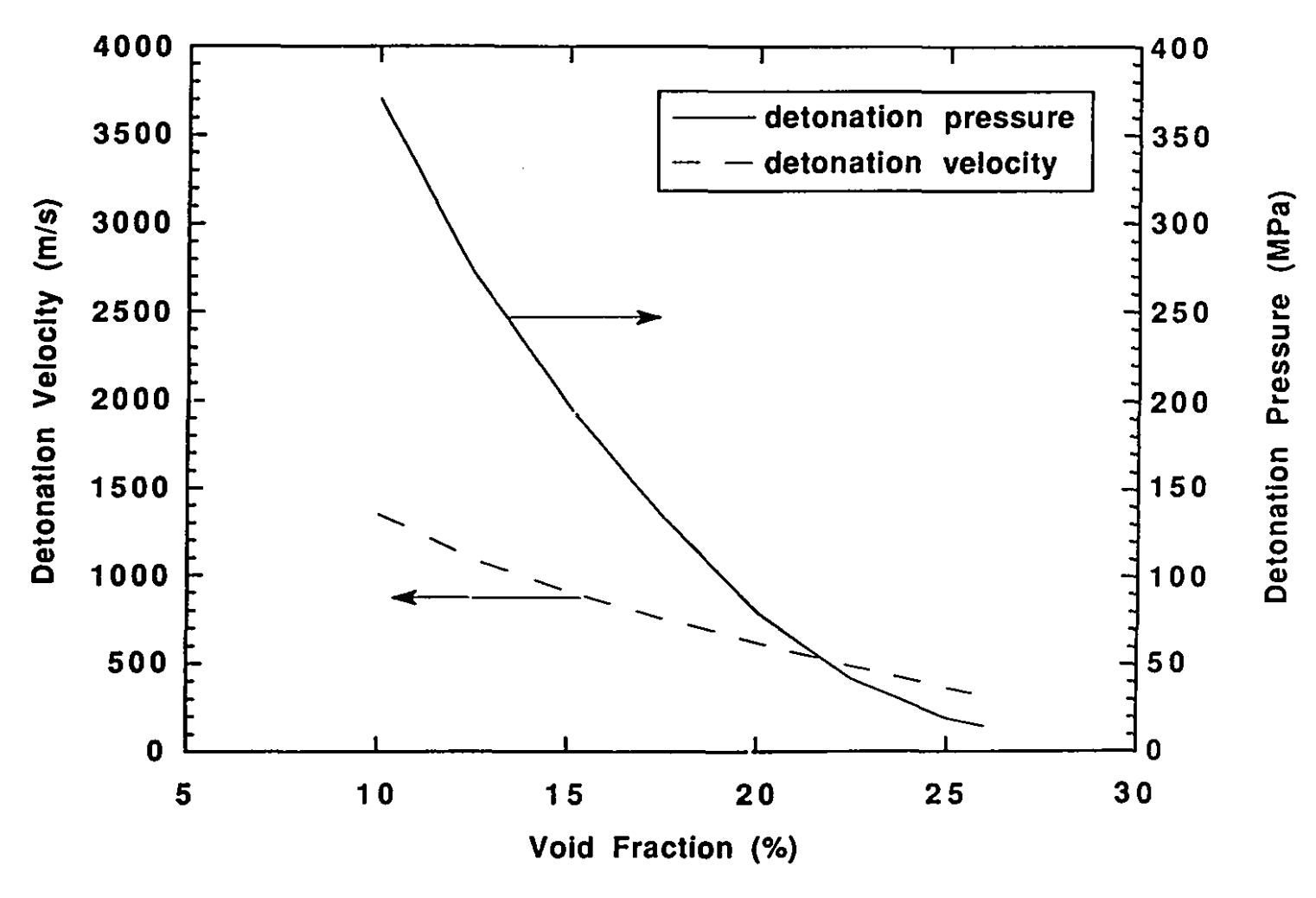


Figure 59: Hugoniot curve for tin at 1500°C (equal volumes of water, tin, and steam)





43

Figure 60: Variation of CJ detonation pressure and velocity as a function of void fraction for a mixture with equal volumes of tin (1000°C) and water

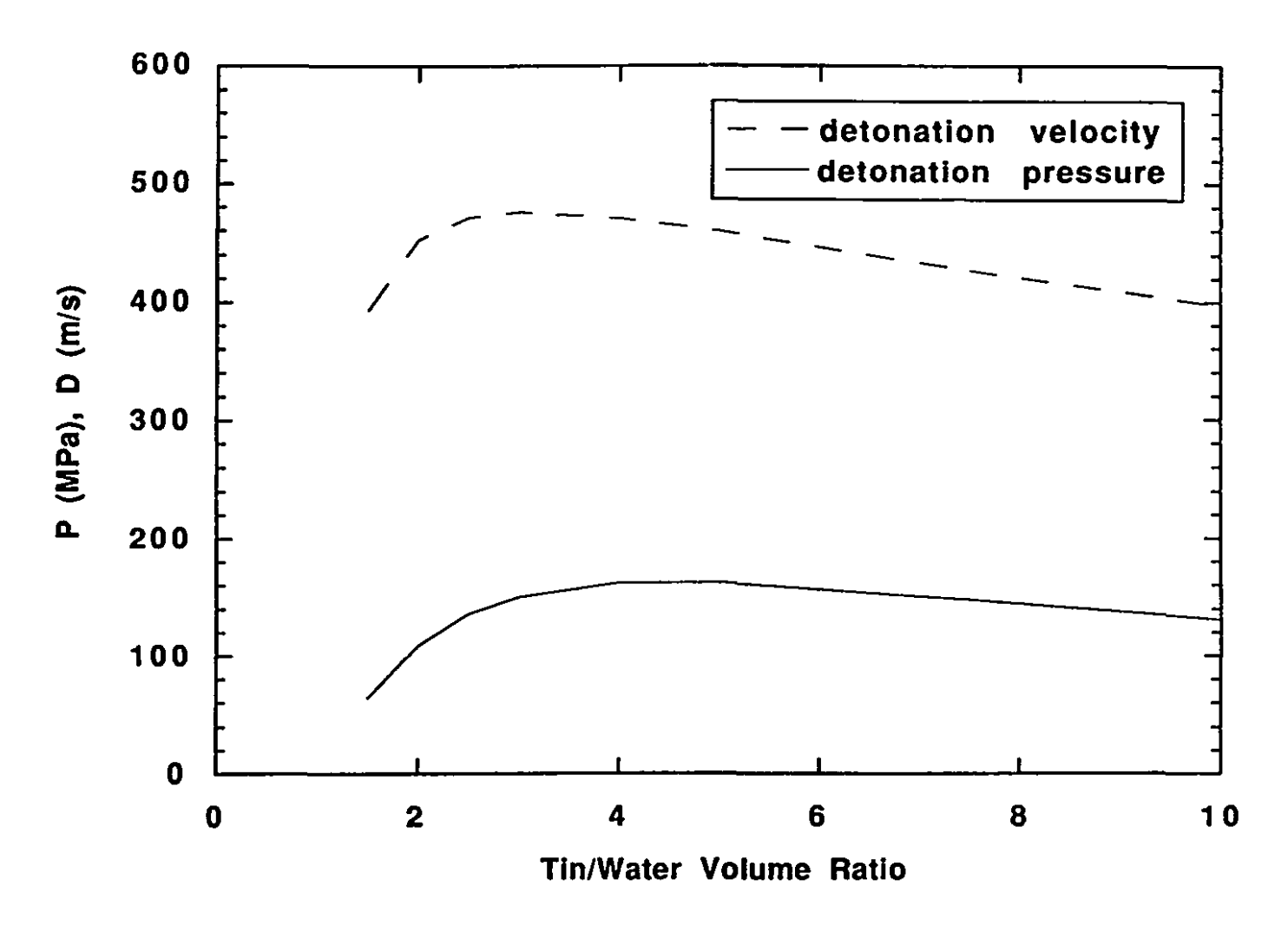


Figure 61: Variation of CJ detonation pressure and velocity as a function of tin/water volume ratio for a mixture containing tin at 1000°C. In each case the void fraction is 33.3%.